INVESTIGATION ON LOCAL STRUCTURES OF VARIOUS THIN FILM HEUSLER ALLOYS BY XAS AND XMCD MEASUREMENTS

By

Nirmalendu Patra

PHYS01201604009

Bhabha Atomic Research Centre

A thesis submitted to the
Board of Studies in Physical Sciences

In partial fulfillment of requirements
For the Degree of

DOCTOR OF PHILOSOPHY
of

HOMI BHABHA NATIONAL INSTITUTE

December 2019

HOMI BHABHA NATIONAL INSTITUTE
Recommendations of the Viva Voce Committee

As members of the Viva Voce Committee, we certify that we have read the dissertation prepared by Shri Nirmalendu Patra entitled "Investigations on local structures of various thin film Heusler alloys by XAS and XMCD measurements" and recommend that it may be accepted as fulfilling the thesis requirement for the award of Degree of Doctor of Philosophy.

Sr.No.	Name	Designation	Signature	Date
1.	**Dr. D.V. Udupa**	Chairman		13/12/2019
2.	**Prof. S. Mahamuni**	Examiner	SRMahamuni	Dec. 13, 2019
3.	**Dr. P.K. Mishra**	Member		13/12/2019
4.	**Dr. A. Biswas**	Member	Aniruddha	13/12/19
5.	**Dr. D. Bhattacharyya**	Guide & Convener		13/12/19

Final approval and acceptance of this thesis is contingent upon the candidate's submission of the final copies of the thesis to HBNI.

I hereby certify that I have read this thesis prepared under my direction and recommend that it may be accepted as fulfilling the thesis requirement.

Date: 13/12/19
Place: Mumbai

Dr. Dibyendu Bhattacharyya
(Guide)

STATEMENT BY AUTHOR

This dissertation has been submitted in partial fulfillment of requirements for an advanced degree at Homi Bhabha National Institute (HBNI) and is deposited in the Library to be made available to borrowers under rules of the HBNI.

Brief quotations from this dissertation are allowable without special permission, provided that accurate acknowledgement of source is made. Requests for permission for extended quotation from or reproduction of this manuscript in whole or in part may be granted by the Competent Authority of HBNI when in his or her judgment the proposed use of the material is in the interests of scholarship. In all other instances, however, permission must be obtained from the author.

NIRMALENDU PATRA

DECLARATION

I, hereby declare that the investigation presented in the thesis has been carried out by me. The work is original and has not been submitted earlier as a whole or in part for a degree / diploma at this or any other Institution / University.

NIRMALENDU PATRA

List of Publications arising from the thesis

Journal publications:

1. Structural and magnetic characterization of the $Ni_{55}Fe_{19}Ga_{26}$ shape memory alloy thin film.
   N. Patra, A. Biswas, C.L. Prajapat, A. Ghosh, P.U. Sastry, S. Tripathi, P.D. Babu, Arup Biswas, S.N. Jha and D. Bhattacharyya.
   Journal of Alloys and Compounds723 (2017) 1098-1112.

2. Correlation of structural ordering with magnetic properties of Pulsed Laser Deposited Co_2FeGa Heusler alloy thin films.
   N. Patra, C.L. Prajapat, Rajnarayan De, K.D. Rao, P.D. Babu, A.K. Sinha, SijuJohn, H.C. Barshilia, S.N. Jha and D. Bhattacharyya,
   Journal of Alloys and Compounds748 (2018) 653 – 670.

3. Pulsed laser deposited Co_2FeSi Heusler alloy thin films: Effect of different thermal growth processes.
   N. Patra, C.L. Prajapat, P.D. Babu, S. Rai, S. Kumar, S.N. Jha, D. Bhattacharyya.
   Journal of Alloys and Compounds 804 (2019) 470 – 485.

4. Effect of growth temperature on the structural and magnetic properties of the Pulsed laser deposited Co_2FeAl thin films.
   N. Patra, C.L. Prajapat, P.D. Babu, S. Rai, S. Kumar, S.N. Jha and D. Bhattacharyya.
   Journal of Alloys and Compounds779 (2019) 648 – 659.

5. First result from the XMCD facility at the Energy Dispersive EXAFS beamline, Indus-2 synchrotron source,
   N. Patra, U.G.P.S. Sachan, S. Sundar Rajan, Sanjay Malhotra, Vijay Harad, Ankur Agarwal, Ashutosh Diwedi, S. N. Jha and D. Bhattacharyya.
   Journal of Synchrotron Radiation *26* (2019) 445 – 449.

6. DFT study on full Heusler alloys (X_2YZ) for magnetic moment calculations and XAS and XMCD simulations.
   N. Patra, Aparna Chakrabarti, Arup Banerjee and D. Bhattachryya.
   (Manuscript under preparation).

Conference presented:

1. Structural characterization of $Ni_{55}Fe_{19}Ga_{26}$ ferromagnetic shape memory alloy thin film by X-ray absorption spectroscopy.**N. Patra**, A. Biswas, C. L. Prajapat, P.U. Sastry, S. Tripathy, S.N. Jhaand D. Bhattacharyya. European Congress & Exhibition on Advance

Materials and Processes (EUROMAT-2017), Thessaloniki, Greece. 17 – 22 September, 2017.

2. Cationic antisite disorder between the constituent atoms of Co_2FeGa Heusler alloy thin film: a detail EXAFS study. N. Patra. 2nd International Conference on Recent Trends in Environment and Sustainable Development (RTESD-2019), Vivekananda Global University, Jaipur, Rajasthan, India. 17 – 19 October 2019. (Oral presentation)

NIRMALENDU PATRA

Dedicated to My Beloved Parents

ACKNOWLEDGEMENT

At first I would like to convey my grateful and sincere thanks to my Ph.D. supervisor Dr. Dibyendu Bhattacharyya for his guidance, understanding and patience during my doctoral studies at Bhabha Atomic Research Centre, Mumbai. His mentorship was paramount in providing a well-rounded experience consistent with my long term carrier goal. Despite of his very busy schedule and countless responsibilities, he has been guided me very selflessly and unflinchingly and constantly encouraged me in every step of my PhD. I am also very much thankful to Dr. Shambhu Nath Jha, who acted as a very supporting role for discussing about the scientific problems, expert guidance and supervision during my experiments at Indus-2. I would like to thank all the members of the Synchrotron Science & Multilayer Physics Section and XAFS research group Dr. Arup Biswas, Dr. Ashok Kumar Yadav, Dr. Chandrani Nayak, Shri Ankur Agrawal and Shri Ashutosh Diwedi and other endearing colleagues of Atomic & Molecular Physics Division who helped me in every possible way. I am deeply indebted to Dr. Parasmani Rajput for all the support she has given me during my trips to RRCAT, Indore. She was ever-ready for motivational discussions and always had valuable advice to give me. I am also very much thankful to Dr. N. K. Sahoo, former Associate Director, Physics Group and former Head of Atomic & Molecular Physics Division, BARC for his continuous encouragement during my Ph.D. work. I am also thankful to Dr. M. N. Deo, present Head of Atomic and Molecular Physics Division, BARC for his kind support. I would also like to thank Shri Sanjay Malhotra, Head, EmA&I Division, BARC and his group memebers for their help in the development of theelectromagnet used for XMCD study in this thesis and also Dr. P.D. Babu, UGC-DAE-CSR, Mumbai for helping me with magnetic measurements of my samples.

I thank the members of my doctoral committee for their valuable suggestions and inputs during throughout my PhD tenure. I would like to thank my friends at BARC and RRCAT for several stimulating and fruitful discussions and lending me mental support. I would like to thank the Indus-2 control room members for their unrelenting support and for honoring our beam time requests at odd hours despite many inconveniences. I am also thankful to my collaborators for stretching their supportive hands in PhD. works. Without their support this work would not have been completed.

Finally, I acknowledge with deepest regards the sustained support of my parents who have stood by me through all the situations of my life. Without them, I would be nothing.

CONTENTS

SYNOPSIS

Heusler alloys, one of the solid state intermetallics, have immense technological importance in both the field of fundamental science and technological applications such as in spintronics devices due to their very interesting structural and spin related physical properties [1,2]. Heusler alloys are one of those materials whose atomic arrangements are the most fundamental in defining their electronic and magnetic properties [3]. These alloys are mainly ternary intermetallic compounds (X_2YZ), where X, Y and Z are associated with different lattice positions of the atoms and they can have different stoichiometric compositions also [4]. Heusler alloys are essentially formed from two ordered binary composition of XY and XZ and their ability of forming the ordered binary composition defines the possibility of forming a new alloy. In the Heulser alloys X and Y atoms are mainly transition metal elements having nearby atomic numbers and atomic scattering factors and Z is the sp element [5, 6]. In an ordered Heusler structure the atoms maintain a certain bond distances and co-ordinations around each atom. However, even in stoichiometric Heusler alloys, disorders can exist depending upon the partial interchange or occupation of the atoms on each other sub lattices [7, 8]. These half metallic ferromagnets exhibit high spin polarization of ~100% near to the Fermi energy level with a gap for the minority electrons [9]. Till now extensive experimental studies have shown that the majority of Heusler alloys are ferromagnetic in nature in a stoichiometric composition, however the off-stoichiometric Heulser alloys can be of ferromagnetic, antiferromagnetic and non-ferromagnetic in nature [10 - 13]. So characterization of these alloys at their atomic scale exploits a deep understanding about their structure and interactions in between.

Though X-ray diffraction has been used extensively in structural characterization of Heusler alloys, however with laboratory based XRD measurements, due to the similar atomic scattering factors of the constituent atoms in a heusler alloy system, precise evaluation of different kinds of atomic disorder in the samples is difficult. In this context synchrotron radiation based X-ray absorption spectroscopy (XAS) technique which involves measurement of element specific local structures is very important. XAS analysis provides information about the local structure around the respective atoms of an alloy system and thus elucidates the disorder effects at the atomic level which cannot been well understood from the X-ray diffraction study. Apart from this X-ray Magnetic Circular Dichroism (XMCD), which is basically XAS measurements under magnetic field using polarized synchrotron radiation, is also a very powerful technique to study element specific magnetic moments in a material particularly in a multi-components system like Huesler alloys [14, 15]. It can also determine the spin and orbital magnetic moment contributions separately and is rapidly becoming popular for probing the magnetic properties of materials as diverse as molecular magnets, multilayers, nanoparticles, etc.

This thesis work is divided into three parts: (i) preparation of four Heusler alloy thin film systems by Pulsed Laser Deposition (PLD) and their extensive investigations by XAS and other structural and magnetic characterizations techniques, (ii) development, installation and testing of the XMCD facility at Energy dispersive EXAFS beamline (BL-08) at Indus-2 Synchrotron source, Indore, India and (iii) theoretical simulations of the XMCD spectra of the Heusler alloy systems studied above by an-initio Density Functional Theory (DFT) based calculations. The above work has been presented in this dissertation in nine (9) chapters, which are summarized as follows:

Chapter-1: Introduction

In this chapter, we have first discussed the basic introduction and theoretical background to the Heulser alloys, their classifications, various electronic and magnetic properties and band structures. For this thesis two different types of full Heusler alloys have been studied viz., Ni_2FeGa and Co_2FeZ (Z= Ga, Al and Si). The Ni based Heusler alloy mentioned here is a ferromagnetic shape memory alloy. These alloys show both the changes in their structural and magnetic phases from an austenite to martensite phase due to the application of external magnetic field or by lowering temperature sufficiently enough. However, the Ni_2FeGa alloy shows the martensite phase transition at temperature near to room temperature [16]. So in this chapter the shape memory properties of these samples have been explained briefly. On the other hand, the Co based Heusler alloys are known as the half metallic ferromagnet due to some specific band structure near to the Fermi energy level. The details band structure, magnetic interaction and the Slater-Pauling rule used to estimate the value of magnetic moment of the half metallic ferromagnets have been explained in this chapter. Later we have mentioned about the applications of these alloys in the field of spintronics like in magnetic tunnel junctions, magnetic actuator devices, spin transistors and magnetoresistance devices etc. Subsequently in this chapter, the necessity of preparation of the Heulser alloys in thin film forms and the utility of PLD for the deposition of Heusler alloy thin films have been explained briefly.

Subsequently, the necessity of using XAS technique to investigate the element specific local structure of the above thin films Heusler alloy systems, which gives important information regarding the antisite disorders present in the system and in-turn help in explaining their macroscopic magnetic properties have been explained in this chapter. Finally, a brief introduction to the phenomenon of X-ray magnetic circular dichroism and its importance to study element specific magnetic moments in a material particularly in a multi-components system like Huesler alloys has been given in this chapter. Thus this chapter gives a clear idea about the objective and scope of the present thesis work.

Chapter-2: Experimental techniques and data analysis:

This chapter is divided into two parts. In the first part we have discussed about the preparation of the samples using Pulsed laser deposition (PLD) technique and in the second part we have discussed about the various characterization techniques used alongwith brief descriptions of the equipments employed for these characterizations. In the first part we have explained basics of the PLD technique along with its advantage and disadvantages vis-vis other deposition techniques of thin films. In this thesis work, Ni and Co based full Heusler alloy thin films of Co_2FeAl and Co_2FeGa were prepared on the c-Si substrates at elevated substrate temperatures, while the Co_2FeSi thin film samples were prepared at elevated substrate temperature as well as on substrates kept at room temperature followed by post deposition annealing to investigate the effect of different thermal growth processes on the properties of the thin films.

In the second part of the chapter discussions on various characterization techniques along with brief description of the apparatus used have been provided. It starts with a brief introduction to synchrotron radiation with its process of generation and special properties and subsequently, a brief description about the Indian synchrotron source Indus-2 at RRCAT, Indore, India [17] has been given. The two EXAFS beamlines at Indus-2 SRS viz., the Energy Scanning EXAFS beamline (BL-09) and Energy Dispersive EXAFS beamlines (BL-08) which have been extensively used in this thesis work have been described in detail. A brief overview on the theory of XAS technique which actually comprises of two measurement techniques viz., X-ray near edge structure (XANES) and Extended X-ray absorption fine structure (EXAFS), have been given subsequently with appropriate physical interpretations. Later the reduction and analysis processes of XAS data using the IFEFFIT software package [18] including ATHENA and ARTEMIS subroutines have been briefly described in this chapter. Subsequently the XMCD technique, including its fundamentals, measurement procedure and applications has been discussed in details. Finally, brief descriptions about other experimental techniques used for characterizations of samples in this thesis viz., X-ray Diffraction (XRD) along with Grazing Incidence X-ray Diffraction (GIXRD), Grazing Incidence X-ray Reflectivity (GIXR), Field Emission Scanning Electron Microscopy (FESEM), Energy Dispersive X-ray Scattering (EDXS) and magnetic measurement by Vibrating Sample Magnetometer (VSM) have been included in this chapter.

Chapter-3: Structural and magnetic characterization of off stoichiometric Ni_2FeGa Heusler alloy thin film

In this chapter the preparation of off-stoichiometric thin films of Ni_2FeGa ferromagnetic shape memory alloys by Pulsed Laser Deposition technique on c-Si (111) substrates at different substrate temperature form RT to 1073K temperatures have been described alongwith the study of the structural evaluation and magnetic properties of these films as a function of substrate temperature [19]. The long-range structure and surface morphology of the thin films were characterized by Grazing Incidence X-Ray Diffraction (GIXRD), Grazing Incidence X-Ray Reflectivity (GIXR) and Field Emission Scanning Electron Microscopy (FESEM) techniques. These ferromagnetic Heusler alloys show structural and magnetic phase transitions by lowering the temperatures near to room temperature. GIXRD results show the formations of polycrystalline film with the presence of multiple cubic phases ($L2_1$ and γ). The presence of the non-cubic martensite (NM) phase was observed at the highest substrate temperature (1073K) though the cubic $L2_1$ phase is found to be the major structural phase of this sample. The low temperature XRD measurement on the samples shows that by lowering the temperature the L21 phase decreases though the NM phase remains constant. The local structural study on the samples was done by EXAFS techniques at room temperature and low temperatures. The EXAFS analysis of these samples was done by considering mixed contributions of $L2_1$ and γ phases at room temperature measurements and it has been observed from EXAFS studies that with an increase in the substrate temperature the disordered γ phase gets reduced. EXAFS study also suggests stronger p-d hybridization between Ni and Ga atoms throughout the series and stronger hybridization at low temperature leads which might have led to the breaking of cubic symmetry leading to martensite phase transition. Magnetization measurements at 5K show ferromagnetic behavior of the samples with increasing saturation magnetization as the substrate temperature is increased. However, for the sample deposited at the highest temperature, due to the presence of anti-ferromagnetic interaction, martensite phase and decrease in γ phase, saturation magnetization decreases and coercive field increases.

Chapter-4: Structural and magnetic characterization of Co_2FeGa Heusler alloy thin film

In this chapter we have described the structural and magnetic characterizations of the Co_2FeGa Heusler alloys thin films prepared by PLD technique at different substrate temperatures from RT to 873K temperatures [20]. XRD measurement with lab source ascertains that the target material used for the deposition of the thin films have only A2 (or DO3) type of disordered cubic phase. However, in case of thin films, PLD grown from the above target, $L2_1$ appears to be the dominating phase whose fraction decreases with increase in substrate temperature, manifesting significant increase of disorder in the samples. Synchrotron based Anomalous X-ray Scattering measurement also supports the above result. Structural investigation by GIXRD measurement however shows presence of the A2-like phase similar to the bulk target which contradicts the XRD results and might be due to a two-layer structure of the films with a less density surface layer on the top of the bulk layer. X-ray reflectivity measurement shows that the thicknesses of the films were near to 1200 Å with a density of 9.25 gm cm^{-3}. Formation of droplet type of morphology was observed from the FESEM study and EDXS result shows that the film remains Ga deficient though the proper stoichiometry was arrived with increasing the substrate temperature. Analysis of EXAFS data of the samples was done by considering two structural models (i) without any anitiste disorder and (ii) by considering antisite disorder between the Co-Fe, Co-Ga and Fe-Ga atomic pairs. EXAFS measurements confirm $L2_1$ structure of the films and a possibility of stronger Co-Ga (*d*-*p*) hybridization. EXAFS measurements have also been able to establish the presence of A2 and DO3 phases unambiguously which occur due to Co/Fe/Ga and Co/Fe types of antisite disorders in the samples and could not be clearly detected by XRD measurements. Fitting of FT-EXAFS data also gives quantitative estimation of the disorder parameters which are found to increase gradually with an increase in substrate temperature Due to this antisite disorder the saturation value of magnetization is the samples are found to be less than the theoretically expected value. From the magnetic characterization the value T_C estimated as 1117K which matches with the theoretical value, though the T_C value is found to decrease with increase in substrate temperature. The contribution of the spin waves for the thermal demagnetization was observed for the films grown at RT and 473K.

Chapter-5: Effect of substrate temperature on structural and magnetic properties of Co_2FeAl Heusler alloy thin films

Structural and magnetic characterizations of Co_2FeAl thin films at different substrate temperatures using PLD technique have been studied in detail [21]. The GIXRD spectra on the samples show the presence of cubic Heusler phase and crystallinity of the samples is found to increase with substrate temperature though the structural phases due to specific atomic ordering could not be identified from the GIXRD spectra. Thickness around 1000 Å with a density of 6.64 gm cm^{-3} for the films were observed from the GIXR study. Surface morphology and elemental compositions of the films were obtained from FESEM and EDXS characterizations. EXAFS results show stronger d-d hybridization between the Co and Fe *3d* elements which is the characteristic of a half metallic Heusler alloy. The result also shows a gradual decrease in the Fe-Fe bond length with increase in substrate temperature, which manifests increase in the Fe-Fe ferromagnetic interactions. The saturation magnetization of the samples increases with increase in the substrate temperatures and reaches a maximum value of 6.5μB/f.u for the film deposited at 723K which is higher than the theoretical value 5 μB/f.u predicted from the Slater-Pauling rule. The variation in the value of coercivity shows a good resemblance with the variation of crystallite size obtained from the GIXRD spectra. A modified Bloch theorem was used considering the spin wave excitation ($T^{3/2}$ term) and stoner excitation (T^2 term), but for all the samples only the spin wave excitation contributes to the thermal demagnetization.

Chapter-6: Structural and Magnetic characterization of Co_2FeSi Heusler alloy thin films deposited with substrate heating and post deposition annealing

In this chapter the effects of two thermal growth processes on the structural and magnetic properties of PLD grown Co_2FeSi thin films have been studied in detail. Two series of Co_2FeSi thin films were prepared using PLD technique, by two separate routes, viz., (i) by depositing the films at elevated substrate temperature (S-series) and (ii) by depositing the films with substrate at room temperature followed by post-deposition annealing under vacuum (A-series) [22]. GIXRD measurements show that the structural phase of the samples which is not fully ordered $L2_1$, is same as that of the bulk target and is maintained in the films throughout the substrate and annealing temperature range. GIXR results show that the films grown at elevated substrate temperatures however have higher density, higher crystallite size and higher surface roughness than the films obtained by post deposition annealing. It has been observed from EXAFS studies that there is presence of Co-Fe antisite disorders which increases with increase in the substrate temperature and Fe atoms are more ordered in the structure. A strong *p-d* and *d-d* hybridizations were observed for the S and A series samples respectively which characterizes their magnetic interactions. Magnetic measurements show that the films are ferromagnetic in nature where the value of total magnetic moment was less than the bulk ferromagnetic CFS material, though the films grown at elevated substrate temperature show values (6.30μB/f.u), close to the bulk value which is due to higher crystallinity in the samples. There is however an initial decrease of saturation magnetization with increase in substrate temperature for these samples which is possibly due to the presence of Co-Fe type antisite disorder. It has also been observed that the spin wave stiffness constant (D_0) derived using the modified Bloch's theorem, is higher for the 'A' series samples than for the 'S' series samples manifesting the fact that spin waves are much stiffer for the samples of 'A' series.

Chapter-7: Development of XMCD facility at Energy dispersive EXAFS beamline

This chapter presents the development, installation of the XMCD facility at the Energy Dispersive EXAFS beamline (BL-08) at Indus-2 SRS. This is the first ever XMCD measurement facility in India at the hard x-ray regime. The facility uses an in-house built electromagnet having maximum magnetic field up to 2T custom-made with a hole of 10 mm for passage of the X-ray beam through the pole pieces. The magnet is placed at the sample position of the BL-08 beamline using a locally fabricated precision (X-Z-θ) motion stage for aligning the axis of the magnetic field and the beam hole along with synchrotron beam direction [23]. The design of the electromagnet core and coil has and the above set-up has been described in this chapter The measurements have been carried out by choosing the top-most portion of the incident synchrotron beam using a precision slit which ensures left circularly polarised beam and by placing the sample under the magnetic field. The XMCD signal is obtained by the difference of the X-ray absorption spectra recorded with forward and reverse magnetic fields. The set-up has been tested by carrying out XMCD measurements on standard samples and XMCD spectra on two standard sample viz., Gd foil at L_3 edge and Fe_2O_3 at Fe K-edge (7112 eV) have been shown in this chapter.

Chapter-8: DFT computation on Heulser alloys for electronic property study and XMCD simulation.

In this chapter of the thesis ab-initio Density Functional Theory (DFT) based electronic structure calculations have been carried out to generate XMCD spectra of the Heusler alloy samples which will be helpful in analyzing the experimental XMCD spectra and to determine the element specific orbital and spin moments in the samples. In this thesis work, for the DFT calculations the Green's function based Spin Polarized Relativistic Korringa-Kohn-Rostoker (SPR-KKR) program package has been used [24]. The Self Consistent Field (SCF) calculations on the systems were done by using two exchange correlation functions i.e., Local Density Approximation (LDA) and Generalized Gradient Approximation (GGA) and it was observed on a comparative study that by considering the GGA approximation over LDA as exchange co-relation function, a better result of total magnetic moment was obtained, though the ratio of (μ_l/μ_s) remains almost same for both the cases. The dependence of the magnetic moments upon the neighborhood of atoms, hybridization between them and the spin-orbit coupling between the atoms have been explained here elaborately. It was observed that in the off-stoichiometric compounds where there is a presence of the antisite disorder, the disorder atoms interact ferromagnetically with the properly sited atoms. However, the values of spin polarization for the off-stoichiometric compounds are found to be less than the stoichiometric compounds.

Subsequently XAS and XMCD spectra of the samples at different elemental edges of their constituent elements have been generated and the effect of non-stiochiometry on the spectra have been studied. To explain the variation in the spectral features the total DOS and the partial DOS of the constituent atoms w calculated. An interesting observation was made from the calculation that using GGA XC function though the value of the magnetic moment matches to the expected value, it is unable to give the proper band structure near to E_F. So full potential was taken upon GGA XC function which gave expected value of band structure and the value of the spin polarization. However, the problem was not solved for the Co_2FeSi since it is a strongly correlated material. In this case the onsite Coulomb interaction term (+U) was added with the GGA and it gave the positive spin polarization and the value of magnetic moment near to the S-P rule (6 µB/f.u) [4]. Consequently, from the XMCD spectra it was observed that the splitting in the XMCD spectra at the Fe edge are more prominent than the Co edge spectra, suggesting a more localized nature of the Fe atoms than Co.

Chapter-9: Conclusion

Finally, in this chapter the conclusions on the results obtained from each study performed under this thesis work are summarized and the future scopes of work are also mentioned.

References:

1. I. Zutic, J. Fabian, S. Das Sarma, Rev. Mod. Phys. 76 (2004) 323 – 410.
2. A. Hirohata, K. Takanashi, J. Phys. D Appl. Phys. 47 (2014) 193001 – 193040.
3. R.Y. Umetsu, A. Okubo, R. Kainuma, J.Appl. Phys. 111 (2012) 073909 – 073915.
4. I. Galanakis, Ph Mavropoulos, P.H. Dederichs, J. Phys. D Appl. Phys. 39 (2006) 765 – 775.
5. Z. H Liu, H.N. Hu, G.D. Liu, Y.T. Cui, M. Zhang, J.L. Chen, G.H. Wu, X. Gang, Phys. Rev. B 69 (2004) 134415.
6. Balke Benjamin, Sabine Wurmehl, Gerhard H. Fecher, Claudia Felser, Jürgen Kübler, Sci. Technol. Adv. Mater. 9 (2008), 014102.
7. P.J. Webster, J.Phys.Chem. Solids 32 (1971) 1221 – 1231.
8. M. Belmeguenai, H. Tuzcuoglu, M.S. Gabor, T. Petrisor Jr., C. Tiusan, F. Zighem, S.M. Cherif, P. Moch, J. Appl. Phys. 115 (2014) 043918 – 043924.
9. Burkard Hillebrands and Claudia Felser, J. Phys. D: Appl. Phys. 40 (2007).
10. Claudia Felser, Lukas Wollmann, Stanislav Chadov, Gerhard H. Fecher, and Stuart S. P. Parkin. APL Materials 3, 041518 (2015).
11. T. Sakon, Y. Hayashi, N. Fujimoto, T. Kanomata, H. Nojiri, and Y. Adachi. J. Appl. Phys. **123**, (2018) 213902.
12. M. Tas, E. Sasiogiu, C. Friedrich, S. Blügel, and I. Galanakis. Journal of Applied Physics 121, (2017) 053903.
13. Stefano Sanvito, Corey Oses, Junkai Xue, Anurag Tiwari, Mario Zic, Thomas Archer, Pelin Tozman, Munuswamy Venkatesan, Michael Coey, Stefano Curtarolo, Sci. Adv.3 (2017)1602241.

14. Shigeaki Uemura, Hiroshi Maruyama, Naomi Kawamura, Hitoshi Yamazaki, Shin-ichi Nagamatsu and Takashi Fujikawa. J. Syn. Rad. (2001).8, 452 – 454.
15. Lakhan Bainsla, Resul Yilgin, Jun Okabayashi, Atsuo Ono, Kazuya Suzuki and Shigemi Mizukam. Phys. Rev. B 96, (2017) 094404.
16. A. Sazinov, A. A. Likhachev, N. Lanska and K. Ullakko, *Appl. Phys. Lett*. 80 (2002) 1746.
17. A.K. Poswal, A. Agrawal, A.K. Yadav, C. Nayak, S. Basu, S.R. Kane, C.K. Garg, D. Bhattachryya, S.N. Jha, N.K. Sahoo, AIP Conf. Proc. 1591 (2014) 649 – 651.
18. M. Newville, B. Ravel, D. Haskel, J.J. Rehr, E.A. Stern, Y. Yacoby, Physica B 208 (1995) 154 – 156.
19. N. Patra, A. Biswas, C.L. Prajapat, A. Ghosh, P.U. Sastry, S. Tripathi, P.D. Babu, Arup Biswas, S.N. Jha and D. Bhattacharyya. *Journal of Alloys and Compounds* 723 (2017) 1098-1112.
20. N. Patra, C.L. Prajapat, Rajnarayan De, K.D. Rao, P.D. Babu, A.K. Sinha, Siju John, H.C. Barshilia, S.N. Jha and D. Bhattacharyya, Journal of Alloys and Compounds748 (2018) 653 – 670.
21. N. Patra, C.L. Prajapat, P.D. Babu, S. Rai, S. Kumar., S.N. Jha and D. Bhattacharyya. Journal of Alloys and Compounds 779 (2019) 648 – 659.
22. N. Patra, C.L. Prajapat, P.D. Babu, S. Rai, S. Kumar, S.N. Jha, D. Bhattacharyya. Journal of Alloys and Compounds 804 (2019) 470 – 485.
23. N. Patra, U.G.P.S. Sachan, S. Sundar Rajan, Sanjay Malhotra, Vijay Harad, Ankur Agarwal, Ashutosh Diwedi, S. N. Jha and D. Bhattacharyya. *Journal of Synchrotron Radiation 26* (2019) 445 – 449.
24. http://olymp.cup.uni-muenchen.de/ak/ebert/SPRKKR.

List of Figures

List of Tables

Chapter-1

INTRODUCTION

1.1 Introduction:

In the year of 1903 a German mining engineer and chemist Friedrich Heusler discovered an alloy of Cu_2MnSn and the name of the alloy was given after him as Heusler alloy [1]. The first discovered alloy was a ferromagnetic alloy though the constituent elements are non-magnetic in nature. Since the year of discovery and after more than 100 years of journey, the Heusler Alloysremained asmaterials of keen interest to the scientific community because of theirseveral fascinatingproperties. Key factors forthese interesting properties of Heusler alloys are their crystal structure and elemental compositions. Structural studies of Cu-Mn-Al alloy revealed that all constituent of this system are ordered on an f.c.c super lattice [2, 3] and a relation between the chemical ordering and the magnetic properties was established. Though the first discovered Heulser alloy was a ferromagnetic alloy, later on it has been discovered by several workers that the Heusler alloys can be non-ferromagnetic. Presently, two classes of materials are called Heusler alloys due to their structural composition i.e., full Heusler alloy and half or semi Heusler alloy. Full Heusler alloys have a general formula of X_2YZ and the half Heusler alloys have a composition of XYZ. The X and Y elements are transition metal (*3d*) element and the Z comes from the III-V group (*s*-*p*) in the periodic table. These two kinds of Heusler alloys are generally characterized by $L2_1$ and $C1_b$ structures respectively. Unit shell of $L2_1$ structure isformed by four interpenetrating f.c.c sub lattices with the positions (0,0,0) and (½, ½, ½) for X atom, (¼, ¼, ¼) for Y atom and (¾, ¾, ¾) for Z atom, while for $C1_b$ structure one of the sub lattice of X atom is unoccupied and this structure is not cento-symmetric. As both the transition metal elements belong to the same row in the periodic table, the atomic number or the nuclear charge of these atoms defines their corresponding atomic positions in the lattice [4]. The schematic representation of the various structures of full and half Heusler alloys have been shown in the figure-1.1.

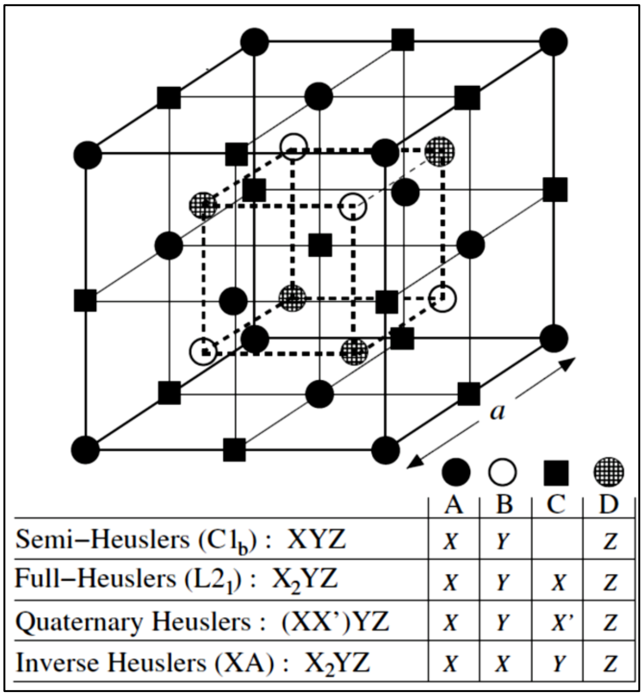

	● A	○ B	■ C	▦ D
Semi–Heuslers ($C1_b$) : XYZ	X	Y		Z
Full–Heuslers ($L2_1$) : X_2YZ	X	Y	X	Z
Quaternary Heuslers : (XX')YZ	X	Y	X'	Z
Inverse Heuslers (XA) : X_2YZ	X	X	Y	Z

Figure 1.1: Schematic representation of the various structures of the full- Heusler and half-Heusler alloys.

Apart from crystallographic orientation, there are also various kinds of atomic disorders that can be present in a Heusler alloy sample. In a stoichiometric composition the disorder can occur due to partial occupancy or random substitution of the atoms at different sub lattices. In case of a X_2YZ type of Heusler alloy, if X atoms occupy their assigned position but the Y and Z atoms randomly share each other sub lattices, it leads to the B2 type of disorder, random mixing between X and Y atoms gives rise to DO3 disorder, while all X, Y and Z atoms randomly share their positions, A2 disorder arises [5] The unit shell of full Heusler alloy with different atomic disorders is shown in the figure-1.2.

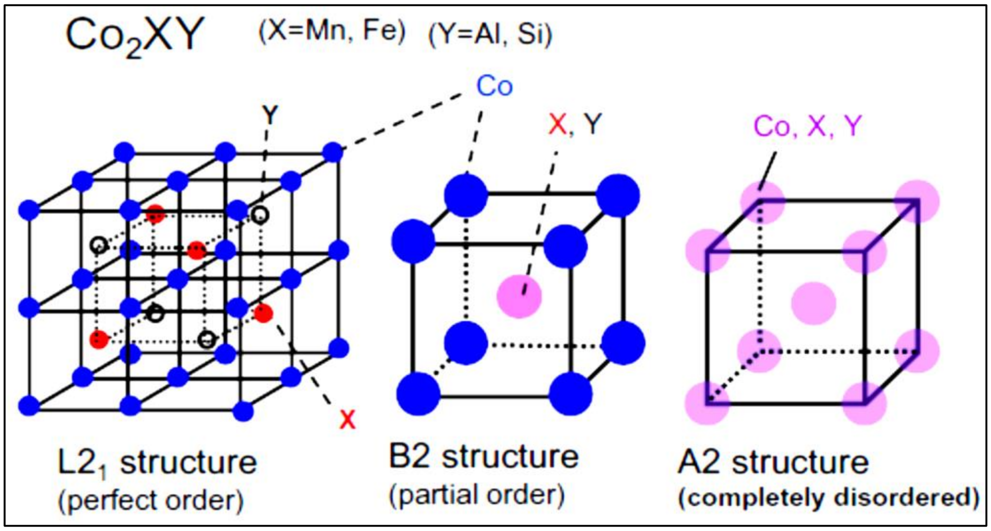

Figure 1.2: Different atomic ordering in a full Heusler alloy [6]

Several traditional analysis approaches are reported to evaluate the degree of atomic ordering in the Full Heusler alloy for bulk samples [7]. This kind of antisite disorder between the atoms leads to a decrease in the ferromagnetic ordering and creates additional states at the Fermi level resulting in reduction in spin polarization [8]. As the B2 type structure has lower interatomic distances, an antiferromagnetic ordering is favorable to form. However, the improvement in the structural ordering or the transformation from a disorder to order phase can be obtained by the heat treatment.

1.2 Important Heusler alloy systems:

Several kinds of Heusler alloys have been reported in the literature by varying the transition metal elements at the X and Y positions and the *sp* elements. Depending upon the elemental compositions these alloys show ferromagnetic, antiferromagnetic and ferrimagnetic behaviors, though majority of the Heusler alloys show ferromagnetic nature. It is reported that mainly those kinds of Heusler alloys show the anti-ferromagnetic behavior where the Y site is generally occupied by Mn atoms. Anti-ferromagnetism is more favorable for those Mn based alloys which have smaller Mn – Mn distances which interact through another atom [9]. The composition of the Heusler alloys can be off-stoichiometric also though the crystal structure remains same and this affects their magnetic properties. As has been mentioned earlier, first discovered Heusler alloy was Cu_2MnSn, though over the years several alloys have been proposed and their structural and magnetic properties were characterized. A list of the Heusler alloys with several compositions is shown in the Table-1.

Magnetic property	**Alloys**
Ferromagnetic	Co_2MnSi [10], Co_2MnSn [10], Co_2FeSi [11], Co_2FeGa [12], Ni_2MnGa [13], Ni_2FeGa [14], Ga_2MnCo [15]
Antiferromagnetic	Cu_2MnSb [16], Pt_2MnGa [17], Mn_2VAl [18], Pd_2MnIn [19]
Ferrimagnetic	Mn_2CoSn [20], $Mn_2V_{0.5}Co_{0.5}Al$ [21]
Non magnetic	Ni_2TiGa [22] (Unstable)

Table-1.1: List of different kinds of full Heusler alloys on the basis of magnetic property

1.3 Properties of Heusler alloys:

1.3.1 Electronic structure of full Heusler alloy:

Heusler alloys are such kind of metallic compounds which exhibits the half metallic properties. In the year of 1983 using the first-principle electronic structure calculations, the concept of half metallic ferromagnetism was first introduced by de Groot and collaborators on NiMnSb [23]. This means that one of the subbands, usually the majority spin band is metallic and the other sub-band, usually the minority spin band is semiconductor in nature i.e., the Fermi energy (E_F) falls into the gap. The comparison of band structure of a full Heulser alloy as a half metallic ferromagnet with a non magnetic metal and a ferromagnetic metal is shown in the figure-1.3. This leads to a ~100% spin polarization at E_F. Ishida and collaborators were the first to introduce the half metallic behavior in full Heusler alloys of Co_2MnZ compound, where Z stands for Si and Ge [24, 25]. There are other half metallic ferromagnets, such as oxides (Fe_3O_4, CrO_2), magnetites($La_{1-x}Sr_xMnO_3$) [26], double perovskites (Sr_2FeReO_6) [27], pyrites (CoS_2) [28], dilute magnetic semiconductors [29] etc., which give 100% spin polarization near to E_F, however they work at low temperature and hence are not suitable for application in ambient temperature. Heusler alloys have gained interest due to having larger spin polarization in ambient condition and having very high Curie temperatures (~1100 K) [30].

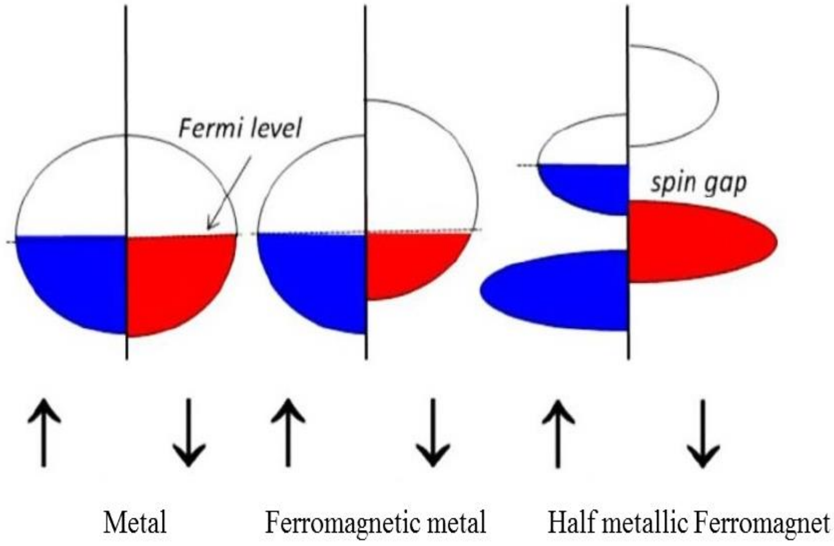

Figure-1.3: Schematic of band structure comparison of metal, ferromagnetic metal and half metallic ferromagnetic material.

Half metallicity has been demonstrated in other Heusler alloy compounds also apart from those mentioned above. Electronic band structures of these Hesuler alloys completely depend upon their atomic environment or symmetry. In a $L2_1$ structure of Co_2FeGa, both the Fe and Ga atoms are surrounded by 8 Co atoms in the 1st co-ordination shell, sitting in an octahedral symmetry position, while the Co atom is surrounded by 4 Fe and 4 Ga atoms in the 1st co-ordination shell and the symmetry of the crystal is reduced to the tetrahedral one. However, the Co atoms occupying the 2nd co-ordination shell of the Co atoms, their interaction with the core Co atom and Fe atoms are much important to determine their magnetic behavior. As the Fe atom is surrounded by the 8

Co atoms, so the hybridization between the Co atom with Fe (*d-d* hybridization) or the *sp*elements (*p-d* hybridization) changes the magnetic moment of Fe atoms.

All these hybridizations are either bonding or antibonding type which gives rise to a band gap near to the Fermi level [31]. The detail band structure and the process of the hybridization are shown in the figure-1.4 in case of Co_2MnGe.

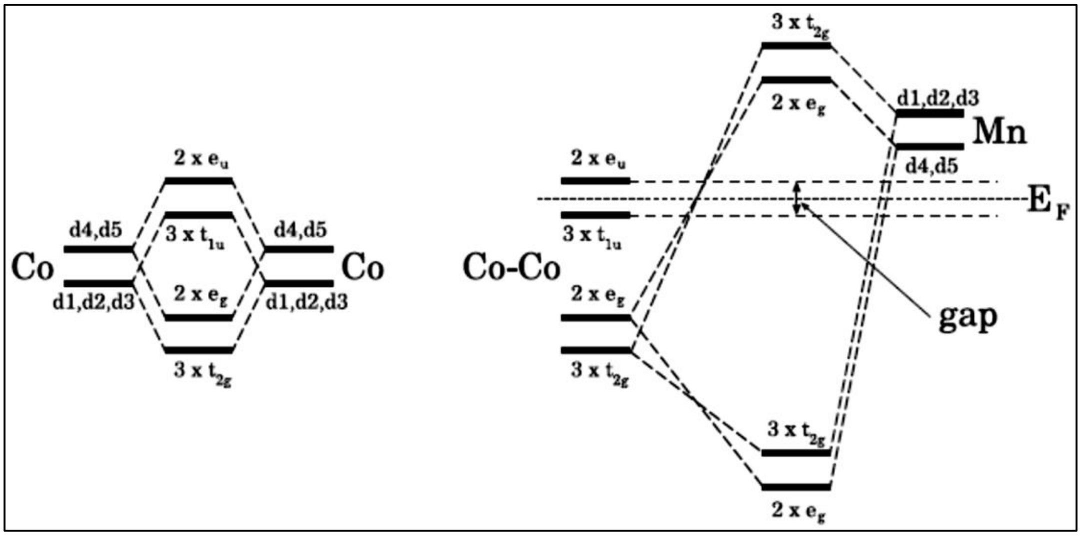

Figure-1.4: Schematic illustration of the origin of the gap in the minority band in full-Heusler alloys [31]

As it has been mentioned that the hybridization is quantitatively very important for the system, the *d* orbitals of Co atom are divided into total two d_r^2, $d_{x^2-y^2}$ and three d_{xy}, d_{yz}, d_{zx} degenerate states. In the first step these orbitals of the two Co atoms form the two bonding ($e_g$ort_{2g}) and two anti-bonding (e_u or t_{1u}) hybrids between them. In the second step the hybridized Co-Co orbitals make the further hybridization with the degenerate states of the Mn atoms. This hybridization forms resultant five bonding orbital above the Fermi level and five bonding orbitals below the Fermi level which are completely filled. However, the two anti-bonding orbitals (e_u and t_{1u}) of the hybridized Co-Co orbital do not couple with any of the Mn orbitals and remains completely empty. The Fermi energy lies between these anti-bonding orbitals and give rise to a band gap 0.1 – 0.3 eV. In these alloys the Co (X position) are ferromagnetically coupled to the Fe or the Mn atom (Y position) and the main magnetic moment of the material is mostly contributed by the Fe and Mn atoms [31]. The *sp* element in a Hesler alloy is of not much importance for defining its physical properties, its main role being in stabilizing the structure.

1.3.2 Magnetic interactions in full-Heusler alloy:

As has been mentioned earlier, the total magnetic moment of a Heusler alloy is contributed by the 3d transition metal elements. In a fully ordered $L2_1$ (X_2YZ) Heusler system the main magnetic moment is localized at the atom situated at 'Y' position (as example Fe, Mn) which may interact ferromagnetically with the nearby atom situated at 'X' position (as example Co, Ni). This 'Y' atom further can interact ferromagnetically or non-ferromagnetically with the nearby 'Y' atoms depending upon the atomic type [32]. From the ab-initio calculations it is known that for a half-metallic full Heusler alloy the magnetic properties are mainly controlled by the minority spin density of states and the total magnetic moment depends upon the total number of electrons present in the valance state [33]. In the materials containing transition metals magnetism occurs because the magnetic moments couples to each other and form a magnetically ordered state. This kind of coupling is called the exchange interaction which is completely a quantum mechanical phenomenon and follows the Pauli's exclusion principle. This exchange interaction between the nearby magnetic atoms forces the other magnetic moments to align parallel or antiparallel to each other. It is well known that in these systems the interaction between the *d* elements (Co, Mn, Fe etc.) is a direct exchange type or specifically the Heisenberg direct exchange interaction, on the other hand the interaction between the *d* and the *sp* elements (Ga, Al, Si etc.) is the RKKY type of interaction [34]. From the theoretical calculationsusing DFT, it has been observed that while moving from the Ni based series to the Co based series as the X element, the RKKY interaction between the *p* and *d* elements decays and the *d-d* interaction increases [35].

1.3.2.1 Direct exchange interaction: Direct exchange is a strong, yet short range interaction between the magnetic moments which are close enough to have overlapped wave functions. This interaction decreases as the separation increases. When the two atoms are close enough, the Coulomb interaction between the electrons in between two nuclei is minimum. However, to place the two electrons at the same place in space and time the Pauli's exclusion principle has to be followed and because of the exclusion principle the two electrons must have opposite spins. This give rises to the antiparallel alignment and negative exchange interaction. Similarly, when the two atoms are far enough, the electrons reduce the Coulomb repulsion by a parallel alignment. This gives rise to a positive interaction. The interaction between the atoms with the interatomic distance for the direct exchange is governed by the Bathe –Slater rule. The Bathe-Slater curve is given in the figure-1.5.

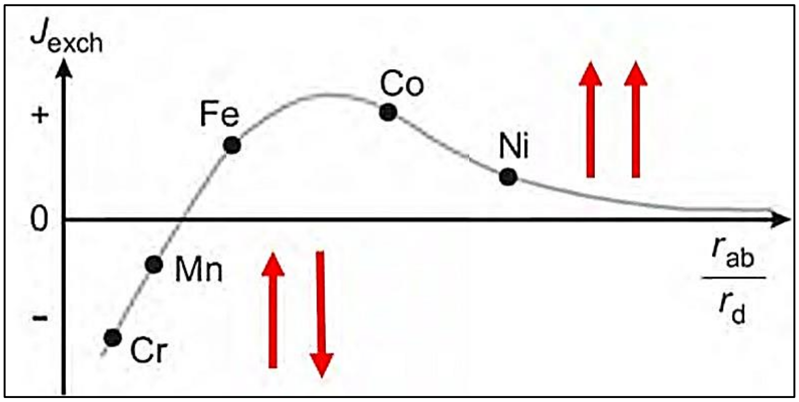

Figure-1.5: Bathe-Slater curve of direct exchange interaction

In this curve the Cr and the Mn atoms remain in the negative exchange side and the Co remains in the positive exchange side of the curve. Depending upon the crystal structure the Fe atom remains around zero crossing point.

1.3.2.2 RKKY interaction: There is also another kind of interaction between the atoms which is indirect exchange interaction.This is a dominant interaction in the metals where electrons are separated at large distances and there is no any direct overlapping of wave functions. The interaction occurs through intermediary itinerantelectrons. This interaction is known as the RKKY exchange interaction named after Ruderman, Kittle, Kasuya and Yoshida [36, 37].This interaction has a damped oscillatory nature with the separation of the ions as shown in the figure-1.6. In the figure the interaction oscillates between positive and negative values depending upon the sepeartion and this sepeartion gives the ferromagnetic or anti-ferromagnetic coupling and the amplitude of oscillation is reduced at high temperature. Here the spin polarized itinerant electrons in the condution band feels the moment of other magnetic ions within a certain range

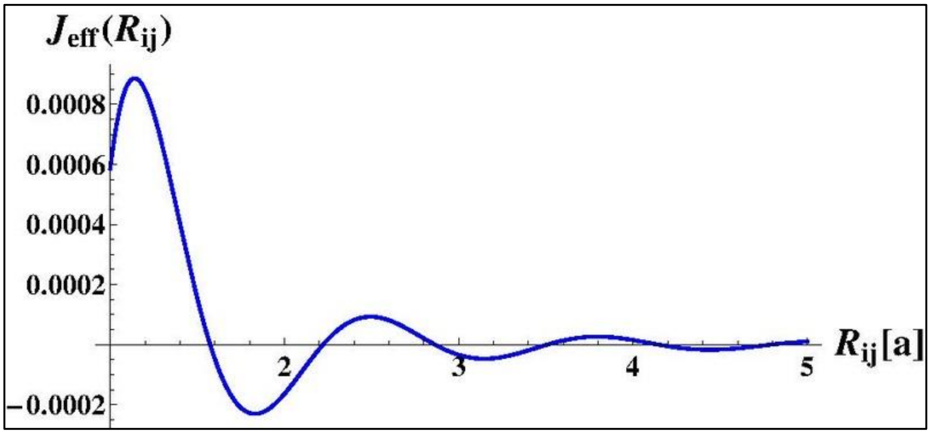

Figure 1.6: The RKKY inter action as a function of atomic distance.

1.3.2.3 Slater-Pauling rule in ferromagnetism:

In the above discussions it has been said that these Heusler alloys have half metallic ferromagnetic property which depends completely upon their band structure. It is known from the ab-initio calculations that for a half metallic full Heusler alloy the electronic and the magnetic properties are mainly correlated with their minority spin density of states, where the total spin moment depends upon the total number of valance electrons. According to the Slater- Pauling (SP) rule for a half metallic full Heusler alloy the total value of spin magnetic moment (M_t) is defined by the relation $M_t = Z_t - 24$, where Z_t be the total number of valence electrons per unit cell or the value of Z_t is given by the sum of the number of spin-up and spin-down electrons and M_t is given by the difference between the spin-up and spin-down electrons.

$$Z_t = N\uparrow + N\downarrow \text{ and } M_t = N\uparrow - N\downarrow \text{ or } M_t = Z_t - 2N\downarrow \tag{1.1}$$

The rule of 24 comes from the fact that the minority band contains 12 electrons per unit cell. For the case of alloys with ‘Z’ element as Ga and Al, the value of Z_t is 28 and for Si it is 29 which give the spin magnetic moment of $4\mu_B$/f.u and $5\mu_B$/f.u respectively and the “magic number” 24 comes from the position and the number of spin down state comes from the strong d-d hybridization [33].

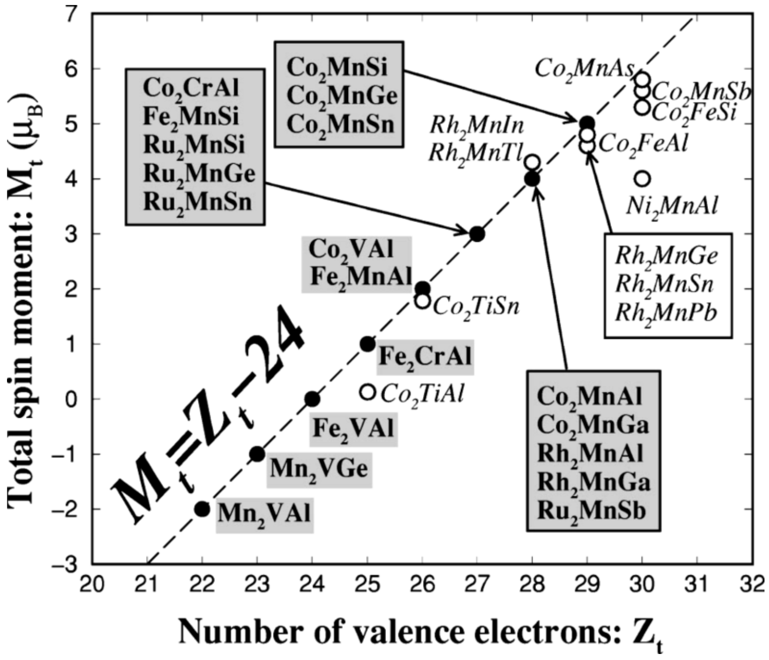

Figure-1.7: Calculated total spin moments for all studied Heusler alloys. The dashed line represents the Slater-Pauling behaviour. The white circles denote ferromagnetic Heusler alloys which are not half-metallic and have a non-integer total moment, thus deviating from the S-P curve [33]

It can be seen that maximum number of occupied spin up states in the unit cell of a full Heusler alloy systems, which have been extensively studied in this thesis, can be 12 electrons per unit cell: where 4 are occupying the low lying *s* and *p* bands of the *sp* element and 8 of the Co like minority *d* bands. Since 7 minority bands are unoccupied, the largest possible moment can be 7μ_B/f.u and it occurs when all the majority *d*-states are occupied [11].

1.3.3 Shape Memory effect:

The Heusler alloys that show shape memory effect, goes from a highly symmetric austenite phase to a lower symmetric martensite phase which is known as a magneto structural phase transition where both the structure and the magnetic phases transform to another phase. Unlike any other order-disorder transition at the atomic level, the martensite transition is caused by diffusion-less co-operative movement of the atomic layers in the crystal by means of applied external magnetic field, lowering temperature or externally applied mechanical stress. So it was suggested that martensite transition is driven by the Jahn-Teller distortion in the cubic environment and experimentally was proved by neutron diffraction study. The martensite phase transition of a cubic ferreomagnetic material to a non-cubic phase by lowering the temperature is shown in the figure-1.8. This deformation is recoverable along with some hysteresis with the strain level depending upon the composition of the austenite matrix and the crystal structure at the austenite and martensite phases. For major cases it has been observed that the auatenite phase has a cubic structure and the martensite phase has the non-cubic structures like tetragonal [38] or orthorhombic [39]. This martensite phase can be magnetic and nonmagnetic in nature. When the martensite phase is magnetic then they exhibit the Magnetic Shape Memory (MSM) effect. In these alloys the externally applied magnetic field can induce a large strain at the martensite phase, which is known as the magnetic field induced martensite transition. In this martensite phase the elastic energy is released by the formation of a twin structure and the boundary between them is known as the twin boundary [40, 41]. The twins have similar kind of structures but oriented at different crystallographic directions and this orientation is even switchable by applied external stress. So an appropriate twin microstructure is required to induce magnetic field induced reorientations.

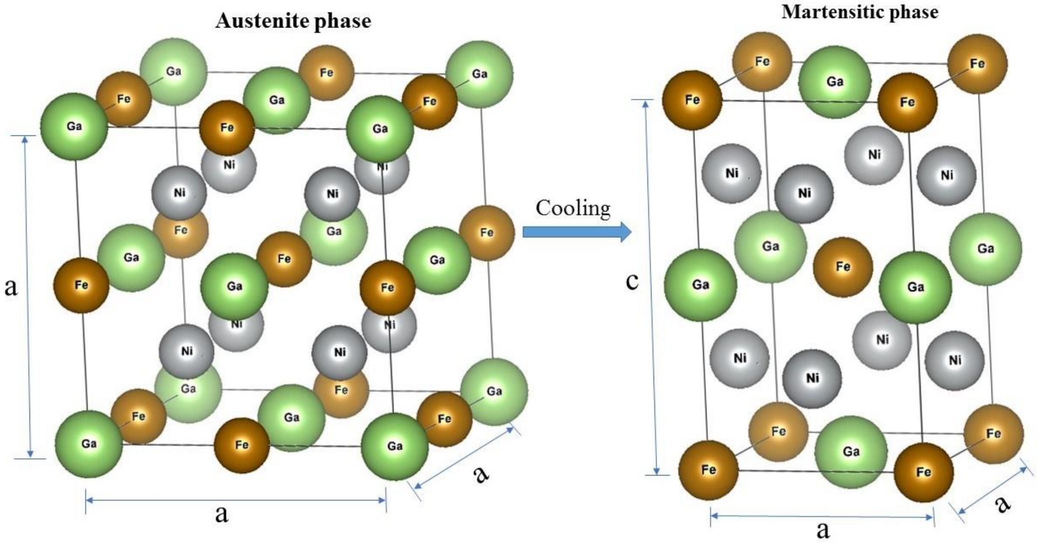

Figure-1.8: Structural phase transformation from a cubic austenite to tetragonal marteniste phase by lowering the temperature.

There are two different kinds of martensite phases depending upon the austenite phase i.e., non modulated (NM) and modulated martensite phases. When a transition from a cubic austenite to tetragonal martensite is occurred it is assigned as the non-modulated structure ($L1_0$) and this is the ground state of a martenite phase. The origin of the modulated phase is explained by two different models (i) adaptive phase model and (ii) soft phonon mode based displacive modulation model. In the former model the NM phase undergoes periodic nanotwining in two opposite direction of the austenite {110} planes to achieve minimum interfacial energy [42]. In the second model there is a softening of the TA_2 acoustic phonon mode of the austenite phase at (1/3, 1/3, 0) position [43]. There can be different kinds of modulate phases depending upon the layered structure such as 3M, 5M, 7M etc. Though the first reported Heusler alloy was Ni_2MnGa to show the MSM effect with Mn atom at the Y position, there are several other Ni based Heusler alloys like Ni_2FeGa [44], Ni_2MnSn [45], Ni_2MnIn [46], Mn_2NiGa [47] and Cu based Heulser alloys like Cu_2MnAl, Cu_2MnSn

[48] are also reported to show the MSM effect. The martensite transformation can be done by lowering the temperature also. So the transformation from the austenite to the martensite phase is an exothermic process or the heat realizing process from the system and on the other hand the transformation from the martensite phase to the austenite phase is an endothermic process or the heat absorbing process by the system. A graphical representation of the thermal hysteresis during martensite transformation is shown in the figure-1.9. The phase transformation between martensite and austenite phases shows a thermal and a mechanical hysteresis; M_s and M_f represent the martensite start and finish temperatures while A_s and A_f are the austenite start and finish temperatures.

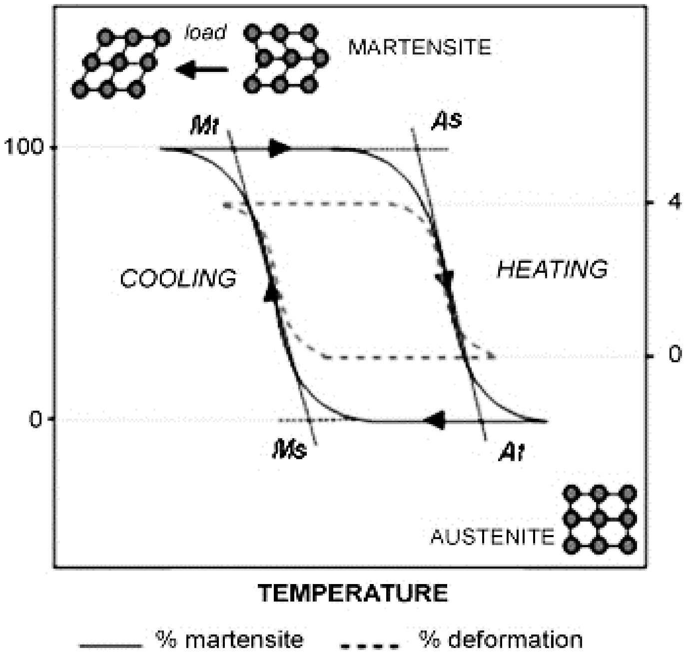

Figure 1.9: A graphical representation of the thermal hysteresis during martensite transformation

1.3.4 Magneto caloric effect:

The magnetocaloric effect (MCE) is defined as the heating or cooling process of a magnetic material due to the application of magnetic field. This process is also known as the adiabatic demagnetization of a magnetic material. It is due to the coupling of the magnetic sublattice with the magnetic field, which changes the magnetic entropy of a solid. All magnetic materials intrinsically show MCE, although the intensity of the effect depends on the properties of each material. The magnetocaloric effect is the strongest near the material's Curie temperature, i.e., the temperature of its spontaneous magnetic ordering/disordering. When the magnetic ordering coincides with a structural change affected by the field, an additional heat is released or absorbed, thus strongly enhancing the magnetocaloric effect that can be used to efficiently refrigerate.

When the magnetic field is applied adiabatically in a reversible process, the magnetic entropy decreases and increases the temperature of the system. On the other way when the magnetic field is applied isothermally, the total entropy decreases due to the decrease in the magnetic contribution and therefore the entropy changes [49]. The change in the magnetic entropy (ΔS_m) in an isothermal process is given by –

$$\Delta S_m(T, \Delta H) = \int_{H1}^{H2} \left(\frac{\partial M(T,H)}{\partial T}\right)_H \, dH \qquad (1.2)$$

Especially, the shape memory alloys like Ni_2FeGa or Ni_2MnGa etc. alloys show a magnetic phase transition with lowering the temperature. Now the change in the magnetic entropy occurs significantly at the martensite transition temperature which gives a very large magnetocaloric effect.

1.4 Applications of Heulser alloys:

Due to having unique structural and magnetic properties like half metallic ferromagnetism, magnetic caloric effect (MCE), large tunneling magneoresistance (TMR)etc., Heusleralloys are used in various spintronic devices such as Magnetic Tunnel Junctions (MTJ), Spin Transistor, spin injector, Magnetic Random Access Memory (MRAM), magnetic actuator devices, magnetoresistance devices etc. [50].

1.4.1 Magnetic Tunnel Junctions (MTJ):

A magnetic tunnel junction (MTJ) consists of two layers of magnetic metal separated by an ultrathin layer of insulator. The insulating layer is so thin that electrons can tunnel through the barrier if the biasvoltage is applied between the two metal electrodes. The basic phenomenon of MTJ is that when electrons are tunneling between two ferromagnetic metals, the magnitude of the tunneling current depends on the relative orientation of magnetizations of the two ferromagnetic layers, which can be changed by an applied magnetic field. This phenomenon is called tunneling magneto resistance (TMR) which is a consequence of spin dependent tunneling [51]. The tunneling current depends on the density of states of the electrodes at Fermi level. For a ferromagnetic material the majority and minority bands are shifted in energy with opposite spins near to Fermi level. Thus assuming conservation of the spin moment for the tunneling process, two parallel currents of spin up and spin down flows and as a result the current between electrodes with same magnetization have higher than the electrons with opposite magnetization. A schematic illustration of the MTJ has been shown in the figure-1.10.

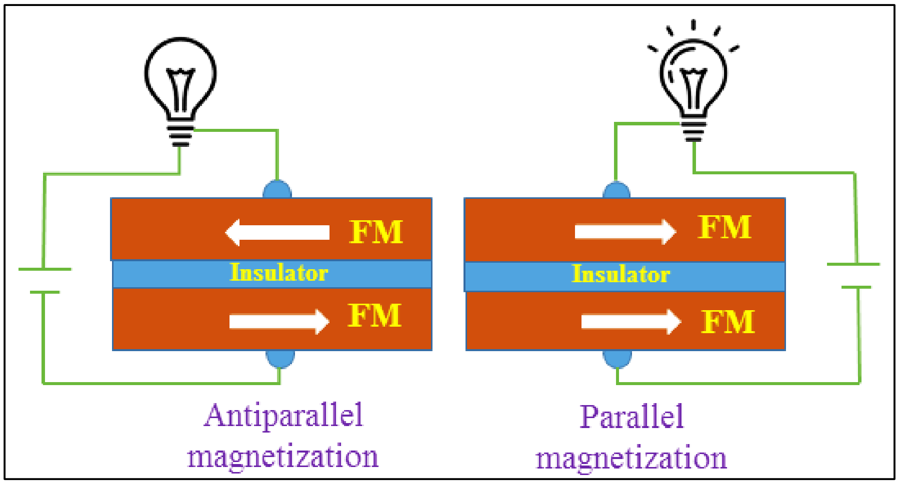

Figure 1.10: A schematic illustration of the Magnetic Tunnel Junction (MTJ)

The tunneling magnetoresistance is given by

$$TMR = \frac{R_{AP} - R_P}{R_P} \tag{1.3}$$

where R_{AP}, $R_P$are called as the tunnel resistances for the antiparallel and parallel magnetization

Or this can be written as

$$TMR = \frac{2P_1P_2}{1-P_1P_2} \tag{1.4}$$

where P_1 and P_2 are the spin polarization of the two ferromagnetic layers [52]. As discussed above because of the specific band structure of the Heusler alloys, they deliver a very high spin polarization (~100%) at the Fermi level even at ambient temperature. This makes Heusler alloys important candidates for the application in magnetic tunnel junction devices.

1.4.2 Magnetic actuator devices:

Actuators are electrical devices that transform input energy (control variable) to output mechanical work (acting variable). In electromagnetic actuator input energy is electric current and output mechanical work is force interaction and its effects. The principle of transformation in these actuators is based on force interaction in a magnetic field. The actuator consists of two basic parts – electric and magnetic circuits. The electric circuit is formed by a cylindrical coil wound fixed on the frame. The magnetic circuit is formed by the shell and movable core. Movable core is placed on the axis of the actuator and can move freely in it. To reduce the frictional force between the moving core and shell as well as to prevent their mutual impact the core is placed in a nonmagnetic sliding tube. The current in the coil produces magnetic field that gives rise to the Maxwell force which acts on the ferromagnetic core. Thus several ferromagnetic shape memory alloys like Ti_2NiCu [53], Ni-Mn-Ga [54], Ni-Mn-Sb, Ni-Mn-In [55] have been proposed for the application of magnetic actuator devices.

1.5 Motivation of the thesis:

As has been dicussed above in detail, in case of Heusler alloys atomic arrangements of the constituent elements are the most fundamental for defining their electronic and magnetic properties. Any deviation from the lattice position or from the stoichiometry of these ternany alloys dramatically introduces a structural or cationic (antisite) disorder in the system, which leads to the modification in the electronic band structure as well as magnetic properties. From this point of view, a deeper understanding of the structural properties of these alloys and their effect on magnetic properties is essential. Although, several studies on the structural and magnetic properties have been carried out in the last two decades, the field lacks some level of clarity about their short-range structural information. Over the years, X-ray diffraction has been extensively used in the structural characterization of the Heusler alloys, however due to similar kind of atomic scattering factors of the constituent atoms precise evaluation of cationic antisite disorder between different kind of atomic species is a difficult task. In this regard the element specific technique like X-ray Absoprtion Spectroscopy (XAS) serves as a complemetary technique which gives element specific local sutructure information including cationic antisite disorder. Along with this it also gives detail information regarding the oxidation state, co-ordination symmetry, hybridization between the atoms, band structure, atomic bond distances, static disorder factors, co-ordination number and the co-relation between the different atomic shells. Apart from this, based on orbital selective properties of XAS, another characterization technique viz., X-ray Magnetic Circular Dichrosim (XMCD) offerselement specific information about the total magnetic moment of the constituent elements. XMCD is a very powerful technique which tells about the element specific magnetic moment and the magnetic interactions between the constituent atoms in a multicomponent system like Heulser alloy. All the above characterization techniques require X-ray source of high brilliance, energy tunability and circularly polarized X-ray photons. The synchrotron radiation gives all its advantageous properties for characterizing the material with a highly brightness photons from infra-red to hard X-ray region. In this thesis, the XAS and XMCD studies on the samples have been carried out at the Indian synchrotron source at Indus-2, RRCAT, Indore.

In this thesis we have prepared a series of Heusler alloy samples viz., Ni_2FeGa, Co_2FeGa, Co_2FeAl and Co_2FeSi in thin film form using the pulsed laser deposition (PLD) technique on crystalline Si (111) substrate by varying the growth temperatures. The XAS characterization has been done at the Ni, Co, Fe and Ga K-edges in fluorescence mode and the experimental data has been analyzed using standard procedures. The results also have been complemented with other measurement techniques like grazing incidence X-ray diffraction (GIXRD), Grazing incidence X-ray reflectivity (GIXR), field emission scanning electron microscopy (FESEM), energy dispersive X-ray spectroscopy (EDXS) and vibrating sample magnetometer (VSM). All the above mentioned studies yield detail understanding regarding both long range and short range structural properties, morphology, elemental stoichiometry and magnetic properties of the Heulser alloys. At the end elemental and total magnetic moments, band structure and the XAS and XMCD spectra (at both K and L edges) of the above Heulser alloy samples have been simulated theoretically using density functional theory (DFT) calculations using SPR-KKR code. As it has been mentioned that the variation in the elemental stoichiometry affects the structural and magnetic properties and band structure of the alloys, the DFT study reveals the information of the effect of anitisite disorder due to variation in the elemental stoichiometry on electronic properties, band structure as well as XAS and XMCD spectra. The thesis also includes description of the indigenous development of a set-up to carry out XMCD measurements at the Energy Dispersive EXAFS beamline (BL-08) at Indus-2 Synchrotron source at Indore, India.

1.5.1 Necessity for the preparation of thin film:

Since the processing of materials into thin films allows simple integration into various types of devices, they are the key elements of continued technological advances made in the field of spintronic and magnetic devices. It is obvious that for any spintronic applications like in magnetic tunnel junction (MTJ), tunneling magneto resistance devices etc., and the Heusler alloys are needed to be prepared in thin film form. Therefore, a large number of research works have been carried out on half-metallic behaviors of Heusler Alloy thin films and the main aim of these studies have been fabricationsof thesefilms with proper crystallography and high spin polarization [56, 57, 58]. Thin film studies have directly or indirectly advanced many new areas of research in solid state physics and chemistry, however, preparation of the Heusler alloy in thin film form is much more challenging task from the perspective of material chemistry and chemical preparation. Besides the chemical stoichiometry, a well ordered Heusler phase is also expected to maintain its half metallicity and high spin polarization, through $L2_1$ or B2 structures. For the preparation of the Heusler alloys in thin film form, the main problem that is generally observed is the structural disorder due to lattice mismatch between the crystalline substrate and the deposited material and the phase separation is also frequently encountered. Similarly, the problem of ordering in Heusler alloy thin films are one of the key issues for the application in spintronics devices. Apart from structural orientation, surface or interface of the thin films are also important as the half metallicity is critically connected with the surface and interface properties of the sample [59]. Difficulties are encountered in preparation of these films with good ordering and without any trace of oxidation.

1.5.2 Necessity of PLD for the deposition of Heusler alloy thin film:

There are several deposition processes of the Co based Heusler alloy thin films have been reported such as RF magnetron Sputtering [60], Co-sputtering [61], Ion beam deposition [62] and Pulsed laser deposition (PLD) [63, 64, 65]. Among these, PLD is a technique that makes it possible to ablate the target material instantaneously and impinge it on the substrate with high kinetic energy which helps in maintaining the stoichiometry of the target in the films. Moreover, the high kinetic energy of the ad atoms reaching on the substrate assists migration of the film precursors on the surface and thereby makes the film growth at low temperature possible with desired crystalline structure and morphology. In PLD it is also possible to control the growth of the films by varying parameters such as the laser energy, the pulse repetition rate, fluency (i.e., energy density), the target to substrate distance etc. PLD is now established as one of the simple and versatile methods of growing thin films of a very wide range of materials (including numerous complex oxide systems, ceramics, ferroelectrics, High-Tc superconductors and materials exhibiting giant magneto-resistance) on a wide variety of substrates [66, 67, 68]. Good stoichiometry, morphology and crystalline quality are essential for the films to conserve the ferromagnetic and half metallic properties of the bulk material. To achieve these requirements in the present work we have used PLD to prepare the Heusler alloy films. To obtain the structurally ordered Heusler alloy thin films generally two approaches have been explored, viz., (i) employing post deposition annealing and (ii) depositing at elevated substrate temperature [69].

1.6 Outline of the thesis:

Subsequent chapters of the thesis are arranged as follows. Chapter2 deals with the details of the pulsed laser deposition technique and preparation of the thin films. This chapter also includes desctrtiption of several experimental techniques used for the characterization of the samples. Generation and properties of synchrotron radiation source have been briefly described including components and different generation of synchrotron radiation source. The details of the X-ray absorption spectroscopy techniques i.e., extended X-ray absorption spectroscopy (EXAFS), X-ray absorption near edge spectroscopy (XANES) and X-ray magnetic circular dichroism (XMCD) with their data analysis processes have been explained in this chapter. Subsequently, the other thin film characterization techniques like grazing incidence X-ray diffraction (GIXRD), grazing incidence X-ray reflectivity (GIXR), field emission scanning electron microscopy (FESEM), energy dispersive X-ray scattering (EDXS) and magnetic measurement using vibrating sample magnetometer (VSM) have also been described briefly.

Subsequently, in Chapter3 we have presented the results and discussions on the $Ni_{55}Fe_{19}Ga_{26}$ thin films prepared with different substrate temperatures using the above mentioned techniques. In the next chapters (Chapters 4-6) we have presented the results on Co based Heulser alloys of Co_2FeGa, Co_2FeAl, Co_2FeSi thin films respectively prepared using PLD technique on c-Si substrates. In Chapter4 possible antisite disorders which can be present in Co_2FeGa samples have been estimated by using EXAFS techniques and their effect on the magnetic properties has been explained in details. Similar model was also used for the characterization of the Co_2FeSi thin films described in Chapter6. Detail magnetic characterizations on these thin films and the variations in their magnetic anisotropy have been explained.

In Chapter 7 the development of the XMCD facility which includes the development of the 2T electromagnet along with the X-Z-θ motion stage to align the electromagnet with the synchrotron beam and installation of this facility at the Energy Dispersive EXAFS beamline at Indus-2 SRS have been described. XMCD measurementsof a standard Gd foil at Gd L_3-edge (7243 eV) measured using this set-up has also been mentioned in this Chapter.

The next chapter (Chapter8) is divided into two parts. In the first part the theoretical calculations using density functional theory (DFT) done on the Co based Heulser alloys using SPR-KKR code have been described. The theoretical calculations were done to study the electronic properties of the material alongwith to estimate their element specific magnetic moments. The partial density of states (PDOS) and the total density of states (DOS) were plotted to find out the values of spin polarizations of the materials. Along with this the XAS and the XMCD spectra were simulated on the compounds by varying the stoichiometry to see the effect on the XMCD spectra. In the second part of the chapter, Fe K-edge XMCD measurements at the Energy Dispersive EXAFS beamline (BL-08) on Co_2FeAl thin film deposited on free standing X-ray transparent B_4C substrates has been described. Finally, in Chapter 9 the conclusions drawn in all the previous chapters have been summarized and the future direction of the work has also been indicated

Chapter-2

EXPERIMENTAL TECHNIQUES AND DATA ANALYSIS

In this chapter we have discussed in detail about the preparation of the thin film samples along with the different experimental techniques and their data analysis processes used for the characterization of the samples. For this thesis four different series of full Heusler alloy thin films of Ni_2FeGa, Co_2FeZ (Z = Ga, Al, Si) were prepared on c-Si (111) substrate using pulsed laser deposition (PLD) technique. Later we have discussed about the various characterization techniques including synchrotronX-ray and other labsource based structural, morphological and magnetic characterization tools. Since the thesis is mainly focused on the characterization on the Heusler alloy thin films by X-ray absorption spectroscopy (XAS) technique using synchrotron radiation, this has been discussed in this chapter in more details.

2.1 Samples preparation:

2.1.1 Pulsed Laser Deposition (PLD) technique:

Pulsed laser deposition (PLD), also known as the laser ablation technique, is a thin film deposition technique where the high power laser (gas or solid state laser) is used for the deposition of the thin film from a bulk target. In this technique a high power laser is focused on a target and it ablates the target material instantaneously and produces the plume of plasma. The materials of the substrate are carried by the plasma and impinge it on the substrate. In this way the adatoms get high kinetic energy which helps in maintaining the stoichiometry of the target in the films. The schematic diagram of the PLD setup is shown in the figure- 2.1. Moreover, the high kinetic energy of the adatoms reaching on the substrate assists diffusion of the film precursors on the surface and thus makes the film growth at low temperature possible with desired crystalline structure and morphology. In PLD it is also possible to control the growth of the films by varying parameters such as the laser energy, the pulse repetition rate, fluency (i.e., energy density), the target to substrate distance etc. PLD is now established as one of the simple and versatile methods of growing thin films of a very wide range of materials (including numerous complex oxide systems, ceramics, ferroelectrics, High-Tc superconductors and materials exhibiting giant magneto-resistance) on a wide variety of substrates [66, 67, 68].

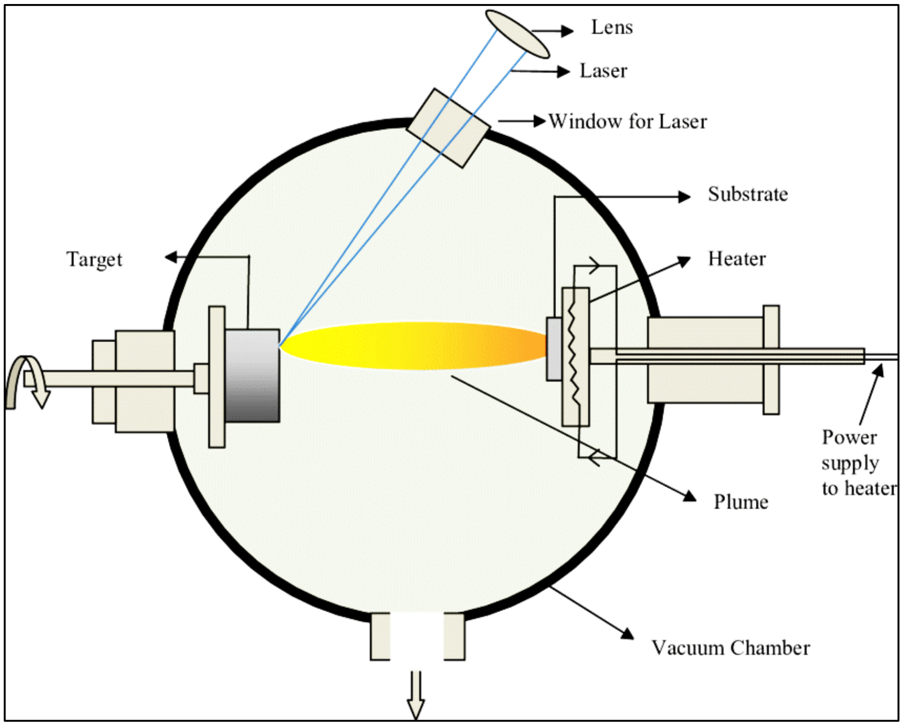

Figure 2.1: A schematic diagram of the PLD setup

Good stoichiometry, morphology and crystalline quality are essential for the films to conserve the ferromagnetic and halfmetallic properties of the bulk material. To achieve these requirements in the present work we have used PLD to prepare the Heusler alloy films.

2.1.2 Sample preparation method:

The thin films were deposited using four circular bulk targets of 3-inch diameter and 3 mm thickness. The off-stoichiometric $Ni_{55}Fe_{19}Ga_{26}$ target was prepared with high purity (~99.99%)

elemental precursors by vacuum arc melting process in ultra-pure inert gas atmosphere explained elsewhere [70]. The product material was subsequently pressed into a pellet to have the shape of a pancake. Later the target was smoothly polished from both side and cut into 3-inch diameter with 3 mm thickness. However, for the deposoition Co based Heusley alloys, circular targets of same size with 99.99% purity were procured commercially. c-Si substrates of 10 mm × 10 mm size were used for the deposition and prior to loading in the PLD chamber each substrate was cleaned for 5 minutes by placing then in a crucible inside of an ultrasonic bath and subsequently dryingby blowing Argon gas on it. The target was mounted in the vacuum chamber in such a way that the laser beam falls on the target at an angle 45° to the surface. The laser used for the deposition was a KrF excimer laser having wavelength 248 nm with a pulse rate of 5Hz and maximum output energy 0.8J / pulse. Finally, the deposition was carried out at a base pressure of ~10^{-6} mbar by heating the c-Si substrate to a desired temperature. For each taerget material, a series of thin films were prepared by varying the substrate temperature in order to monitor the effect of growth temperature on the structural and physical properties of the alloys.

2.2 Characterisation tools:

This section of thesis consists on mainly two parts. In the 1st part the details of synchrotron radiation source, Indus-2 synchrotron source, beamline optics, two beam lines used in this thesis work, detectors and EXAFS data analysis technique have been explained. In the 2nd part other characterization techniques like GIXRD, XRR, FESEM, EDXS and VSM and their data analysis techniques have been discussed in detail.

2.2.1 Synchrotron radiation:

2.2.1.1 Background of synchrotron radiation:

Synchrotron is basically a particle accelerator and the name ‘synchrotron’ came from the way of operation i.e., synchronously accelerating electrons. Thus the synchrotron is a machine which accelerates the charge particles (generally electrons) to an extremely high energy, so that they attain speed close to the speed of light, while moving in a circular path, generating photons in the tangential direction of the circular orbit. It is well known that motion of an electron is governed by the Lorentz force in a strong electric and magnetic fields. The Lorentz force is given as $F = e(E+v\times B)$, where E and B are the electric and magnetic fields and e and v are the charge and velocity of the moving electrons respectively. In 1897 an expression for the instantaneous total power radiated by an accelerated charged particle was derived by Larmor and in the following year Liénard raises the case of a relativistic particle undergoing centripetal acceleration in a circular trajectory. However, the interest in radiation form a charged particle due to the energy loss mechanism was reawakened in the year of 1920 on betatrons. This was a machine to produce intense beams of X-rays by directing the accelerated beam to a suitable target. Later it was realized that the tangential fan of the synchrotron radiation comes due to the loosing of energy of the accelerating electrons which can be utilized to characterize the material. In 1956 Tomboulian and Hartman were able to confirm the spectral and angular distribution of the radiation with a grazing incidence spectrograph in the ultraviolet from 80 Å to 300 Å and reported the first soft X-ray spectroscopy experiments with synchrotron radiation, measuring the transmission of Beryllium and Aluminum foils at the K-and L-edges. [74]

2.2.1.2. Properties of synchrotron radiation:

The electrons that are subjected to an accelerating field emit electromagnetic waves. In a circular high-energy electron accelerator, the energy of the electrons goes upto GeV energy, and the bending magnet gives a very strong centripetal acceleration with highly relativistic electrons ($E >> mc^2$, m be the rest mass of electron). Thus this acceleration induces an electromagnetic radiation over a wide energy range staring from ultraviolet to hard X-ray region. The synchrotron X-ray source is composed of three main components, i.e linear accelerator, and booster synchrotron and storage ring.

After generating electrons by thermionic emission from a low work function material, the electrons are injected into the linear accelerator for initial acceleration upto certain energy, say few MeV. In some cases, a microtron is also used for the initial acceleration. Subsequently, the accelerated electrons enter into the booster synchrotron ring and the electrons achieve the relativistic speed with energy near to GeV. At this point the electrons are transferred to the storage ring. This storage ring consists of periodic array of bending magnets for bending the path of the moving electron in circular orbit and quadruple and hexapole magnets for focusing and correction of aberrations respectively. Electrons passing through the bending magnet feel a centripetal acceleration, which is perpendicular to the direction of the motion and emits the synchrotron radiation of wide range of energy. In the storage ring the electrons are further accelerated by a higher electric field of radio frequency to maintain the energy and keep moving in the storage ring.

This synchrotron radiation has very interesting properties which makes is advantageous than the lab source.

1. Very high brightness (flux) or intensity: The intensity is of the order of ~10^{12}photon/s/mm2/0.1% BW for the bending magnetbased source and higher order for next generations. The concentration of the beam depends of the beam divergence and size of the beam. This higher intense beam helps to measure the element at a very low quantity or very weakly scattering samples. Synchrotron source also helps to identify impurities present in a material in ppm level.

2. Broad energy spectrum: The synchrotron radiation delivers a wide range of energy starting from the ultraviolet (10 – 120 eV) to the hard X-ray (5 - 120 keV) region. This wide range of energy felicitates a higher degree of tunability, which helps studying absorption spectra of a wide range of elements.

3. Very high collimation: Synchrotron radiation highly collimated with divergence in the order of few mrads, collimation being higher in vertical plane than in horizontal plane. This helps to reduce loss of radiation significantly in its passage through the optical components towards the sample along a beamline and also to achieve greater spatial resolution in measurements.

4. Polarization: Synchrotron radiation is also highly polarized. At the plane of the storage ring orbit it is plane polarized and is right circularly and left circularly polarized if we move above and below the plane of the orbit. A typical diagram of polarization of the synchrotron beam to the observer is shown in figure-2.2. This is particularly useful for detection of anisotropic structural changes or the characterization of the magnetic materials.

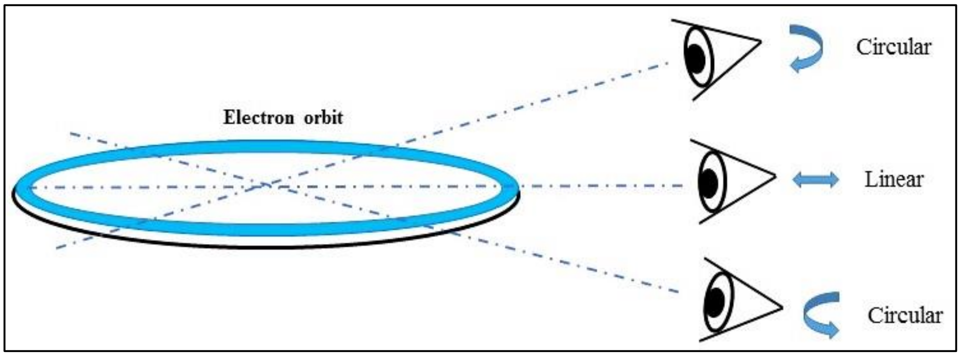

Figure-2.2: Linear and circular polarization of synchrotron radiation

5. Coherence: The beam is both spatially and temporally coherent. The most recent synchrotron sources are "fully spatially coherent" down to wavelengths in the ultraviolet and soft-X-ray range – and quite coherent for shorter wavelengths while the tempral cohenrence depends of the nature of application or requirement of monochromaticity.

6. Time structure: As the electrons in the storage ring are accelerated in electron bunches, it has a precise "flashing" time structure. This consists of very short pulses of femto-second width and separated by longer intervals (pico-second), allowing resolution of processes on the same time scale.

7. Cleanliness of the source: As the light emission takes place in an ultra-high vacuum, in contrast to the situation in gas discharge or spark lamps the synchrotron source is a clean source of X-ray.

2.2.2 Different sources of synchrotron radiation:

It has been mentioned that the radiation in a synchrotron comes due to the relativistic motion of the electrons, which is forced to deviate from straight path by applying a strong magnet.

2.2.2.1 Bending magnet: Bending magnets are the first ever sources to generate the synchrotron radiation. Bending magnets are the dipoles with uniform magnetic field. As the electrons are deflected from their straight path when passing through these magnets, they emit beam of X-rays tangentially to the plane of the electron beam which delivers a flux of 10^{10} - 10^{13} photon/s/mm^2/0.1% BW. The bending magnets are also needed to produce the closed path in the storage ring. A wide and continuous spectrum, from microwaves to hard X-rays is generally emitted by a bending magnet source. The emission peak is given by $\lambda = c/\nu$, where ν is the “cyclotron frequency”, i.e., the rotational frequency of the motion induced by the magnetic field. The electron travels on the perimeter of a circle of radius derived by the magnetic field strength. Horizontally the light beam sweeps out like a lighthouse and the intensity is flat with horizontal angle. Vertically it is in a narrow cone of typically $1/\gamma$ radians, where γ is the energy of the electrons w.r.t. their rest mass energy. However, it is less focused, or brighter, than the fine beam of X-rays from an insertion device. The generation of the synchrotron radiation from bending magnet is shown in the figure-2.3.

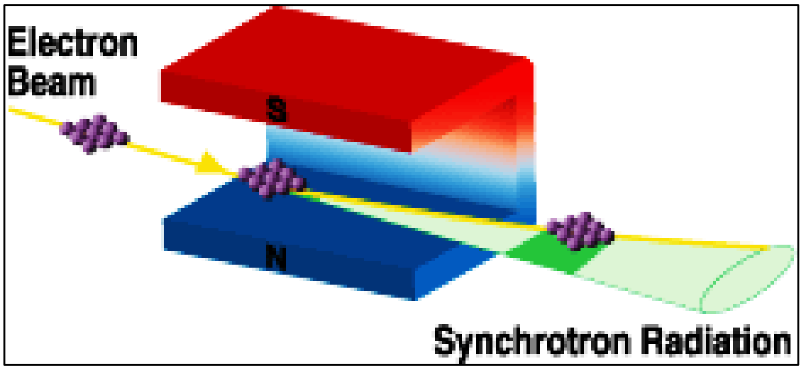

Figure-2.3: Generation of synchrotron radiation from a bending magnet

2.2.2.2. Insertion devices:

In order to produce the required brighter light to build special magnetic systems that make the electrons bend at a specific curvature, insertion devices were proposed. Insertion devices (ID) are made of two magnetic arrays placed in such a way that the trajectory of the electrons follows an oscillatory path. Insertion devices are inserted into straight sections of storage rings. As the electrons pass through the ID the alternating magnetic field experienced by the particles causes their trajectory to undergo a transverse oscillation. The radiation emitted at each consecutive bend overlaps and interferes with that from other bends. This generates a much more focused, or brilliant, beam of radiation than that generated by a bending magnet. There are two kinds of insertion devices i.e (i) wiggler and (ii) undulator. The basic parameters that is used to distinguish the IDs is the 'deflection parameter' K, which is given by-

$$K = \frac{eB_0\lambda_{ID}}{2\pi m_0 c} = 0.0934\lambda_{ID}\,[\mathrm{cm}]\,B_0\,[\mathrm{kG}] \quad (2.1)$$

where, λ_{ID} is the period of the insertion device and $B_0$is the magnetic field amplitude.

(i) Wiggler: Wigglers are used to increase the intensity of synchrotron radiation by lining up a series of magnets which enhances the intensity simply by the number of magnet poles. The generated spectrum by wigglers is identical to the corresponding bending magnet, only the critical angle gets shifted towards the higher energy value. In order to add up the intensity of the individual emission cones, the dipoles are arranged with alternating polarity such that the electrons are essentially moving straight except for small "wiggles" where the radiation is emitted. If there are N periods and the length of each period is λ_{ID}, then the overall length of the wiggler will be $L = N\times\lambda_{ID}$. The magnetic field is applied in an alternating arrangement in the vertical direction so that the sinusoidal trajectory of the electron beam lies in the horizontal plane. The emission cones overlap and the intensity adds up together. The advantage of such a wiggler is that it emits intense radiation over a wide energy range, very much like a bending magnet. The major disadvantage is that most of the scientific experiments usually only need a very narrow range of wavelengths and therefore most of the wiggler radiation power remains unused leading to unwanted heat production within the optical devices. The use of higher magnetic fields increases the critical energy with respect to the values achievable with bending magnets and extends the spectral range of a storage ring towards higher energies. The wiggler delivers the photon intensity as N (periods) × dipole source which is of the order of 10^{16}. For wiggler, the transverse oscillations of the electrons are very large and the angular deviations also. Therefore, $K >> 1$ and the interference effects of the electron beams are negligible and only the overall intensity is obtained by summing over contribution of individual poles.

(ii) Undulator: Undulators are the most powerful generators of synchrotron radiation. They consist of periodic arrangements of dipole magnets generating an alternating magnetic field which deflects the electron beam sinusoidally, like wigglers. For the undulator the angular deflection is very small since $K<1$, thus radiation emitted due to each beanding of the electron bunch interfere with each other giving rise to interference patterns which lead to narrow energy bands. Thus a radiation with the wavelength of its periodic motion is given by the geometric period length λ_{ID} of the undulator dipole arrangement. In the particles' frame, λ_{ID} is shrunk by the factor γ due to Lorentz contraction and the wavelength is further shrunk by another approximate factor 2γ due to the relativistic Doppler Effect. Undulators are built to emit the X-rays with $\lambda \sim 0.1$ nm wavelength, therefore have a magnet structure with a period length of few cm. An undulator delivers the photon intensity as $N^2 \times$ dipole source which is of the order of 10^{17} - 10^{20}. In addition to the fundamental wavelength, the higher harmonics are also generated and their number and intensity increases with K value. Each harmonics has a limited wavelength bandwidth given by $\Delta\lambda/\lambda = 1/nN$. Hence the bandwidth decreases with the number N of periods of the undulator and the harmonic number n. The nature of synchrotron radiation from both the insertion devices is shown in the figure-2.4.

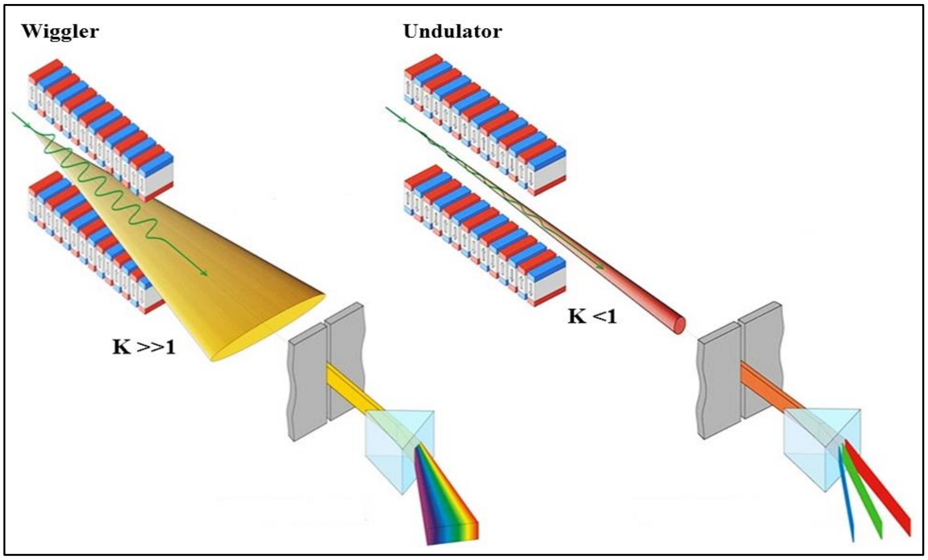

Figure-2.4: Synchrotron radiation from insertion devices i.e wiggler and undulator

2.2.3. Indus synchrotron source:

India has its own synchrotron radiation facility at Raja Ramanna Centre for Advanced Technology (RRCAT), Indore, Madhya Pradesh. This synchrotron source has two storage rings viz., Indus-1 and 2. Indus-1 is the 1st Indian synchrotron which operates at electron energy 450 MeV at 100 mA commissioned in the year 1998 [72]. It has a circumference of 18.97 m in which four combined function 90° bending magnets and 16 quadrupole magnets are arranged in four identical cells. This has 6 bending magnet based operational beamlines with electromagnetic spectrum ranging from infrared to soft X-ray region and due to its shorter wavelength it possesses great capability to explore physical structure with much better resolution than the visible light. The beamline layout of the Indus-1 synchrotron is shown in the figure-2.5.

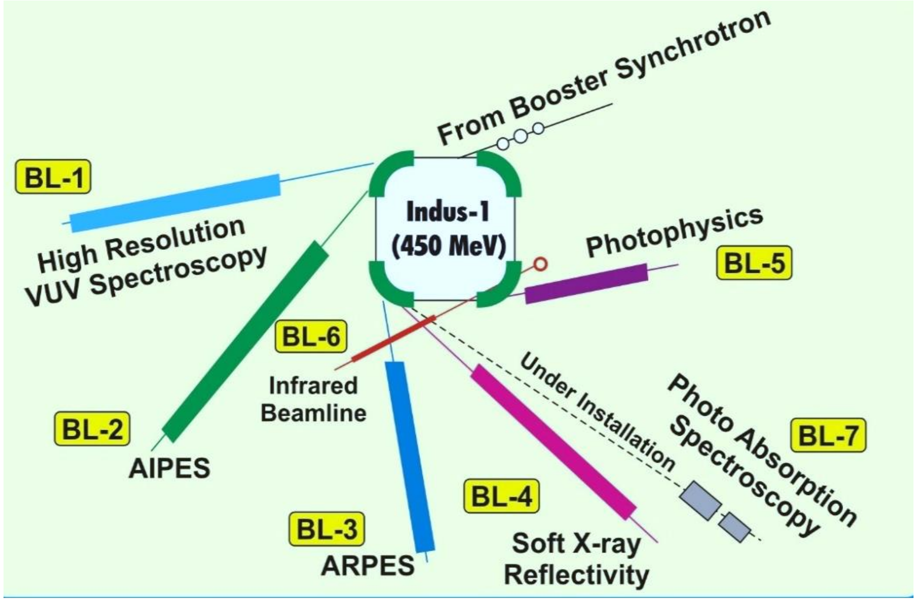

Figure-2.5: Beamline layout of Indus-1 synchrotron source

The second source is the Indus-2 synchrotron which operates at electron energy of 2.5 GeV at 200 mA current and at a critical wavelength of 2Å (commissioned in the year 2012) [73, 74]. This synchrotron source delivers photon energies from soft X-ray to the hard X-ray regime. Indus-

2 storage ring with circumference of 172.47m has 16 bending magnets, 72 quadrupole magnets and 32 sextupole magnets. A set of 4 RF cavities with an operating frequency of 505.812 MHz provides the required energy for beam acceleration from 550 MeV to 2.5 GeV as well as for compensating the energy lost due to emitted synchrotron radiation. The Indus-2 lattice was designed to give low beam emittance and high brightness. Indus-2 storage ring has5 insertion devices among which 2 are pure permanent magnet undulators have already been installed while 1 pure permanent magnet helical undulator APPLE II, and one 3.5 Tesla superconducting multipole wiggler and one 5 Tesla superconducting wavelength shifter are going to be installed in future. At 2.5 GeV the beam lifetime is ~ 18 hours. An RF voltage of 1.5 MV is required to achieve this lifetime at 2.5 GeV. The beamline layout is shown in the figure-2.6.

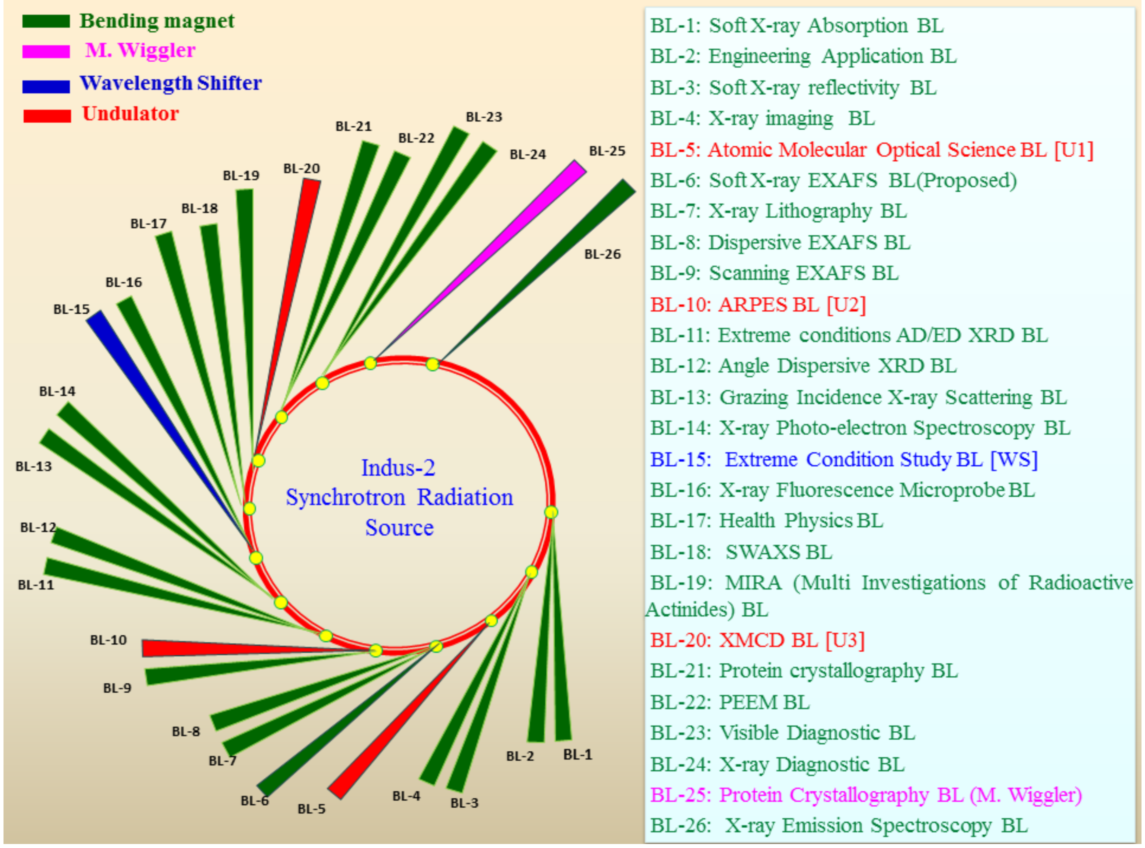

Figure-2.6: Beamline layout of Indus-2 synchrotron source

2.2.3.1. Energy Dispersive EXAFS beamline (BL-08):

The XMCD measurement mentioned in this thesis was carried out at the Energy Dispersive EXAFS beamline (BL-08) at Indus-2 synchrotron source [75]. The Energy Dispersive EXAFS beamline operates within the photon energy range 5 – 20 keV which provides the energy bandwidths of 0.3, 1.0 and 2.0 keV at the photon energies 5, 10 and 20 keV with resolution of 0.5, 1.0, 2 eV. The beamline consists of 460 mm long Si (111) (2d = 6.2709Å) crystal mounted on an elliptical crystal bender and a position sensitive CCD detector of size 25 × 25 mm^2 having 2048 × 2048 pixels. The Si crystal was chosen because of its narrow Darwin width, low thermal expansion coefficient and high thermal conductivity as a polychromator. The optical layout of the beamline is shown in figure-2.7.

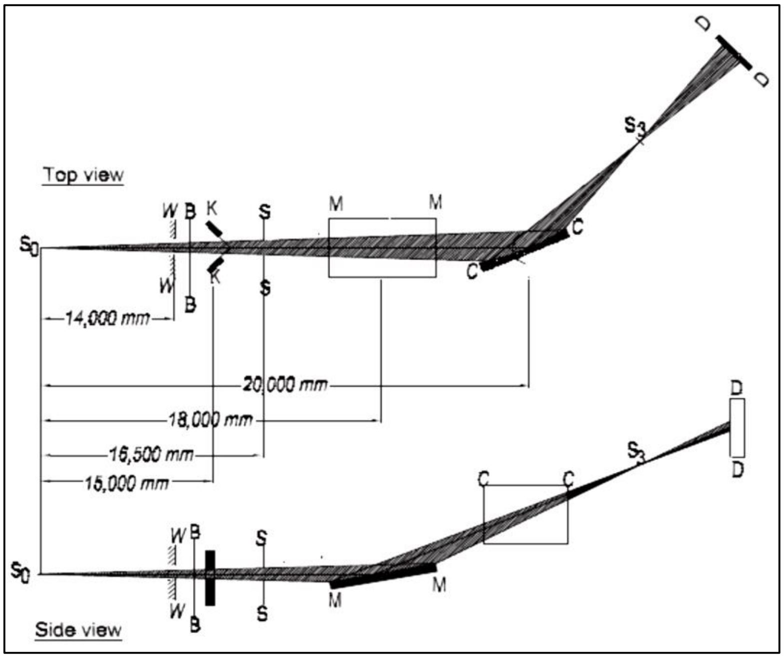

Figure-2.7: Optical layout of the energy dispersive EXAFS beamline (BL-08) [75]

In the beamline the Si (111) crystal (CC) is bent in such a way that the source of the beam S_0 and the sample position S_3 remains at the two foci of the ellipse. This ensures that all the radiation emerging from the source S_0 reaches S_3 with minimum aberration. A beam aperture (KK) made of water-cooled copper blocks and a precision slit system (SS) which uses two sets of water-cooled tantalum jaws, define final horizontal and vertical divergences of the beam coming from the bending magnet through the Be window (BB). After emerging from the slit system the beam having certain horizontal and vertical divergence falls on the Rh coated cylindrical mirror (MM) at a grazing angle of incidence ~0.2°. This mirror is used for the vertical focusing of the beam at the sample position and to cut off the higher energy part of the beam. After getting reflected from the mirror the horizontally diverging beam falls on the Si crystal (CC). Depending upon the radius of curvature of the crystal and the angle of incidence, the crystal reflects a particular band of energy (ΔE). Finally, this spatially dispersed polychromatic beam is focused at the sample position (S_3) due to the elliptical curvature of the crystal. After transmission through sample, the beam diverges further and falls on the position sensitive detector (DD). The whole set-up of the beamline after the mirror is mounted on a goniometer, the crystal chamber is mounted on its θ axis of the goniometer while the sample stage and the detector stages are mounted on the 2θ arm. Thus, the detector records the energy dispersive X-ray absorption spectra over a wide energy range of (ΔE) around a central energy (E_0) as a single snap shot. The typical measurement time of one full EXAFS spectrum in the beamline is 300 msec and hence it is very suitable for carrying out time-resolved EXAFS measurements, though it has limitation that measurement can only be done in transmission mode. The photograph of the BL-08 beamline is shown in the figure-2.8.

Figure-2.8: Photograph of the beamline (BL-08) inside the hutch [75]

2.2.3.2 Energy Scanning EXAFS beamline (BL-09):

The XANES and the EXAFS measurement on the Heulser alloy samples mentioned in this thesis were carried out at the Energy Scanning EXAFS beamline (BL-09) at Indus-2 synchrotron source [79,80]. This beam line operates in the energy range of 4-25 keV and offers a typical resolution ($\Delta E/E$) of 10^{-4}at 10 keV photon energy. This beamline delivers a photon flux of 10^{12}photons/sec/0.1 % band width and the size of the beam at the sample position is 1mm (H)× 0.2 mm (V) and acceptance of the synchrotron radiation is 3mrad (H) × 0.2 mrad (V). The detail schematic diagram of the beamline is shown in the figure-2.9. The beam line optics consist of a Rh/Pt coated meridional cylindrical pre-mirror facing upward which is used for the collimation of the beam. The collimated beam reflected by the mirror is monochromatized by a Si (111) (2d=6.2709) based double crystal monochromator (DCM).

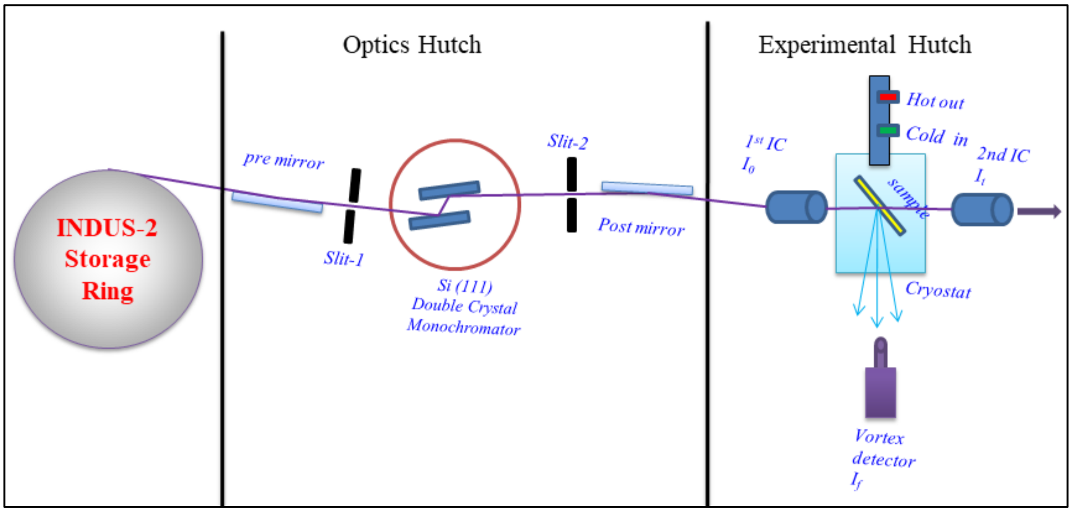

Figure-2.9: Schematic diagram of energy scanning EXAFS beamline (BL-09) with low temperature setup

The first crystal of the DCM isa plane crystal and second one is mechanically bendable (Sagittal) crystal which helps to focus beam horizontally at the fixed sample position. After the DCM there is another Rh/Pt coated facing down bendable post mirror which is used for vertical focusing of the beam at the sample position. Both the mirrors are mounted horizontally on the hexapod. The photographs of both the inside of optics hutch and experimental station are shown in the figure-2.10 (a) and (b).

At the experimental station of BL-09, EXAFS measurements can be done in two different operational modes i.e (i) transmission and (ii) fluorescence modes. For the data collection in the transmission mode three ionization chambers (IC), each of 30 cm length are used. The first IC measures the incident flux (I_0) and the second IC is used for the measurement of the transmitted flux (I_t) after passing through the sample. A third IC is also used after the second IC, where reference metal foils are measured for energy calibration. The X-ray absorption co-efficient is thus determined as $\mu = \ln(\frac{I_0}{I_t})$, Appropriate gas mixtures with optimized pressures are chosen in such a way that 10-20% absorption of beam is occurred in the first IC and 70-90% absorption of beam occurred in the second IC to improve the signal to noise ratio. It is expected that a higher harmonics or lower wavelength beam may come with the fundamental beam. So the rejection of the higher harmonics content in the X-ray is performed by 30% detuning of the second crystal of DCM using the piezo motor. This technique breaks the parallel arrangement of the two crystals by a very little amount so the higher harmonics do not get transimiited along with the fundamental energy. In order to obtain a proper edge jump the samples of appropriate weight and thickness are normally prepared in powder form and palletized to 15 mm diameter and 2-3 mm thickness.

For the EXAFS measurement in the fluorescence mode, only the first IC placed prior to the sample measures the incident beam (I_0). Here the sample is placed at 45° angle to the incident X-ray beam and the fluorescence signal (I_f) is detected using a Si drift detector placed at 90° to the incident beam as shown in the figure-2.11. Here the X-ray absorption co-efficient of the sample is determined by $\mu = \frac{I_f}{I_0}$, and the spectrum is taken as a function of energy by scanning the monochromator over the specified range. For the fluorescence measurement the Si drift detector (Vortex) is used.

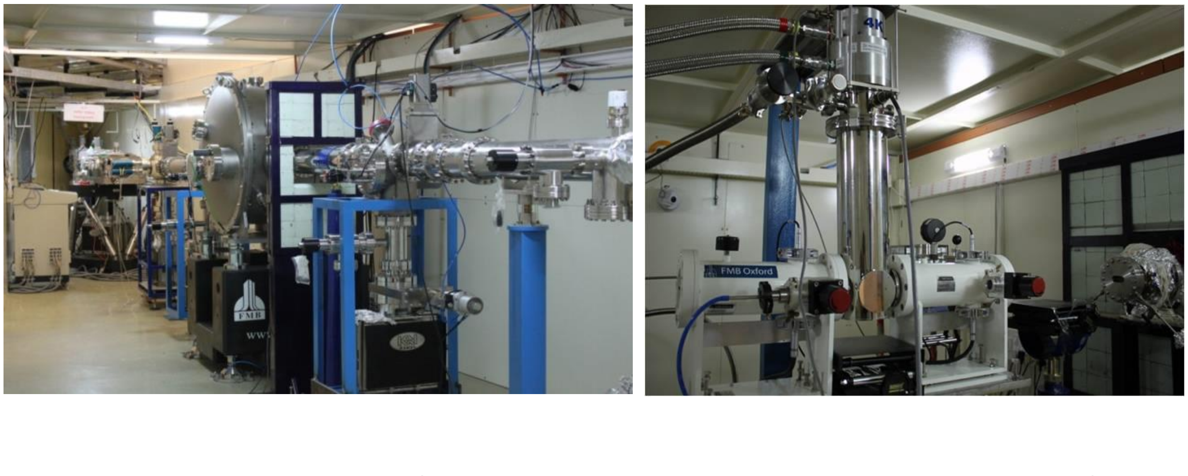

Figure-2.10: Photograph of (a) optics hutch and (b) experimental station of Scanning EXAFS Beamline BL-09

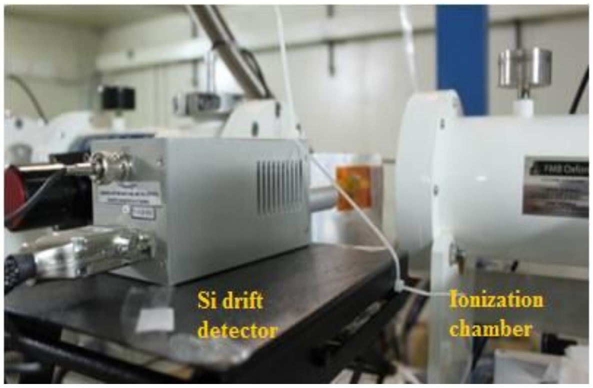

Figure-2.11: Experimental set-up for fluorescence mode of XAFS measurement

The energy range (4-25 keV) available from the beamline is sufficient for K-edge studies of many elements in the range $20 < Z < 47$(viz. V, Ti, to Zr and Rb to Mo etc.). For $Z > 47$(viz. Rare earth elements, Au, Pt, Th, U etc.) one can probe L-edges instead of K edge. The sample thicknesses for experiments are in theμm range for transmission experiments. However, thin film and/or dilute systems studies are possible in fluorescence mode.

The low temperature measurement facility is also available with this beamline which is equipped with a 4K (FMB) closed cycle cryostat and the low temperature measurement mentioned in this thesis has been done here in fluorescence mode using thin film samples.

2.3 X-ray Absorption Spectroscopy (XAS):

2.3.1 Theoretical background of X-ray absorption:

X-ray absorption coefficient μ(E) describes how strongly X-rays are absorbed as a function of photon energyE is the physical quantity that is measured in this technique. When a monochromatic X-ray beam of the energy E passes through a homogeneous sample of the thickness x, it is attenuated (figure-2.12) following the Lambert-Beer law which is described by:

$$I(t) = I_0\, e^{-\mu(E)x} \qquad (2.2)$$

Where, $I_0(E)$ and $I(E)$ are the incident and transmitted X-ray intensities, and $\mu(E)$ is the linear absorption coefficient.E.

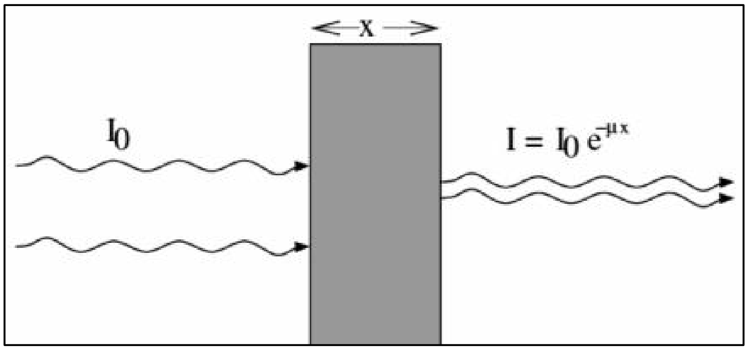

Figure-2.12: Schematic of Lambert-Beer law

Generally, $\mu(E)$ decreases smoothly as the energy increases (approximately as E^{-3}), i.e., the X-rays become more penetrating. The four major processes by which X-rays are absorbed in a material are (i) Thomson scattering (elastic scattering), (ii) Photo-electric absorption, (iii) Compton Scattering (inelastic scattering) and (iv) Pair production, among which in the photon energy range of 1-100 keV, Photo-electric absorption is the dominant one. Due to photoelectric absorption, at certain energies, the absorption increases drastically and gives rise to an absorption jump. Each such jump, which are called absorption edges, occurs when the energy of the incident photons is just sufficient enough excite a core electron of the absorbing atom to a continuum state, i.e. to produce a photoelectron. Thus, the energies of the absorbed radiation at these edges correspond to the binding energies of electrons in the K, L_I, L_{II} and L_{III} etc, shells ($1s_{1/2}$, $2s_{1/2}$, $2p_{1/2}$ and $2p_{3/2}$ orbitals (states)) of the absorbing elements (figure-2.13). Accordingly, the K absorption edge arises due to the electronic transition from innermost 1s state (K level) to unoccupied states above the Fermi energy (E_F) level. Beyond the absorption edge the absorption coefficient decreases monotonically with increasing the incident photon energy, until the next absorption edge is arrived.

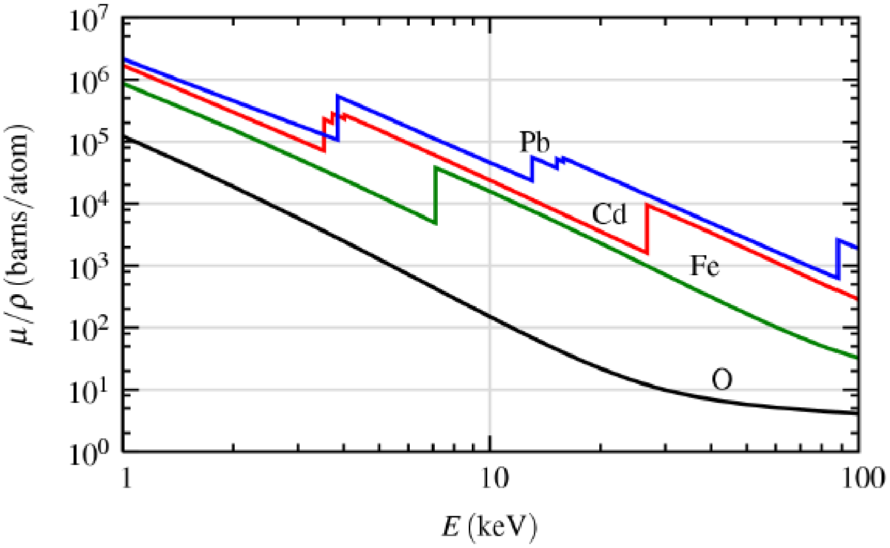

Figure-2.13: Photo absorption cross section of different elements for different phenomenon of interaction of X-ray with matter. [78]

2.3.2 Theoretical description of Extended X-ray Absorption Fine Structure (EXAFS):

A typical X-ray absorption spectrum is divided into two regions viz., X-ray Absorption Near Edge Structure (XANES) and Extended X-ray Absorption Fine Structure (EXAFS) regions. Though both of themhave the same physical origin, this distinction comes intheir interpretation and provides different information about the system. XANES is strongly sensitive to formal oxidation state and coordination geometry (e.g., octahedral, tetrahedral coordination) of the absorbing atom, while EXAFS is used to determine the distances, coordination number, and species of the neighbors of the absorbing atom.

Here the physical description of EXAFS process and the origin of the EXAFS equation will be discussed. As has been mentioned above, X-Ray absorption in the regime of photon energy (1-100 keV) is dominated by photoelectron absorption process. As discussed earlier in the photoelectric absorption process, an X-ray is absorbed by a core-level with binding energy, and a photo-electron with wave number *k* is created and propagates away from the atom. When a neighbouring atom is included in the structure, the photo-electrons get scattered back from the electrons of this neighbouring atom, and the scattered photo-electrons finally return to the absorbing atom. The schematic of the scattering phenomena is shown in the figure-2.14.

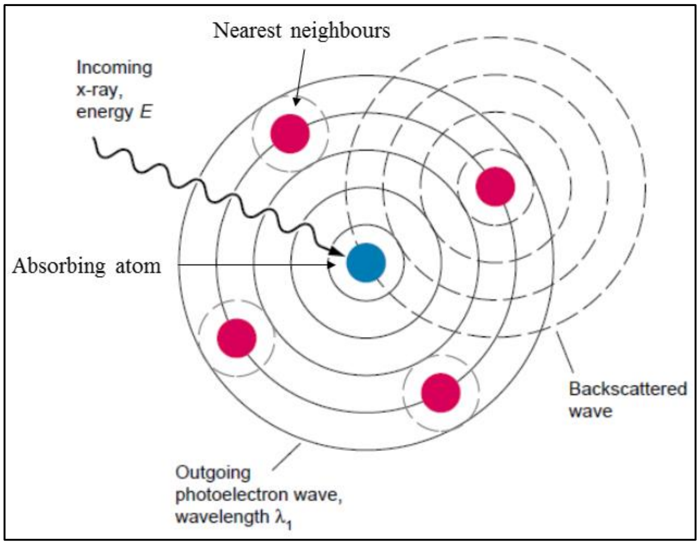

Figure-2.14: Schematic of scattering phenomena in X-ray absorption spectroscopy [79]

Typical X-ray absorption spectrum is shown in the figure-2.15. Thus the final state of the ejected photoelectron is a free electron state for an isolated atom, however the photoelectron is backscattered when there are neighboring atoms around. These backscattered electrons wave then interferes with the original outgoing photoelectron wave, giving rise to an oscillatory final state vector. This is the origin of the fine structure oscillations, observed in the EXAFS part of the absorption spectra, where absorption is proportional to the transition matrix between the initial absorbing and final backscattered state vectors.

The final state vector being oscillatory in this case results in an oscillation in the absorption spectra. Now the absorption coefficient μ(E) can be described by the Fermi Golden rule as-

$$\mu(E) \; \alpha \; \left| <i| \, H \, | f> \right|^2 \tag{2.3}$$

where $<i\,|$ *re*presents the initial state (an x-ray, a core electron, but no photo-electron produced), $|\, f >$ represents the final state (no x-ray but a core-hole and a photo-electron produced), and H is the interaction term, which will be explained later.

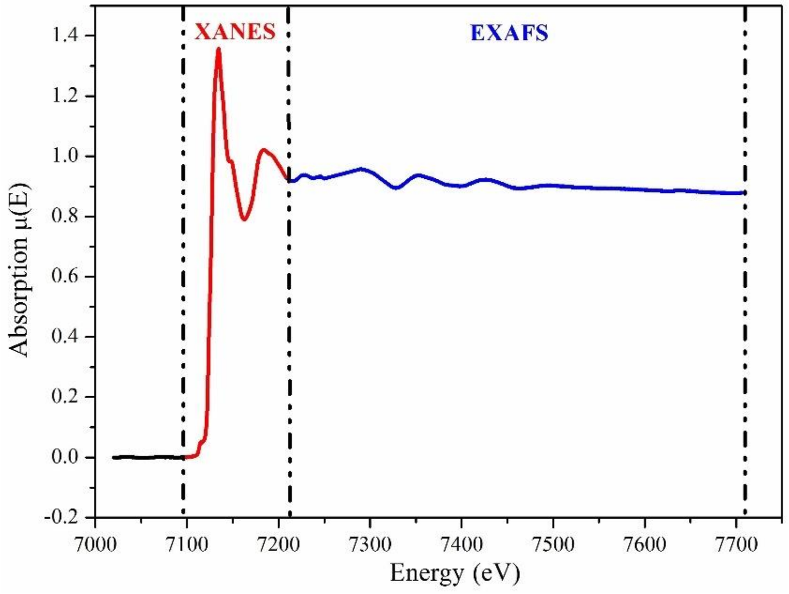

Figure-2.15: Typical X-ray absorption spectra

Since the initial state is the core level which is tightly bound to the absorbing atom, so the initial state will not be affected by the presence of the neighboring atoms. However, as the backscattered photoelectrons are able to see the outermost orbitals, so those will be affected by the neighboring atoms. Considering this if we expand the final state $| f >$into two parts, which can be written as:

$| f > = | f_0> + | \varDelta f >$and by expandingequation (1) can be written as

$$\mu(E)\ \alpha <i|\ H\ |\ f_0>\big|^2[1+ <i|\ H\ |\varDelta f>\frac{<f_0|\ H\ |i>^*}{<i|\ H\ |f_0>^2}]+ C.C. \tag{2.4}$$

C.C is the complex conjugate

Now rearranging the above equation, it can be written as

$$\mu(E) = \mu_0(E)\ [1 + \chi(E)] \tag{2.5}$$

Now comparing equation (2.4) and (2.5) we canassign μ_0 as $\big|<i|\ H\ |\ f_0>\big|^2$ as the 'bare atom absorption', which depends only on the absorbing atom i.e the absorption when there are no neighbor atoms. The fine structure $\chi(E)$ is proportional to $<i|\ H\ |\varDelta f>$ or this can be written as

$$\chi(E) = \frac{\mu(E) - \mu_0\,(E)}{\varDelta\mu_0(E)} \tag{2.6}$$

Where, $\mu(E)$ is the measured absorption coefficient, $\mu_0(E)$ is a smooth background function representing the absorption of an isolated atom, and $\Delta\mu_0$ is the measured jump in the absorption $\mu(E)$ at the absorption edge energy E_0.

The EXAFS is well understood in terms of the wave vector k, which can be written as

$$k = \sqrt{\frac{2m\,(E - E_0)}{\hbar^2}} \tag{2.7}$$

In the equation (2.3) the term *H* is an important term which represents the process of changing between two energies, momentum states. According to the quantum radiation theory the interaction term is proportional to e^{ikR}. As the initial state is a tightly bound core-level, which we can be approximated as a delta function and the change in final state is just the wave-function of the scattered photo-electron, $\psi_{scatt}(R)$. Using all these terms together, we get the simple expression for the EXAFS as:

$$\chi(E) \propto \int \delta R\, e^{ikR}\, \psi_{scatt}(R)\, dR = \psi_{scatt}(0) \tag{2.8}$$

By further evaluating the amplitude of the backscattered photoelectrons at the absorbing atom, we will get the EXAFS equation. In this physical picture the outgoing photoelectron wave functions will be spherical wave as,

$$\psi\,(k,r) = \frac{e^{ikR}}{kR} \tag{2.9}$$

traveling a distance R to the neighbouring atom, then getting back scattered from a neighbour atom and traveling as a spherical wave a distance R back to the absorbing atom. Now the equation (2.9) can be written as

$$\psi_{scatt}(k, r = 0) = \frac{e^{ikR}}{kR}\left[2kf(k)e^{i\delta(k)}\right]\frac{e^{ikR}}{kR} + C.C. \tag{2.10}$$

where, $f(k)$ and $\delta(k)$ are back scattering amplitude and scattering phase shift due to the scattering atoms. The scattering factors $f(k)$ and $\delta(k)$ depends upon the atomic number (Z) of the neighboring atoms. These scattering factors make EXAFS sensitive to the atomic species of the neighboring atom. Now combining equation (2.8) and (2.10and including the complex conjugate, we will end up with a real function as

$$\chi(k) = \frac{f(k)}{kR^2}\sin[2kR + \delta(k)] \tag{2.11}$$

This is the EXAFS equation. However, in the equation (2.11) the treatment has been done for only one pair of absorbing and scattering atoms, however in a real measurement we have to take the average over all the available atomic pairs. Apart from this the thermal and static disorder in the bond distances will give a range of distances that affects the EXAFS oscillations. Including this equation (2.11) becomes to

$$\chi(k) = \frac{Ne^{-2k^2\sigma^2} f(k)}{kR^2}\sin[2kR + \delta(k)] \tag{2.12}$$

where N is the co-ordination number (C.N) and σ^2 is the mean square displacement in the bond length R or more sophistically we can say that it is the thermal and static disorder in the system. For a real system summing over the entire co-ordination sphere the EXAFS equation becomes:

$$\chi(k) = \sum_j \frac{N_j f_j(k)}{kR_j{}^2}\sin[2kR_j + \delta_j(k)]e^{-2k^2\sigma_j{}^2} \tag{2.13}$$

where j represents the individual coordination shells of identical atoms situating at approximately the same distance from the central atom.

Till now in the above discussions we have considered the outgoing photo-electrons as a physical wave, however inelastic scattering of photoelectrons from other sources like, electrons, phonons, etc. have not been considered. On the other hand, the photoelectrons have to return to the absorbing atom before the exited state decays i.e., the core level is filled. So to account for both the process a damped spherical wave has to be used as:

$$\psi\ (k,r) = \frac{e^{ikR} e^{-2R/\lambda(k)}}{kR} \tag{2.14}$$

where λ is the mean-free-path of the photo-electron i.e., the distance it typically travels before scattering in elastically and before the core hole is filled. Now including the $\lambda(k)$, the EXAFS equation becomes as:

$$\chi(k) = \sum_j \frac{N_j S_0^2 f_j(k)}{kR_j^{\,2}} \sin\left[2kR_j + \delta_j(k)\right] e^{-2k^2\sigma_j{}^2} e^{-2R_j/\lambda(k)} \tag{2.15}$$

This is the final EXAFS equation which is widely used for simulating theoretical EXAFS spectra of any species in order to carry out the analysis of experimental data [80].

From here we can see that the because of the $\lambda(k)$ term and the R^{-2} term the amplitude decreases and because of this the EXAFS is called alocal probe and is not able to see beyond 6Å. In the equation (2.15) the term S_0^2 is known as the amplitude reduction factor, which is different for different elements. It is a loss term that accounts for the multi-electron excitations and inelastic scattering. In the equation the amplitude of each wave is a function of parameters N_j and R_j. R_j is the half path length of the photoelectron and the term $sin(2kR_j+\delta_j(k))$ defines the oscillation frequency of each coordination shell. In addition to this, $f_j(k)$ and the phase shift $\Phi_j(k)$ is a function of the atomic number Z_j. The equation (2.15) can be analyzed by a Fourier transform. The EXAFS, $\chi(k)$, which is parameterized in terms of the wave vector k, could be transformed into a radial structure function (R) that represents the data in terms of distances from the absorber.

2.3.3 EXAFS data analysis:

The EXAFS data analysis is mostly a non-trivial and this analysis process can be divided into two steps: i) data processing, which isolates the fine structure oscillations from the experimental data and ii) the data fitting, which involves Fourier transformation of the EXAFS oscillations from the k-space into the r-space, constructing the appropriate structural model, generating theoretical EXAFS spectra in r-spac and finally fitting the experimental data with the theoretically simulated spectra in r-space using a least square fitting method. The processing of the data at the 1st step is performed by ATHENA subroutine and the next data fitting is performed by the ARTEMIS subroutine.

2.3.3.1 Software package:

For the processing and data analysis of the X-ray absorption spectroscopy a comprehensive system programme 'Demeter' has been used in which all the applications related to XAS data analysis have been out together. Dr. Bruce Ravel and co-workers [81] have developed the code of the programme over the years providing a rich Graphical User Interface (GUI) to the extensive analytical and numerical capabilities of the IFEFFIT library [82]. This is a freely available software and it is actively developed and maintained with new versions. This package is based on the IFEFFIT library of numerical and XAS algorithm and it is written in the Perl programming language. This package includes: (i) ATHENA, a program for XAS data processing, (ii) ARTEMIS, a program for analysis of extended X-ray absorption fine structure (EXAFS) data using theoretical standards computed by the FEFF program [83] and (iii) HEPHAESTUS, a collection of beamline utilities based on tables of atomic absorption data.

2.3.3.2 Data processing using ATHENA:

The experimental data is mainly processed with the program called ATHENA. This software involves

(i) Merging of the several scans to reduce the statistical noise.

(ii) Removal of artefacts like glitches presents in the raw absorption data.

(iii) Determination of the absorption energy E_0, which is defined as the 1st intense peak in the derivative spectra.

(iv) Pre-edge and post-edge background removal.

(v) Normalization of the experimental data to the edge step after removing background to make all the datasets comparable.

(vi) Finally extracting the oscillations and interpolating them to an equally spaced grid in photoelectron wavenumber *k*.

The main challenges in the data processing are the background removal from the data as an incorrect background removal will lead to the distorted oscillations and consequently the incorrect structural information. The view of ATHENA window is shown in the figure-2.16.

(i) Choice of E_0: The absorption spectra are mainly collected in the energy space by transmission or the fluorescence mode. To convert the E-space to k-space the value of the threshold energy (E_0) has to be specified. So the threshold energy is energy at which the absorption spectra abruptly raises and it is defined by the half maximum point on the edge or the 1st maxima of the derivative of the XAS signal. The absorption energy E_0 is determined by the software automatically as the data is imported in the software. Any relative shift of E_0 (~3 eV) from the proper inflection point can affect the data at low k-value and significant uncertainty for the analysis. The 1st order derivative for determining the absorption energy is shown in figure-2.17.

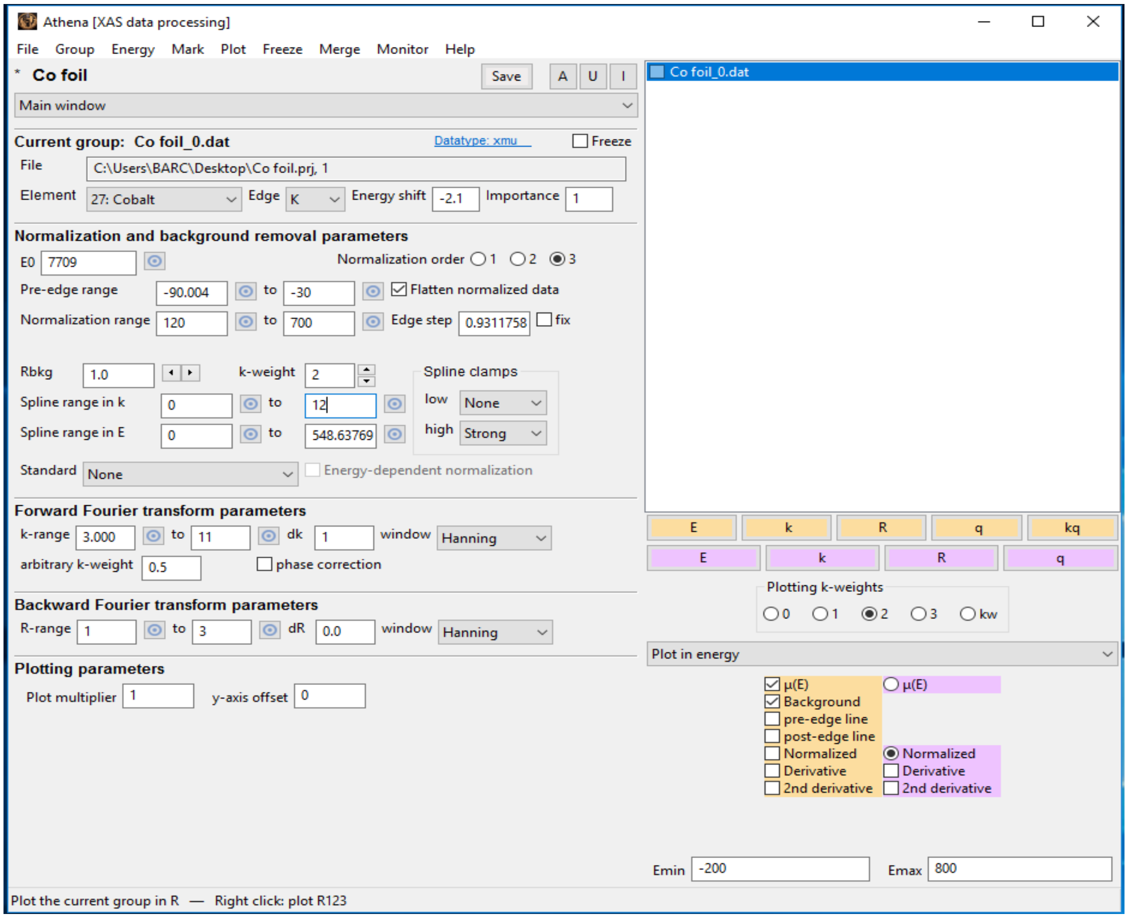

Athena [XAS data processing]

* Co foil

Main window

Current group: Co foil_0.dat Datatype: xmu ☐ Freeze

File C:\Users\BARC\Desktop\Co foil.prj, 1

Element 27: Cobalt Edge K Energy shift -2.1 Importance 1

Normalization and background removal parameters

E0 7709 Normalization order ○1 ○2 ●3

Pre-edge range -90.004 to -30 ☑ Flatten normalized data

Normalization range 120 to 700 Edge step 0.9311758 ☐ fix

Rbkg 1.0 k-weight 2 Spline clamps

Spline range in k 0 to 12 low None

Spline range in E 0 to 548.63769 high Strong

Standard None ☐ Energy-dependent normalization

Forward Fourier transform parameters

k-range 3.000 to 11 dk 1 window Hanning

arbitrary k-weight 0.5 ☐ phase correction

Backward Fourier transform parameters

R-range 1 to 3 dR 0.0 window Hanning

Plotting parameters

Plot multiplier 1 y-axis offset 0

☐ Co foil_0.dat

Plotting k-weights ○0 ○1 ●2 ○3 ○kw

Plot in energy

☑ μ(E) ○ μ(E)
☑ Background
☐ pre-edge line
☐ post-edge line
☐ Normalized ● Normalized
☐ Derivative ☐ Derivative
☐ 2nd derivative ☐ 2nd derivative

Emin -200 Emax 800

Plot the current group in R — Right click: plot R123

Figure-2.16: The main window of ATHENA program

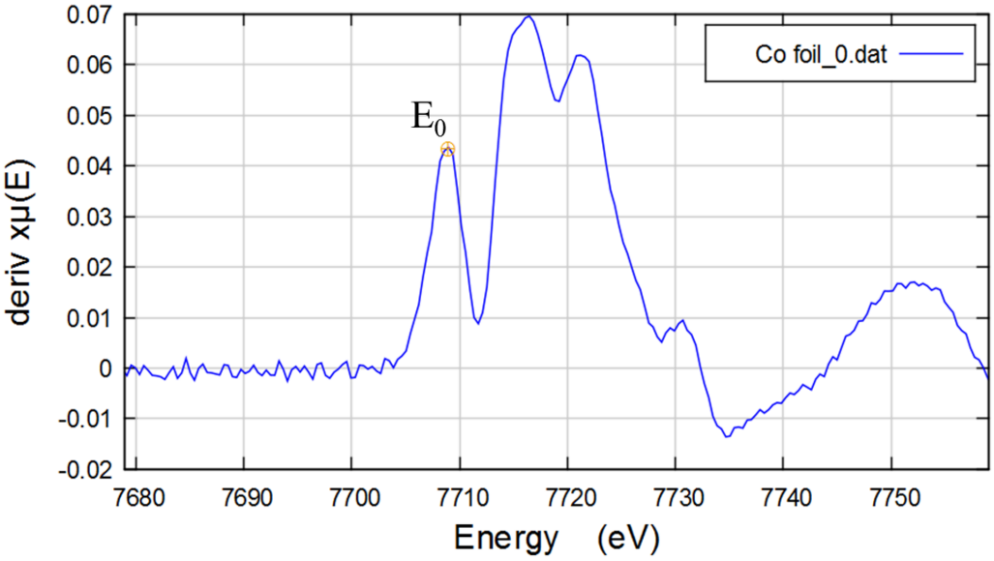

Figure-2.17: First order derivative of the absorption spectra to define the absorption edge (E_0)

(ii) Normalization of μ(E): In most of the cases the thickness and the concentration of the absorbing atom are not precisely known, which causes the observed signals to be multiplied by the energy dependent absorption factors. In transmission mode the logarithm of the ration of the two currents, the multiplicative factor turns into an additive background which varies with energy slowly. In fluorescence mode no logarithm is taken and the energy dependent factor is carried out throughout the process. This causes an improper standardization of the absorption spectra. So it is necessary to measure the baseline spectrum separately and then subtract it out. A common method of determining the edge step is to fit the data within few hundred eV below the absorption edge and the furthest region above the absorption edge with linear or quadratic polynomials and then extrapolate them to the edge. Typically, the range of the pre-edge background region is -200 eV to -30 eV and the post edge region is +100 eV to +300 eV. In this normalization process the data are divided by the size of the edge step i.e the difference between the pre-edge and post-edge polynomials after the absorption edge. The substraction of the pre-edge and post-edge polynomials from the absorption spectra is shown in the figure-2.18.

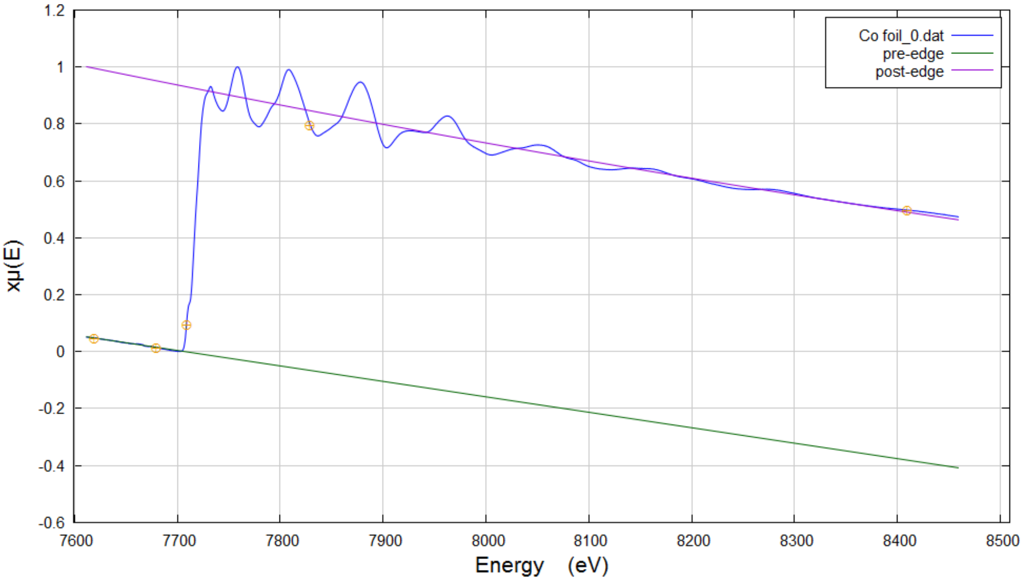

Figure-2.18: Pre-edge and post-edge polynomial subtraction from the absorption spectra

(iii) Background subtraction: The background subtraction isdone to isolate the oscillatory EXAFS signals from the atomic part of the absorption spectra μ_0(E) and the background absorption or the scatter from other elements in the beam path. In principle the isolated atom absorption μ_0(E) is subtracted from the total absorption coefficient μ(E), and the result is divided by μ_0(E), which is a slow function of energy in the EXAFS region. A straight forward background subtraction is satisfactory as the errors in the background vary in k-space. Typically, the background subtraction is important to remove the background without altering the data. If the background reduction is too severe the first shell EXAFS amplitude will be reduced and distorted. The most common functional form used for the background subtraction is the least squares cubic spline. AUTOBK algorithm is used for the background subtraction [84], which determines an empirical background spline based on a distinction between data and background in terms of Fourier components. The normalized absorption spectra with a background function are shown in the figure-2.19.

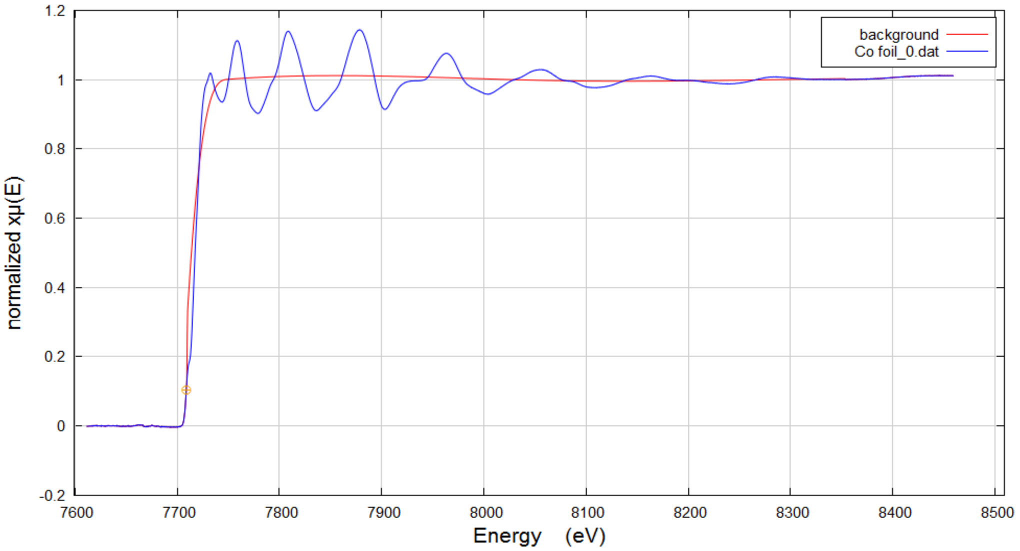

Figure-2.19: Typical normalized absorption spectrum μ(E) vs E with background function

(iv) Fourier Transformations: As mentioned above the normalizedEXAFSoscillationsare given by:

$$\chi(E) = \frac{\mu(E)-\mu(E_0)}{\mu_0(E_0)} \tag{2.6}$$

where the E-space data is converted to k-space by the formula

$$k = \sqrt{\frac{2m(E-E_0)}{\hbar^2}} \tag{2.7}$$

As theEXAFSsignal is a sum of the sine waves with the amplitude depending on wave-number *k*, *to* get information about the atomicenvironment the EXAFS spectrum is Fourier transformed. The Fourier transform (FT) of the EXAFS signal is written as FT[$\chi(k)k^w$] indicating that the EXAFS signal $\chi(k)$ has been multiplied by a *k* weighting of *w* (such as k, k^2, k^3). As we have seen that the *k*-dependent spectra have a damped oscillation at the higher *k* value, the k^w is used to amplify the oscillation at the higher k region to have a better information. A k^2 weighted χ(k) spectra is shown in the figure-2.20. The units of the Fourier transformed spectrum are Å^{-1-w}. The Fourier transform of the EXAFS signal is a function of *R* and can also be written as $\chi(R)$ [85]. The information content in the EXAFS spectrum can be described by a sum of sine waves, which is characterized by amplitude and phase that depend on the distance between the absorber atom and the coordinating atoms, and the type of coordinating atoms.

Any signal is a sum of sine waves and can be Fourier transformed to separate each frequency component with corresponding distance *R*. Thus a Fourier transform separates a signal into its Fourier components and is a complex function containing both real and imaginary parts. Each Fourier component is defined by an amplitude and phase.

However, one of the important practical problems in doing the Fourier transform of EXAFS data is due to the finite data range which can give rise to appearance of ripples in the Fourier transformed χ(k) spectra. So prior to Fourier transform the finite range data is always convoluted with a smoothly varying turnacation function or “Window funcftion” such as:

$$W\ (r) = \exp(ik_0 r)\frac{\sin(\Delta kr)}{r} \tag{2.16}$$

where k_0 is the centre of the transformed range and Δk is the width of the window. Several window functions are available in the Athena software which gives different shapes for data turncations. The available window functions are Hanning, Kaiser-Bessel, Welch, Parzen, Sine and Gaussian. For this thesis work we have always used Hanning window function, which is explcitely represented as [80]:

$$W\ (k) = \ cos^2\left(\frac{k-k_0}{\Delta k}\right) \text{ for } |\ k - k_0\ | < \Delta k$$

$$= 0 \qquad\qquad \text{for } |\ k - k_0\ | > \Delta k \tag{2.17}$$

which gives a flat region with the certain range around the centre k value and at the end there is smooth truncation of the data which goes as zero after the window, as shown in figure-2.20.

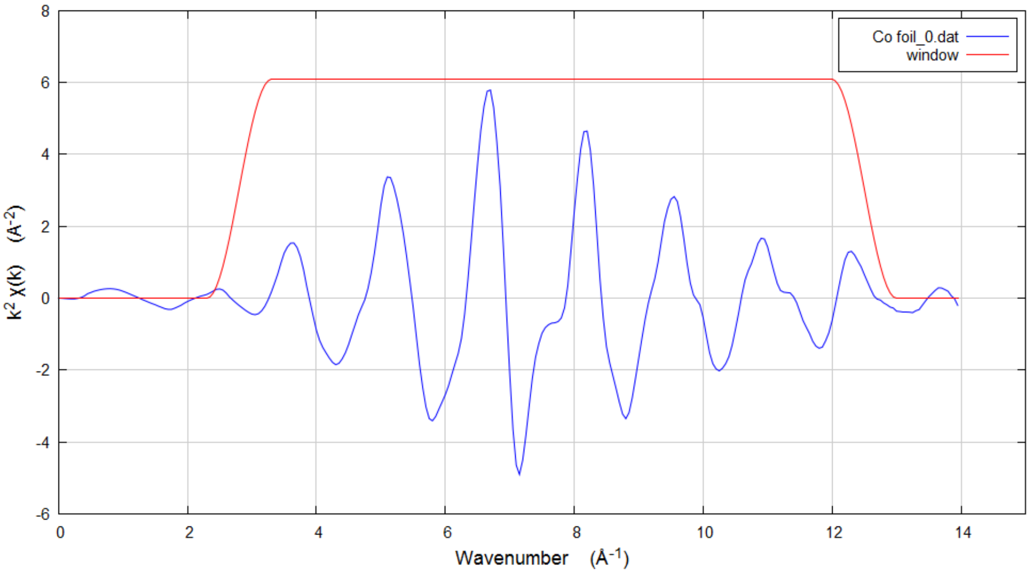

Figure-2.20: k space EXAFS oscillation($k^2 \times \chi(k)$) along with hanning window.

A typical Fourier transformed EXAFS spectrum or $\chi(R)$ vs Rplot is shown in the figure-2.21. This $\chi(R)$ vs R plotactually consists of a complex function, with real and imaginary parts, or alternatively a modulus and phase. The modulus is the most frequently used quantity, though the real and imaginary parts are also useful. They exhibit significantly more structure than the modulus does, and they don't suffer from nonlinear interference and hence during the fitting, modulus as well as real and imaginary parts should be monitored.

The *χ(R)* is like a radial distribution function of the atoms, where the position of the peaks shows the distance (R) of the corresponding atoms from the absorbing core atom. The intensity of the peaks represents the co-ordination number (C.N) of the neighbourhood shell and the broadness represents the thermal or static disorder (σ^2) of the system.

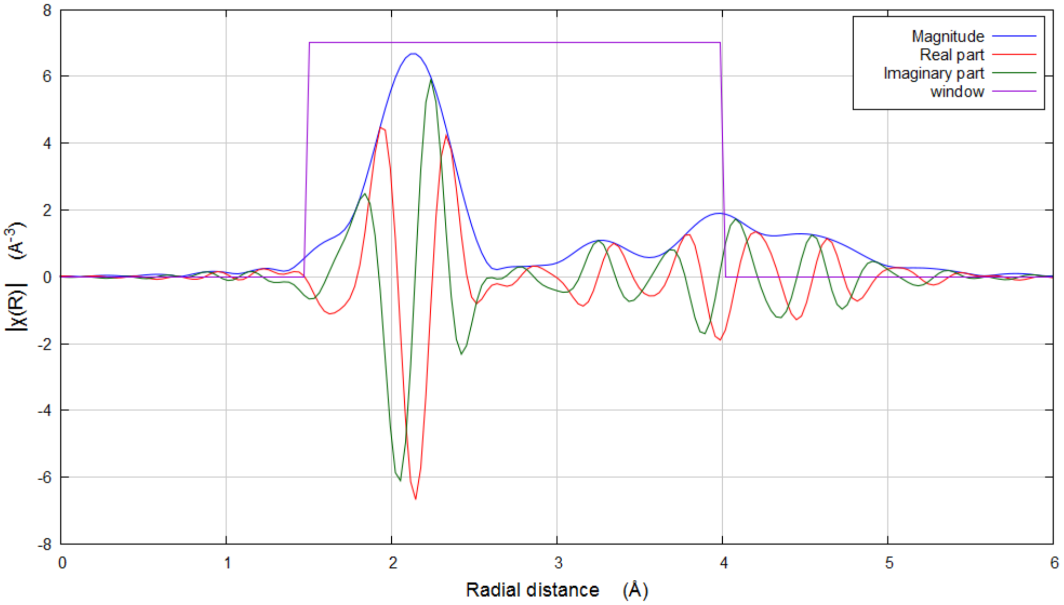

Figure-2.21: Amplitude of Fourier transformed EXAFS spectra along with real and imaginary part and window function.

(v) Fitting range: Information theory is used to correlate the amount of information in the original EXAFS spectrum to the information in the Fourier transform spectrum is determined from the Nyquist criteria as:

$$N_{IP} = \frac{2}{\pi}\,\Delta k \Delta R + 1 \tag{2.18}$$

where, N_{IP} is the number of the independent points, Δk is the Fourier transformed data range and ΔR is the region used in EXAFS data analysis. In general, a robust fitting model uses much fewer variables than N_{IP}. The recommended number of variables should be less than N_{IP} because the information contained within the EXAFS signal is not ideally packed.

(vi) Linear Combination fitting: Apart from data processing, ATHENA also provides utilities for linear combination fitting (LCF), principal component analysis (PCA), peak fitting using different line shapes (arctangent, Gaussian, Lorentzian) and generating the difference spectra. In LCF, the spectrum from a sample of unknown species is fitted by a linear combination of spectra of known standards exploiting the additive nature of the absorption from each species in the sample. These programs compute the scaling factors applied to different standard spectra that provide the best representation of the measured spectra over a defined energy range and thus the best fit gives the connetrations of the various standard species present in the unknown sample. It is a good practice for all spectra included in the LCF to have similar energy resolution. The PCA approach, on the other hand provides insight on the number of unique species in the set of samples, and the significance of different standards to represent species in the unknown.

2.3.3.3 Data fitting using ARTEMIS:

Artemis is a graphical user interface (GUI) for the EXAFS data analysis and a front end for FEFF and IFEFFIT built using DEMETER. ARTEMIS includes access to the functionality of the ATOMS program, which generates input file format suitable for FEFF.

In the analysis process, a theoretical model of the sample measured is constructed based on some apriori knowledge about the sample and with some variable parameters, the best fit values of which are obtained by fitting the theoretically generated spectra with that derived from the experimental data. ARTEMIS works within the framework of FEFF's multiple scattering path expansion [81, 86] which is quite subtle and complicated, however it has made the use easier by providing a graphical form of inputs. This software is able to read the inputs in theform of crystallographic information file (. cif) or in the form of an ATOMS input. In the consecutively way the ARTEMIS converts the data into FEFF input file and the geometrical distribution of the neighboring atoms, to calculate the scattering contribution from each of them. The FEFF is an *ab-initio* multiple scattering code used to generate the theoretical fitting standards for the EXAFS analysis. Starting with the inputs as given above the software calculates the scattering amplitude $f(k)$, phase shifts $\delta(k)$ and the mean free path $\lambda(k)$ theoretically using its in-built data base. Once these theoretical input parameters are obtained after structural inputs are given the EXAFS equation is calculated by the software itself. Finally, these are used to modify the structural parameters like atom to atom bond distance *(R)*, co-ordination numbers *(C.N)*, Debye-Waller factor (σ^2) and allow E_0 to change until we get the best-fit to the $\chi(k)$ data. Because of the availability of the Fourier transform, we actually have a choice of doing the refinement with the measured χ(k) or with the Fourier transformed data.

To explain the fitting process, we will work through an example of fitting of Fe_2O_3 experimental data. The ARTEMIS window along with different inputs and scattering paths are shown in the figure-2.22. A typical fitting on the k-space and R-space at Fe K-edge of the Fe_2O_3 is shown in the figure-2.23.

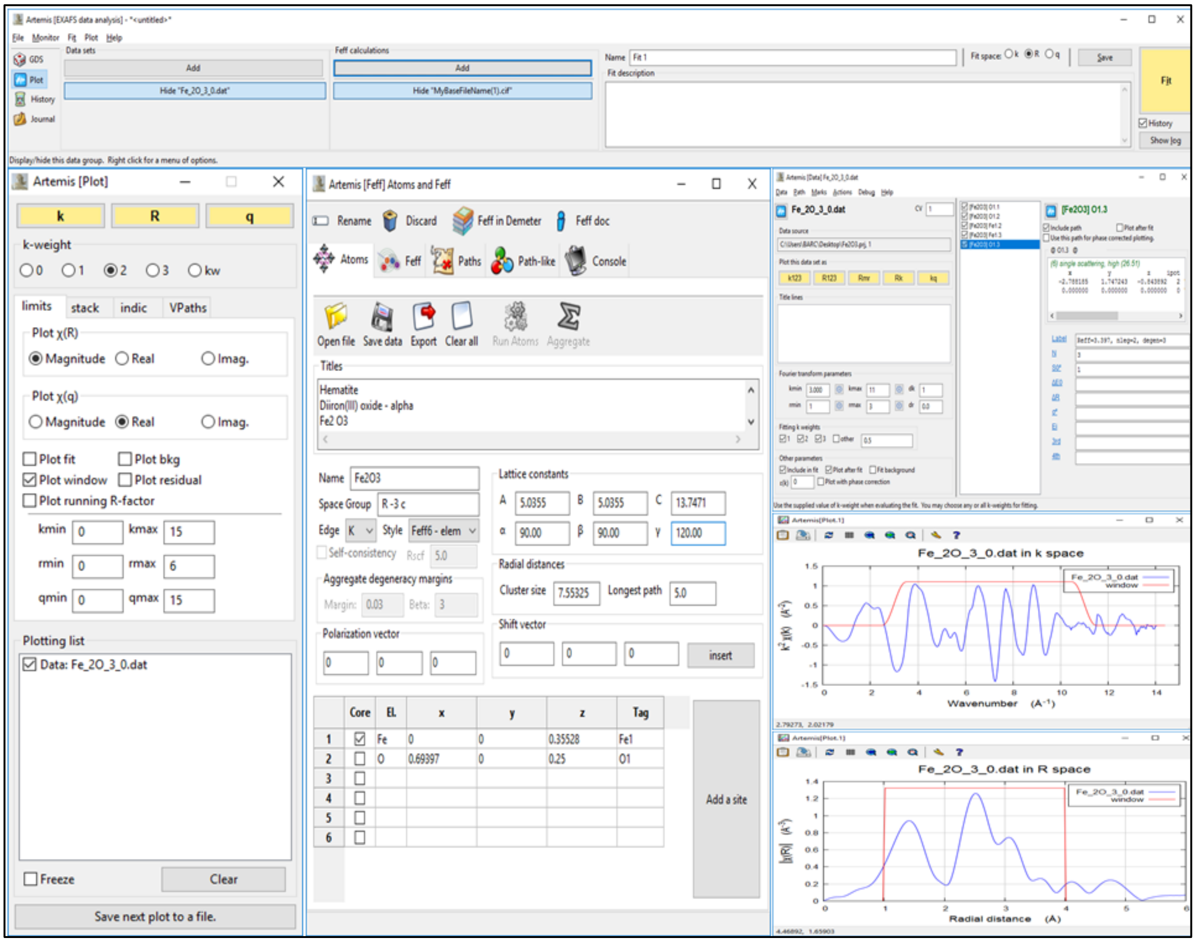

Artemis [EXAFS data analysis] - *<untitled>*

Name: Fit 1

Fit space: ○k ●R ○q

☑ History

Hide "Fe_20_3_0.dat"

Hide "MyBaseFileName(1).cif"

Display/hide this data group. Right click for a menu of options.

Artemis [Plot]

k-weight: ○0 ○1 ●2 ○3 ○kw

Plot χ(R): ●Magnitude ○Real ○Imag.

Plot χ(q): ○Magnitude ●Real ○Imag.

☐ Plot fit ☐ Plot bkg

☑ Plot window ☐ Plot residual

☐ Plot running R-factor

kmin 0 kmax 15

rmin 0 rmax 6

qmin 0 qmax 15

Plotting list: ☑ Data: Fe_20_3_0.dat

☐ Freeze

Artemis [Feff] Atoms and Feff

Titles:
Hematite
Diiron(III) oxide - alpha
Fe2 O3

Name: Fe2O3

Space Group: R -3 c

Edge: K Style: Feff6 - elem

☐ Self-consistency Rscf 5.0

Aggregate degeneracy margins: Margin: 0.03 Beta: 3

Polarization vector: 0 0 0

Lattice constants: A 5.0355 B 5.0355 C 13.7471

α 90.00 β 90.00 γ 120.00

Radial distances: Cluster size 7.55325 Longest path 5.0

Shift vector: 0 0 0

	Core	EL	x	y	z	Tag
1	☑	Fe	0	0	0.35528	Fe1
2	☐	O	0.69397	0	0.25	O1
3	☐					
4	☐					
5	☐					
6	☐					

Artemis [Data] Fe_20_3_0.dat

Fe_20_3_0.dat CV 1

Data source: C:\Users\BARC\Desktop\Fe2O3.prj, 1

Fourier transform parameters: kmin 3.000 kmax 11 dk 1; rmin 1 rmax 3 dr 0.0

Fitting k weights: ☑1 ☑2 ☑3 ☐other 0.5

Other parameters: ☑ Include in fit ☑ Plot after fit ☐ Fit background

ε(k) 0 ☐ Plot with phase correction

☑ [Fe2O3] O1.1
☑ [Fe2O3] O1.2
☑ [Fe2O3] Fe1.2
☑ [Fe2O3] Fe1.3
☑ [Fe2O3] O1.3

[Fe2O3] O1.3

☑ Include path ☐ Plot after fit

☐ Use this path for phase corrected plotting.

(6) single scattering, high (26.51)

```
    x          y          z       ipot
-2.788185   1.747243  -0.843892    2
 0.000000   0.000000   0.000000    0
```

Label: Reff=3.397, nleg=2, degen=3

N: 3

S02: 1

Use the supplied value of k-weight when evaluating the fit. You may choose any or all k-weights for fitting.

2.79273, 2.02179

4.46892, 1.65903

Figure-2.22: Main window of ARTEMIS program

The results were obtained from the best fitting. In the figure the 1st Fe – O1 (C.N = 6) bond contributes to the 1st peak at distance of 1.944Å ± 0.001 Å and the 2nd peak is contributed by the Fe – Fe1 (C.N = 3) shells at 2.928Å ± 0.002 Å and Fe – Fe2 (C.N = 3) at 3.362Å ± 0.010 distances respectively. The structural values for the bond distances are very much consistent with the Fe_2O_3 structure.

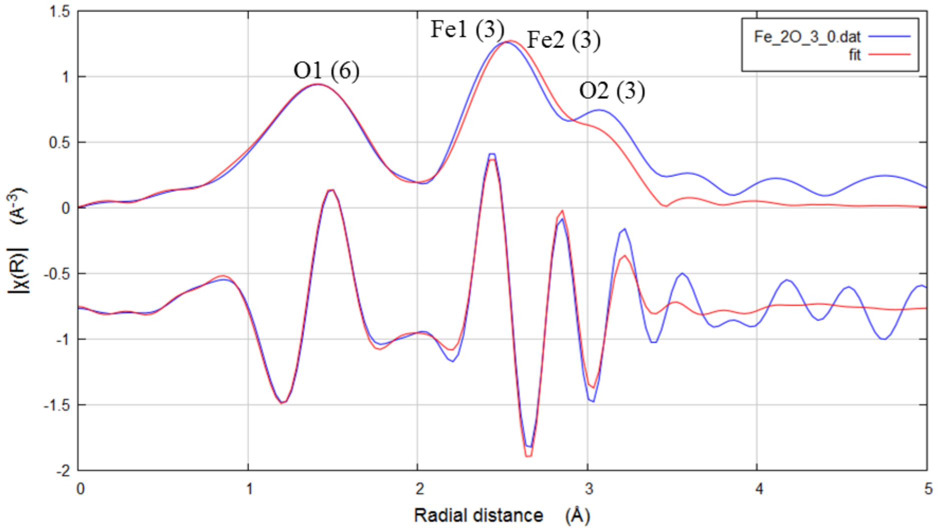

Figure-2.23: Example of experimental data fitting with theoretical model in *R* space

The R_{factor} is the sum of the squares of the differences between the data and the fit at each data point, divided by the sum of the squares of the data at each corresponding point and is defined as:

$$R_{factor} = \sum \frac{[\mathrm{Im}(\chi_{dat}(r_i) - \chi_{th}(r_i)]^2 + [\mathrm{Re}(\chi_{dat}(r_i) - \chi_{th}(r_i)]^2}{[\mathrm{Im}(\chi_{dat}(r_i)]^2 + [\mathrm{Re}(\chi_{dat}(r_i)]^2} \tag{2.19}$$

where, χ_{dat} and χ_{th} refer to the experimental and theoretical $\chi(R)$ values respectively and Im and Re refer to the imaginary and real parts of the respective quantities. In general, the R_{factor} should be less than 0.05 for an acceptable fit. The χ^2 is defines as the sum of the squares of the difference between the predicted fit (χ_t) and the data (χ_d) divided by the uncertainties (ϵ) at each data point (i).

$$\chi^2 = \frac{N_{idp}}{\varepsilon N_{data}} \sum_{i=min}^{max} [Re(\chi_d(r_i) - \chi_t(r_i))^2 + \mathrm{Im}(\chi_d(r_i) - \chi_t(r_i))^2] \tag{2.20}$$

In all the EXAFS fittings presented in this thesis, uncertainties in the fitting parameters have been estimated and typical values are ±0.05 Å in *R*, ± 10% in CN and ±0.001 in DW factor (σ^2).

2.3.4 X-ray Absorption Near Edge Structure (XANES):

In the XANES regime of the absorption spectrum, the kinetic energy of the photoelectron is lower in comparison to the EXAFS region. As the *de-Broglie*wavelength of the photoelectrons is very large (~100 Å) in this region, it spreads over several bond lengths and therefore the resolution to detect the local structural information is lost. On the other hand, the assumptions those are used in the EXAFS are not valid for the XANES regime. The interpretation of XANES is more complex and there is not a simple analytic description. There are several others weak interactions below the absorption edge and multiple scatterings occur after the absorption process. Still XANES analysis have the ability to provide the chemical information like oxidation state, co-ordination environment (i.e regular, octahedral, tetrahedral etc.), molecular orbitals (p-d hybridization, crystal field theory), spin-state information, band structure, those are difficult or impossible to extract from crystallographic measurements. A typical XANES spectra (Fe_2O_3) mentioning all the regions are shown in the figure-2.24. Clearly, the edge position and the shape is sensitive to the valence state, ligand type, and coordination environment. Some XANES spectra show intense narrow transitions on the rising edge. These are often referred to as ‘‘white lines’’ in reference to the fact that when photographic plateswere used to record X-ray absorption spectra, an intense transition would absorb all of the incident X-rays, thus preventing the plate from being exposed and leaving a white line on it. A typical XANES spectrumcan be divided into three regions. The main inflection point, where the spectrum starts raising abruptly is called the absorption edge and defined by energy E_0. The features before the edge is known as the pre-edge region and the oscillations after the while line is known as the post edge region. As mentioned earlier, the absorption energy is not well defined and it is mainly decided from the position of the maximum intense peak in the first order derivative. The position of the absorption edge changes systematically with the change in the oxidation states of the particular elemental species of a material whose X-ray edge is being probed and is a very powerful fingerprinting tool for determination of unknow oxidation states of elements.

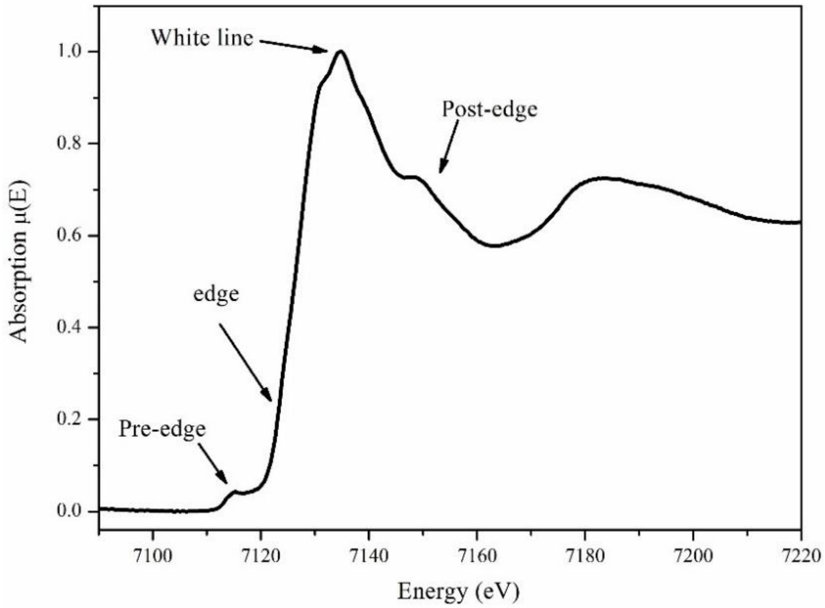

Figure-2.24: Typical XANES spectra of Fe_2O_3 mentioning all regions

Typical XANES spectra of several iron oxides along with that of iron metal are shown in figure-2.25 which show the systematic shift in absorption edge position with change in Fe oxidatioin state. For many systems, XANES analysis based on linear combinations of known spectra from "model compounds" (known as LCF method as discussed earlier) are employed to estimate the ratios of different oxidation states and/or phases. More sophisticated linear algebra techniques such as PCA and Factor Analysis can also be applied to XANES spectra. The weak pre-edge transitions arise from bound state transitions. For the K edge of a first row transition metal, these come from the 1s →3d transitions, and are observed for every metal that has an open 3d shell. Though the 1s→3d transition is forbidden by dipole selection rules, it is not observed due to 3d and 4p mixing and due to direct quadrupole coupling. The sensitivity to 3d and 4p mixing means that the intensity of the 1s→3d transition can be used as a probe of geometry, with the intensity increasing as the site is progressively distorted from a centrosymmetric environment (i.e., octahedral < square–pyramidal < tetrahedral) or to distinguish between square–planar (i.e., centrosymmetric) and tetrahedral sites.

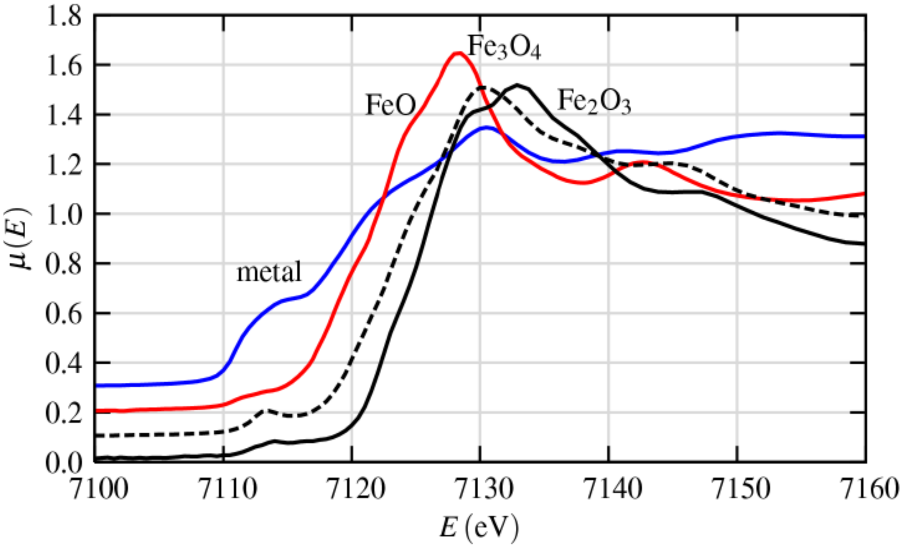

Figure-2.25: Fe K-edge XANES of Fe metal and other Fe oxide compounds. [78]

With careful analysis, the details of the 1s→3d transitions can be used to explore the electronic structure of the absorbing atom. Some materials, such as the spinel and inverse spinel structures have metal ions in non-equivalent sites: 2/3rd of the sites are octahedral, and 1/3rd of them are tetrahedral. Despite the dilution due to octahedral sites, the 3*d* pre-edge peaks are noticeably larger than the pure octahedral case. In some cases, the states associated with pre-edge transitions are full ($3d^{10}$ configuration) in one charge state, however have a hole ($3d^9$) in another charge state. For example, the presence or absence of the 3*d* pre-edge transition can be used to detect the difference between Cu^+ and Cu^{2+}. For second row transition metals, it is still possible to obtain information about the empty bound states by measuring data at the L_3 and L_2 edges, which have 2p→4d transitions. The low energy of these edges makes the transitions relatively sharp, and the 2p→4d transition is allowed, thus making these transitions intense [87].

The effect of hybridization process is much dramatic in the case of Cr^{3+} and Cr^{6+} oxides. Here the strong pre-edge peak in the Cr^{6+} absorption spectra is a consequence of the tetrahedral symmetry causing considerable overdue of the empty *d*-electron orbitals with the *p*-states that the photo-electron must fill. Therefore, the XANES spectra are very much sensitive to the hybridization process. Above the edge, there are a variety of structures that show generally oscillatory behaviour, ultimately becoming the EXAFS oscillations. Multiple scattering is an important property of XANES, which help to determine the three- dimensional structure of the absorbing atom. The XANES region is quite sensitive to small variations in the structure, as an example if there are two different sites having identical EXAFS spectra can have distinct XANES spectra. Due to the fact that geometrical differences between sites alter the multiple scattering pathways, thus the detailed structure in the immediate vicinity of the absorption edge changes.

X-ray absorption spectroscopy (XAS) which comprises of both EXAFS and XANES techniques thus together yields a wide range of information regaring an elemental species present in a sample including its oxidation state, coordination environment, local structure including distance from neighbouring atoms and disorder etc. Since it does not depend on long range order, it can be applied to any form of materails viz., amorphous, disordered or nano-crystalline systems, solution, aggregates, soil etc. where the other techniques like XRD or HRTEM are not able to give the proper structural information. Thus with the advent of modern bright synchrotron radiation sources it is becoming a more and more powerful microstructure determination technique.

2.3.6 X-ray Magnetic Circular Dichroism (XMCD):

X-ray Magnetic Circular Dichroism (XMCD) is considered as one of the most important discoveries in the field of magnetism in the last two decades. In an XMCD experiment, the difference in the X-ray absorption spectra recorded with left and right circularly-polarised photons while the sample magnetisation is kept parallel or antiparallel to the direction of the propagation of the incident X-ray beam. The first theoretical prediction was made in the year 1975 by Erskine and Stern on a ferromagnetic nickel [88] and the first experimental demonstration was given by Schutz et. al. on iron in the year 1987 [89]. Presently XMCD is a powerful spectroscopic technique which is widely used for studying both the localized and itinerant magnetism of a magnetic material and is rapidly becoming popular for probing the magnetic properties of materials. Unlike other dichroism techniques such as the Kerr effect or the Faraday Effect where visible light is used as a probe, XMCD uses X-rays as a probe taking advantage of the orbital and element selectivity properties of X-ray absorption spectroscopy. For a finite XMCD signal to be measured in specific temperature-pressure conditions, the sample must present a net ferromagnetic or ferromagnetic moment. The XMCD signal is then directly proportional to the magnetic moment on the absorber atom.

2.3.6.1 Theory of XMCD:

The physical origin of XMCD isa two-step model. The firststep describes the absorption process of of a circularly polarized X-ray photon that carries an angular momentum (+h for a right-handed circular polarized light and -h for a left-handed circular polarized light), the corresponding helicity vector being parallel (right) or antiparallel (left) to the propagation direction. A circularly polarized X-ray has oscillating electric and magnetic field that are 90° out of phase with each other. The instantaneous electric fields of a right and left circular polarized light are the same and only differ by the direction of rotation. The electric filed of a right circular polarized light is given by-

$$E_{rcp}\,(z,t) = E_0\{\,\mathrm{Sin}[\omega t - kz + \varphi_0]\mathit{i} + \mathrm{Cos}[\omega t - kz + \varphi_0]\mathit{j}\,\} \qquad (2.21)$$

and the left circularly polarized light is given by –

$$E_{lcp}\,(z,t) = E_0\{\,\mathrm{Sin}[\omega t - kz + \varphi_0]\mathit{i} - \mathrm{Cos}[\omega t - kz + \varphi_0]\mathit{j}\,\} \qquad (2.22)$$

In this equations, ω is the angular frequency, $\omega = 2\pi\nu$, k is the wave number, $k = 2\pi/\lambda$, where λ is the wavelength, φ_0 is an arbitrary phase shift, and $\boldsymbol{i}$ and $\boldsymbol{j}$ are unit vectors along the x and y axes, respectively. A schematic diagram of the circular polarization is shown in the figure-2.26.

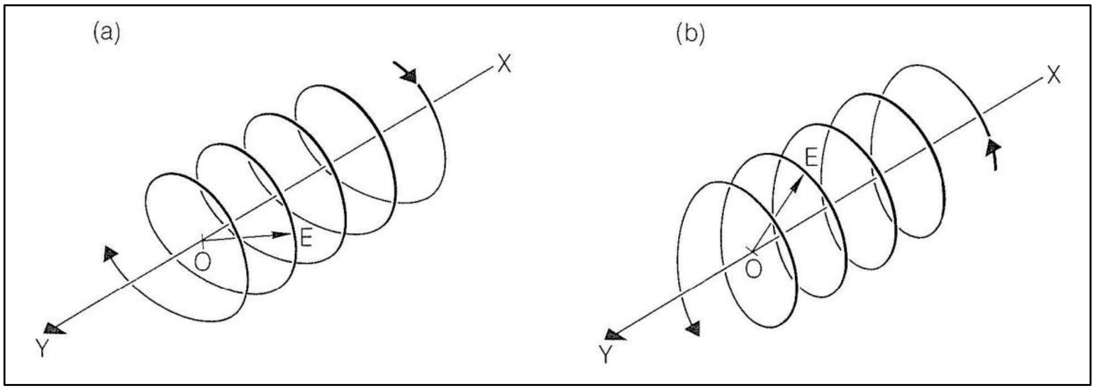

Figure-2.26: Circular polarizations of light

As a consequence of the conservation of angular momentum in the absorption process, the photon's angular momentum is entirely transferred to the photoelectron. Suppose the photoelectron being excited from a spin-orbit-split core level (e.g., L_2 for $2p_{1/2} \rightarrow 3d$, L_3 for $2p_{3/2} \rightarrow 3d$absorption edges), then part of the angular momentum carried by the photon will be converted into spin via spin-orbit coupling. The spin moment is always parallel to the photon propagation direction but its sign depends on the helicity of the incident X-ray photon and on the spin-orbit coupling ($l+s$ at the L_3 and $l-s$ at the L_2). The photo absorption process in the XMCD is shown in the figure-2.27. In the next step the magnetic property of the material drives the main role. A polarised photoelectron occupies the states above the Fermi level and, and depending upon the imbalance in either spin or orbital momentum in the final states, the XMCD spectrum reflects the difference in the density of states with different spin or orbital moments. The interaction of photon with the matter is governed by the Fermi's Golden rule. The absorption co-efficient can be written as-

$$\sigma_{abs} = \frac{2\pi}{h} |< f\ |T| i >|^2 \rho_f\ (h\omega - E_i) \tag{2.23}$$

$\rho_f(E)$ is the density of valance states at E higher than Fermi level. The term T is the transition operator which is given by

$$T = C \sum_q [\ e_q \, . p + i\ (e_q . p)(k . r)] \tag{2.24}$$

The first term in the equation is the dipole operator term and the second term is the quadrupole operator term. Now for an electric dipole approximation ($k.r$) << 1. So the equation becomes to

$$\sigma_{abs} = \frac{2\pi}{h} |< f\ \left| e_q . r \right| i >|^2 \rho_f\ (h\omega - E_i) \tag{2.25}$$

here e_q is thelight polarization vector and k is the light propagation vector.

Here the selection rule for the dipole transition is Δl = ± 1 and for quadrupole transition Δl = ± 2. So in the dipole transition process there may be available states in the higher energy level which may support the quadrupole transition. However, the intensity ration of the quadruple to dipole transition is very low. Generally, the quadruple transition is observed in the rare-earth materials, which have vacant *4f* orbitals, which is hybridized with *5d* orbital. Due to the selection rule, the circularly polarized photons with up spin preferentially excite 2p electrons with upward orbital angular momentum into the 3d level.

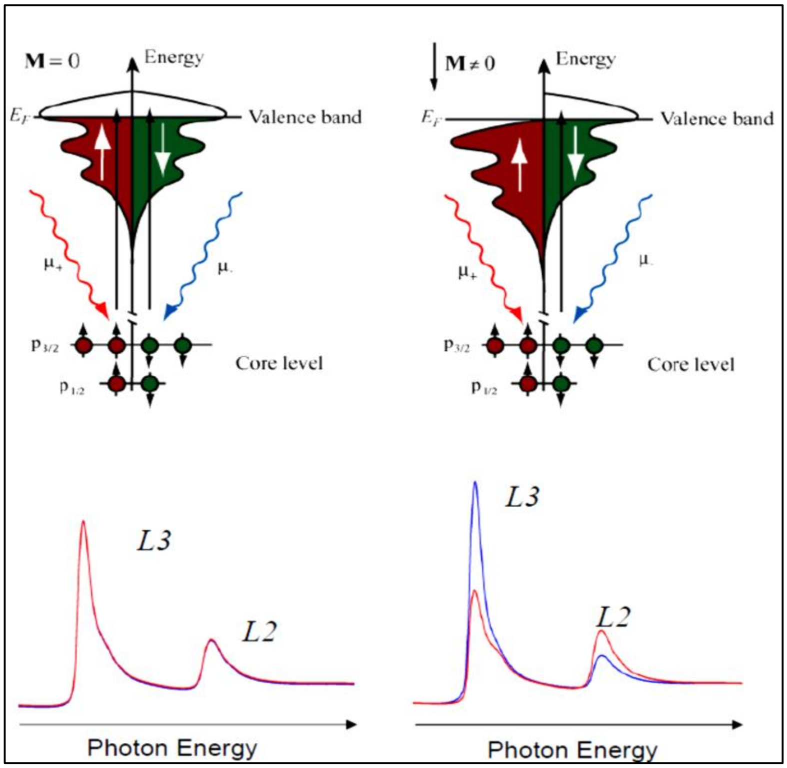

Figure-2.27: Photo absorption process ($L_{2,3}$ edge) in XMCD

An additional effect of the spin-orbit interaction is that, from the $2p_{3/2}$ ($2p_{1/2}$) level, an electron with spin of the same (opposite) direction as the orbital angular momentum, is likely to be excited. Now after doing the calculations it appears that from $2p_{3/2,\ 1/2}$ the electrons of spin up (↑) or down (↓) have different transition probability to the upper states. This gives a different intensity ration of the L_3 and L_2 edge XMCD spectra [90]. The XMCD spectra recorded at the L_2 and L_3 edges reflect only a difference in the orbital moments of the final states, while the difference is proportional to a spin polarisation of the valence states. This is precisely the content of the magneto-optical sum rules. It is worth noting that the summation over two spin-orbit split edges is equivalent to what can be measured for a core level with no spin-orbit interaction. This implies that a dichroic effect at the K-edges is only due to the orbital moments in the valence shell. In the K-absorption edge the transition occurs from the *1s* core level to *4p* vacant orbitals. The first ever recorded XMCD spectrum at K-edge of Fe metal is shown in the figure-2.29.

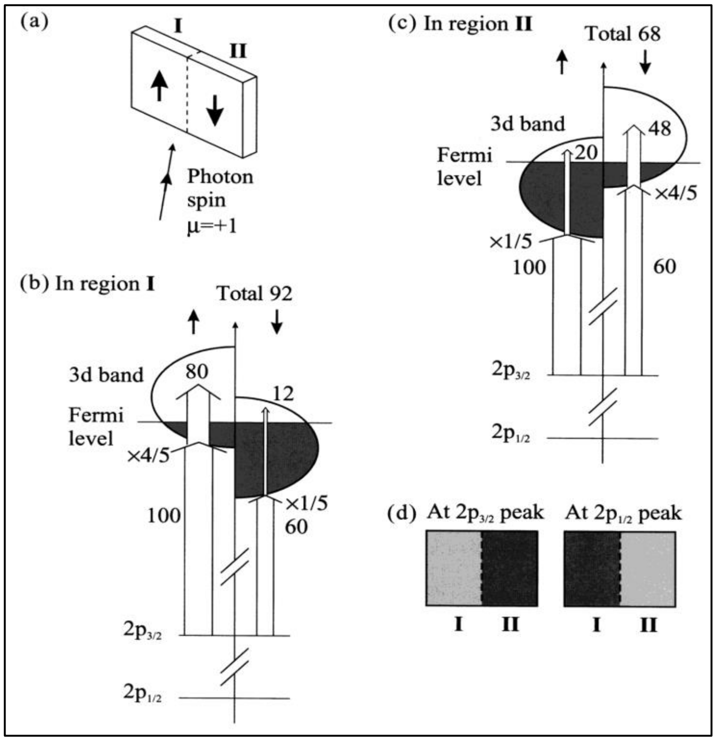

Figure-2.28: Principle of XMCD (a) A model of experimental geometry. (b), (c) Probabilities of transition from $2p_{3/2}$ to 3d ferromagnetic band. (d) Resultant XMCD contrasts [90]

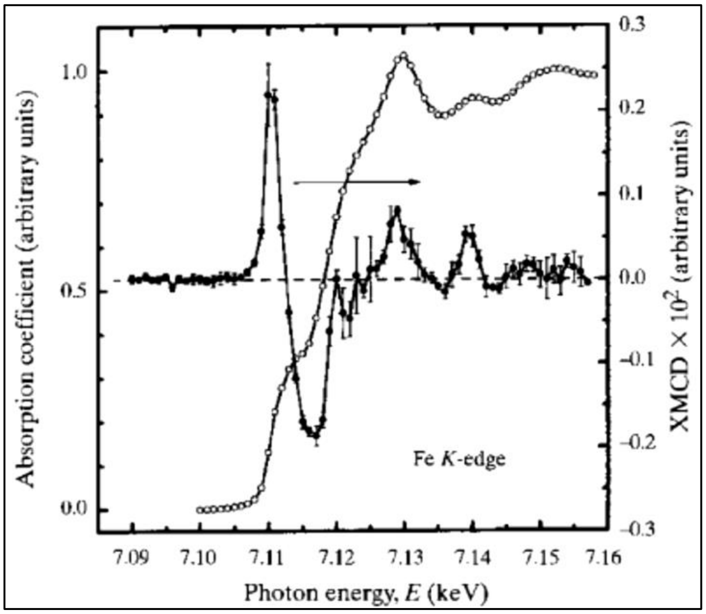

Figure-2.29: First Fe K-edge XANES and XMCD spectra at Fe K-edge [91]

2.3.6.2 Sum rule of XMCD:

The effective spin sum rule is widely used in the quantitative analysis of X-ray magnetic circular dichroism spectra. The sum rule was first introduced by Thole et.al. in 1992 [92] and Carra et.al. in 1993 [93]. Thole et.al. have shown that the integral over the XMCD signal of a given edge allows for the determination of the ground state expectation values of the orbital moment m_{orb} and Carra et.al. have introduced an extra term for the calculation of effective spin magnetic moment m_{spin}. Thus the sum rules were applied to transition between the two-defined shells. Like for K-edge transition between the *1s* core level and *4p* vacant states and for the L-edge the transition between the *2p* core level and *3d* valance states. The sum rule can also be used for the rare earth elements, which required other approximations. According to the XMCD sum rule the orbital and spin magnetic moments can be written as [94, 95]

$$m_{orb} = -\frac{4\int_{L_3+L_2}(\mu_+ - \mu_-)d\omega}{3\int_{L_3+L_2}(\mu_+ + \mu_-)d\omega} \times (10 - n_{3d}) \tag{2.26}$$

$$m_{spin} = -\frac{6\int_{L_3+L_2}(\mu_+ - \mu_-)d\omega - 4\int_{L_3+L_2}(\mu_+ - \mu_-)d\omega}{\int_{L_3+L_2}(\mu_+ + \mu_-)d\omega} \times \frac{(10 - n_{3d})}{(1 + \frac{7<T_Z>}{2<S_Z>}} \tag{2.27}$$

where m_{orb} and m_{spin} are the orbital and spin magnetic moments in units of μ_B /atom, respectively, and n_{3d} is the *3d* electron occupation number of the specific transition metal atom. $L_3 + L_2$ denote the integration range. $<T_Z>$ is the expectation value of the magnetic dipole operator and $<S_Z>$ is equal to half of m_{spin} in Hartree atomic units. Anisotropy of the spin moment (magnetic dipole) can be induced either by anisotropic charge distribution or by spin orbit interaction.

2.3.6.3 Applications of XMCD:

The XMCD technique is now widely used to unravel the microscopic origin of magnetism in various ferromagnetic and ferrimagnetic systems [96]. Furthermore, it has recently been shown that high-quality XMCD spectra could be recorded on paramagnetic systems, including Pauli and van Vleck paramagnets, subjected to high magnetic field [97]. XMCD has also become a remarkable element-specific magnetometry tool for heteromagnetic systems. A particularly outstanding example is presented below for $DyFe_2/YFe_2$ magnetic superlattices. The high sensitivity of XMCD also makes it unique for the study of the magnetic properties of reduced-dimensionality structures: thin magnetic films [98] and multilayers [99], magnetic quantum wires and dots [100].

2.4 Other experimental techniques:

2.4.1 X-ray Diffraction (XRD):

X-ray powder diffraction plays acritical role in materials research and development as most of the materials naturally available or synthesized in the laboratories are polycrysttaline in nature and not readily available in single-crystal form.

When monochromatic X-ray get scattered coherently from atoms arranged in certain lattice planes within a material, constructive interference take place at different angles depending on the spacing between the planes and this is the process of Bragg diffraction. The constructive interfence condition is described by Bragg's Law,

$$n\lambda = 2d \sin\theta \tag{2.28}$$

where, n is an integer is the order of diffraction, λ is the characteristic wavelength of the X-rays impinging on the crystallize sample, d is the interplanar spacing between rows of atoms and θ is the angle of the X-ray beam with respect to these planes. The geometry of the X-ray powder diffraction is shown in the figure-2.30.

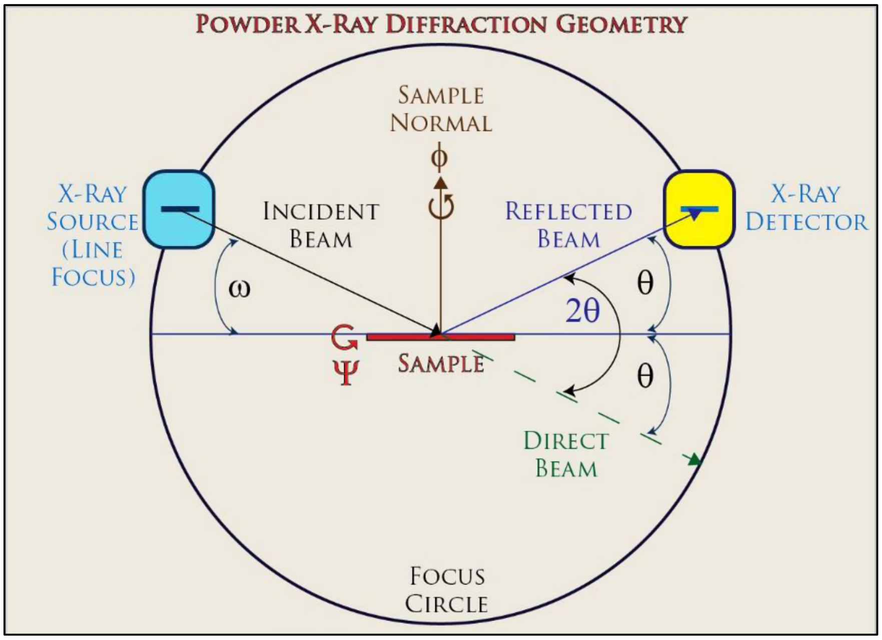

Figure-2.30: Geometry of X-ray powder diffraction (XRD)

The directions of all possible diffractions depend on the unit cell structure of the materialwhile electron density and arrangement of atoms in a unit cell determines the intensities of the diffracted waves. As an example of a powder with randomly oriented crystallites when placed in an X-ray beam, the beam will see all possible interatomic planes and scattered at all possible directions following the Bragg's law. This diffraction pattern can be thought of as a chemical fingerprint, and chemical identification can be performed by comparing this diffraction pattern to a database of known patterns. X-ray diffraction using different X-ray optics has been used to many different types of applications including thin film analysis, sample texture evaluation, monitoring of crystalline phase and structure, and investigation of sample stress. In the powder diffraction measurement, the X-ray source rotates at an angle θ while the detector moves at an angle 2θ with the direction of the incidence beam.

X-ray diffraction measurements when used for thin film samples using conventional θ-2θ scanning methods generally produces a weak signal from the film and gives an intense signal from the substrate. So the proper identification of the diffraction peaks from the samples becomes difficult. One of the ways to avoid intense signal from the substrate and get stronger signal from the film itself is to perform a 2θ scan with a fixed grazing angle of incidence, popularly known as Grazing Incidence X-ray Diffraction (GIXRD). Here the fixed angle of incidence is generally chosen to be slightly above the critical angle for total reflection of the film material. In a GIXRD experiment, the incident X-ray beam impinges onto the surface of a film at a very small angle or grazing angle and the detector is placed in a horizontal plane parallel to the film surface to collect diffraction from lattice planes which are perpendicular to the surface. Here the detector rotates over a wide angular range. However, in this case the footprint of the X-ray beam on the sample is longer which requires a larger size of sample (~10 mm). The schematic of the GIXRD measurement is shown in the figure-2.31.

In symmetric Bragg diffraction, one-dimensional crystallographic information along the surface normal is obtained. In GIXRD, two-dimensional information parallel to the surface is measured. Thus using both methods, three-dimensional crystallographic information can be obtained. The XRD measurement on the bulk target materials and the GIXRD measurement on the thin film samples presented in the thesis were carried out on a Rigaku 3kW Smart Lab X-ray diffractometer and Bruker D8 Discover diffractometer setup equipped with a Cu K_{α}-X-ray source (figure-2.31). The data have been taken within the 2θ range 30-90° with 0.01° step size and for the GIXRD measurement the angle of incidence was chosen to 0.5° to avoid the substrate contribution.

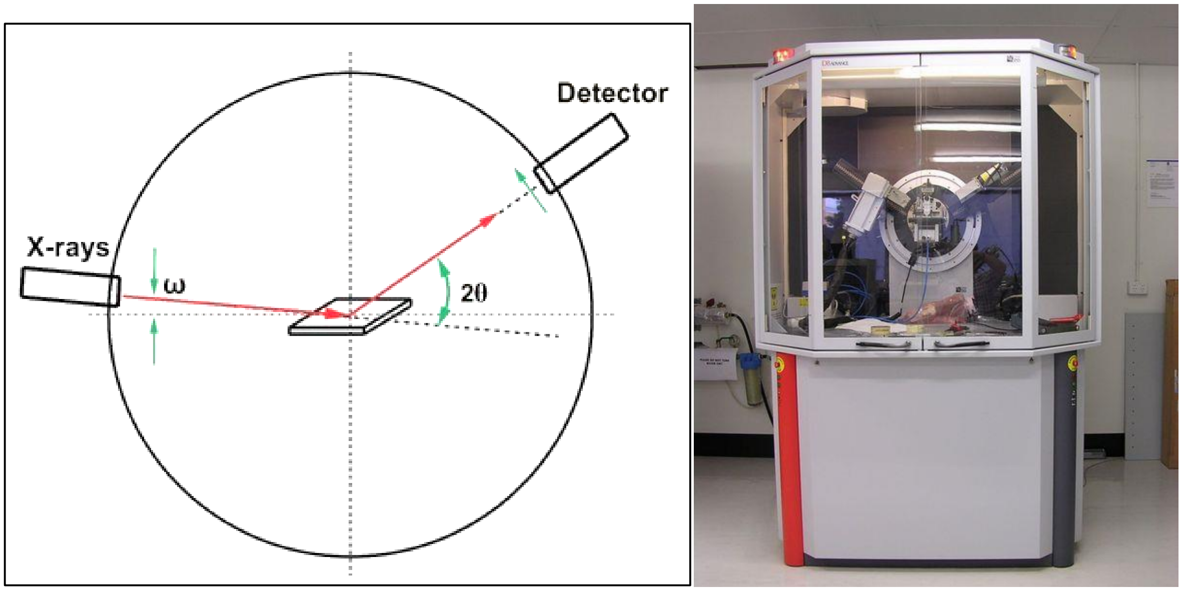

Figure-2.31:(a) Geometry of Grazing Incidence X-ray diffraction (GIXRD) for thin film (b) Bruker D8 Discover diffractometer used for the GIXRD and GIXR measurement

2.4.2 Grazing Incidence X-ray Reflectivity (GIXR):

X-ray reflectivity is a unique technique that can determine surface and interface roughness, film thickness, and the density of the thin film samples in a nondestructive manner.X-ray reflectivity uses total external reflection from surfaces and interfaces and it is useful for layer thickness between 10 and 500 Å.

This technique involves measuring the reflected X-ray intensity as a function of incidence angle over a range of angles close to the critical angle for total reflection. Above this critical angle, the specularly reflected intensity decreases depending on the structural properties of the interface. A typical reflectivity curve is essentially a combination of the Fresnel reflectivity pattern modulated by interference pattern (Kiessig fringes) of rays reflected from each interface. It is an advantage of the reflectivity measurement that it can evaluate the property of thin films of multilayer structures irrespective of whether the substance is crystalline or amorphous. The refractive index of X-ray in a material is given by the equation:

$$n = 1 - \delta - i\beta \qquad (2.29)$$

and the critical angle (θ_C) is given by

$$Cos\theta_C = n \approx 1 - \delta \qquad (2.30)$$

where δ and β account for the scattering and absorption of the material, respectively. The sign preceding β depends on the convention of signs used to define the propagation of the electric field. The values of δ and β (which are positive) depend on the electron density and linear absorption coefficient of the material.

As the refractive index of any material for X-rays is slightly less than 1, when X-rays enter the surface of a flat substance at a glazing angle, the X-rays cause total external reflection. By measuring the total reflection intensity (reflectivity) as a function of the incident angle with respect to the thin film surface a profile such as shown in figure-2.32, can be obtained. In the figure the oscillations are called as the Kiessig fringes, the distance between the consecutives fringes defines the thickness of the film. Similarly, the slope and the amplitude of the oscillations define the roughness of the film. If the roughness of the film is too high, the amplitude of oscillations may vanish and if the thickness of the film is very high the smaller oscillations merges to each other and the oscillations will not be properly distinguishable. The density (ρ) of the film is calculated from the critical angle (θ_C) with the given relation:

$$\theta_c = \sqrt{2\delta} = \sqrt{\frac{r_e\lambda^2}{\pi}\rho} \qquad (2.31)$$

where r_e is the electronic radiusand λ is the wavelength of light.

Here all the X-ray reflectivity measurements have been done with the Bruker D8 Discover diffractometer setup equipped with a Cu K_α-X-ray source. Before doing the measurement, the alignment of the sample and the detector position was optimized and the data were taken within the 2θ range 0 to 5°.

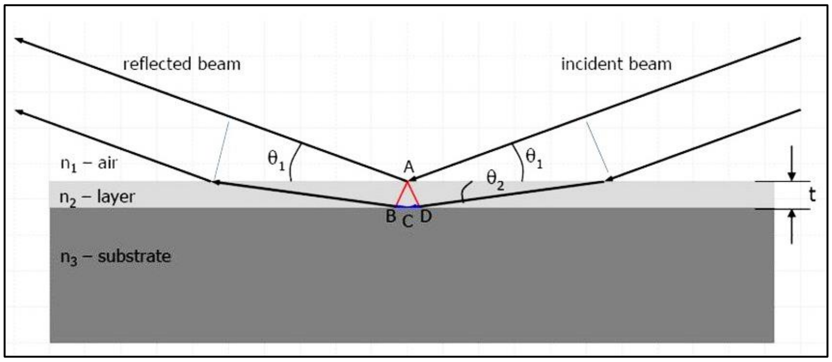

Figure-2.32:X-ray Reflectivity measurement from a single layer thin film

The experimentally obtained data was analyzed using the IMD software [101], which works on the well-known Parrat's formalism [102]. This software generates the model of thin film or multilayers with a certain thickness (z), density (ρ) and surface or interface roughness (σ) on a given substrate and try to fit with the experimental data by optimizing the fitting parameters. A schematic of the IMD software input window and IMDXPLOT graphical window are shown in the figure-2.33 and figure-2.34 respectively.

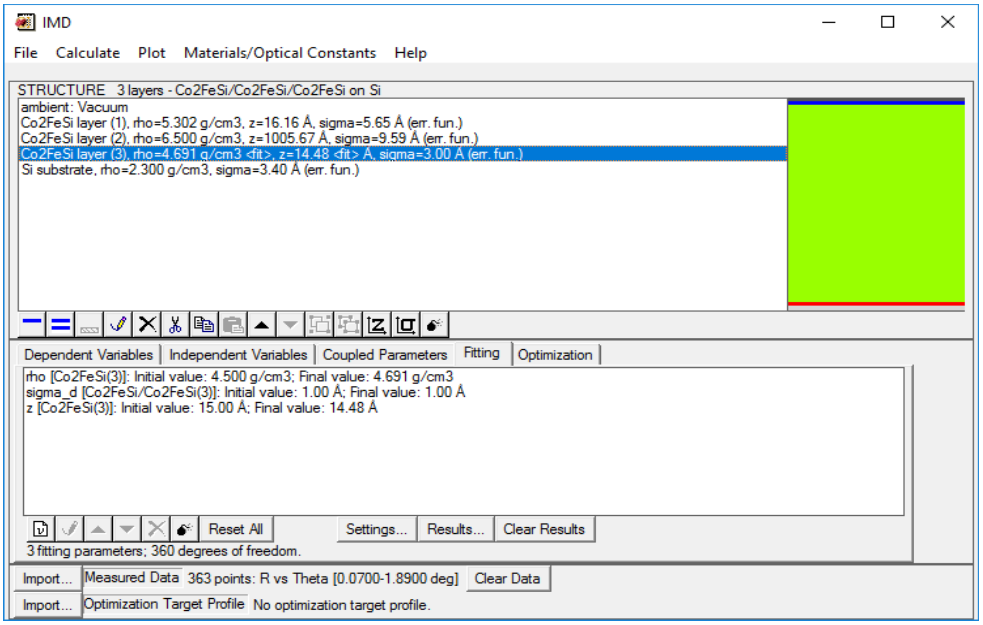

```
STRUCTURE   3 layers - Co2FeSi/Co2FeSi/Co2FeSi on Si
ambient: Vacuum
Co2FeSi layer (1), rho=5.302 g/cm3, z=16.16 Å, sigma=5.65 Å (err. fun.)
Co2FeSi layer (2), rho=6.500 g/cm3, z=1005.67 Å, sigma=9.59 Å (err. fun.)
Co2FeSi layer (3), rho=4.691 g/cm3 <fit>, z=14.48 <fit> Å, sigma=3.00 Å (err. fun.)
Si substrate, rho=2.300 g/cm3, sigma=3.40 Å (err. fun.)
```

```
rho [Co2FeSi(3)]: Initial value: 4.500 g/cm3; Final value: 4.691 g/cm3
sigma_d [Co2FeSi/Co2FeSi(3)]: Initial value: 1.00 Å; Final value: 1.00 Å
z [Co2FeSi(3)]: Initial value: 15.00 Å; Final value: 14.48 Å
```

3 fitting parameters; 360 degrees of freedom.

Measured Data 363 points: R vs Theta [0.0700-1.8900 deg]

Optimization Target Profile No optimization target profile.

Figure-2.33: IMD software structural input window

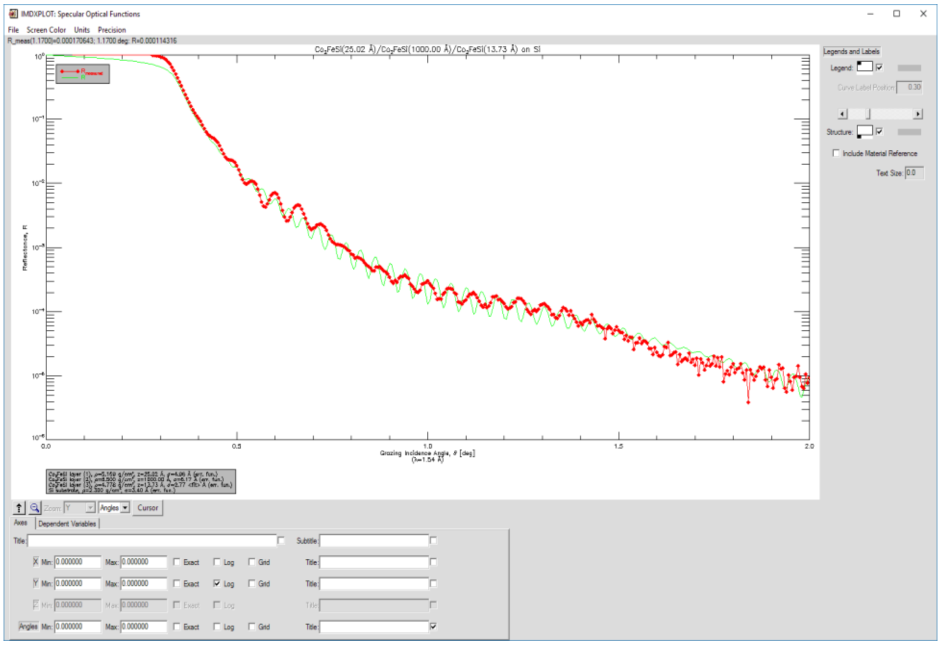

R_meas(1.1700)=0.000170643; 1.1700 deg: R=0.000114316

X Min: 0.000000 Max: 0.000000 ☐ Exact ☐ Log ☐ Grid

Y Min: 0.000000 Max: 0.000000 ☐ Exact ☑ Log ☐ Grid

Z Min: 0.000000 Max: 0.000000 ☐ Exact ☐ Log

Angles Min: 0.000000 Max: 0.000000 ☐ Exact ☐ Log ☐ Grid

Figure-2.34: IMDXPLOT graphical window: red line shows the experimental data and the green line shows the theoretically fitted spectra.

2.4.3 Field Emission Scanning Electron Microscopy (FESEM):

A Field Emission Scanning Electron Microscopy(FESEM) is a microscope that works with electrons as a probe. These electrons are emitted by a field emission source and the object is scanned by electrons according to a zig-zag pattern which is used to visualize very small topographic details on the surface. A sharply etched monocrystalline tungsten or lanthanum hexaboride (LaB_6) field emission gun tip is generally used as source from where electrons are ejected by field emission sourceinstead of thermionic emission and are accelerated by a high electric field gradient. Within the high vacuum column, the primary electrons are focused and deflected by electronic lenses to produce a narrow scan beam that bombards the object. As a result, secondary electrons emit from each spot on the objectwhose angleof emission and velocity relates to the surface structure of the object. A detector detects the secondary electrons and produces an electronic signal. This signal is amplified and transformed to a video scan-image that can be seen on a monitor in the form of a digital image.

Figure-2.35: The photograph of Auriga 455 FESEM instrument attached with a EDXS spectroscopy

FESEM's have much brighter electron sources and smaller beam sizes than a typical SEM increasing the useful magnification of observation and imaging up to 500,000 times larger. The second advantage of the FESEM technique is that the high-resolution imaging can be performed with very low accelerating voltage. This enhances the observation of very fine surface features, electron beam sensitive materials, and non-conductive materials. Thus FESEM is ideal for imaging polymer materials and thin films.

For this thesis the FESEM measurement on the prepared Heulser alloy thin films were done using the Carl Zeiss Auriga 4553 electron microscope of electron energy 30 kV under high vacuum in secondary electron (SE) image mode and backscattered electron (BSE) mode with a maximum resolution of 1.0 nm at 15 kV at optimum working distance.

2.4.4 Energy Dispersive X-ray Spectroscopy (EDXS):

Energy Dispersive X-Ray Spectroscopy, referred to as EDS or EDXS, is an X-ray based technique used to identify the elemental composition of materials. EDXS systems are attachments to Electron Microscopy instruments (Scanning Electron Microscopy (SEM) or Transmission Electron Microscopy (TEM)) instruments where the imaging capability of the microscope identifies the specimen of interest. The data generated by EDXS analysis consist of spectra showing the peaks corresponding to the elements making up the composition of the sample to be analyzed. In a properly equipped FESEM, the energetic electron beam while bombarding the atoms of the sample surfaceknock out electrons from their core shells, electrons from upper shells fill up the core holes and thus charactaeristic X-rays of the particular element species are emitted. Spectra of X-ray energy versus counts can thus be generated by using an energy dispersive detector (typically lithium-drifted silicon, solid-state device) which are then analysed vis-a-visthe standard spectra to determine the elemental composition of the sampled volume. A typical EDXS spectrum of a multicomponent system is shown in the figure-2.36.

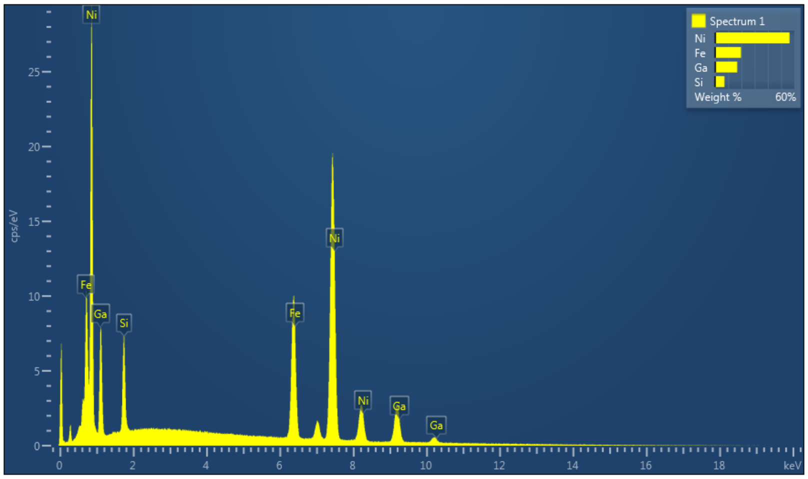

Figure-2.36: A typical EDXS spectrum of a multicomponent system (Ni_2FeGa thin film on Si substrate)

However, there are some limitations to this technique. Firstly, X-ray spectrometry detects elements and it is not capable of distinguishing between ionic and nonionic species. Moreover, in the EDXStechnique since electron beam is used as the probe, thesamples have to be placed underhigh vacuum condition and obviously this has serious implications for the preparation of the specimens. Generally, X-ray detection is not influenced by the chemical state of elements but it is influenced by inter-elements interference, known in X-ray spectrometry as peak overlap, causing serious problems in the elemental analysis. Therefore, it is possible to detect those elements with atomic number larger than 10. The EDXS measurement on the prepared thin film Heusler alloy samples discussed in this thesis have been carried out usingan Oxford X-Max instrument attached to the FESEM.

2.4.5 Vibrating Sample Magnetometer (VSM):

A vibrating sample magnetometer (VSM) system is used to measure the magnetic properties of materials. The vibrating component causes a change in the magnetic field of the sample, which generates an electrical field in a coil based on Faraday's Law of Induction. According to the Faraday's law the induced electromagnetic force (ξ) due to the change in the magnetic flux (Φ) is given by-

$$\boldsymbol{\xi = -\frac{d\Phi}{dt}} \tag{2.32}$$

The change in the magnetic flux can be done by changing the position of the sample with time or vibrating the sample then the induced electromagnetic force can be written as

$$\boldsymbol{\xi = -\frac{d\Phi}{dt} = -\frac{d\Phi}{dx} \times \frac{dx}{dt}} \tag{2.33}$$

If a magnetic sample is placed within a uniform magnetic field H, a magnetization M will be induced in the sample. The diagram of the measurement components is shown in the figure-2.37. The electromagnet activates before the testing starts so if the sample is magnetic, it will become stronger within the field produced. A magnetic field H appears around the sample and the sample is made to undergo sinusoidal motion, i.e., mechanically vibrated. Once the vibration begins, then the magnetization of the sample can be analyzed as changes occur in relation to the timing of movement since magnetic flux changes induce a voltage in the sensing coils that is proportional to the magnetization of the sample. Changes in the signal are converted by a suitable software to generate magnetization M versus the magnetic field H strength plots, often referred to as a hysteresis loop. A typical hysteresis loop is shown in the figure-2.38. The hysteresis loop shows the nature of magnetization of a ferromagnetic material. Once the material has been driven to saturation, the magnetizing field can then be dropped to zero and the material will retain most of its magnetization. The value of the magnetization that remains within the sample after removal of the magnetic field is known as the residual magnetization (B_R) (or remanence) and by providing a filed in the negative direction the residual magnetization can be brought to zero. This filed is known as the coercive field (or coercivity) (H_C).

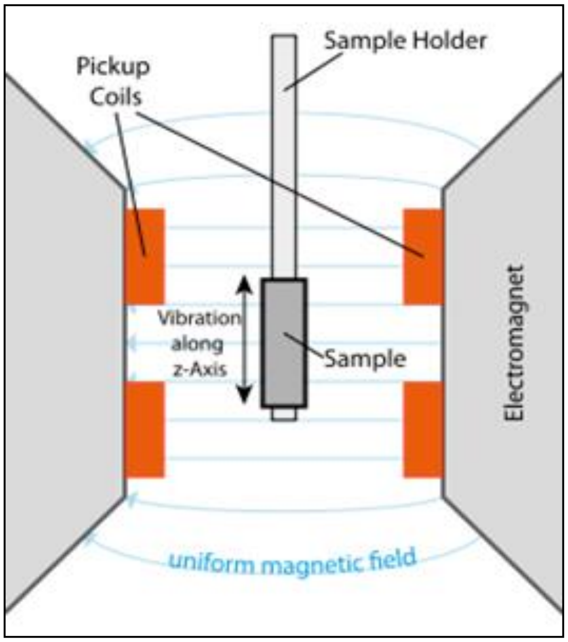

Figure-2.37: Diagram of different components of magnetic measurement using VSM

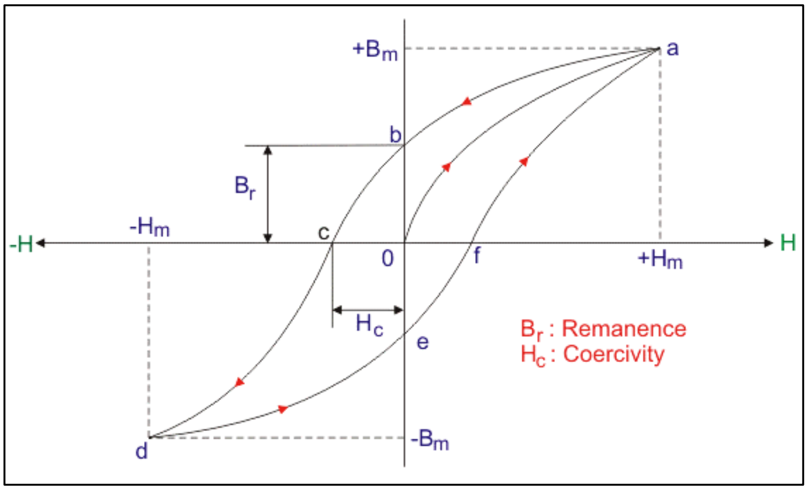

Figure-2.38: Typical hysteresis loop of ferromagnetic material

For this thesis the magnetic measurements have been carried out in a temperature range of 5 - 350 K using a PPMS-9T (Quantum Design) platform with the Vibrating Sample Magnetometer (VSM) module by placing the sample surface parallel to the direction of magnetic field. The photograph of a PPMS 9-T VSM module is shown in the figure-2.39.

Figure-2.39: The photograph of a PPMS 9T VSM system (Quantum Design)

2.4.6 Computational facility:

The density functional theory (DFT) calculations on the Heusler alloys have been carried out in this thesis using Spin-Polarized Relativistic Korringa-Kohn-Rostoker (SPR-KKR) program package [103]. The program was installed at Khistish-3 computing cluster of RRCAT, Indore, India which has 768 processing cores with an aggregate memory of 6TB. The ***Dual Intel Xenon (Hex Core)***3.07 GHz processor was used for this computation in a ***Red Hat Enterprise Linux*** (64 bit) based operating system.

Chapter-3

STRUCTURAL AND MAGNETIC CHARACTERIZATIONS OF $Ni_{55}Fe_{19}Ga_{26}$ FERROMAGNETIC SHAPE MEMORY ALLOY THIN FILM

3.1 Introduction:

In this chapter we have discussed deposition of the Ni_2FeGa Heulser alloy thin films using pulsed laser deposition technique and their structural and magnetic characterizations. The thin films were deposited from an off-stoichiometric bulk target and the structural characterizations were done using X-ray diffraction and X-ray absorption spectroscopy techniques both at room temperature and low temperatures and the magnetic characterization was done using vibrating sample magnetometry as described in Chapter-2. The main objective of this study is to correlate the structural property of the system with its magnetic properties.

3.2 Experimental:

3.2.1 Preparation of the samples:

The off-stoichiometric $Ni_{55}Fe_{19}Ga_{26}$ target was prepared using high purity (~99.99%) raw materials by arc melting process in an ultra-pure inert gas atmosphere as explained elsewhere [70]. The product material was subsequently pressed into a pallet to have the shape of a pancake. The smoothly polished 6 cm diameter target was used for the deposition of the thin film on Si (111) substrate using the Pulse Laser Deposition (PLD) system described in Chapter-2. Films of ~500Å thickness were obtained after 15 min of deposition using the KrF excimer laser (248 nm, 10Hz pulse) with output energy of 0.8J per pulse. A series of 4 samples were prepared at substrate temperatures of 311K, 473K, 673K and 873K. The samples have been referred to as H.A-1, 2, 3 and 4 respectively in the subsequent discussions.

3.3 Characterization techniques:

For structural characterization of the films, GIXRD measurements were carried out on a Rigaku 3kW Smart Lab X-ray diffractometer setup described in Chapter-2 at an angle of incidence 0.5° to avoid substrate contribution. Similar equipment has been used to record the low temperature XRD patterns of the samples in the temperature range of 17-300K. Microstructures of the films have been characterized by Field Emission Scanning Electron Microscopy (FESEM) with different accelerating voltages and magnifications. The Energy Dispersive X-ray Spectroscopy (EDXS) tool attached to the FESEM setup has been used to determine the elemental composition the thin film samples. In order to study the magnetic behavior of the Heusler alloys, magnetization measurements were performed in the temperature interval of 5-380 K using a PPMS-9T platform with the Vibrating Sample Magnetometer (VSM) module described in Chapter-2.Finally, XAS measurements comprising of Extended X-ray Absorption Fine Structure (EXAFS) and X-ray Absorption Near Edge Structure (XANES) at Ni and Fe and Ga K-edges have been carried out in fluorescence mode at the Energy Scanning EXAFS (BL-09) beamline of Indus-2 at Raja Ramanna Centre for Advanced Technology (RRCAT), Indore, India [76, 77] to determine the local structural changes around the constituent atoms of the alloy films due to change in substrate temperature. The EXAFS measurement on the samples at Fe (7112 eV), Ni (8333 eV) and Ga (10367 eV) K-edges were recorded at room temperature and 120 K in the fluorescence mode. For the room temperature measurement, the samples were kept in the ambient surroundings and the low temperature measurement at 120K have been carried out by taking the sample inside a cylindrical shaped vacuum cryostat. The details of the EXAFS measurements procedure have been described in Chapter-2.

3.4 Results and Discussions:

3.4.1 Room Temperature Grazing Incidence X-ray Diffraction (RT-GIXRD):

Figure-3.1 shows the room temperature GIXRD data of the thin film samples deposited at different substrate temperatures (T_S), which show that the films are polycrystalline in nature with multiple phase microstructures similar to the bulk ternary $Ni_{55}Fe_{19}Ga_{26}$ alloys [23]. Two intense reflections within 2θ range of 42-46° represents the austenite cubic $L2_1$ phase along with disordered f.c.c γ solid solution phase, which have Ni_3Fe structure. Figure-3.1 shows that in case of the film deposited at room temperature, the γ phase forms the primary phase and the $L2_1$ phase forms the secondary phase, which is a characteristic of Fe-rich stoichiometry. This is in agreement with the results reported by Nath and Phanikumar [4]in case of Ni_2FeGa alloy, Ga stabilizes the austenite phase while Fe stabilizes the γ phase. The γ (220) reflection manifests the solidification texture of the material at the substrate temperature of 473K which may arise due to the limited number of grains present in the microstructure [104].It can be clearly seen that with increase in the substrate temperature, the intensity of the $L2_1$ (220) peak increases significantly and becomes more pronounced for the sample deposited at 873K, while the intensity of the γ (111) peak decreases drastically. This may be due to the increase in Ga concentration in the sample as has been revealed by EDXS measurements discussed later. The above observations also suggest that with an increase in substrate temperature, the crystallinity of the film improves along with an increase in the crystallite size by the elimination of the internal stress of the material. It was also observed from figure-3.1 that in case of the film grown at 873K, the position of the $L2_1$ peak gets shifted a little towards the lower 2θ value possibly due to slight change in the lattice parameters of the cubic phase. However, from the GIXRD measurement, the other possible phases (B2 or DO_3) could not be clearly identified, possibly because as Waikawa et.al. have reported, in $Ni_{54}Fe_{19}Ga_{27}$ Huesler alloy, solid solution of (Ni/Fe) Ga or B2 phase is formed at a very high temperature [105].

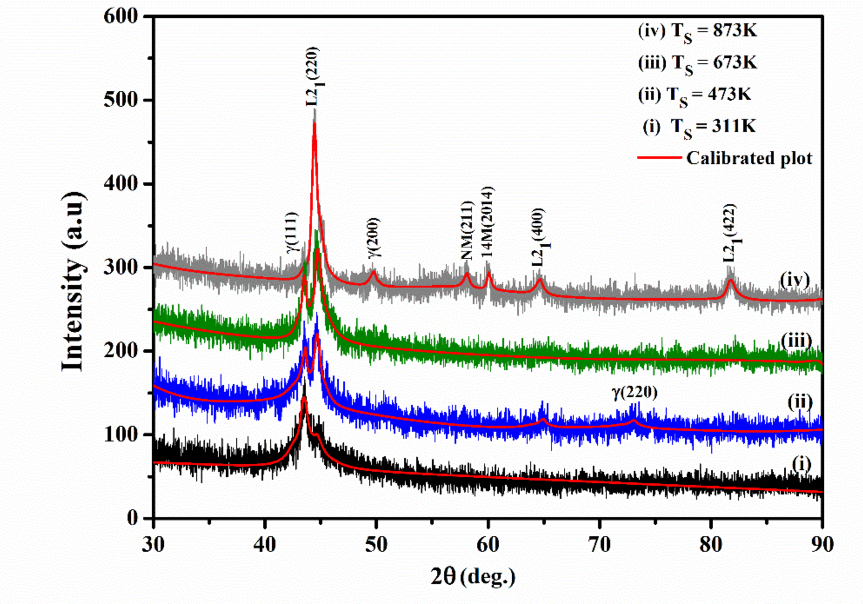

Figure-3.1: Room temperature GIXRD spectra of the Heusler Alloy thin films deposited at different substrate temperatures.

Though the γ phase provides the ductility to the alloy, once the γ phase is formed it would obstruct the formation of pure $L2_1$ phase. It has been clearly explained by Suzuki et.al. that high temperature chemical ordering is able to suppress the formation of the disordered γ phase for the thin film samples [106]. The GIXRD measurement thus indicates that by increasing the substrate temperature for the present PLD-grown thin films formation of the disorder f.c.c γ phase can also be reduced.

The film deposited at 873K (sample no. HA-4) shows an interesting feature that was not observed in other films. It shows the presence of some new phases in addition to the cubic phases. The peak at 2θ position of 58° is due to the tetragonal non-modulated martensite (NM) structure; while the other peak at 60° appears due to the 7 layered (14M) modulated stacking structure. The interesting issue in this transformation from the austenite $L2_1$ to the martensite 14M phase with a modulated structure is related to the shape memory effect in the Ni-Fe-Ga ternary alloys. For the alloy with near stoichiometric composition the NM phase has the body centred tetragonal structure (c/a >1) whereas the 14M phase has the body centered monoclinic structure (c/a <1) with the periodic shuffling of the basal planes (110) of the cubic austenite structure along the <100> direction [28]. Pons et.al. have shown that the group of alloys with their martensite start temperature (M_S) above the room temperature exhibit NM and 7 layered 14M martensite structures [107]. It is worth noting that in case of r.f. sputtered and heat-treated Ni-Mn-Ga films the martesniste phase could not be unambiguously identified from the XRD pattern even in 5 μm thick film possibly due to significant variation in stoichiometry of the films from the parent target materials. Thus the co-existence of the low and the high temperature crystal phases in these PLD deposited Heusler alloy films manifests the presence of temperature induced 1st order phase transition near room temperature in these samples. To elucidate this aspect further we have carried out XRD measurement of the sample grown at 873K (HA-4) as a function of temperature discussed below.

3.4.2 Low Temperature X-ray Diffraction (LT-XRD):

Figure-3.2(a) shows the XRD pattern of the HA-4 sample (deposited at 873 K) measured over the temperature range of 17-300K. As observed from the RT-GIXRD pattern discussed above, the sample has three phases at room temperature viz., austenite $L2_1$ phase, γ phase and non-modulated (NM) martensite phase, indexed in figure-3.2(a), the enlarged XRD pattern of these three peaks are shown in figure-3.2(b). By lowering the temperature of measurement, the constituent structural phases of the films do not change though few noticeable changes in the XRD pattern have been observed. Fitting of the austenite peak with Gaussian peaks suggests that the crystalline structure of the sample actually consists of two austenite phases of different amplitudes. It can be seen from figure-3.2(b) that as the temperature decreases the intensity and widths (FWHM) of the peaks corresponding to cubic austenite phases decrease gradually by releasing the internal stress, however the positions of the peaks do not change indicating that the lattice parameters or the volume of the unit cell remains same over the whole temperature range of measurement. The enlarged view of the martensite peak that appears within the 2θ range of 58.7-59.1° also consists of two distinct martensite peaks due to non-modulated NM (211) and 14M (20-14) modulated martensite phases.

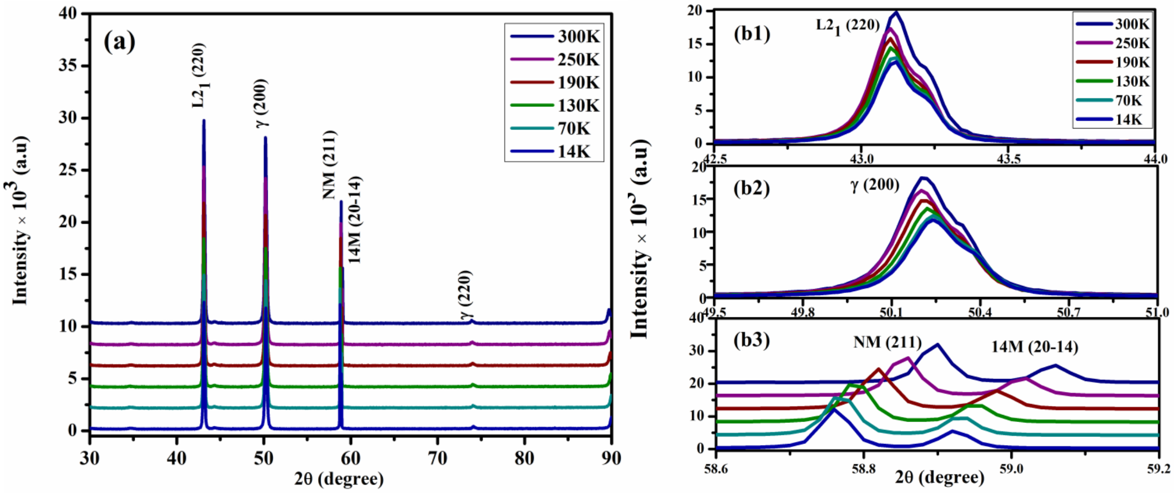

Figure-3.2: Low temperature (a) XRD profiles (b) enlarged XRD profiles of three intense peaks of the HA-4 Heusler Alloy thin film sample

It is clear from figure-3.2(b) that by lowering the temperature both the reflections shifted towards the lower 2θ value in a symmetric fashion though the intensity and width of the peaks remains almost same. This suggests that by lowering the temperature, the contribution of the martensite phases to the lattice remains same; however, there is an increase in the value of the lattice parameters with increasing cell volume possibly due to the negative thermal expansions of the lattice parameters a, b and c corresponding to the martensite phases. Similar negative thermal expansion has been observed by Li.et.al. also in case of NiMnGa alloy [108]. It has been attributed to reorganization of martensite invariants to minimize the macroscopic deformation caused by the structural transformation.

3.4.3 Field Emission Scanning Electron Microscopy (FESEM):

Figure-3.3 shows the back scattering electron images taken from the film. From the figure it has been observed that the film deposited at room temperature (HA-1) has a dendritic morphology possibly due to high concentration of the Fe-rich γ-phase in this sample [104,109]

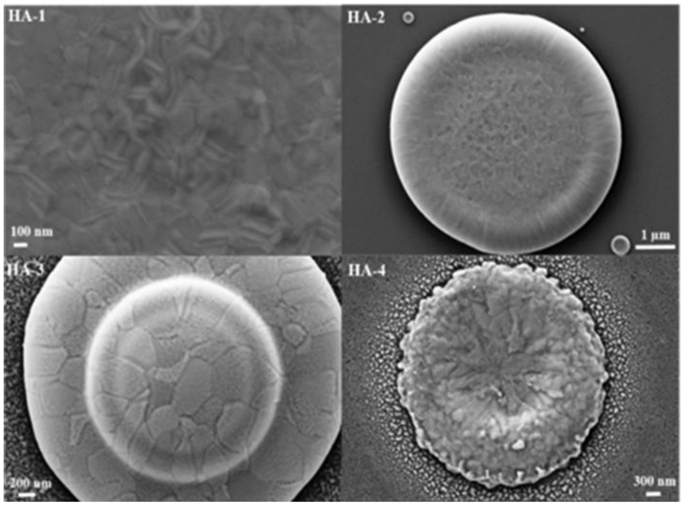

Figure-3.3: FESEM electron back scattering images of the films grown at different substrate temperatures.

As the substrate temperature increases the film morphology changes to inhomogeneously distributed circular droplet-type on an otherwise smooth surface, with average size of the droplet varying from 2- 6 µm. With increasing the substrate temperature, the number of the droplets increases and accumulated around the bigger droplets as depicted in the figure-3.3. A magnified observation into the droplets shows that there is a presence of parallel lamellas of average length 200–300 nm with different orientations, which is typical for the shape memory alloys and similar droplet-like morphology was observed by other workers also in case of PLD-grown NiMnSb thin films [110]

3.4.4 Energy Dispersive X-ray Spectroscopy (EDXS):

The compositions of the films were estimated by EDAX analysis and by averaging the data collected over several regions of the film. The variation in the stoichiometry as a function of substrate temperature, depicted in figure-3.4 shows that the composition of the film deposited at room temperature is Ni and Fe rich and Ga deficient,

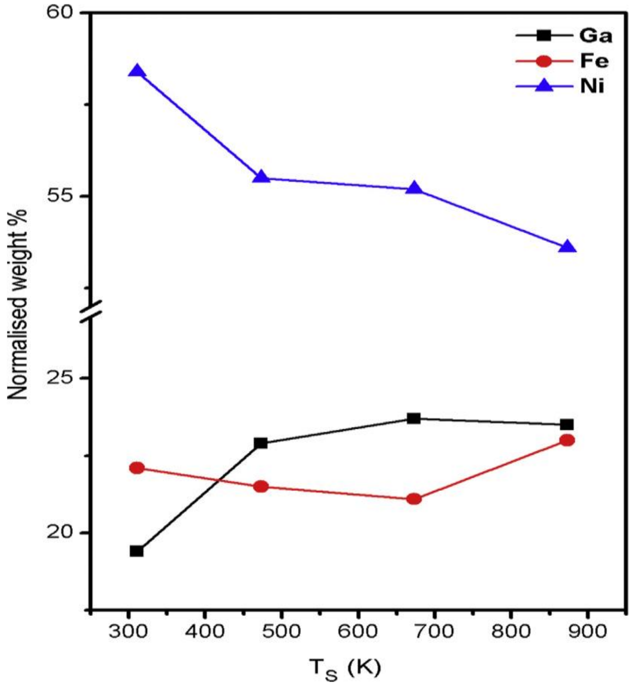

Figure-3.4: Variation of composition of the film as a function of substrate temperature. The composition of the film deposited at room temperature is Ni and Fe rich and Ga deficient.

The composition approaches that of the bulk target with increase in substrate temperature, though even for the film deposited at the highest temperature the composition remains slightly Fe rich and Ga deficient compared to the bulk target composition of $Ni_{55}Fe_{19}Ga_{26}$.

3.4.5 X-ray Absorption Spectroscopy (XAS):

3.4.5.1 X-ray Absorption Near Edge Structure (XANES):

Inset of figures 3.5(a), (b), (c) show the room temperature XANES spectra of the alloy films measured at Ni, Fe and Ga K-edges which show that there is no significant shift in the positions of the absorption edges across the samples implying that the valance states of the constituent elements in the samples do not change with change in substrate temperatures. It can be clearly observed that the features just above the edge positions are significantly different in case of the HA-4 sample deposited at 873 K. The features of the sample deposited at 673 K (HA-3) are also found to be similar to the 873K (HA-4) sample at least for Ni K-edge data. The peak height is a measure of the austenite phase present at a particular temperature and it demonstrates the strong correlation between the crystal structure and the electronic states in the compound [111]. The lesser peak height at Ni and Fe K-edges in the case of HA-3 and HA-4 samples may suggest a lesser amount of austenite phase present in the sample in comparison to the others due to the appearance of non-cubic martensite phases as observed from the GIXRD spectra. The significant difference that has been observed at the point B ($\Delta E \sim 24$ eV above the absorption edge) in the XANES spectra indicates the change in the crystal symmetry around the Ni and Fe atoms undergoing martensitic transition. However, the low temperatures XANES spectra of the HA-4 film do not show any significant difference from the room temperature spectra.

3.4.5.2. Extended X-ray Absorption Fine Structure (EXAFS):

Figure-3.5(a) - (c) show the normalized EXAFS spectra of the alloys at Ni, Fe and Ga K-edges deposited at different substrate temperatures. Since from the GIXRD results discussed above, the austenite $L2_1$ phase appears as the major structural phase along with a disordered phase in all the samples, in the EXAFS analysis a two phase model of austenite b.c.c $L2_1$ phase and disordered f.c.c γ phase have been employed and the atomic phase fraction of each phase has been determined from the EXAFS data fitting. $L2_1$ (Fm-3m space group) cubic structure of Ni_2FeGa has lattice parameter of 5.77 Å [70] and in this structure four interpenetrating sub-lattice form a unit shell where the Fe atoms occupy the 4(b) (½, ½, ½) positions while Ga atoms occupy the 4(a) (0, 0, 0) Wyckoff positions and Ni atoms occupy the 8(c) (¼, ¼, ¼) Wyckoff positions in the lattice. On the other hand, the γ phase has the crystal structure similar to the B2 type structure which crystallizes in the (Pm-3m space group) cubic structure with the lattice constant of 3.58 Å. In this structure Ni atoms occupy 4(b) (½, ½, ½) positions while both the Fe and Ga atoms share the same positions with the atomic coordinates of 4(a) (0, 0, 0). In this structure Fe and Ga atoms occupy the above positions at absolutely random fashion causing a Y-Z disorder or B2 type structure. Thus the co-ordination sphere involving the Fe/Ga atoms as backscatters have the identical surroundings. Figure- 3.6(a)-(c) show the phase-uncorrected $\chi(R)$ versus R plots at the Ni, Fe and Ga K-edges of the samples fitted with the theoretically generated model. The structural model discussed above has been used for the fitting process following the manner used by Bhobe et al. [112] with the bond length (R) and the Debye Waller factor (σ^2) of the individual shells varied independently by keeping the coordination number fixed according to the crystallographic value. The relative concentration of the two phases has also been used as a fitting parameter in case of Ni K-edge data and the best fit values have been kept constant in case of Fe and Ga K-edge fitting.

The Forier transform was carried out in the k range of 2.5 - 11 $Å^{-1}$ andfitting has been done in R space in the range of 1.2 - 4.1 Å and the best fit results have been summarized in Tables 3.1 – 3.3 for the Ni, Fe and Ga K-edge data respectively. The detail structural investigation of the atoms involved in the 1st co-ordination shell explains about the variation in the bond length and disorder factor present in the systems around the respective atoms. In the phase uncorrected χ(R) versus R plots, the peaks within the R range of 1.6 - 2.6 Å appear due to back scattering from the atoms in the 1st co-ordination shell of both the cubic austenite phases. In case of Ni atoms, the 1st peak appears due to the contribution of 4 Ga and 4 Fe atoms at 2.50 Å of the $L2_1$ phase along with the 4 Fe and 8 Ni atoms at 2.53 Å of the γ phase.

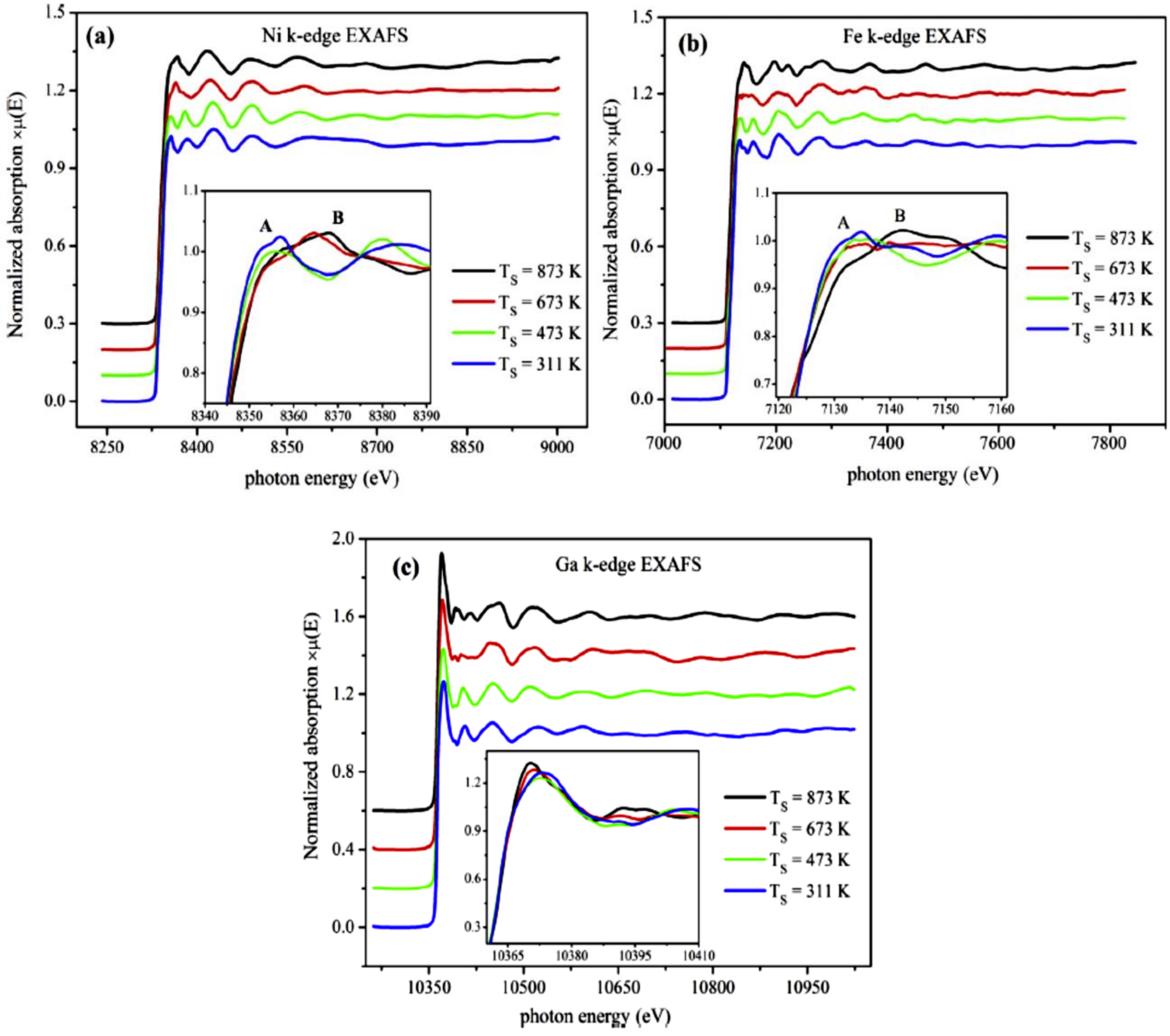

Figure-3.5: Normalized EXAFS spectra of the Ni55Fe19Ga26 alloy films deposited at different substrate temperature (T_S) and measured at (a) Ni K-edge, (b) Fe K-edge and (c) Ga Kedge. (Inset shows the respective XANES spectra).

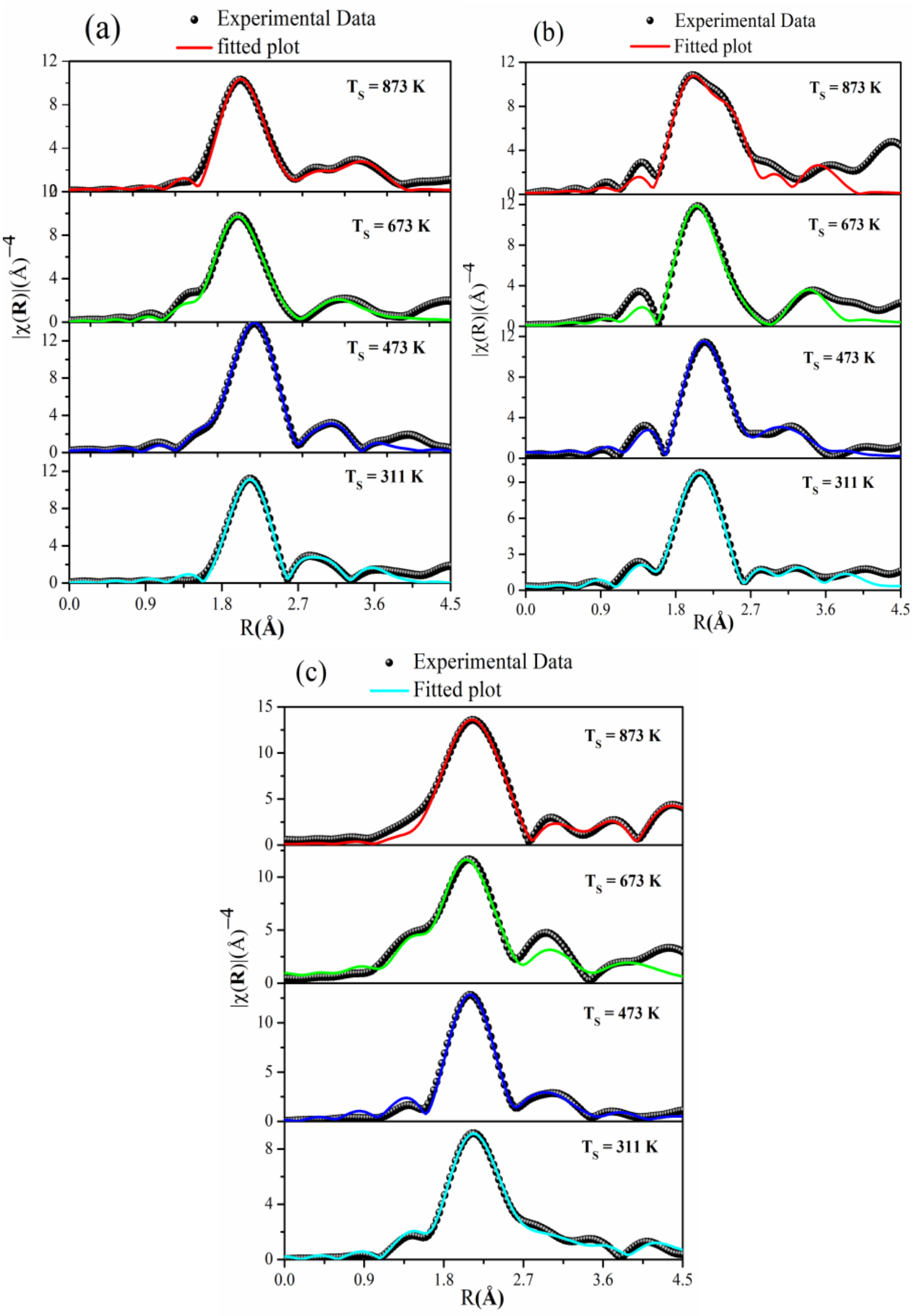

Figure-3.6: The experimental phase uncorrected χ(R) versus R plots along with theoretical fitted model of the samples at (a) Ni K-edge, (b) Fe K-edge and (c) Ga K-edge.

Table-3.1: Values of structural parameters obtained from RT-EXAFS analysis at Ni K-edge of the alloy

Scattering paths × Co-ord. No.	Parameters	311 K	473 K	673 K	873 K
	% contribution of $L2_1$ (Fm-3m) phase	42.30 ± 0.005	46.14 ± 0.060	80.65 ± 0.018	84.83 ± 0.011
Ni – Ga × 4	R (Å) σ^2 ($Å^2$)	2.29 ± 0.01 0.003 ± 0.001	2.42 ± 0.02 0.013 ± 0.002	2.43 ± 0.01 0.010 ± 0.001	2.43 ± 0.01 0.005 ± 0.001
Ni – Fe × 4	R (Å) σ^2 ($Å^2$)	2.31 ± 0.01 0.015 ± 0.001	2.44 ± 0.01 0.013 ± 0.002	2.44 ± 0.01 0.009 ± 0.001	2.46 ± 0.02 0.021 ± 0.003
Ni – Ni1 × 6	R (Å) σ^2 ($Å^2$)	3.01 ± 0.01 0.009 ± 0.001	2.95 ± 0.03 0.020 ± 0.005	2.80 ± 0.02 0.023 ± 0.003	2.86 ± 0.02 0.022 ± 0.003
Ni – Ni2 × 12	R (Å) σ^2 ($Å^2$)	4.03 ± 0.01 0.011 ± 0.001	3.93 ± 0.01 0.003 ± 0.001	3.83 ± 0.04 0.029 ± 0.010	3.99 ± 0.02 0.019 ± 0.004
	% contribution of γ (Pm-3m) phase	57.70	53.86	19.35	15.17
Ni – Fe × 4	R (Å) σ^2 ($Å^2$)	2.35 ± 0.01 0.016 ± 0.001	2.32 ± 0.03 0.025 ± 0.009	2.63 ± 0.01 0.005 ± 0.002	2.60 ± 0.01 0.002 ± 0.001
Ni – Ni1 × 8	R (Å) σ^2 ($Å^2$)	2.46 ± 0.01 0.004 ± 0.001	2.50 ± 0.01 0.008 ± 0.001	2.57 ± 0.06 0.025 ± 0.010	2.67 ± 0.01 0.005 0.001
Ni – Ni2 × 6	R (Å) σ^2 ($Å^2$)	3.80 ± 0.01 0.013 ± 0.001	3.79 ± 0.02 0.001 ± 0.001	3.55 ± 0.01 0.002 ± 0.005	3.68 ± 0.02 0.002 ± 0.005
	R_{factor}	0.0009	0.003	0.009	0.012

On the other hand, due to having the similar kind of atomic arrangement around the Fe and Ga atoms, 8 Ni atoms of the $L2_1$ phase and 12 Ni atoms of the γ phase in the 1st co-ordination shell contribute to the 1st peak in Fe and Ga K-edge data. However, the other peaks above 4 Å get suppressed drastically with much higher σ^2 values. This implies the larger distribution of the bond lengths and an unstable cubic structure with the unequal movement of the constituent atoms from their crystallographic positions at larger distance. So for the fitting purpose such paths having R value greater than 4.1 Å have been neglected for all the edges.

Table-3.2: Values of structural parameters obtained from RT-EXAFS analysis at Fe K-edge of the alloy

Scattering paths × Co-ord. No.	Parameters	311 K	473 K	673 K	873 K
	% contribution of $L2_1$ (Fm-3m) phase	42.30 ± 0.005	46.14 ± 0.060	80.65 ± 0.018	84.83 ± 0.011
Fe – Ni × 8	R (Å) σ^2 (Å^2)	2.30 ± 0.01 0.006 ± 0.001	2.43 ± 0.01 0.010 ± 0.001	2.45 ± 0.02 0.023 ± 0.002	2.46 ± 0.01 0.014 ± 0.001
Fe – Ga × 6	R (Å) σ^2 (Å^2)	3.07 ± 0.01 0.010 ± 0.003	2.82 ± 0.02 0.013 ± 0.003	2.68 ±0.03 0.019 ± 0.003	2.68 ± 0.01 0.007 ± 0.001
Fe – Fe × 12	R (Å) σ^2 (Å^2)	4.06 ± 0.02 0.021 ± 0.009	4.00 ± 0.03 0.027 ± 0.013	3.79 ± 0.03 0.025 ± 0.013	3.88 ± 0.02 0.019 ± 0.003
	% contribution of γ (Pm-3m) phase	57.70	53.86	19.35	15.17
Fe – Ni × 12	R (Å) σ^2 (Å^2)	2.44 ± 0.01 0.006 ± 0.002	2.51 ± 0.01 0.008 ± 0.001	2.45 ± 0.01 0.003 ± 0.001	2.43 ± 0.01 0.007 ± 0.001
Fe – Fe × 6	R (Å) σ^2 (Å^2)	3.72 ± 0.01 0.013 ± 0.006	3.47 ± 0.02 0.010 ± 0.003	3.59 ± 0.02 0.001 ± 0.001	3.70 ± 0.02 0.001 ± 0.003
	R_{factor}	0.004	0.019	0.015	0.014

It can be observed from figure-3.7 that the quality of fitting appears to be better in case of Ni and Ga K-edge data compared to Fe K-edge data. The cause of this is antisite disorder between the Fe and Ni atoms and due to higher concentration of Fe in these samples. Similar observation of antisite disorder between Mn and Ni atoms has been made by Sathe et al. while analyzing Mn K edge EXAFS data of their NiMnGa alloy sample [111]. As reported by Zhu et al., Fe atoms are known to prefer the Y positions as well as the X positions in the lattice by producing the antisite disorder with the Ni atoms [113]. However, in such structure there is also a possibility of the occurrence of antisite disorder between Fe and Ga atoms also [111].

Table-3.3: Values of structural parameters obtained from RT-EXAFS analysis at Ga K-edge of the alloy

Scattering paths × C.N	Parameters	311 K	473 K	673 K	873 K
	% contribution of $L2_1$ Phase	42.30 ± 0.005	46.14 ± 0.060	80.65 ± 0.018	84.83 ± 0.011
Ga – Ni × 8	R (Å) σ^2 (Å^2)	2.29 ± 0.01 0.010 ± 0.001	2.42 ± 0.01 0.003 ± 0.001	2.43 ± 0.01 0.004 ± 0.003	2.43 ± 0.01 0.006 ± 0.003
Ga – Fe × 6	R (Å) σ^2 (Å^2)	3.12 ± 0.01 0.007 ± 0.001	2.92 ± 0.05 0.026 ± 0.010	2.68 ± 0.04 0.029 ± 0.008	2.68 ± 0.05 0.029 ± 0.010
Ga – Ga × 12	R (Å) σ^2 (Å^2)	4.07 ± 0.01 0.028 ± 0.010	4.00 ± 0.05 0.029 ± 0.010	3.94 ± 0.03 0.019 ± 0.008	4.07 ± 0.05 0.015 ± 0.005
	% contribution of γ phase	57.70	53.86	19.35	15.17
Ga – Ni1 × 12	R (Å) σ^2 (Å^2)	2.47 ± 0.01 0.009 ± 0.001	2.33 ± 0.02 0.024 ± 0.006	2.33 ± 0.01 0.001 ±0.001	2.55 ± 0.03 0.001 ± 0.002
Ga – Fe × 6	R (Å) σ^2 (Å^2)	3.60 ± 0.02 0.014 ± 0.003	3.45 ± 0.04 0.013 ± 0.004	3.48 ± 0.03 0.001 ± 0.003	3.51 ± 0.05 0.001 ± 0.002
	R_{factor}	*0.005*	*0.007*	*0.007*	*0.010*

It may be noted that Fe and Ni atoms have nearby atomic numbers, 26 and 28 respectively, hence X-ray diffraction is not likely to differentiate between X-ray scattering from them, EXAFS, on the other hand, being an element specific technique, can differentiate their nearby surroundings. From the above EXAFS best fit results, it has also been observed that with an increase in the substrate temperature the disordered γ phase gets reduced which clearly agree with the GIXRD result [114]. The values of the parameters resemble the cubic austenite structure at room temperature. The variations of various bond lengths as obtained from EXAFS analysis are also shown in figure-3.7 as a function of substrate temperature along with the variation of the relative fraction of the $L2_1$ and γ phases.

The theoretical bond distances of the Ni-Fe and Ni-Ga pairs have the same value (2.50 Å) i.e., if the crystal structure is perfectly cubic then Ni atoms sitting at the body center position would be equidistant to the Fe and Ga atoms, however from EXAFS analysis it has been observed that there is a slight difference in these bond lengths.

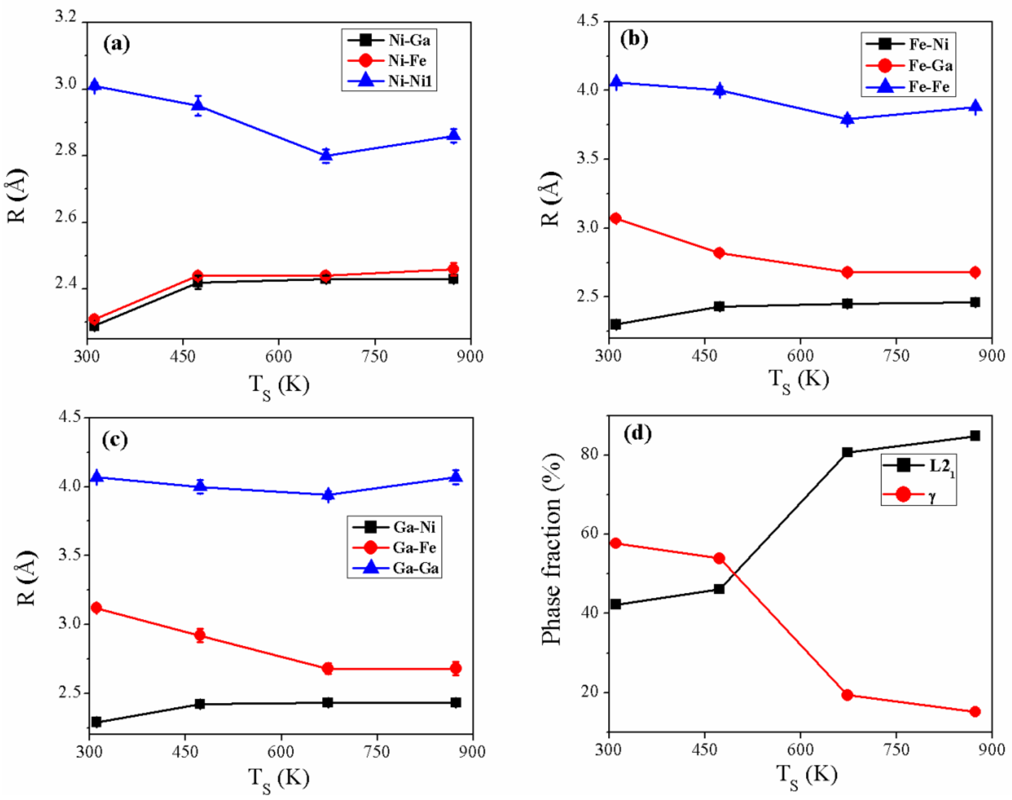

Figure-3.7: Variations in different bond lengths as obtained from EXAFS analysis at (a) Ni, (b) Fe and (c) Ga K-edges (d) variation of the relative fraction of $L2_1$ and γ phases as a function of substrate temperature.

The difference increases with an increase in substrate temperature and is prominent for the HA-4 sample. This is due to static structural disorder associated with martesnite phase and appears in the sample since the martensite temperature of the Heusler alloy is close to the room temperature [111]. Another important aspect which emerges from the EXAFS analysis is that the Ni-Ga bond length is slightly shorter than the Ni- Fe bond length suggesting the rigidness of the Ni-Ga bond with lesser σ^2 value in comparison to its counterpart.

For the samples deposited at lower substrate temperatures, these bond lengths are smaller than their crystallographic values, which may be due to the presence of large fraction of the disordered f.c.c γ phase which produces a hindrance to the atomic movements. It has also been found that there is a small difference between the Ni-Fe bond distance found from Ni K-edge data and Fe-Ni bond distance obtained from Fe K-edge data which also indicates the movement of the atomic species from their crystallographic positions [115]. However, the Ga-Ni bond distance obtained from Ga K-edge data and Ni-Ga bond distance obtained from the Ni K-edge data remain exactly same in the 1st co-ordination shell with a smaller value of σ^2. This result suggests that the Ga atom at the Z position is strongly bound with Ni atom at the X position. Ga atoms are sluggish and do not get much displaced from their crystallographic positions and remain almost stable cubic structure in the 1st co-ordination sphere. This also leads to the p-d hybridization in the sample discussed later. In similarity with the Ni K-edge data, the Ga K-edge data also shows that the Fe atoms moves away from the Ga site giving a higher value of σ^2. Another cause of larger deviation of the Ga-Fe bond length from Fe-Ga bond length may be due to lager value of the γ phase present in the samples deposited at lower substrate temperatures. It is believed that the γ phase is rich in Fe content, where few Fe atoms are occupied by the Ga atoms and this substitution is random, which forms a disordered f.c.c structure.

On the basis of the LT-XRD result the LT- EXAFS analysis on the HA-4 sample has been carried out with the mixed phase of cubic $L2_1$ and tetragonal NM martensite phases. The Non Modulated (NM) phase (space group I4/mmm) has the lattice parameters of a = 3.77 Å and c = 6.25 Å. [70], with an elongation along the z axis and contraction along the x and y axes in comparison to the cubic phase. In this structure the Ni atom occupies (0, ½, ¼) positions, Fe atoms (0, 0, 0) and Ga atoms (0, 0, ½) positions. Figures-3.8 (a) and (b) show the normalized EXAFS spectra at Ni and Fe K-edges of the HA-4 sample measured at RT and 120 K while figures-3.9 (a) and (b) show the corresponding phase uncorrected $\chi(R)$ versus R plots fitted with the austenite $L2_1$ and NM martensite phases. The fitting quality improves by more than 10% by considering a mixed austenite and martensite phase instead of only austenite phase. The significant changes observed in the $\chi(R)$ vs R plots of the samples in the R range of 2 - 4 Å, corroborates to the lowering of symmetry from parent cubic phase undergoing the martensitic transformation and this hints to a modulation in the crystal structure [112].

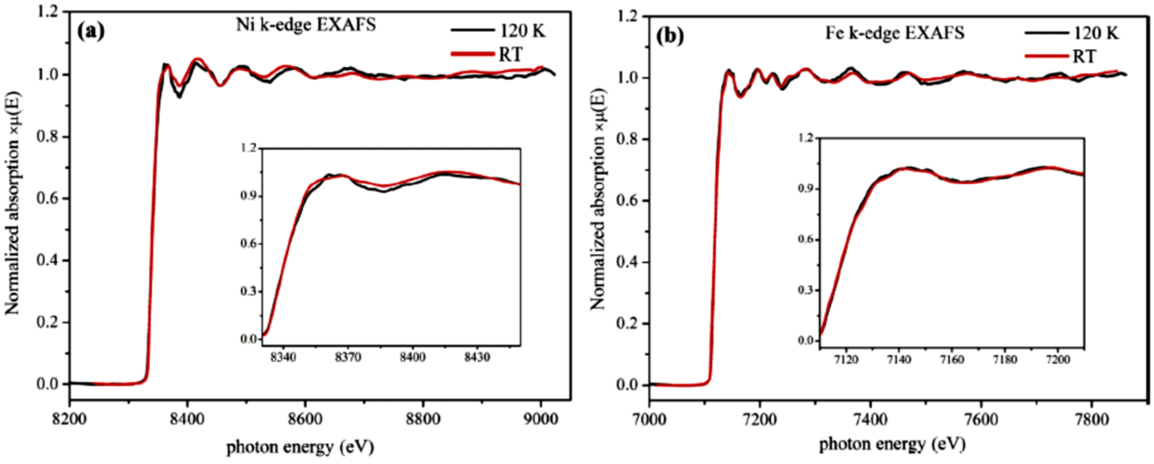

Figure-3.8: RT and low temperature normalized EXAFS spectra of the HA-4 sample deposited at 873 K and measured at (a) Ni K-edge and (b) Fe K-edge. (Inset shows the respective XANES spectra).

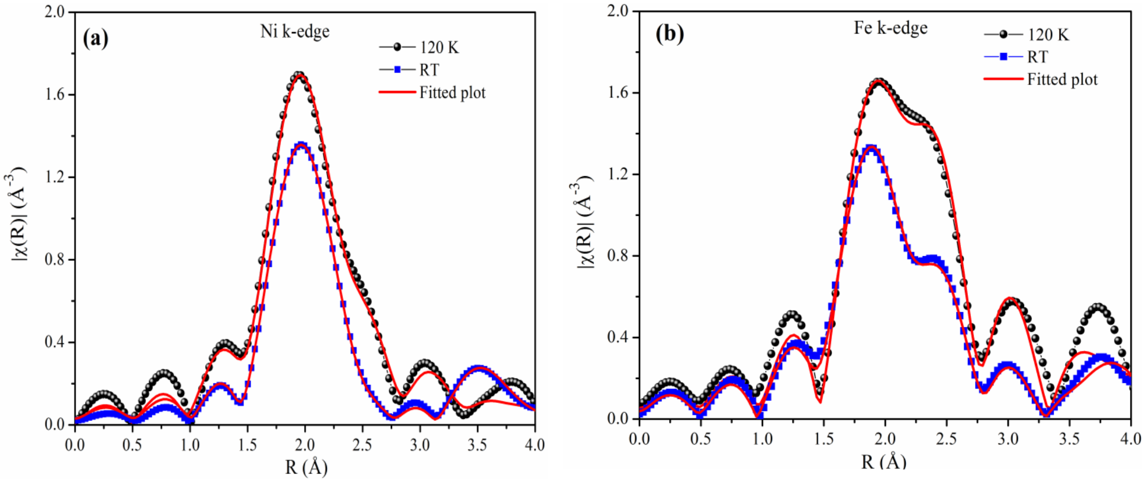

Figure-3.9: The experimental phase uncorrected $\chi(R)$ versus R plots (dots) measured at RT and at 120 K along with theoretical fitted model (red line) of the HA-4 sample deposited at 873 K at (a) Ni K-edge, (b) Fe K-edge.

The fitting of the above data has been carried out following similar procedure as the room temperature data where the relative concentrations of the two phases has also been used as a fitting parameter and the best fit parameters have been shown in Tables- 3.4 and 3.5

Table-3.4: Values of structural parameters obtained from LT- EXAFS analysis at Ni K-edge of the HA-4 alloy

Scattering Paths × C.N	Parameters	RT	120 K
	% contribution of $L2_1$ phase	46.51 ± 0.01	18.99 ± 0.01
Ni – Ga × 4	R (Å) σ^2 (Å^2)	2.40 ± 0.01 0.003 ± 0.001	2.32 ± 0.01 0.002 ± 0.002
Ni – Fe × 4	R (Å) σ^2 (Å^2)	2.49 ± 0.01 0.001 ± 0.001	2.51 ± 0.01 0.003 ± 0.001
Ni – Ni × 6	R (Å) σ^2 (Å^2)	2.65 ± 0.01 0.004 ± 0.001	2.75 ± 0.01 0.001 ± 0.001
	% contribution ofNM phase	53.49	81.01
Ni – Fe × 4	R (Å) σ^2 (Å^2)	2.42 ± 0.01 0.026 ± 0.001	2.43 ± 0.04 0.016 ± 0.003
Ni – Ga × 4	R (Å) σ^2 (Å^2)	2.39 ± 0.01 0.018 ± 0.001	2.36 ± 0.01 0.006 ± 0.009
Ni – Ni1 × 4	R (Å) σ^2 (Å^2)	2.77 ± 0.01 0.028 ± 0.002	2.65 ± 0.01 0.012 ± 0.003
Ni – Ni2 × 2	R (Å) σ^2 (Å^2)	2.90 ± 0.01 0.002 ± 0.001	2.88 ± 0.01 0.009 ± 0.003
	R_{factor}	0.0002	0.0007

For the present fitting process, the values of σ^2 as obtained from austenite $L2_1$ phase of room temperature data of this sample have been used as the starting values of the parameter. However, the σ^2 values obtained by the above fitting process considering the martensite phase have been found to be lower indicating the reduction of the thermal disorder. The major aspect that can be observed from figure-3.9 is the significant increase in the intensity of the 1st shell from room temperature to the low temperature. This observation can not only be attributed to the decrease in the thermal disorder but also it shows that the static disorder around the respective absorbing atoms decreases due to martensitic transformation. Similar observation has been made by Sathe et. al. also in the EXAFS data of their NiMnGa samples [111].

Table-3.5: Values of structural parameters obtained from LT- EXAFS analysis at Fe K-edge of the HA-4 alloy

Scattering Paths × C.N	Parameters	RT	120 K
	% contribution of $L2_1$ phase	46.51 ± 0.01	18.99 ± 0.01
Fe – Ni × 8	R (Å)	2.49 ± 0.01	2.48 ± 0.07
	σ^2 (Å^2)	0.020 ± 0.002	0.026 ± 0.006
Fe – Ga × 6	R (Å)	2.96 ± 0.04	2.78 ± 0.01
	σ^2 (Å^2)	0.025 ± 0.006	0.001 ± 0.001
Fe – Fe × 12	R (Å)	4.24 ± 0.04	3.97 ± 0.02
	σ^2 (Å^2)	0.018 ± 0.007	0.003 ± 0.002
	% contribution of NM phase	53.59	81.01
Fe – Ni × 8	R (Å)	2.43 ± 0.01	2.47 ± 0.01
	σ^2 (Å^2)	0.013 ± 0.001	0.011 ± 0.001
Fe – Ga1 × 4	R (Å)	2.69 ± 0.01	2.70 ± 0.01
	σ^2 (Å^2)	0.001 ± 0.001	0.002 ± 0.005
Fe – Ga2 × 2	R (Å)	3.25 ± 0.01	3.31 ± 0.01
	σ^2 (Å^2)	0.003 ± 0.001	0.003 ± 0.008
Fe – Fe × 4	R (Å)	3.90 ± 0.01	3.81 ± 0.04
	σ^2 (Å^2)	0.007 ± 0.001	0.013 ± 007
	R_{factor}	0.004	0.003

From Table-3.4 we can see that by lowering the temperature from room temperature, the fraction of the NM martensite phase increases and leads to a major phase in the structure. It also shows that in both the phases the Ni – Ga bond length decreases while Ni – Fe bond distance increases as the temperature is lowered to maintain the conservation of the cell volume. Thus the lattice containing Fe atoms expands while the lattice containing Ga atoms shrinks and as has been pointed out by Sathe et al. in case of NiMnGa alloy, this is due to martesntise transformation in the sample with modulated structure [111]. Bhobe et al. have carried out EXAFS measurements on a series of NiMn based Hausler alloy samples and have observed that in case of NiMnGa [112], Ni-Ga bonds are shorter which leads to *p-d* hybridization between Ga and Ni orbitals, while in case of NiMnIn [115] and NiMnSn [116] alloys, Ni-Mn bond lengths are shorter leading to *d-d* hybridization between Ni 3d and Mn 3d orbitals. In case of the present Ni-Fe-Ga samples also since Ni – Ga bond lengths are shorter than Ni-Fe bond lengths, *p-d* hybridization is more likely to occur than *d-d* hybridization and the *p-d* hybridization grows stronger at low temperature. This *p-d* hybridization is possibly responsible for the martenstic phenomenon observed in the Ni-Fe-Ga alloys. Thus to summarize the EXAFS results, atoms are found to move from their designated crystallographic positions, movement of Fe being more than Ni and Ga leading to antisite disorders. Ni – Ga bond distance is found to be slightly less than Ni – Fe bond distance manifesting stronger Ni – Ga bonding which results in *p-d* hybridization among Ni and Ga orbitals. EXAFS analysis at low temperature suggests an enhancement of martensite phase leading to breaking of the atomic arrangement by rearrangement of the atomic shells. The essential criteria for the martensite transition are the modulation of the atomic planes in trying to maintain the volume conservation has been fulfilled.

3.4.6 Magnetic Characterizations:

In Ni_2FeGa Heusler alloys contribution to the magnetization is mainly localized at the Fe atom which is similar to the Ni_2MnGa alloys for Mn atoms. Liu. et al. have reported that in Ni_2YZ based Heusler alloys the contribution of Ni moment is very much less because of the equal contribution of majority and minority spins inthe valance band [14].

3.4.6.1 Thermal demagnetization (M-T) curves:

In order to understand the magnetic behaviourof the alloy films with temperature, the temperature dependentmagnetization M (T) has been studied by applying a constantmagnetic field. The M (T) data have been collected in the Zero FieldCooled (ZFC), Field Cooled Cooling (FCC) and Field Cooled Warming(FCW) conditions by applying the magnetic field parallel to theplane of the film surface. Prior to the magnetization measurementthe sample was cooled from room temperature to 5 K in theabsence of any external magnetic field. Consequently, the samplewas heated up to 380 K with the application of pre-determinedmagnetic field and the ZFC data were measured. Subsequently, without removing the external magnetic field the FCC data weretaken while cooling the sample from 380 K to 5 K. At the last stepthe FCW magnetization was measured by increasing the temperatureto 380 K with the same applied magnetic field. The variation of the temperature dependent magnetization M (T) has been shown in figure. 3.10(a)-(d).

Figure-3.10(a)-(c) show that the heating curve (ZFC) retraces the cooling curve (FCC), which suggests the reversibility of the magnetization due to the orientation of the magnetic dipoles. From figure-3.10(d) it can be seen that for the film deposited at the highest substrate temperature, there is a splitting between ZFC and FCC curves, which lasts for a long temperature region. According to Krenke. et al., the splitting is associated with the co-existence of the anti-ferromagnetic exchange interaction [117]. Thus the thermo-magnetization measurement shows that in the sample grown at the highest substrate temperature, a mixture of ferromagnetic and anti-ferromagnetic phases exists. The magnetization measurement has been carried out on this sample at low magnetic field (0.05 T) also which is shown figure-3.10(d) and shows a unique feature. In the M-T plot a small cusp at 25 K is observed, which is known as the Neel temperature of antiferromagnetism and manifests the presence of the antiferromagnetic behavior at the low temperature. Below this temperature, the value of the magnetization decreases with decrease in the temperature. The antiferromagnetic ordering observed in this sample can be a result of the antisite disorder of Fe atoms with the Ni atoms in the samples. As observed from the RT-EXAFS study, the Fe - Fe bond length in the samples gradually decreases with an increase in substrate temperature manifesting increasing antisite disorder between the Fe and Ni atoms. Lazpita et al. have presented a model regarding the relation between magnetic moment and chemical ordering for shape memory alloys [118].

3.4.6.2 M-H curves:

Taking an analogue of Mn atoms in Ni-Mn-Ga alloy from the above model, it can be suggested that in case of Ni-Fe-Ga alloy for a cubic $L2_1$ phase the properly sited Fe atoms interact ferromagnetically with the nearby Ni atoms or other Fe atoms; however, in an off-stoichiometric Ni-Fe-Ga heusler alloy the Fe atoms sited at Ni or Ga positions may couple antiferromagnetically with the nearest neighbour properly sited Fe atoms. So the antisite disorder of Fe atoms with Ni atoms is likely to introduce anti-ferromagnetic characteristic in the sample.

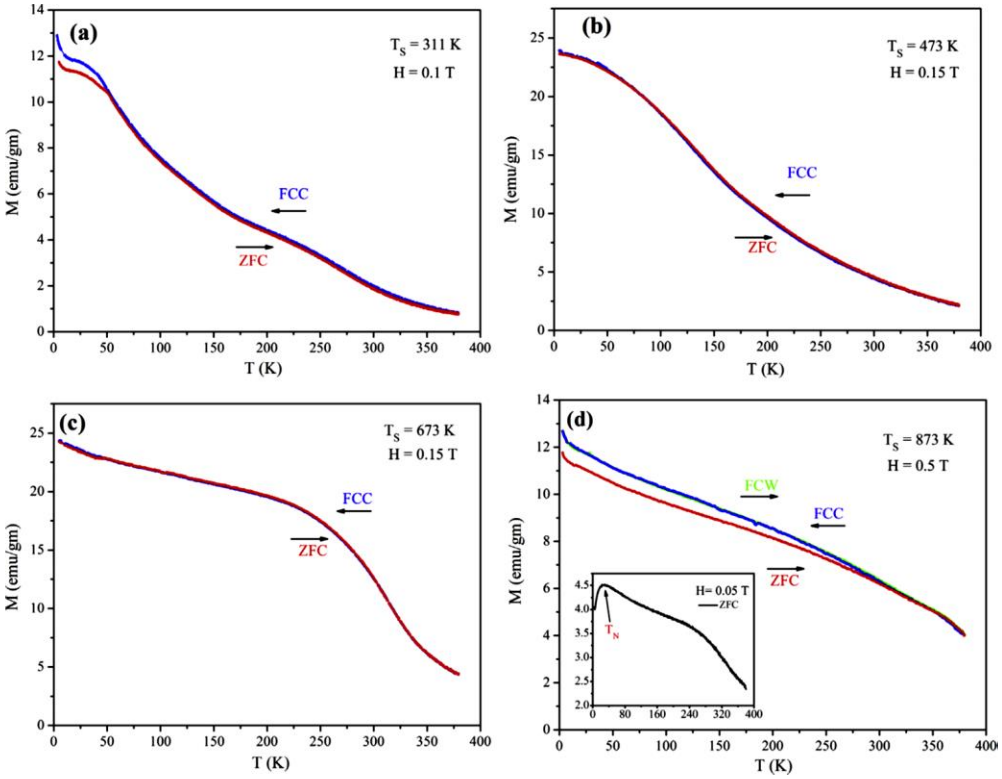

Figure-3.10: Thermo magnetization (M-T) curve of the thin films alloy samples deposited at different substrate temperatures, (a) 311 K, (b) 473 K, (c) 673 K and (d) 873 K.

For further characterization of the magnetic properties of the alloy films, their magnetic field dependent magnetization M (H) behaviours were measured at 5 K, 300 K and 380 K. Figure-3.11

shows the M-H plots for the thin film samples deposited at different substrate temperatures. To obtain the magnetic contribution of the thin film the diamagnetic contribution of the Si substrate was subtracted from the experimentally obtained data of each sample. Figure-3.11 shows that magnetization decreases with the increase in substrate temperature. It can be noticed from figure-3.10 that in case of measurement at 5 K, the samples show a well-defined coercive field (Hc) and remnant magnetization (M_R) manifesting ferromagnetic ordering. It has also been observed that with an increase in the substrate temperature as the crystallinity of the film increases the saturation magnetization also increases which is as expected since with an improvement in the atomic ordering in the lattice the exchange interaction enhances which inturn increases the magnetization of the alloys.

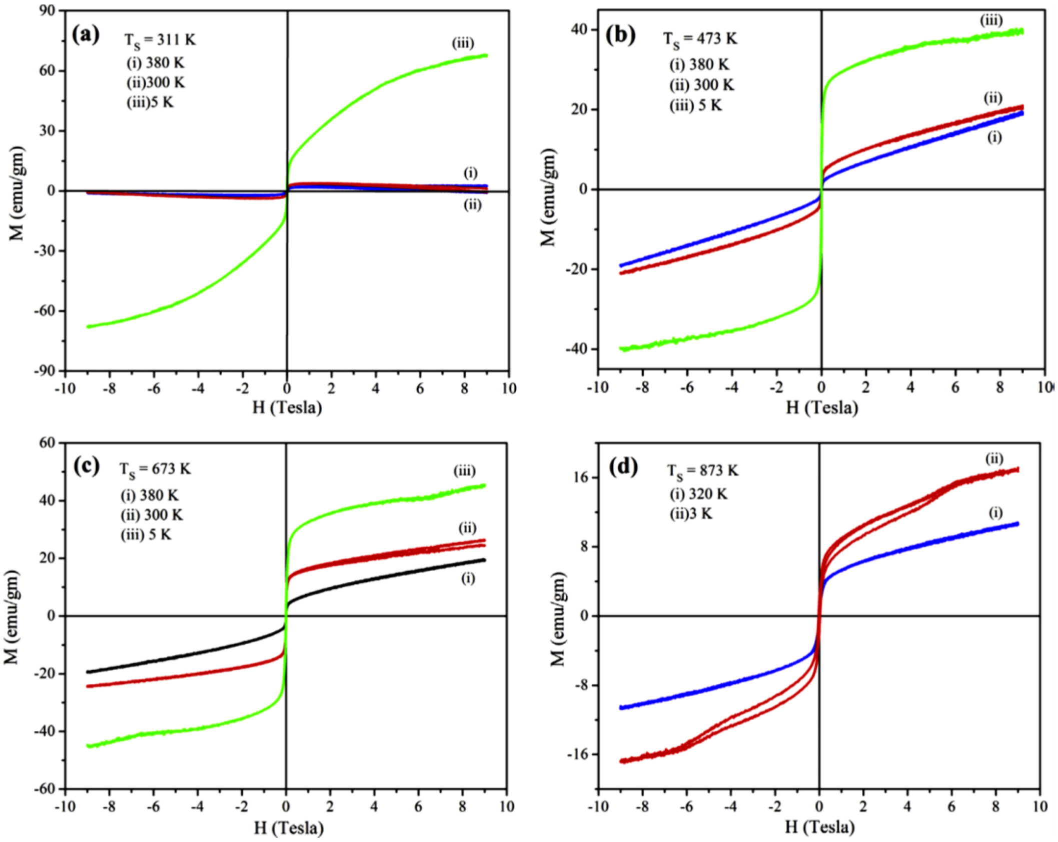

Figure-3.11: Magnetization (M-H) curves measured at three different temperatures for the thin films alloy samples deposited at different substrate temperature, (a) 311 K, (b) 473 K, (c) 673 K and (d) 873 K.

However, for the film deposited at 873 K (HA- 4), M_R and M_S decrease while the H_C increases significantly. The magnetization saturates at a very high value of magnetic field which is a consequence of magnetic inhomogeneity in the sample which can further be concluded from the broader maxima in the ZFC curve at 0.05 Tesla field at ~25 K [119] (Figure-.3.10(d)). To further study the magnetic nature of the HA-4 film the Arrott plot (M^2 versus H/M curve) determined from the magnetization value has been shown in the figure-3.12 which shows small intercepts on the M^2 axis implying low spontaneous magnetization at zero field. It should be noted that the data at very low field have not been given in the above plots due to small value of magnetization of the samples in this region. Negligible spontaneous magnetization at the zero field in the Arrott plot, the existence of non-saturating nature at a very high magnetic field and hysteresis at the low field region indicates the short range ferromagnetic ordering which arises possibly due to a competition between long-range FM interaction and short-range AFM interaction [119,120].

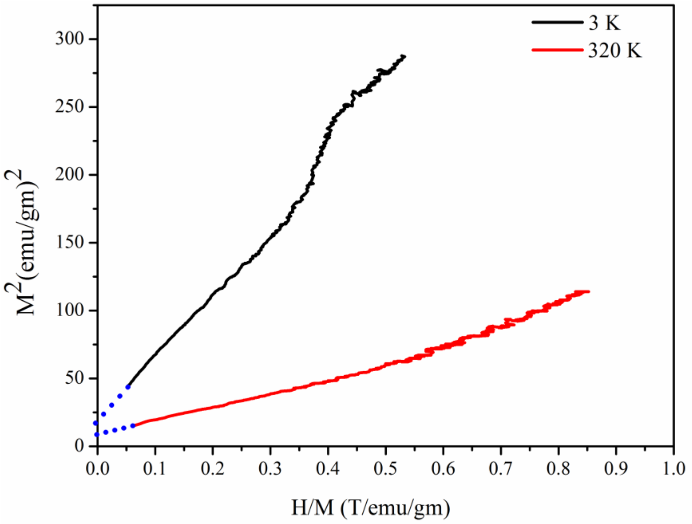

Figure-3.12: M^2 vs H/M plot (Arrot plot) of the HA-4 film deposited at 873 K at two different temperatures.

The low value of saturation magnetization in the HA-4 sample is possibly due to the presence of anti-ferromagnetic phases as discussed above. The decrease in the γ phase fraction in this sample may also lead to this since saturation magnetization of γ phase is less than that of the austenite phase [104, 121] or the presence of 10M orthorhombic martensite phase in this sample which has been observed from GIXRD measurements. Similar observations have been made by H.D. Nguyen [23] and Rama Rao et al. [123] for NiMnSn and NiMnSb Heusler alloy samples also. It is also worth noting here that the saturation magnetization of martensite phase obtained in NiMnGa alloy is higher than in the austenite phase while the reverse is true for Ni-Mn-X (X = Sn, In,Sb) alloys [118] and the present sample appears to follow the later.

3.5 Conclusions:

$Ni_{55}Fe_{19}Ga_{26}$ ferromagnetic Heusler alloy thin films have been prepared by (PLD) technique at different substrate temperatures. The structural characterization carried out using GIXRD technique showsthat the samples deposited at lower substrate temperatures are rich in γ phase. As the crystallinity of the films increases with the substrate temperature the disorder γ phase gets reduced and at the highest substrate temeperaure the non cubic martensitic phase appears which are expected to be of tetragonal symmetry. Low temperature XRD data of the sample deposited at the highest substrate temperature shows that the intensity of martensite peak remains same throughout the temperature range down to 5K while there is a systematic shift in peak position showing negative thermal expansion which is a characteristic of the martensite phase. Formation of granular morphology was observed from FESEM study and it was observed that the filmsare deffiecient in Ga and rich in Fe. The EXAFS results at Ni, Fe and Ga K-edges also show that with increasing substrate temperature, the disorder γ phase get reduced. A strong Ni-Ga bond, characterized as stronger *p-d* hybridization was observed which leads to the martensite transition. Magnetic measurements show non saturating behaviour of the films though the spontaneous magnetization increases with increasing substrate temperature. However, for the sample deposited at the highest temperature, due to the presence of short range ferromagnetic ordering, martensite phase and decrease in Fe-rich γ phase, saturation magnetization decreases and coercivity increases. The hysteresis between heating and cooling curves form cubic austenite to martensite phase, was however, not observed in the samples may due to the admixture of both the phases at room temperature.

Chapter-4

CORRELATION OF STRUCTURAL ORDERING WITH MAGNETIC PROPERTIES OF PULSED LASER DEPOSITED Co_2FeGa HEUSLER ALLOY THIN FILMS

4.1 Introduction:

In this chapter, the properties of a series of PLD grown Co_2FeGa thin films prepared at different substrate temperatures have been discussed. The goal in this investigation is also to find out the correlation between the long and short range structural orders in the samples with their magnetic properties. A combined approach of lab source XRD, GIXRD and GIXR measurements along with synchrotron based XRD have been used to characterize the bulk structure and surface of the thin films, while synchrotron based element specific EXAFS technique has been utilized to provide the information on short range order in the samples. The magnetic mearuremernts have been carried out is a VSM.

4.2 Experimental:

The Co_2FeGa thin films were grown using PLD at substrate temperatures of RT, 473K, 673K, 873K and 1073K and at a base pressure ~10^{-6} mbar using the system described in Chapter-2. Details of the characterization techniques have also been explained in Chapter-2.

4.3 Results and Discussions:

4.3.1 X-ray Diffraction on bulk target:

The room temperature X-ray diffraction patterns using laboratory based Cu K_α source, of the CFG thin films grown at different substrate temperatures (T_S) along with that of the bulk (target) material have been shown in figure-4.1. In order to estimate the value of the lattice parameter, the structural refinement of the target material was performed using the FullProff code [124] based on the Rietveld analysis process. The refinement depicted in figure-4.1 has been carried out assuming the cubic crystal structure of Co$_2$FeGa with space group *Fm-3m*, where the cubic structure consists of four interpenetrated *f.c.c* lattice in a unit shell where Co (X) atom occupies the Wyckoff position at 4*c* (¼, ¼, ¼), Fe atoms occupy positions at 4*a* (0, 0, 0) and the Ga atoms at 4*b* (½, ½, ½) [125]. The refinement result shows the value of lattice parameter a = 5.748Å, which is in good agreement with the reported result for the bulk sample [62].

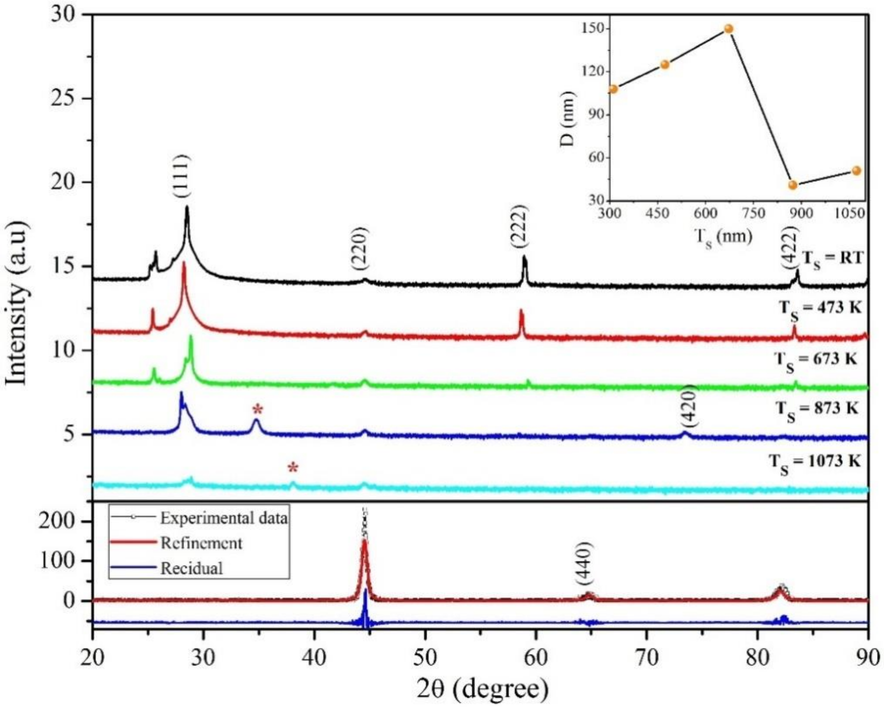

Figure- 4.1: Room temperature XRD spectra of the (a) Co$_2$FeGa thin films with varying substrate temperature, (b) Rietveld refinement of the target. (Inset shows the variation in the crystallite size with substrate temperature

There are different kinds of order structures present in these alloys and the only way to identify the various disorder is to monitor the relative intensity of the (111) and (200) super lattice reflections along with the fundamental reflection (220). (220) peak should always be present in the full Heusler alloy system irrespective of whether atomic disorder is present or not, whereas the appearance of the superlattice (111) peak confirms the presence of $L2_1$ phase and that of the additional (200) peak confirms the presence of B2 phase. From the XRD pattern of the target, presence of three reflections of (220), (400), (422) planes are clearly observed where the (220) peak, known as the fundamental diffraction peak of a full Heusler alloy (X_2YZ) structure appears to be the most intense. All these diffraction patterns correspond to the rule $(h+k+l) = 4n$ reflection, where n is a positive integer. However, absence of the (111) and (200) super lattice reflections in the XRD pattern of the target indicates the absence of the $L2_1$ and B2 phases [126] and the presence of A2 phase in the bulk target which occurs due to the atomic disorder between Co (X)-Fe(Y), Ga(Z) atoms [5, 61]. Broad diffraction peaks in the XRD pattern of the target material manifests small crystallite size of the samples.

In the room temperature XRD pattern of the thin films, however, the (111) peak appears to be the most significant along with weak (220) peak, it signifies the absence of fully ordered $L2_1$ phase and presence of significant amount of atomic disorder in the films. According to the analysis approach introduced by Webster, the degree of order of the $L2_1$ and B2 structure is evaluated from the ratio of the intensity of the odd and even superlattice reflections to the intensity of the fundamental reflection peak [127]. The fundamental diffraction peak which follows $h+k+l = 4n$ reflection is independent of atomic ordering. The even reflection which is defined by $h+k+l = 4n+2$ e.g. (200) suggests the formation of the B2 phase. The above mentioned structural phases occur due to the exchange of the site occupancy of the constituent atoms from their respective lattice sites. However, the absence of (200) reflection in the present set of CFG films manifests the inability of lab XRD measurements to identify the B2 phase arising due to disorder in atomic positions. Also due to similar atomic scattering factors of Fe and Co atoms, at the Cu K_α energy of 8046 eV or 1.54 Å the Co/Fe (DO3) type disorder and Co/Ga (A2') type disorder merges and could not be distinguished from the above measurements.

The intensity of the (220) peak remains same throughout the series though the intensity of the (111) peak decreases with substrate temperature and becomes negligibly small for the film deposited at the highest T_S. This suggests that with increase in the substrate temperature, ordereding of $L2_1$ phase decreases consequently increases the disorder in the samples. The crystallite size (D) of the samples shown in the inset to the figure-4.1 has been estimated by considering (111) reflection as the reference peak using the well-known Debye-Sherrer formula, $D = \frac{0.9\times\lambda}{\beta Cos\theta}$, where β be the FWHM of the peak, λ be the wavelength of the X-ray and θ be the position of the peak. The result shows linear increase in the crystallite size with the substrate temperature and reaches to a maximum upto 152 Å for the 673K sample. However, the grain size abruptly decreases when the substrate temperature is further increased beyond 873K. Similar observations have also been made by Yadav and Chaudhary for Co_2FeAl thin films [61]. It was suggested that with an increase in substrate temperature the diffusion of the ad atoms increases promoting the island-coalescence and resulting in an increase of the crystallite size. However, at still higher substrate temperature a higher growth rate in the transverse direction may cause the reduction in the lateral grain size [128]. It may be noted here that for the films grown at 873K and 1073K additional small peaks appear within the 2θ range of 34.14–35.46° and 37.73–38.41° respectively which might be due to experimental artifacts [129] and also there is a peak at 25° due to Si (111) substrate which is present in the RT, 473 and 673 K samples and absent in the films grown at 873 and 1073 K.

4.3.2 Anomalous X-ray Diffraction using synchrotron radiation (AXRD):

We have observed that the laboratory based XRD (Cu K_α energy) measurement was unable to distinguish between the Co/Fe and Co/Ga disorders because of the same atomic scattering factors of Co (f_{Co}) and Fe (f_{Fe}) atoms. However, there is a huge contrast in the atomic scattering factors of the atoms at their respective absorption edge energy which is (7.112 KeV) for Fe and (7.709 KeV) for Co due to the phenomena known as Anomalous X-ray Scattering (AXS) [130]. Therefore, the superlattice diffraction due to the DO3 and B2 phase will be reflected in the XRD spectra. In our case this has been carried out by the measurements at energies of 15.47 KeV and 7.11 KeV at the Angle Dispersive X-ray Diffraction beamline (BL-12) at Indus-2 Synchrotron source [131]. The XRD data measured at higher energy of 15.47 KeV is equivalent to the lab source based XRD measurement, where both Fe and Co atoms have almost similar atomic scattering factors and the XRD pattern obtained with lower X-ray energy of 7.112 KeV shows the anomalous scattering having different atomic scattering factors.

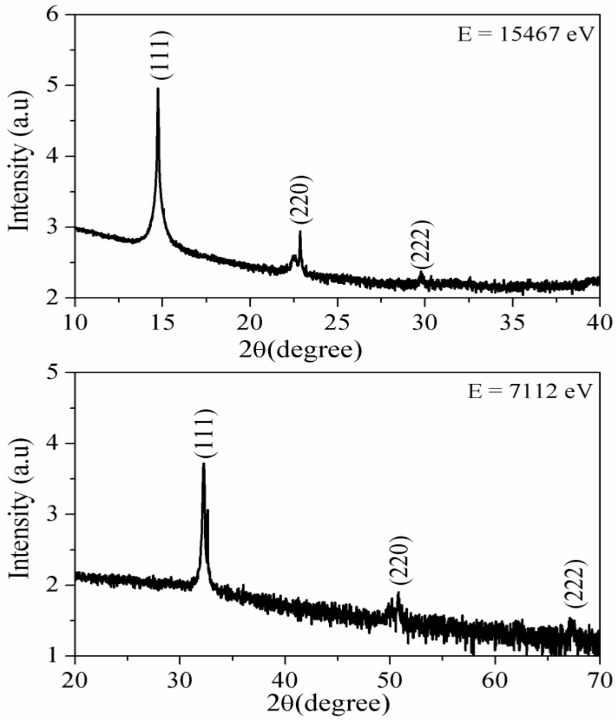

Figure- 4.2: Synchrotron based XRD spectra of the Co_2FeGa thin film grown at Room Temperature with different X-ray energy.

Figure-4.2 shows the XRD patterns of the film deposited at room temperature at both the energies. All the figures show identical nature of the XRD pattern as that of the lab source based data manifesting preferred orientation of the films along (111) direction and the (200) peak which represents the presence of B2 phase could not been observed in the samples in this measurement also. From these studies it can be concluded that in the CFG films the order L2$_1$ phase acts as major phase at the low growth temperatures and it diminishes at elevated growth temperature.

4.3.3 Grazing Incidence X-ray Diffraction (GIXRD):

In order to study the surface structure of the CFG films, GIXRD measurements within the 2θ range of 20-90° have been carried out with a constant grazing angle of incidence of 0.5°. Figure-4.3 shows the GIXRD spectra of the CFG thin films deposited at different substrate temperatures. The two peaks for (220) and (422) planes appearing within the 2θ range 44.2-45.2° and 81.2-83.2° agree with that of the target material, which indicates the dominant presence of the A2 phase at the surface.

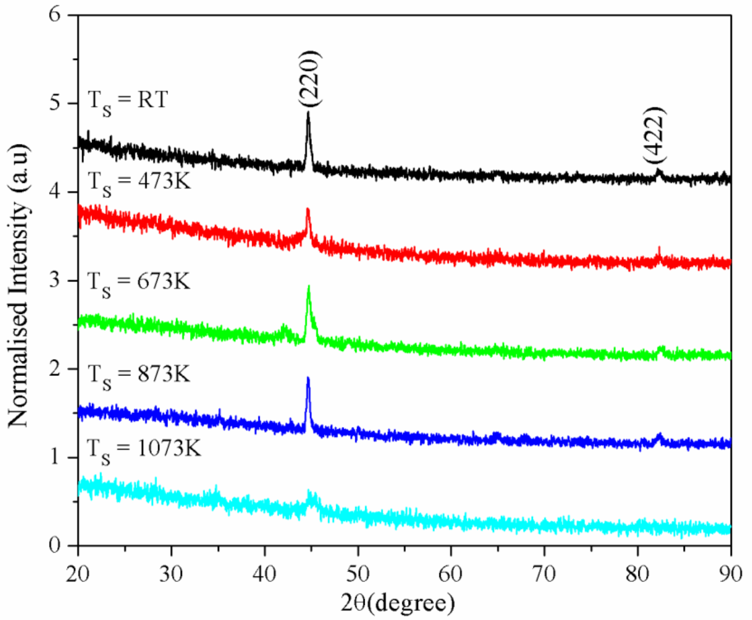

Figure-4.3: Room temperature GIXRD spectra of the Co_2FeGa thin films with varying substrate temperature.

In contrast to the XRD pattern the GIXRD data do not show the (111) reflection. Though for the film deposited at highest substrate temperature the (220) peak almost vanishes, a gradual increase in the intensity and decrease in the FWHM of the peak upto the film deposited at 873K shows an improved crystallinity at the surface due to reduction of the internal strain in comparison to the bulk. GIXRD measurement shows that the surface structure of the thin film samples is quite different from their bulk structure which is possibly due to the bi-layer structure of the samples explained by GIXR measurement discussed below.

4.3.4 Grazing Incidence X-ray Reflectivity (GIXR):

To estimate the density, thickness and roughness of the CFG films grown at different temperatures, specular grazing incidence X-ray reflectivity measurement of the thin film samples have been carried out using a diffractometer by varying the 2θ angle from 0-4˚. The values of the parameters were estimated by fitting the experimental data with a theoretical model using the IMD software described in Chapter-2. The experimentally obtained data show good quality of fitting with the simulated GIXR plot for a bi-layer model of CFG1/CFG2/Si with different density and thickness of the two layers (Figure-4.4(a)). During the fitting the values of the thickness of the bottom layer was kept constant to 1200Ǻ for all the samples, obtained from the ex-situ thickness calibration of the films with different times of laser ablation. Later the density of the bottom layer and thickness of the upper layer, density and surface roughness have been varied independently.

The theoretical reflectivity plots fit well with the experimental data except for the film deposited at 873K. No distinct Kissig fringes have been observed in the GIXR data of the films due to their large thickness except for the film deposited at 673K and the data becomes noisier for the films deposited at 873K and 1073K manifesting an increase in surface roughness of the films deposited at higher temperatures. The increase in surface roughness of the films deposited at higher substrate temperature can be attributed to high temperature induced inter-grain agglomeration of the films [62]. These observations are quite consistent with observed FESEM back scattering images of the films as discussed below. The variation in the estimated values of the GIXR parameters for the two layers has been shown in figure-4.4(b)–(d). The estimated density of the lower layer remains close to 9.25 gm cm^{-3} which is close to the value of a standard Heusler alloy compound for the film deposited at RT, 473K and 673 K temperatures, though it falls drastically below 6 gm cm^{-3} for the samples deposited at substrate temperatures of 873K and 1073K. The bi-layer structure of the samples with different growth morphology explains the contradiction of XRD and GIXRD measurements.

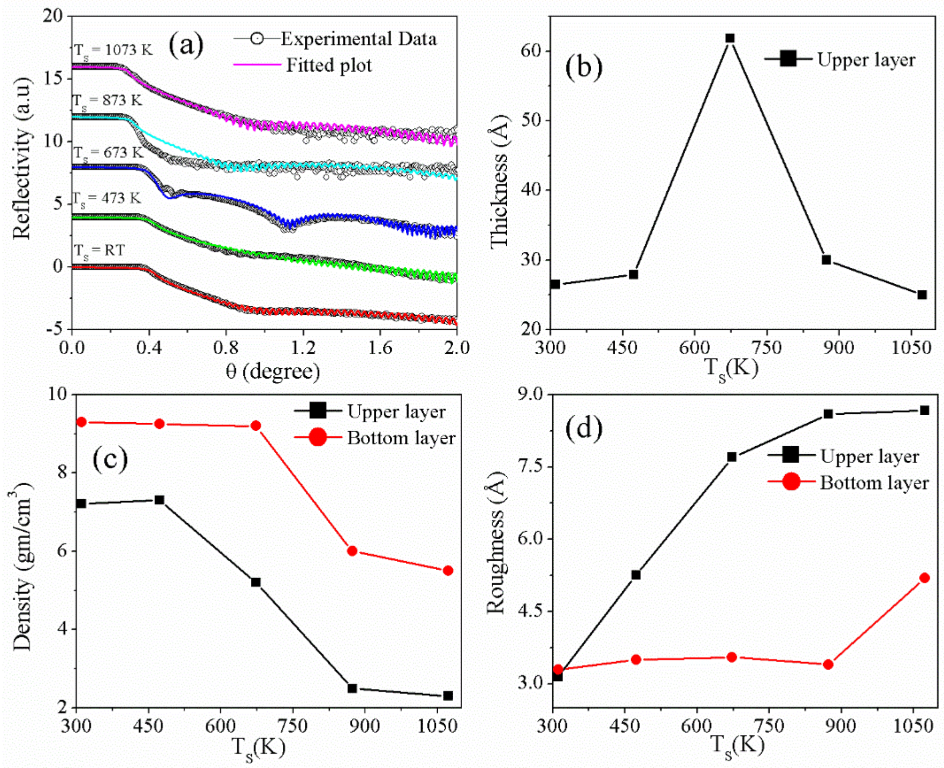

Figure- 4.4: (a) Experimental data fitted with theoretical model, variation in (b) thickness of upper layer, (c) density and (d) surface roughness of both layers.

4.3.5 Field Emission Scanning Electron Microscopy (FESEM):

The back scattering electron micrographs of the ~1200Å thick CFG films grown at various substrate temperatures have been presented in figure-4.5. The morphology of the films shows droplet-like structure grown on an otherwise smooth surface with average size of the droplet varying from 1 to 6 µm. Similar droplet-type morphology has been observed for the PLD grown films [65]. As the substrate temperature is increased beyond 473K, densities of the droplets increase drastically and the droplets agglomerated to each other to form a homogeneous microstructure, though it assumes a rough surface as observed from the GIXR data. The formation of the grain structure is observed for the film deposited at 873K and it also shows a surface with deep trenches with the size of the grains varying from 100 nm to 300 nm. Here the microstructure of the present samples matches with the microstructure of the epitaxial grown CoCrFeAl films reported by Jacob et.al. [132].

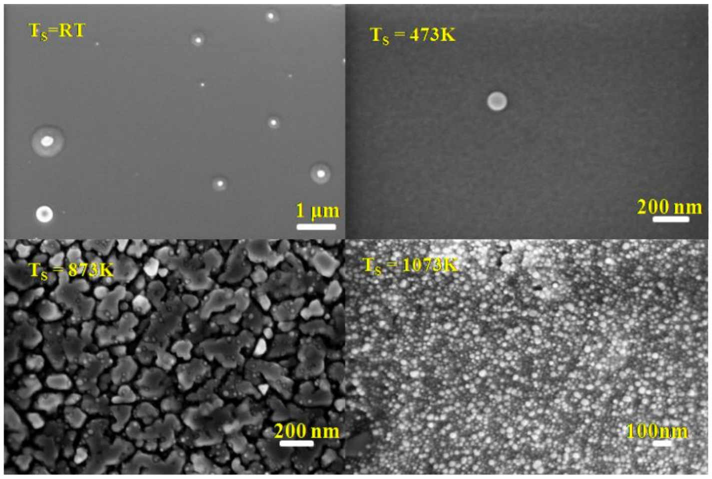

Figure- 4.5: FESEM back scattering electron image of thin film samples grown at different substrate temperature.

4.3.6 Energy Dispersive X-ray Spectroscopy (EDXS):

In order to get the estimation about the composition of the CFG films, the EDX spectra have been taken by averaging the data collected over different regions of the film. Figure-4.6 (a) and (b) show the EDX spectra of the samples grown at RT and 1073K, while the variation in the stoichiometry as a function of substrate temperatures has been shown in figure-4.6(c). The results indicate formation of off-stoichiometric films in which ratio of the metallic components slightly deviates from their ideal stoichiometric ratio of (C:F:G = 2:1:1) except for the films deposited at RT and

673 K where the Co and Fe maintain the ratio of 2:1. However the films are rich in Fe and Co and deficient in Ga content throughout the series with a drastic variation in the ratio of Co and Ga being observed for the films grown at the highest substrate temperature. Such kind of deficiency in Ga atom is likely to happen in PLD grown systems beyond certain temperature limit. This happens due to preferential scattering or sputtering of the ablated atoms at that particular substrate temperature [133].

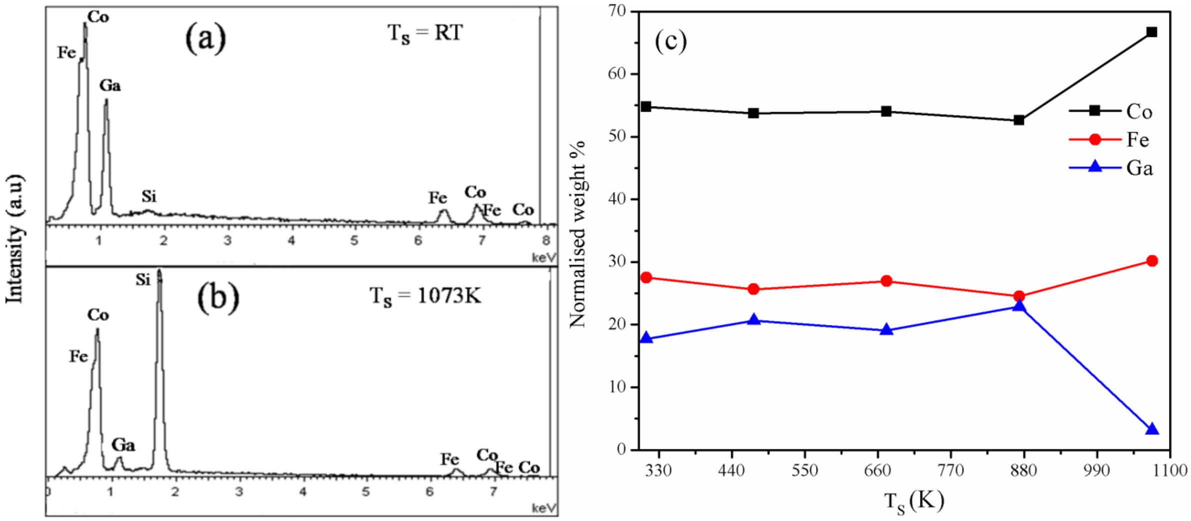

Figure- 4.6. (a) - (b): The EDX spectra of the RT and 1073 K deposited films, (c) Variation in the elemental stoichiometry of the film with varying the substrate temperature.

Riet et al. have explained that Ga atoms have a higher driving force for being segregated from the surface which enhances the preferential sputtering of Ga atoms from the film surface [134]. No significant peak of oxygen which can correspond to the oxide formation has been observed in the EDX spectra of the samples, rather a large Si peak around 1.83 KeV is observed as shown in Fig. 4.6 (b). This manifests significant diffusion of Si atoms from substrate to the film [135] with an increase in the substrate temperature, which may lead to silicidation reaction due to high reactivity of Co with Si atoms. This observation correlates with the drastic decrease in the magnetization value of the sample with an increase in substrate temperature as discussed later.

4.3.7 X-ray absorption spectroscopy (XAS):

Further, XANES and EXAFS measurements have been carried out at Co, Fe and Ga K-edges on the CFG thin films grown at different substrate temperatures. The main aspect of this XAS analysis is to provide the information about the local structure around the respective atoms and to investigate the disorder effects on the atomic structure which could not been well understood from the X-ray diffraction study. As has been explained in detail in earlier chapters, determining structures of Heusler alloys, particularly when disorders are present, by employing only X-ray diffraction is not very fruitful [136,137,138] and XAS can be a complementary method for determining structural information unambiguously. Figure-4.7 (a)-(c) show the normalized XANES spectra ($\mu(E)$ versus E) of the films at Co, Fe and Ga K-edges deposited at different substrate temperatures. XANES results show that in all the samples the absorption edges match with their respective metallic states. However, a significant change above the absorption energy was noticed for the films deposited at 873 K and 1073K.

At both the Co and Fe K-edges the appearance of a shoulder and the variation in the oscillations in the XANES feature above ~30 eV of the absorption edge (E_0) may suggest a variation in the structural symmetry in these samples. In order to get into the clear understanding about the structural information, the experimentally obtained EXAFS absorption data have been analyzed following the procedure described in detail in Chapter-2. In the case of the present samples, the experimentally obtained k^2 weighted $\chi(k)$ data over the k range of 2.5 – 11.5 Å^{-1} have been used for Fourier transform using Hanning window function and the fittings have been carried out within the R range of 1.0-4.1 Å. Initially the EXAFS data of the samples have been fitted with theoretically generated spectra assuming a structural model which does not include any antisite disorder. A schematic diagram of the atomic configuration surrounding the Co, Fe and Ga atoms in the L2_1 structure have been shown in figure-4.9 where the arrows show the scattering paths of the 1st co-ordination shell of all the atoms.

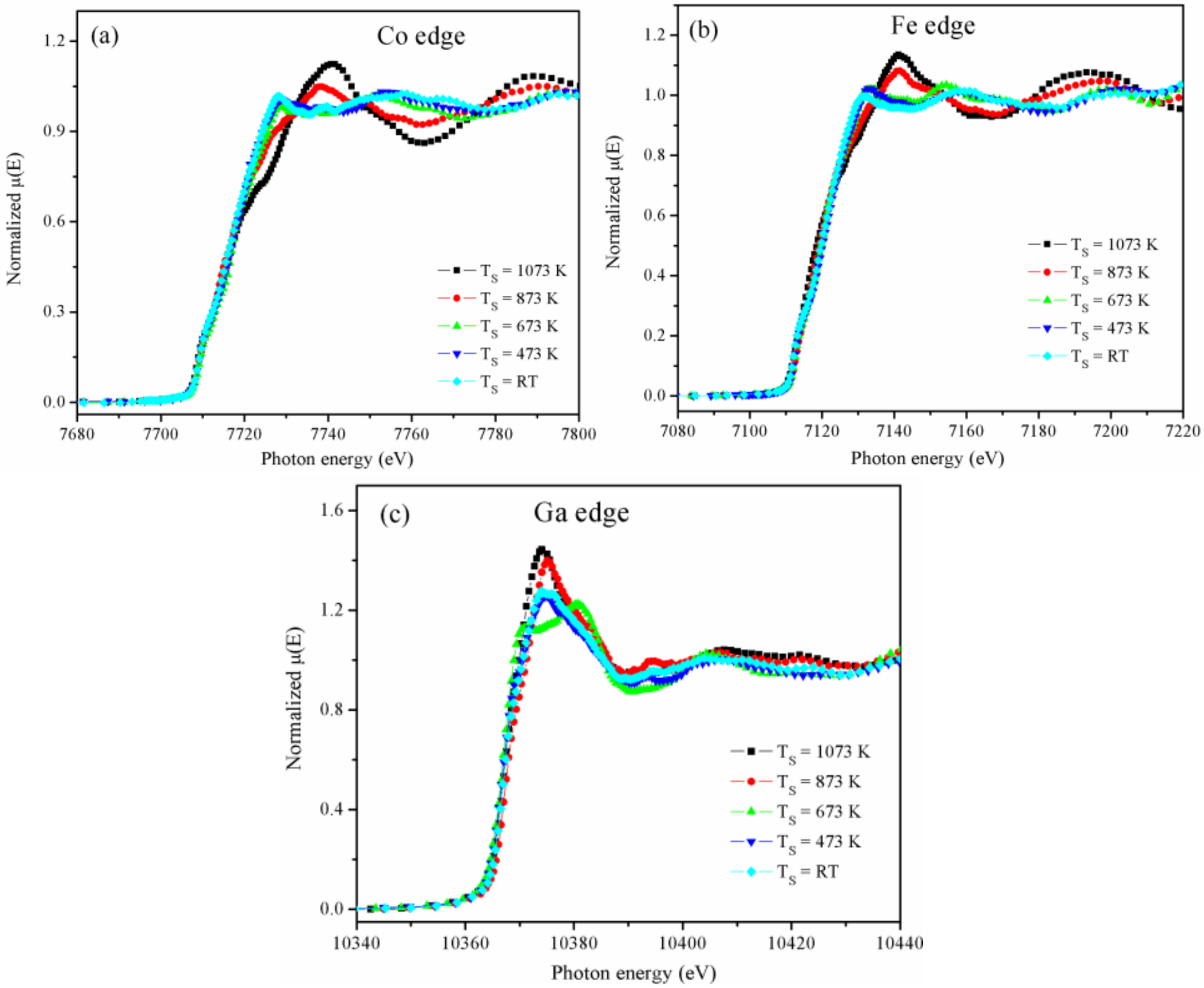

Figure- 4.7: Normalized XANES spectra (*μ(E)* vs *E*) of the CFG thin films at (a) Co, (b) Fe and (c) Ga *K*-edges.

In the octahedral structure the Co atom is coordinated with 4 Fe and 4 Ga atoms at bond distances of 2.48Å in the 1st co-ordination sphere [139] while the 2nd and 3rd co-ordination shells at 2.87Å and 4.05Å are due to Co atoms. On the other hand, as the Fe and the Ga atoms are situated at the equivalent site of each other, the Fe or the Ga atoms are surrounded by 8 Co atoms in the 1st co-ordination shell and 6 Ga or Fe atoms in the 2nd shell forming an octahedron.

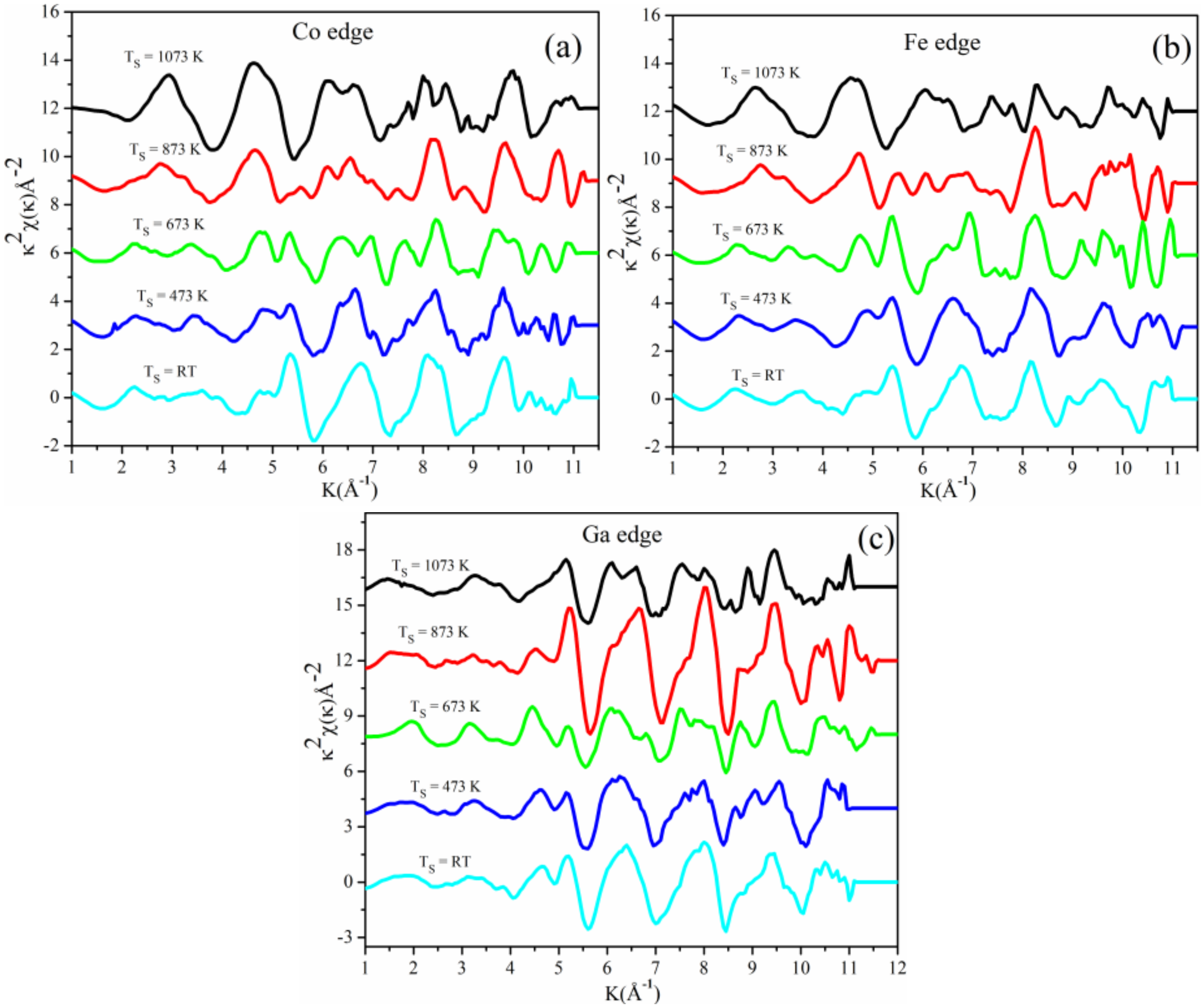

Figure- 4.8.k^2 weighted c(k) of the CFG thin film samples at (a) Co, (b) Fe and (c) Ga Kedges

The 3rd shell at 4.01 Å consists of by 12 Fe or Ga atoms from the Fe or Ga absorber. The phase uncorrected $\chi(R)$ versus R plots at all the three edges fitted with the theoretically generated model (without antisite disorder) have been shown in the figure-4.10(a)-(c). The positions of the different back scattering paths for the different absorbers have also been shown in figure-4.10.

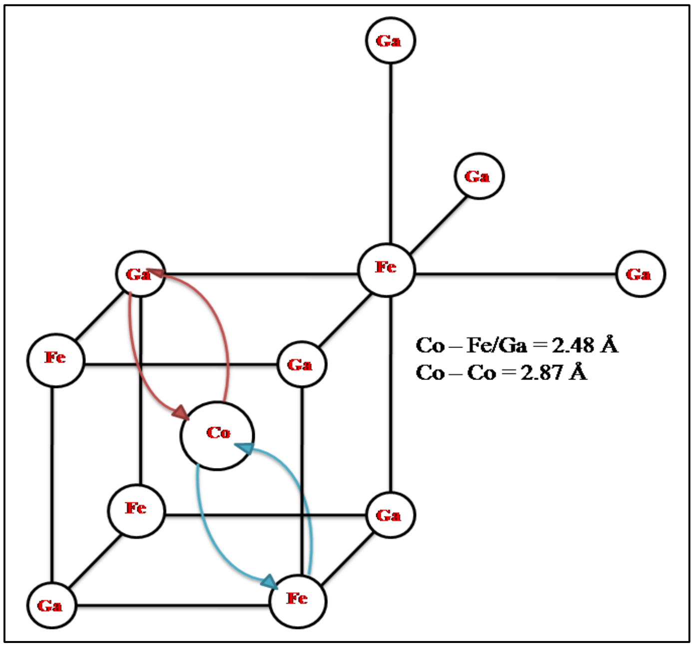

Figure- 4.9: Schematic diagram of the atomic configuration surrounding the Co, Fe and Ga atoms in the L21 structure. (The cubic shell is 1/8th of $L2_1$ structure) (Fe/Ga atoms are surrounded by 6 Ga/Fe atoms in an octahedron configuration; the arrows show the scattering paths of the 1st co-ordination shell of all the atoms).

For the case of the Co edge the 1st intense peak that appears within the R range of 1.4-2.4 Å is due to the combined effect of the 4 Fe and 4 Ga atoms as explained above, while the back scattering path from 6 Co atoms contributes to the shoulder within 2.5-2.8Å distance. Similarly, for the case of the Fe or Ga edges the 1st peak within the R range of 1.5-2.5 Å appears due to the back scattering from 8 Co atoms only and the next lesser intense peak within the R range of 2.5-2.8 Å comes due to the back scattering from 6 Ga or Fe atoms respectively. As in the 1st co-ordination of the Co atom is contributed by 4 Fe and 4 Ga atoms and for Fe or Ga atom it is contributed by 8 Co atoms the ratio of intensities of the path due to the Fe or Ga shell to that of the path due to Co coordination shell should be 1:2 regardless to the fact that Fe and the Ga atoms have different scattering factors [140]. However, in our case none of the Fe or Ga paths at the Fe or Ga edges follows this relation exactly which might be due to the structural disorders present in the thin films. The splitting in the 1st peak at the Co and Fe edges has been observed for the films deposited at 873K and 1073 K and the 1st intense peak is shifted towards lower R value by a little amount. The splitting of the 1st peak at Co edge is worth noting as the Fe and Ga atoms having different atomic scattering factors contribute to the same co-ordination shell.

To facilitate the comparison between the values of the EXAFS parameters, the results have been summarized in Table-4.1 – 4.3 for the Co, Fe and Ga K-edges respectively. The results show little difference between the bond lengths of the Co-Fe and Co-Ga pairs. Similar difference in Co-Fe and Co-Ga paths have been observed by other workers also in Co_2FeGaHesuler alloy samples due to deviation from a perfect ordered $L2_1$ structure [139]. It is to be noted that for an ideal cubic structure as the Co atom is situated at the body centre position so the Fe and the Ga atoms will be equi-distant from the Co atom forming a Co-Fe-Ga triad. An important aspect that emerges from EXAFS data analysis at Co edge is that the Co-Ga bond length is slightly shorter than the Co-Fe bond length and has lesser values of σ^2 suggesting the rigidness of the Co-Ga bond in comparison to in its counterpart. The rigidness of the bond may suggest to a stronger hybridization between the Co-Ga atoms, which is the characteristic of a half metallic alloy. This kind of hybridization between the transition metals leads to the formation of band gap near to the Fermi level, which is highly recommended for a half metallic Heusler alloy [11]. The Fe K-edge result also does not show any dramatic change in the $\chi(R)$ vs. R plot and corresponds to the result obtained from the Co edge. The result shows that Co-Fe and Fe-Co bond lengths remain almost same maintaining the perfect cubic structure though the Ga-Co bond lengths differ from the Co-Ga bond distance in the 1st co-ordination shell. This kind of observation is not expected for an ideal cubic structure and the difference in this correlation agrees with the argument that the atoms move from their crystallographic positions by little order of amplitudes [31] (see Table-4.4).

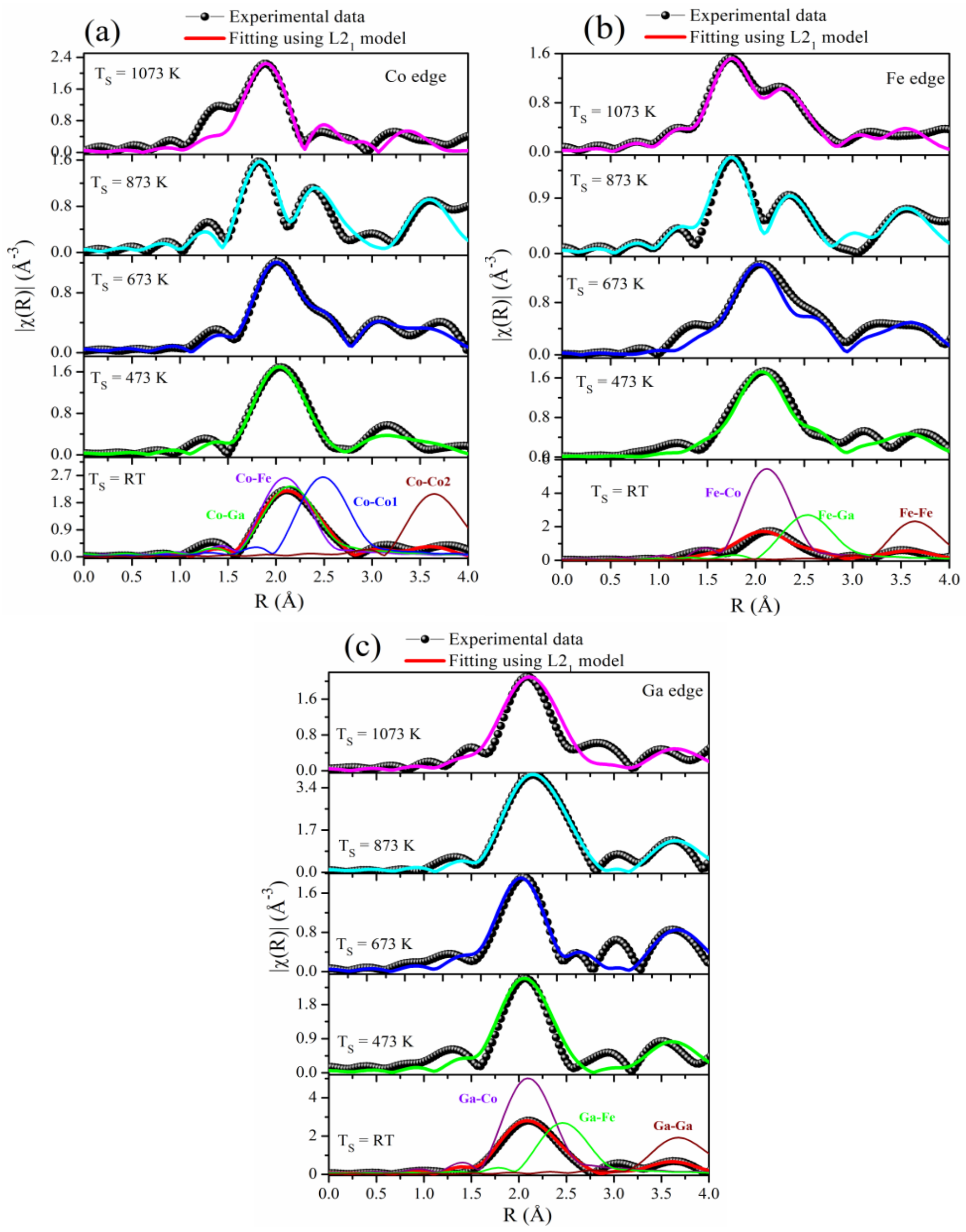

Figure- 4.10. Experimental χ(R) vs R data fitted with theoretically generated model (without antisite disorder) of the CFG thin film samples at (a) Co, (b) Fe and (c) Ga K-edges with varying the substrate temperature. (Position and contribution of the individual scattering paths have been shown with RT deposited sample).

Table-4.1: Values of structural parameters obtained from EXAFS analysis at Co K-edge considering ordered $L2_1$ phase

Scattering paths × C.N	Parameters	RT	473 K	673 K	873 K	1073 K
Co-Fe × 4	R (Å) σ^2 (Å^2)	2.46 ± 0.02 0.019 ± 0.002	2.45 ± 0.02 0.027 ± 0.004	2.47 ± 0.01 0.018 ± 0.001	2.55 ± 0.01 0.003 ± 0.001	2.53 ± 0.02 0.002 ± 0.002
Co-Ga× 4	R (Å) σ^2 (Å^2)	2.40 ± 0.01 0.005 ± 0.001	2.41 ± 0.01 0.006 ± 0.001	2.47 ± 0.01 0.007 ± 0.001	2.38 ± 0.01 0.003 ± 0.001	2.36 ± 0.01 0.004 ± 0.001
Co-Co1× 6	R (Å) σ^2 (Å^2)	2.82 ± 0.02 0.014 ± 0.002	2.77 ± 0.03 0.029 ± 0.007	2.76 ± 0.01 0.015 ± 0.001	2.72 ± 0.04 0.006 ± 0.005	2.67 ± 0.04 0.009 ± 0.010
Co-Co2× 12	R (Å) σ^2 (Å^2)	4.00 ± 0.03 0.021 ± 0.004	3.91 ± 0.02 0.021 ± 0.003	4.03 ± 0.01 0.020 ± 0.002	3.90 ± 0.01 0.018 ± 0.002	3.71 ± 0.05 0.028 ± 0.020
	R_{factor}	0.006	0.007	0.008	0.028	0.020

Table-4.2: Values of structural parameters obtained from EXAFS analysis at Fe K-edge considering ordered $L2_1$ phase

Scattering paths × C.N	Parameters	RT	473 K	673 K	873 K	1073 K
Fe-Co × 8	R (Å) σ^2 (Å^2)	2.46 ± 0.01 0.014 ± 0.001	2.46 ± 0.01 0.012 ± 0.001	2.46 ± 0.01 0.016 ± 0.001	2.38 ± 0.01 0.010 ± 0.001	2.41± 0.02 0.008 ± 0.002
Fe-Ga× 6	R (Å) σ^2 (Å^2)	2.79 ± 0.01 0.012 ± 0.001	2.76 ± 0.01 0.013 ± 0.001	2.76 ± 0.02 0.010 ± 0.002	2.60 ± 0.01 0.007 ± 0.001	2.58 ± 0.02 0.005 ± 0.002
Fe-Fe× 12	R (Å) σ^2 (Å^2)	4.02 ± 0.02 0.019 ± 0.004	4.00 ± 0.02 0.019 ± 0.004	4.00 ± 0.03 0.016 ± 0.004	4.18 ± 0.04 0.009 ± 0.004	4.18 ± 0.05 0.015 ± 0.010
	R_{factor}	0.015	0.009	0.029	0.040	0.020

Table-4.3: Values of structural parameters obtained from EXAFS analysis at Ga K-edge considering ordered $L2_1$ phase

Scattering paths × C.N	Parameters	RT	473 K	673 K	873 K	1073 K
Ga-Co × 8	R (Å) σ^2 (Å^2)	2.45 ± 0.01 0.007 ± 0.001	2.47 ± 0.01 0.008 ± 0.001	2.48 ± 0.01 0.009 ± 0.001	2.44 ± 0.01 0.005 ± 0.002	2.47 ± 0.01 0.011 ± 0.002
Ga-Fe× 6	R (Å) σ^2 (Å^2)	2.83 ± 0.02 0.015 ± 0.003	2.81 ± 0.04 0.028 ± 0.009	2.74 ± 0.03 0.015 ± 0.003	2.82 ± 0.03 0.007 ±0.004	2.91 ±0.04 0.022 ±0.007
Ga-Ga× 12	R (Å) σ^2 (Å^2)	3.97 ± 0.02 0.013 ± 0.002	3.98 ± 0.03 0.013 ± 0.003	4.04 ± 0.02 0.010 ± 0.002	4.01 ± 0.02 0.010 ± 0.002	4.14 ± 0.05 0.019 ± 0.013
	R_{factor}	0.003	0.011	0.022	0.003	0.053

The XRD results also show that in the samples there is significant presence of A2 phase along with the ordered $L2_1$ phase though XRD measurement is unable to distinguish and quantify the amount of disorder present between the Co and Fe atoms due to similar atomic scattering factors of the two elements. Next, we introduce a model which can give an idea about the amount of antisite disorder present between the atomic species and their effect to the crystal structure. In order to employ this model to our EXAFS analysis, the theoretical predictions that has been used by Takamura et.al. for explaining the anomalous X-ray diffraction study of Co_2FeSi thin films [136] based on the physical model (known as NRBB model) proposed by Niculescu et.al. [115] has been adopted. This model includes few constraint relationships between the scattering paths by introducing three disorder parameters. The disorder parameters those have been used in the model are indicated as α, β and γ, where the parameter α gives the probability of occurrence of the Fe (Ga) atoms at the Ga(Fe) site, β gives the probability of occurrence of the Co(Ga) atoms at the Ga(Co) site and the γ gives the probability of occurrence of Co(Fe) atom at Fe(Co) site. These sorts of disorders are likely to occur in case of the half as well full Heusler alloy like Co_2MnSi. [141].

In order to introduce the above antisite disorders in the EXAFS analysis of the present samples, few FEFF input paths corresponding to the 1st, 2nd and 3rd shells have been added in the ATOMS program by assigning them same bond length and Debye-Waller factorsas their proper sited paths, however by replacing only the backscattering atoms. Thus the fitting standards were parameterized by multiplication of the values of the disorder parameters with the co-ordination of the improperly sited paths at respective absorption edges. As an example, for the Co (Fe) and Co (Ga) disorder the disordered Co-Ga path is populated by $CN \times \beta$ and disordered Co-Fe path is populated by $CN\times \gamma$. On the other hand, the ordered Co-Fe path is populated with $CN\times (1-\beta)$ and the ordered Co-Ga path is populated with $CN \times (1-\gamma)$. As in the crystal structure the Co atoms are situated at X position with 2 Co atoms per atom the population of the proper Co – Co paths has been given as (CN/2) ×(1-β-γ).

Table-4.4: Definition of the atomic disorder parameters in the constituent scattering paths considering proper L2$_1$ ($Co_2Fe_1Ga_1$) structure + disorder structures

K-edge	(Ordered Co site) C.N/2×	(Ordered Fe site) C.N×	(Ordered Ga site) C.N×	(Disordered Co site) C.N×	(Disordered Fe site) C.N×	Disordered Ga site) C.N×
Co (2)	2-β-γ	1-γ	1-β	…	γ	β
Fe (1)	1-γ	1-α-γ	1-α	γ	…	α
Ga (1)	1-β	1-α	1-α-β	β	α	…

In the fitting process α, β and γ have been used as fitting parameters. It should have mentioned here that we have estimated the values of Co-Ga/Ga-Co and Co-Fe/Fe-Co and Ga-Fe/Fe-Ga disorder from the Co and Ga K-edge data and have used these values for the fitting at Fe K-edge data. Similar methodology was used for the Fe(Ga) type of disorder at the Fe K-edge. It should also be noted that the fitting of the experimental data has been done by taking the data similar to the data range mentioned for the fitting without antisite disorder discussed above to have a comparison. Similar approach has been used by Ravel et al. also for the EXAFS analysis of Co_2MnSi thin films also [141].

The phase uncorrected χ(R) versus R plot along with its real and imaginary parts for the film deposited at RT, fitted with the theoretically generated model at all the three edges have been shown in figure-4.11 (a)-(c). The fitting in both the real and imaginary parts demonstrate very good quality of fitting achieved using the above model. The values of the EXAFS best fitted parameter along with the disorder parameters have been mentioned in Tables-4.5 to 4.8. Table-4.5 shows the presence of significant amount of chemical disorder and a phase mixture of them. It also shows a negligible amount of disorder between the Fe and Ga atoms (B2 disorder) which remains below

2% though a significant amount of the A2 (Co/Fe/Ga) and DO3 (Co/Fe) disorders are present in the sample with a dominating DO3 ordering (Co/Fe disorder) (~48%). The values of the disorder parameters are found to increase gradually with the increase in substrate temperature which can be clearly correlated with the XRD results of the samples. As obtained from Tables 4.6-4.8, the distances between the various metal atom pairs follow the trend as: Co-Co’≥ Co-Fe and Fe-Fe’< Fe-Co, Co-Co’ ≥ Co-Ga and Ga-Ga’< Ga-Co, Fe-Fe’ ≥ Fe-Ga and Ga-Ga’>Ga-Fe, where the primed numbered atoms represent the atoms at the improperly sited positions. This shows that the Fe–Ga disorder does not follow the proper correlation as per their atomic radii (atomic radii of Co, Fe and Ga are 1.25Å, 1.24Å and 1.22Å respectively). So it can be said that the Fe-Ga disorder or (B2 type disorder) obtained from the above EXAFS analysis is over-estimated and may not be present in the samples significantly, which corroborates with the XRD results also as discussed above.

Table-4.5: Variation in the values of the disorder parameters

Parameters	Atomic disorder	RT	473 K	673 K	873 K
α	Fe & Ga (B2)	0.004 ± 0.010	0.011 ± 0.023	0.029 ± 0.021	0.021 ± 0.072
β	Co & Ga (A2’)	0.125 ± 0.112	0.144 ± 0.188	0.133 ± 0.142	0.149 ± 0.085
γ	Co & Fe (DO3)	0.053 ± 0.301	0.111 ± 0.351	0.284 ± 0.260	0.484 ± 0.052

Thus from figure-4.10 and 4.11 it can be noticed that using the present methodology the quality of fitting of $\chi(R)$ vs. R data improves significantly in comparison to the previous one, which is also reflected in the lower values R_{factor} in Tables-4.6 to 4.8 compared to in Tables-4.1 to 4.3 and thus the above EXAFS analysis of the Co_2FeGa thin films reveals the compositional dependent variation in the local structure which XRD measurements was unable to explain properly. The results obtained from this study also manifests that in the lattice Ga atoms are much strongly bound to the Co atoms than the Fe atoms though the structure remains otherwise cubic.

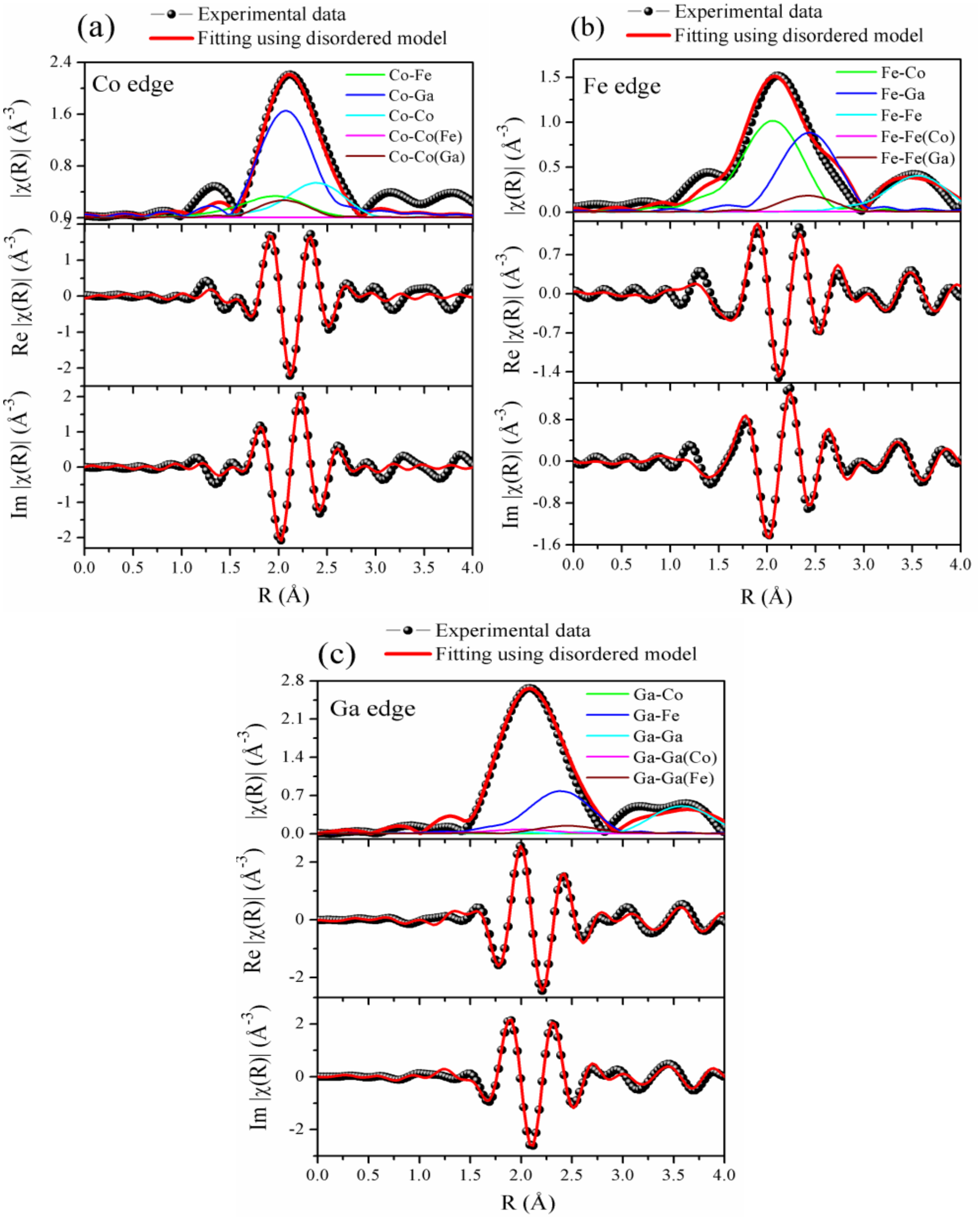

Figure- 4.11. Experimental χ(R) vs R data along with Real and Imaginary part of the CFG thin film grown at RT fitted with theoretically generated model (with antisite disorder) at (a) Co, (b) Fe and (c) Ga K-edges

Table-4.6: Values of structural parameters obtained from EXAFS analysis at Co K-edge considering disordered $L2_1$ phase

Scattering paths × C.N	Parameters	RT	473 K	673 K	873 K
Co-Fe × 4	E.C.N	3.92	3.67	2.93	2.15
	R (Å)	2.40 ± 0.02	2.52 ± 0.01	2.40 ± 0.01	2.49 ± 0.01
Co-Co’(Fe)× 4	E.C.N	0.08	0.33	1.07	1.85
	R’ (Å)	2.40 ± 0.02	2.53 ± 0.02	2.41 ± 0.03	2.49 ± 0.01
	σ^2 (Å^2)	0.005 ± 0.003	0.014 ± 0.002	0.022 ± 0.002	0.002 ± 0.001
Co-Ga × 4	E.C.N	3.59	3.54	3.44	3.48
	R (Å)	2.40 ± 0.01	2.40 ± 0.01	2.43 ± 0.01	2.31 ± 0.01
Co-Co’(Ga)× 4	E.C.N	0.41	0.46	0.56	0.52
	R’ (Å)	2.42 ± 0.02	2.41 ± 0.05	2.43 ± 0.05	2.32 ± 0.05
	σ^2 (Å^2)	0.024 ± 0.001	0.008 ± 0.001	0.007 ± 0.001	0.004 ± 0.001
Co-Co× 6	E.C.N	5.63	5.41	4.77	4.22
	R’ (Å)	2.80 ± 0.01	2.82 ± 0.04	2.68 ± 0.01	2.67 ± 0.01
	σ^2 (Å^2)	0.017 ± 0.002	0.022 ± 0.004	0.011 ± 0.001	0.003 ± 0.001
	R_{factor}	0.002	0.007	0.016	0.003

Table-4.7: Values of structural parameters obtained from EXAFS analysis at Fe K-edge considering disordered $L2_1$ phase

Scattering paths × C.N	Parameters	RT	473 K	673 K	873 K
Fe-Co × 8	E.C.N	7.79	7.33	5.85	4.28
	R (Å)	2.46 ± 0.01	2.46 ± 0.01	2.47 ± 0.01	2.43 ± 0.03
Fe-Fe’(Co) × 8	E.C.N	0.21	0.67	2.15	3.72
	R’ (Å)	2.46 ± 0.02	2.42 ± 0.04	2.44 ± 0.02	2.44 ± 0.01
	σ^2 (Å^2)	0.016 ± 0.001	0.012 ± 0.001	0.016 ± 0.001	0.012 ± 0.002
Fe-Ga× 6	E.C.N	6.00	5.94	5.83	5.87
	R (Å)	2.79 ± 0.01	2.73± 0.02	2.76 ± 0.01	2.65 ± 0.02
Fe-Fe’(Ga) × 8	E.C.N	0.00	0.06	0.17	0.12
	R’ (Å)	2.76 ± 0.02	2.74± 0.05	2.77 ± 0.05	2.67 ± 0.05
	σ^2 (Å^2)	0.012 ± 0.001	0.014 ± 0.001	0.011 ± 0.001	0.007 ± 0.002
Fe-Fe× 12	E.C.N	11.68	10.87	8.44	6.17
	R’ (Å)	4.01 ± 0.03	3.98 ± 0.02	3.98 ± 0.02	3.86 ± 0.04
	σ^2 (Å^2)	0.017 ± 0.003	0.018 ± 0.003	0.013 ± 0.002	0.004 ± 0.002
	R_{factor}	0.012	0.006	0.019	0.030

Table-4.8: Values of structural parameters obtained from EXAFS analysis at Ga K-edge considering disordered $L2_1$ phase

Scattering paths × C.N	Parameters	RT	473 K	673 K	873 K
(c)Ga-Co × 8	E.C.N	7.16	7.11	6.98	7.01
	R (Å)	2.45 ± 0.01	2.47 ± 0.01	2.48 ± 0.01	2.43 ± 0.01
(a)Ga-Ga’(Co) × 8	E.C.N	0.84	0.88	1.01	0.99
	R’ (Å)	2.41 ± 0.03	2.41 ± 0.04	2.44 ± 0.04	2.43 ± 0.01
	σ^2 (Å^2)	0.008 ± 0.001	0.010 0.001	0.009 ± 0.001	0.007 ± 0.001
(d)Ga-Fe× 8	E.C.N	6.00	5.94	5.82	5.87
	R (Å)	2.82 ± 0.01	2.84 ± 0.05	2.74 ± 0.02	2.81 ± 0.02
(b)Ga-Ga’(Fe) × 8	E.C.N	0.00	0.06	0.18	0.13
	R’ (Å)	2.82 ± 0.01	2.85 ± 0.06	2.95 ± 0.05	2.83 ± 0.01
	σ^2 (Å^2)	0.015 ± 0.003	0.029 ± 0.008	0.014 ± 0.004	0.007 ± 0.002
(e)Ga-Ga× 12	E.C.N	10.74	10.54	10.13	10.25
	R’ (Å)	3.96 ± 0.02	4.00 ± 0.02	4.04 ± 0.01	4.00 ± 0.02
	σ^2 (Å^2)	0.013 ± 0.002	0.012 ± 0.022	0.008 ± 0.002	0.008 ± 0.002
	R_{factor}	0.002	0.007	0.015	0.002

* ECN= Effective Co-ordination Number = C.N × disorder factor

4.3.8 Magnetic Characterizations:

To characterize the magnetic behavior of the PLD grown CFG/Si films, the externally applied magnetic field dependent in-plane magnetization M (H) have been carried out at three different temperatures of 5K, 300K and 350K with varying the magnetic field upto 9T. The magnetization curves of the films with different substrate temperatures and measured at the above three temperatures have been depicted in figure-4.12 (a)–(c). The diamagnetic contribution of the c-Si substrate has been subtracted from the magnetization of the films prior to the calculations. Fig. 13 shows a good correspondence of the magnetization property with the crystallinity of the film which decreases gradually with an increase in the substrate temperature. All the samples show soft ferromagnetic nature with a very small amount of coercive field (Hc) and started to saturate at low magnetic field. The saturation magnetization value of the films has been calculated by linearly fitting the M vs H curve at very high magnetic field and then extrapolating the line towards the

H=0 line or the intercept of the straight line. The values of the various magnetization parameters i.e., saturation magnetization (M_S), coercive field (H_C), remnant magnetization (M_R) and the squareness of the curve which is the ratio between the remnant magnetization to the saturation magnetization (M_R /M_s) have been depicted in figure-4.13 (a)-(d).No significant variations between the values of the parameters have been observed at temperatures of 300 K and 350 K with increase in the substrate temperature which may be due to high Curie temperature of the films compared to the temperature of measurement. The result shows that the films deposited at RT and 473 K have very small amount of H_C (~2.5 mT or 25 Oe) and high $M_R$in comparison to the others suggesting soft ferromagnetic behavior of these films. The coercive field increases for the film deposited at 673 K, however, it again decreases drastically as the substrate temperature is increased further. The decrease in Hc with increasing substrate temperature for a magnetic thin film has been observed by other workers also for PLD deposited Co_2FeSi films [142]. The highest value of H_C for T_S = 673K sample may be due to a change in the magnetic anisotropy [62].

It is quite observable from the XRD and EXAFS studies that the structural properties of the films deposited at 873K and 1073K are similar and are significantly different from the films deposited at relatively lower substrate temperatures. The sudden decrease in the value of H_C for these films is thus attributed to the presence of relatively higher structural disorder in the films with a decrease in their crystallite sizes. The $M(H)$ curves of these films at very low field region and at 300K and 350K show lesser ferromagnetic behavior with negligible amounts of M_R which is a characteristic of paramagnetic ordering. The film deposited at RT and 473K have higher squareness value (~70%) indicating lesser defect films, and the films with elevated T_S the squareness ratio suddenly falls to 40-50% possibly due to higher defect in the films. Galanakis et.al. have shown by ab-initio calculations that electronic and magnetic properties of these compounds are intrinsically co-related with their minority spin density of states [11]. It has also been explained that according to the Slater-Pauling rule, the total spin magnetic moment (M_t) of the Co_2FeGa full Heusler alloy is defined by the relation $M_t = Z_t - 24$, where Z_t is the number of valance electrons. The compounds containing Al and Ga have total spin magnetic moment ~ 4μ_B from Slater-Pauling rule.

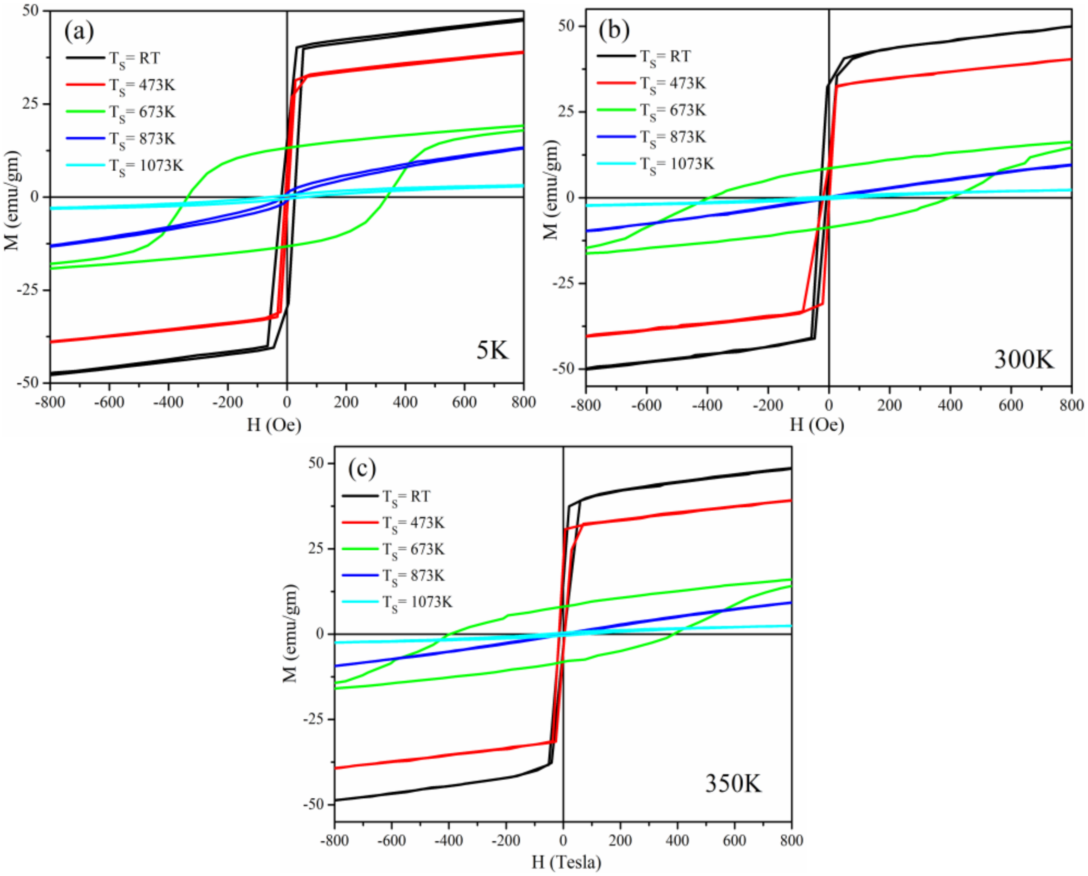

Figure- 4.12: Variation in the parallel magnetization (M(H) vs H) curves of the samples at three temperatures with varying the substrate temperature.

Experimentally it has been observed for CFG films that the maximum value of the saturation magnetization (M_s) ~ 2.68μ_B/f.u for the RT grown film, which is much smaller than the value obtained experimentally by Umetsu [143] et.al. (~5.2 μ_B/f.u) and Galanakis et.al (~4.89μ_B/f.u) for bulk polycrystalline samples [144]. With an increase in the substrate temperature it decreases to ~2.19 μ_B/f.u for the film grown at 473K and suddenly falls in the following samples. The decrease in the value of M_s with increasing substrate temperatures suggests the reduced magnetic moment due to the presence of some structural disorder or the intrinsic chemical inhomogenity in the film [33]. Umetsu et.al. have also explained the reason of decrease of M_S from the electronic structure [143].

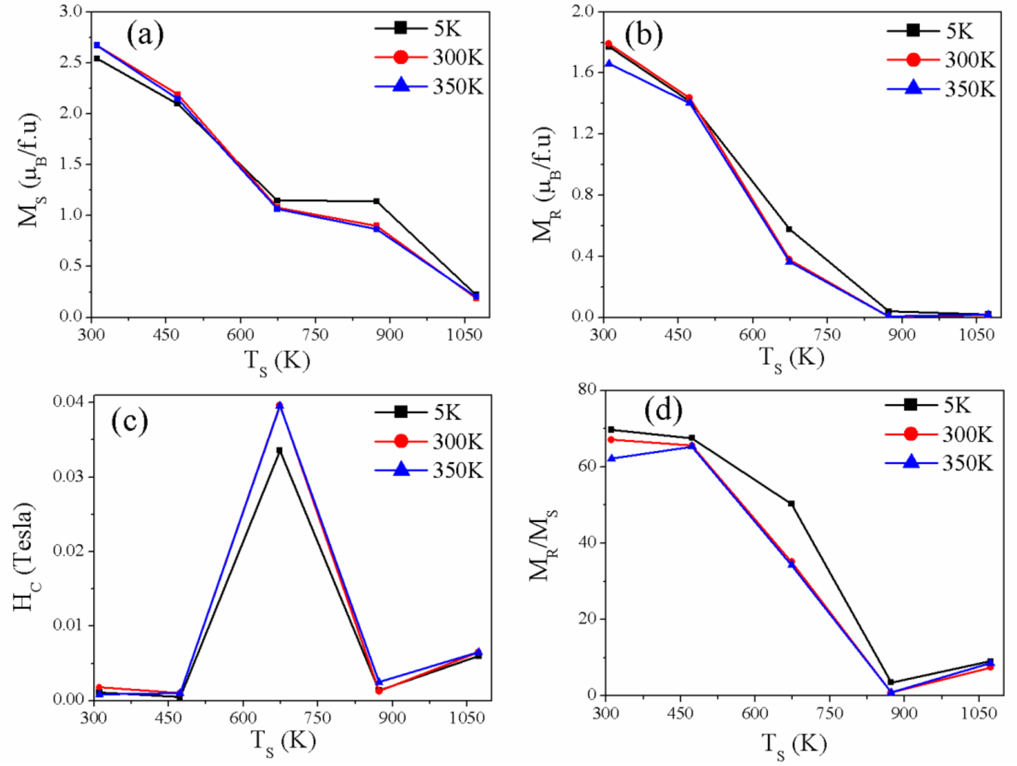

Figure-4.13. Summary of the value of the magnetization parameters as (a) saturation magnetization, (b) remnant magnetization, (c) coercive field and (d) sureness of the hysteresis curves of the samples with varying the substrate temperature.

Significant presence of Stoner excitation in the RT and473 K grown samples can also play a responsible role for the suppressionin the value of the Ms from their theoretically predictedvalue [142]. EXAFS results show that in the film there is a presence ofatomic disorder between the constituent atoms giving rise to A2 orDO3 kind of structure along with very negligible amount of B2. Yadav et al. have mentioned that the B2 structure does not affectmuch to the suppression of the Ms, but the presence of A2 typedisorder is very much able to diminish the value of saturationmagnetization by decreasing the spin magnetic moment of Featoms [145,33]. The highly diminished value of Ms for the filmdeposited at the highest substrate temperature deposited may alsobe due to the formation of a silicide layer as observed from theEDXS study. Thus our magnetization study corroborates with theobservation made from the structural characterizations.

In order to understand the magnetic behavior of the metallic alloy thin films with temperature, the temperature dependent magnetization $M(T)$ study has been carried out over the temperature range of 5-350 K in a constant external magnetic field parallel to the surface of the film (Figure-4.14 (a) – (d)). Here the external field was selected such that the $M(H)$ curve at a constant temperature saturates. The $M(T)$ data has been collected in the Zero Field Cooled (ZFC) and Field Cooled Cooling (FCC) mode. The process of the ZFC and FCC mode has been explained in the earlier chapter. In the samples no bifurcation between the ZFC and FCC curves has been observed at the applied magnetic field even at very low temperature (not shown in the figure), suggesting the reversibility of the magnetization due to the orientation of the magnetic dipoles. The $M(T)$ curves of the films deposited at RT and 473 K show good quality data with the variation of temperature. The films grown at RT and 473K, magnetization varies as $T^{3/2}$ below 280 K and as T^2 beyond 310 K as shown in the inset to the figure-4.14 (a) and (b), however magnetization of the other samples deviates from these relations. The magnetization value follows the spin wave theory with the Bloch's theorem $M(T) = M(0)[1-AT^{3/2}]$ [142], where $M(0)$ be the spontaneous saturation magnetization at 0 K. Linearly fitting the $M(T)$ vs $T^{3/2}$data for the films grown at RT and 473K with the above mentioned relation yield the best fit values of $M(0)$ = 2.70 μ_B/f.u and 2.35 μ_B/f.u respectively which is closer to the value of saturation magnetization (M_s) mentioned before. The value of the spin stiffness co-efficient (D) was estimated from the spin wave dispersion law $\hbar\omega = Dq^2$, where the value of D can be calculated from the slope of the curve A via relation $A = 2.612V_0S^{-1} \times (k_B/4\pi D)^{3/2}$, where V_0 be the volume per magnetic atom and S be the average spin per atom and

k_B is the well-known Boltzmann constant. The calculated value of the slope A were obtained as 5.458×10^{-6} $K^{-3/2}$and 6.8122×10^{-6} $K^{-3/2}$ which gives rise to the value of D as 130 meVÅ^2 and 113 meVÅ^2 for the films grown at RT and 473K respectively, which are lesser than the values obtained from Co_2FeSi alloy [126].

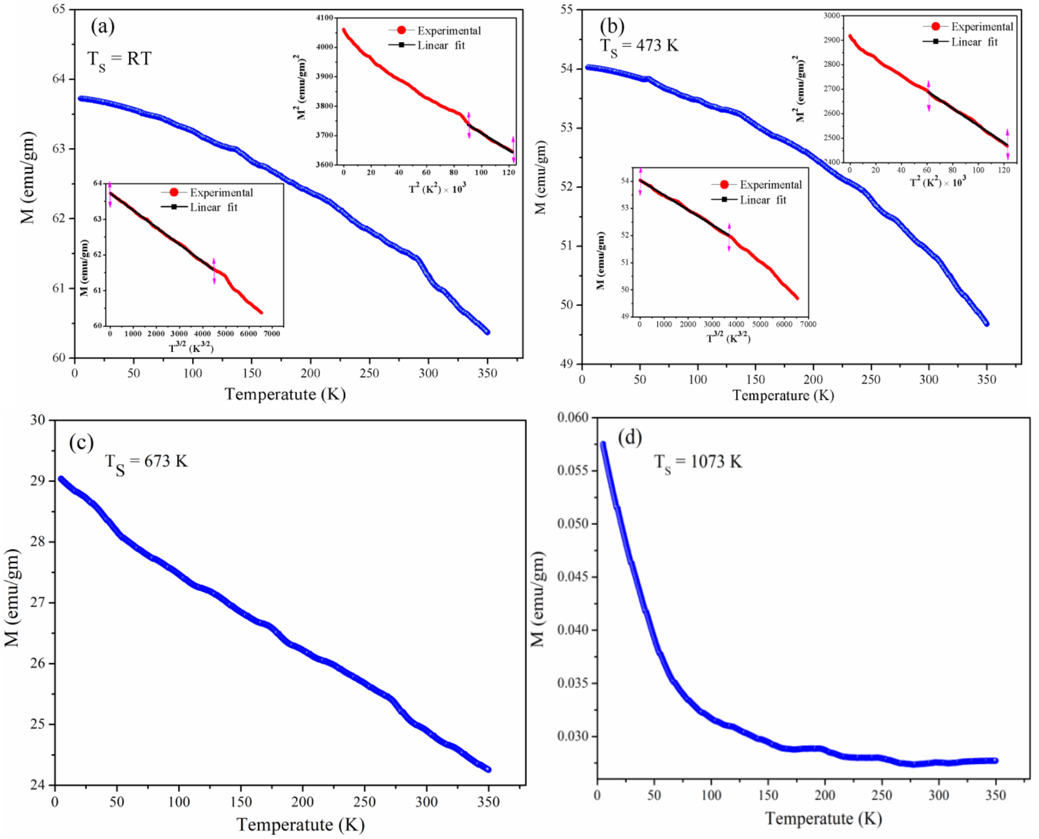

Figure-4.14: Thermo magnetization (M vs T) curves of the samples with varying the substrate temperatures. (Inset to the Fig. 15 (a) and (b) show $T^{3/2}$ and T^2 dependence).

As has been mentioned earlier, beyond 300K the temperature dependence of magnetization changes from a $T^{3/2}$ type to a T^2 type variation (Stoner excitation). The shifting of $M(T)$ vs. T relationship to a quadratic type with temperature has also been observed by other workers for the case of thin film [66] and single crystals [146] due to a moment ordering phase transition manifested by a hump around 300K in the $M(T)$ curve. The typical variation is attributed to the change in the nature of ferromagnetism from localized to itinerant-like ferromagnetism [146].

4.4 Conclusions:

This chapter presents detail structural and magnetic characterization of the PLD grown Co_2FeGa thin films on c-Si substrates deposited at five different substrate temperatures of RT, 473K, 673K, 873K and 1073K. The structural chracterizations by XRD study shows that due to the presence of (111) reflection with (220) reflection, $L2_1$ appears to be the dominating phase in the thin film samples, whose fraction decreases with increase in substrate temperature, manifesting significant increase of disorder in the samples. The interesting observations were made from the EXAFS study, where the antisite disorder parameters were defined using Webster model and it was observed that there is a presence of significant amount Co/Fe and Co/Ga disorder in the samples. By increasing the susbtate temperature the Co/Ga disorder remans almost constant, however the Co/Fe antisite disorder increases gradually. From the EXAFS study a stronger Co-Ga bond or p-d hybridization was also observed which distorted the local symmetry around the Co atoms. Finally, magnetization results show soft ferromagnetic nature of the films with a saturation value of magnetization less than the theoretically expected value which may be due to the presence of antisite atomic disorder in the films. The M-T curves shows that at the lower substrate temperature the samples follow the proper ferromagnetic ordering and the themal demagnetization happens due to the excitation of spin waves upto the room therperature above which Stoner excitation contributes.

Chapter-5

EFFECT OF GROWTH TEMPERATURE ON THE STRUCTURAL AND MAGNETIC PROPERTIES OF THE PULSED LASER DEPOSITED Co_2FeAl THIN FILMS

1.1 Introduction:

In this chapter we have discussed the resuls obtained on Co_2FeAl (CFA) thin films and as the previously discussed samples, in this case also the samples have been prepared by PLD technique to achieveproper stoichiometry and structural ordering in the samples. The main objective of our present work is to study the effect of growth temperature on the structural and magnetic properties of the PLD deposited CFA films and to find the correlation between them. The combined approach of structural tools of Grazing Incidence X-ray diffraction (GIXRD) and Extended X-ray Absorption Fine Structure (EXAFS) has been used to provide a better understanding about the improvement in the crystal structure and the local environment and the nature of bonding between the constituent atoms. The above information has been utilized to explain the nature of magnetic interaction in the films and the contribution of spin waves in the thermal demagnetization and their variation with substrate temperatures has also been discussed.

1.2 Results and Discussions:

1.2.1 Grazing Incidence X-ray Diffraction (GIXRD):

For the investigation of long range structural ordering of the bulk target and CFA thin films, the X-ray diffraction study has been carried out using laboratory based Cu K_α source, as shown in the figure-5.1 (a). Presence of different atomic orderings in a cubic CFA alloy is well known which takes place due to the exchange or the intermixing of the constituent elements. The XRD pattern of the target shows the presence of the (220), (400) and (422) peaks, which follows the law of reflection $h+k+l = 4n$ (n be the positive integer) along with very smaller intense (200) and (420) peaks which follow the relation $h+k+l = 4n+2$. Among these peaks the (220) reflection is known as the fundamental peak which is independent of the atomic ordering. A fully ordered $L2_1$ phase is identified by the presence of the super lattice reflections (111) and (200) along with the fundamental (220) peak. However smaller intensities of (200) and (420) peaks for the bulk target may indicate the presence of the B2 structure due to the atomic disorder between Fe (Y) and Al (Z) atoms, whereas the absence of the (111) and (200) peaks confirms the absence of fully ordered $L2_1$ [126] phase.

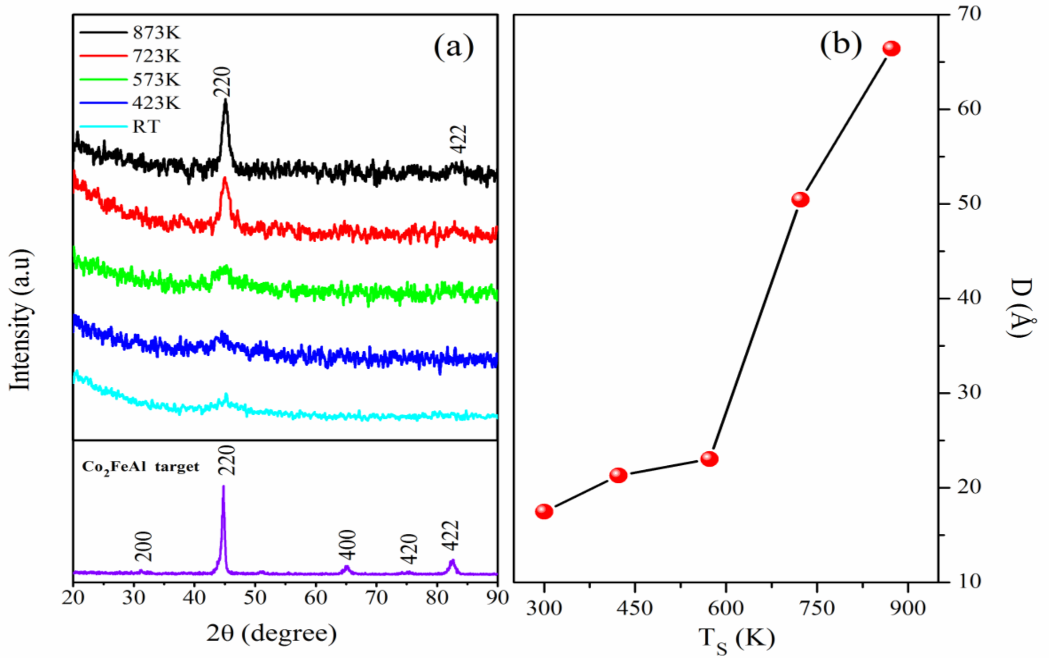

Figure-5.1: (a) GIXRD pattern of the Co_2FeAl thin films deposited at various substrate temperatures along with the XRD pattern of the bulk target. (b) Variation in the crystallite size as a function of substrate temperature.

Though the occurrence of A2 (DO_3) phase is also possible due to the disorder between Fe and Co atoms, it is undetectable from the XRD study due to the similar X-ray scattering factors of both the Co and Fe atoms. A precise evaluation of different kinds of chemical disorder present in the samples is very much difficult to estimate due to the absence and rather low intensity of the diffracted peaks. The room temperature GIXRD pattern of the films show the presence of only fundamental (220) peak, and the intensity of this peak is low for the films deposited upto 573K suggesting lesser crystallinity of the film. Though because of a noisy data few important peaks could not be identified, though a smaller intense peak around 2θ value of 82° corresponding to (422) reflection can be found similar to the target material. For all the above reflections, h, k, l values follow the relation $h+k+l = 4n$ and we consider the structure to be a slightly disordered $L2_1$phase. On this basis we concentrate our investigation only on the variation of the fundamental peak. This shows that with increase in the substrate temperature the intensity of the peak increases significantly and the FWHM of the peak decreases and reaches a maximum value for the film grown at 873K. Thus the observed variation in the peak intensity and the width of the diffraction peak strongly reveals an improvement in the crystallinity of the film with the growth temperature. Correspondingly the lateral crystallite size (D) was estimated using the (220) reflection using the well-known Debye- Scherrer formula $D=\frac{0.9\lambda}{\beta Cos\theta}$, where β is the FWHM of the peak, λ is the wavelength of the X-ray and θ is the position of the peak. The result shows a linear increase of the crystallite size upto 23Å for the film with T_S= 573K, however subsequently the crystallite size increases rapidly to 72 Å as shown in the figure-5.1(b). It can be suggested that with the increase in the substrate temperature the diffused ad atoms form an island type growth on the substrate which increases the crystallite size.

1.2.2 Grazing Incidence X-ray Reflectivity (GIXR):

The values of the density, thickness and roughness of the CFA films were estimated from specular grazing incidence X-ray reflectivity study using a diffractometer by varying the 2θ angle from 0 to 5°. In order to obtain the values of the parameters the experimentally obtained data were fitted with a theoretically generated model using the IMD software as described in Chapter-2. No distinct Kissig fringes have been observed except for the film deposited at RT and the data become little noisy at higher substrate temperature due to the higher roughness of the films. During the fitting process the thickness, density and the surface roughness of the CFA layer were varied independently. The result shows good quality of fitting by considering an approximate thickness near to 1000 Å of the CFA structure. This thickness was estimated from the knowledge of rate of deposition which was earlier obtained by depositing few films with lower thickness at known deposition times and estimating their thickness by GIXR measurements. The experimental data fitted with the theoretical model has been shown in the figure-5.2(a) and the variations in the best fit parameters have been summarized in the figure-5.2 (b) – (d).

The result confirms that except for the film deposited at RT, thickness and the density of the films remain almost unchanged throughout the series, though the surface roughness shows significant increment in the value at highest substrate temperature. The density of the film obtained from the fitting process (~6.5 g cm^{-3}) nearly matches with the results reported by other workers [26]. It may be noted that for the sample grown at RT the density and the thickness are lower compared to the samples grown at higher temperature which might be due to low sticking coefficient and less mobility of the ad atoms at lower substrate temperature.

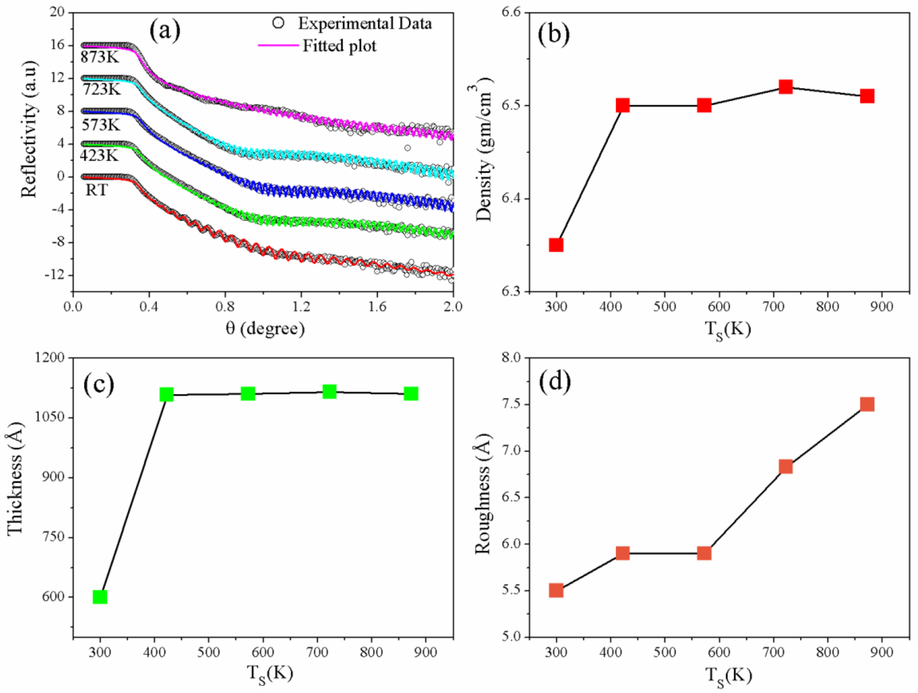

Figure-5.2: (a) Experimental Grazing Incidence X-ray Reflectivity (GIXR) data of the films fitted with the theoretical model, (b) - (d) variation of density, thickness and surface roughness respectively as a function of substrate temperature

1.2.3 Field Emission Scanning Electron Microscopy (FESEM):

The back scattering electron image from the CFA film grown at different substrate temperatures have been depicted in figure-5.3.

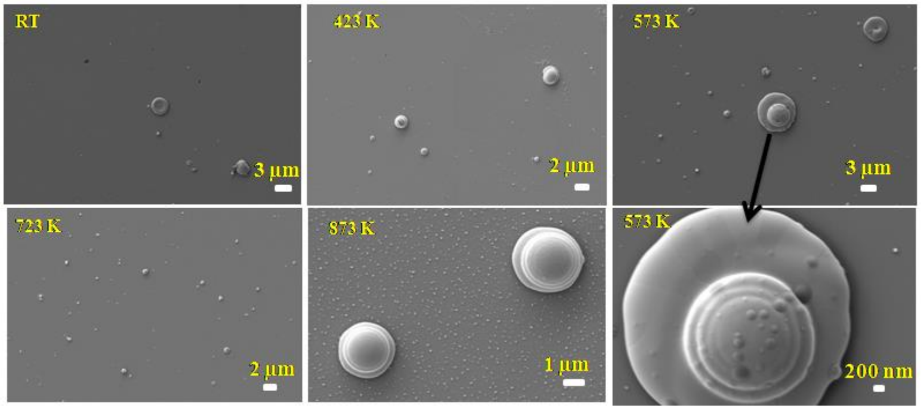

Figure-5.3. FESEM back scattering electron image of the CFA films deposited at various substrate temperatures.

1.2.4 Energy Dispersive X-ray Spectroscopy (EDXS):

The variation in the elemental composition of the films, as shown in the figure-5.4, was estimated by averaging the compositions taken over several droplets which shows an improvement in the elemental stoichiometry with increase in the substrate temperature up to a certain value. Initially the films grown at RT and 423K deviate from their proper stoichiometric ratio (2:1:1) with an excess of Co and deficiency in Fe, though concentration of Al remains same for all these samples. Later with an increase in the substrate temperature above 423K the films become more stoichiometric.

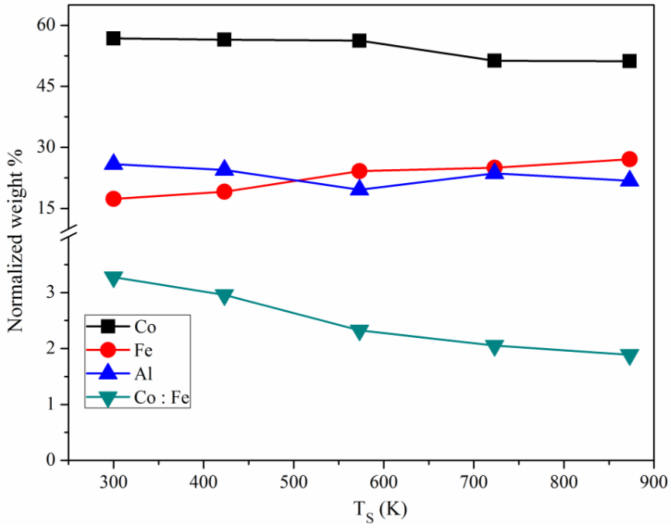

Figure-5.4. Variation in the elemental compositions of the CFA films as a function of substrate temperature.

1.2.5 X-ray Absorption Spectroscopy (XAS):

X-ray absorption spectroscopy (comprises of XANES and EXAFS) measurements have been carried at both Co and Fe K-edges on the CFA thin films grown at different substrate temperatures. Figure-5.5(a) and (b) show the normalized XANES spectra ($\mu(E)$ vs.E) at the Co and Fe K-edges of the CFA films. The absorption spectra of the samples show that the positions of absorption edges at both the Co and Fe K-edges exactly match with their corresponding metallic foils and remain constant throughout the series, suggesting that pure metallic phase (0 oxidation states) of the elements are present in the samples and increase in substrate temperature does not create any oxide phase in the materials. In the absorption spectra at both the edges the broader peak above ~110 eV of the absorption edges splits into two distinct peaks, where the strong crest (peak A) appears above 118 eV of the absorption edge. In order to have a detail understanding about the local structural information around the constituent species, the experimentally obtained data have been processed as mentioned bellow. The k^2 weighted $\chi(k)$ spectra at Co and Fe edges have been shown in the figure-5.6(a) and 5.7(a) respectively. In comparison to the f.c.c metal, the presence of the crest and the oscillations in the k^2 weighted $\chi(k)$ spectra demonstrate a higher crystallinity and a characteristics of cubic environment around the Co and Fe atoms [136]. Similar to the XANES spectra the films grown at 723K and 873K show oscillations with higher amplitude than other films due to improved crystallinity observed from the X-ray diffraction study.

We have employed a standard $L2_1$ structural model as input in the ATOMS subroutine [139] in order to generate the theoretical FT-EXAFS spectra. The value of the lattice parameter (5.639Å) and space group (*Fm-3m*) were taken from the literatures [147]. In this structure the Co (X) atom is situated at the body center position *4c* (¼, ¼, ¼), while the Fe (Y) and the Al (Z) atoms occupy the identical lattice position with respect to Co atom at *4a* (0,0,0) and *4b* (½, ½, ½). Finally, the theoretical and experimental $\chi(R)$ vs. R plots were fitted using ARTEMIS subroutine available within the IFEFFIT software package [148] where the atom to atom bond distance (R) and the Debye Waller factor (σ^2) which give the mean square fluctuation in the atomic bond distance were defined as the fitting parameters keeping the corresponding co-ordination number (C.N) fixed to their proper crystallographic values.

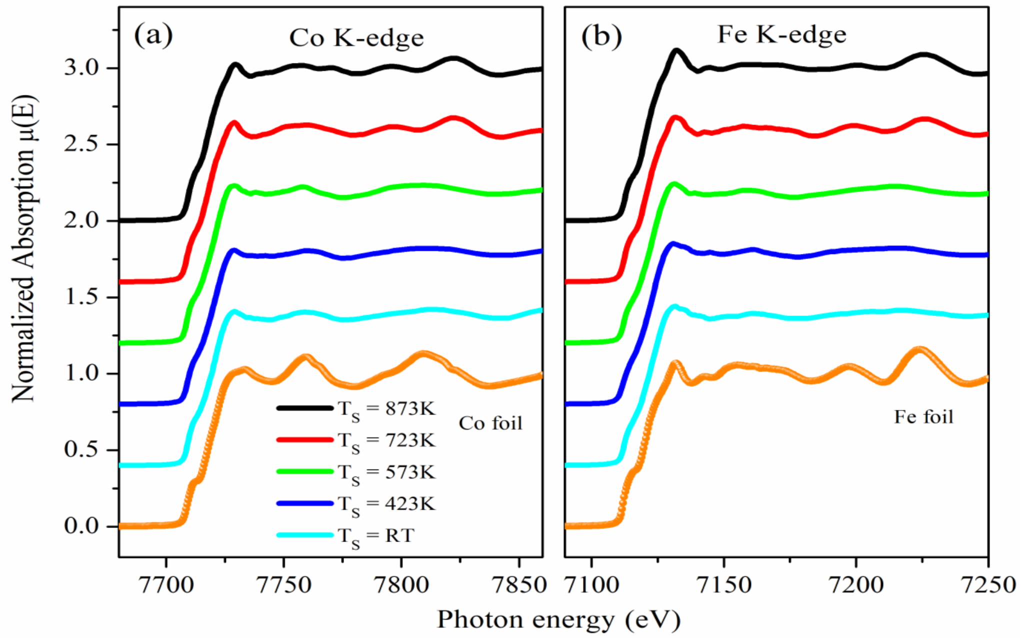

Figure-5.5: Normalized EXAFS spectra of the Co_2FeAl alloy films deposited at different substrate temperature (T_S) and measured at (a) Co K-edge, (b) Fe K- edge.

It should be mentioned here that the constraint relation considering isotropic expansion or contraction of the atomic bond distances used by Sathe et al. [111] for a bulk cubic system, could not be employed for our thin film system. In fact, it was observed that our theoretical model agrees well with the experimental data when the parameters were varied without defining them any constraint relationship. Thus with the above mentioned exercises, the experimentally obtained data was fitted over the k range 2.5 – 12.5 $Å^{-1}$ in the k^2 weighted $\chi(k)$ spectra and within the R range 1.2 – 4.1 Å in the $\chi(R)$ spectra. The fitting of the theoretical data with the experimentally obtained data have been shown in figure-5.6 (b) and 5.7(b).

In the above structure Co atoms, being situated at the body center position is coordinated by 4 Fe and 4 Al atoms at a distance of 2.44Å, which strongly contribute to the 1st intense peak that appears within the *R* range of 1.5 – 2.5 Å. Along with this the second nearest neighbor shell of 6 Co atoms also contribute to the shoulder to this peak at 2.82 Å and contribution of the next shell comprising of 12 Co atoms appear at a larger distance of 3.99Å from the absorbing Co atom. In the similar way at Fe K-edge as the symmetry changes the 1st intense peak is mainly contributed by the nearby 8 Co atoms and the contribution of the next shell of 6 Al atoms appears later. The next shell of 12 Fe atoms contributed to the peak appearing at a distance of 3.99Å.

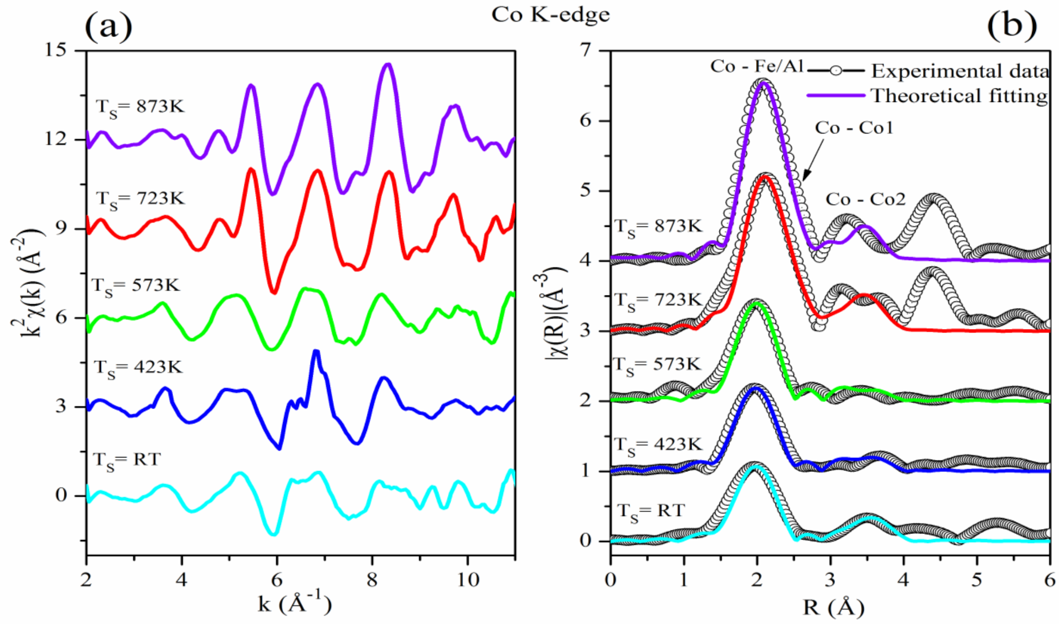

Figure-5.6: (a) k^2 weighted $\chi(k)$ spectra and (b) experimentally obtained FT-EXAFS ($\chi(R)$ vs R) plots of the films fitted with theoretically generated model at Co K-edge.

As the Fe atoms in the 1st co-ordination shell is surrounded by the 8 Co atoms, the intensity of the 1st peak is higher than the 1st peak of the Co K-edge where the 1st co-ordination shell is co-ordinated with two atoms Fe and Al having a larger contrast in their atomic number. The values of the best fit parameters obtained by EXAFS fitting have been summarized in Table-5.1 and 5.2 and the variation in the atomic bond lengthshas been depicted in figure-5.8 for the Co and Fe edges respectively.

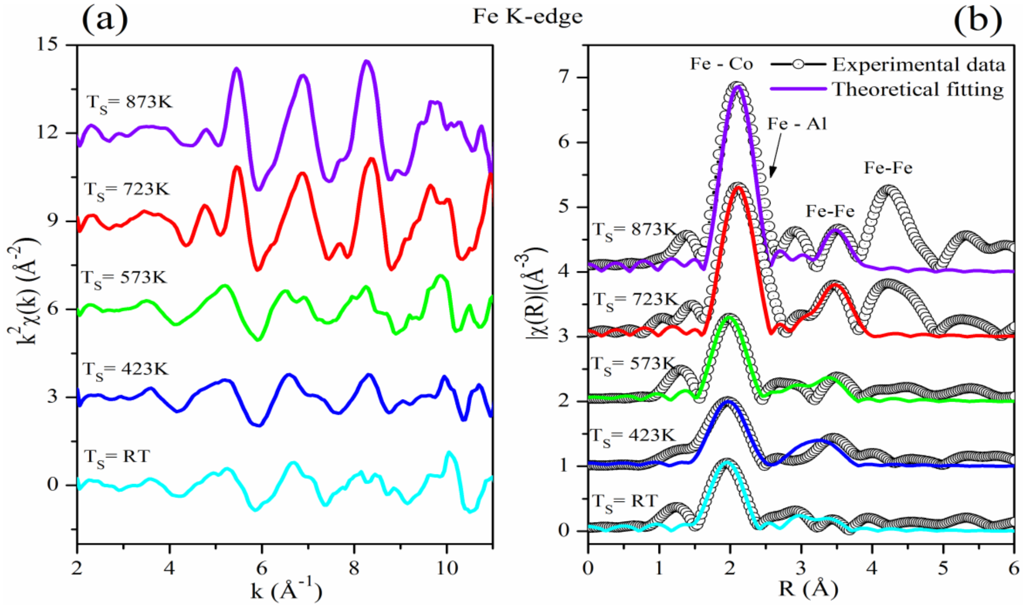

Figure-5.7: (a) k^2 weighted $\chi(k)$ spectra and (b) experimentally obtained FT-EXAFS ($\chi(R)$ vs R) plot of the films fitted with theoretically generated model at Fe K-edge.

The interesting aspect that emerges from the 1st shell fitting that the Co – Fe bond length (2.39Å) is much shorter than the Co – Al bond length (2.57Å) with a lesser value of σ^2, though the bonds are supposed to be equal forming a Fe-Co-Al triad. This may suggest the rigidness of the Co – Fe bond in comparison to the Co – Al bond or the possibility of stronger Co (*3d*) and Fe (*3d*) hybridization, which does not get affected with the growth temperature. This *d-d* hybridization between the transition metal elements is a characteristic of the half metallic Heusler alloy [31]. Moreover, a lesser value of σ^2 for the Fe scattering path than Al scattering path also suggests that Fe atoms are much ordered around the Co atom and have smaller amplitude of displacement. The value of the EXAFS parameters at the Fe K-edge corroborate with the results obtained at Co K-edge as the Co – Fe and Fe – Co bonds remains same, maintaining a perfect cubic environment. A stronger *d-d* hybridization has been reported by other workers for the case of Co based Heusler alloy also [149].

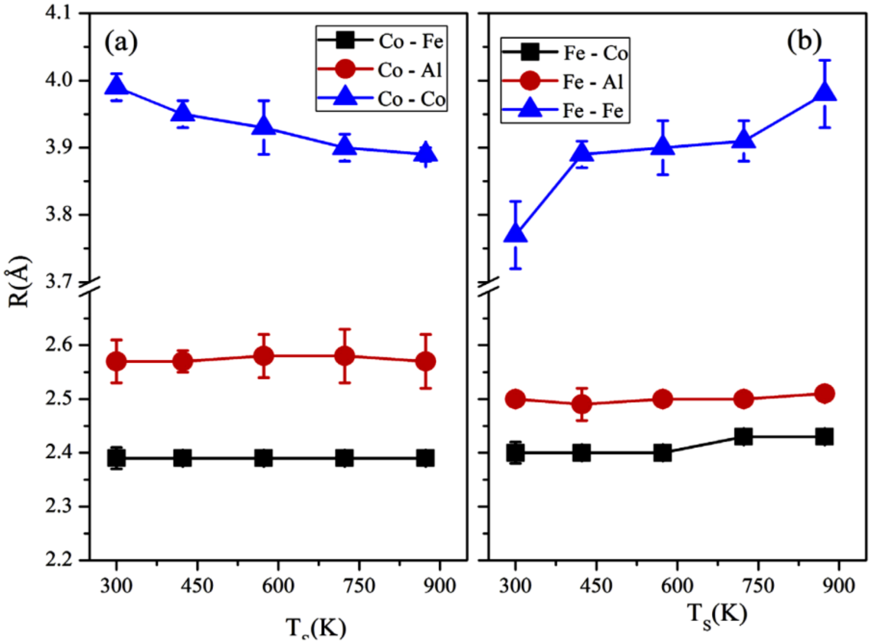

Figure-5.8: Substrate temperature dependence of the atomic bond lengths of the various coordination shells obtained from the best fit EXAFS data at (a) Co and (b) Fe K-edges.

Table-5.1: Values of structural parameters i.e bond lengths (R), Debye Waller factor (σ^2) obtained from EXAFS data analysis at Co K-edge.

Scattering Paths × C.N	Parameters	RT	423 K	573 K	723 K	873 K
Co – Fe × 4	R (Å) σ^2 (Å^2)	2.39 ± 0.02 0.010 ± 0.001	2.39 ± 0.003 0.008 ± 0.001	2.40 ± 0.01 0.009 ± 0.001	2.40 ± 0.01 0.007 ± 0.001	2.40 ± 0.01 0.005 ± 0.001
Co – Al × 4	R (Å) σ^2 (Å^2)	2.57 ± 0.04 0.028 ± 0.008	2.57 ± 0.02 0.026 ± 0.004	2.56 ± 0.04 0.028 ± 0.008	2.58± 0.06 0.028 ± 0.013	2.57 ± 0.05 0.029 ± 0.008
Co – Co1 × 6	R (Å) σ^2 (Å^2)	2.59 ± 0.03 0.028 ± 0.004	2.58 ± 0.02 0.028 ± 0.003	2.56 ± 0.02 0.028 ± 0.003	2.77 ± 0.01 0.011 ± 0.002	2.76 ± 0.01 0.013 ± 0.002
Co – Co2 × 12	R (Å) σ^2 (Å^2)	3.99 ± 0.02 0.021 ± 0.003	3.95 ± 0.02 0.028 ± 0.006	3.93 ± 0.04 0.030 ± 0.010	3.90 ± 0.02 0.017 ± 0.003	3.89 ± 0.01 0.018 ± 0.004

Table-5.2: Values of structural parameters i.e bond lengths (R), Debye Waller factor (σ^2) obtained from EXAFS data analysis at Fe K-edge.

Scattering Paths × C.N	Parameters	RT	423 K	573 K	723 K	T873 K
Fe – Co × 8	R (Å)	2.40 ± 0.02	2.40 ± 0.01	2.40 ± 0.01	2.43 ± 0.01	2.43 ± 0.01
	σ^2 (Å^2)	0.011 ± 0.001	0.015 ± 0.002	0.010 ± 0.001	0.006 ± 0.001	0.004 ± 0.001
Fe – Al × 6	R (Å)	2.50 ± 0.01	2.49 ± 0.03	2.50 ± 0.01	2.51 ± 0.01	2.51 ± 0.01
	σ^2 (Å^2)	0.004 ± 0.001	0.024 ± 0.010	0.004 ± 0.001	0.008 ± 0.002	0.003 ± 0.001
Fe – Fe × 12	R (Å)	3.77 ± 0.05	3.89 ± 0.02	3.90 ± 0.04	3.91 ± 0.03	3.98 ± 0.05
	σ^2 (Å^2)	0.029 ± 0.020	0.020 ± 0.003	0.022 ± 0.007	0.013 ± 0.005	0.019 ± 0.008

From Table-5.1 we can see that the Co – Al path and the 1st Co – Co path appear almost at nearby distances from the Co site. It is to be noticed that unlike the Co – Al path the value of the σ^2 for Fe – Al path is much smaller. So it can be suggested that the Al atoms are much ordered in the vicinity of Fe sites than Co sites. In the 2nd co-ordination of Co and Fe atoms the Co – Co bond length decreases continuously while the Fe – Fe bond length increases slowly upto the substrate temperature of 723 K and later it suddenly increases. However, these variations in the Co – Co and Fe – Fe bond distances do not have much effect on magnetization of the samples in comparison to the Co – Fe bond distance [150].

1.2.6 Magnetic Characterizations:

5.2.6.1 M-H curves:

In order to characterize the static magnetization response of the CFA films the variation in saturation magnetization at 5K and 300K were studied. Prior to the calculation the diamagnetic contribution of the Si substrate was subtracted from all the samples. Figure-5.9 shows the variation in the in-plane saturation magnetization (M-H curves) at 300K of the CFA films deposited at various substrate temperatures and inset to this figure shows the raising edge of the M-H curves at

5K. The films show soft ferromagnetic nature at both the temperatures with a negligible amount of hysteresis at 300K. The method of calculation of the saturation magnetization has been explained in the previous chapters

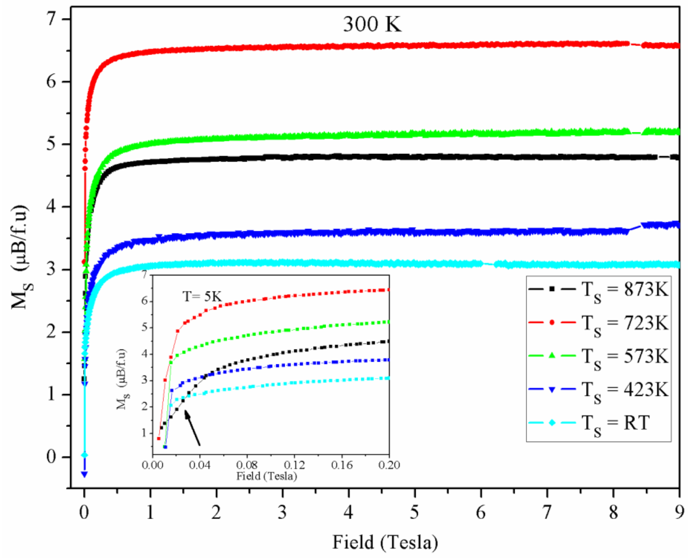

Figure-5.9: Variation in the parallel magnetization (M(H) vs H) curves of the samples measured at room temperature (Inset to the figure shows the comparison of the raising edge of virgin curves of the thin films at 5 K).

Figure-5.10 (a) and (b)show the variation in the hysteresis curves at two measured temperatures of 5K and 300K respectively at lower fields and the variation in the various magnetization parameters i.e., saturation magnetization (M_S), magnetization at 5K treated as the spontaneous magnetization at 0K (M_0), remnant magnetization (M_R) and coercive field (H_C) are shown in the figure-5.11(a) – (d). Inset of figure-5.11(d) shows the variation in H_C with the crystallite size (D) obtained from the X-ray diffraction study. All the hysteresis curves show “S” like feature at both the temperatures. Though a certain value of M_R and H_C existed for all the samples at 5K, M_R and H_C almost vanish at 300K except for the film deposited at 873K and this decrease in the value of H_C with increasing the temperature is expected for a magnetic thin film.

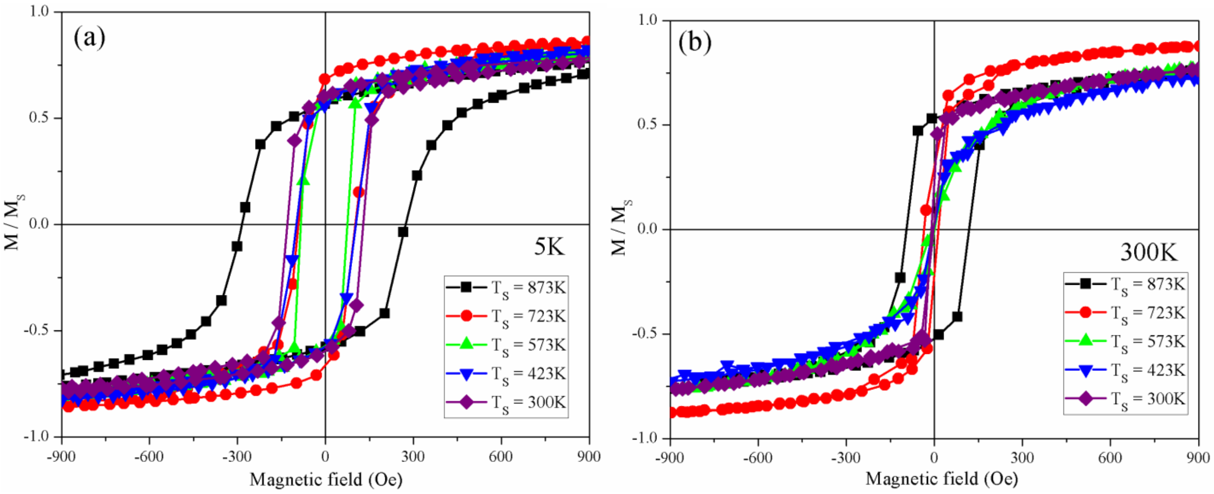

Figure-5.10: Hysteresis curves (M(H) vs H) of the CFA thin films normalized to their corresponding saturation magnetization value (a) measured at 5 K, (b) measured at 100 K.

Figure-5.11(d) shows that H_C decreases as the growth temperature is increased upto 573K and after that it again started increasing and reaches to a maximum value of 280 Oe for the film deposited at 873K. The variation in H_C with crystallite size (D) also agrees with this observation. It should be noted that the decrease in H_C is strongly influenced by the pinning of the domain walls at the pinning centers, such as the size or the concentration of grain boundaries, which vary inversely to the crystallite size / grain size of the thin film [62]. The observed lower value of the H_C for T_S below 723K can be attributed to the lower magnetic ordering or the smaller grain size of the films as observed from the GIXRD study. Thus we can propose that initially as the substrate temperature is increased the size of the grain increases slowly upto T_S = 573K and reaches to a critical size to form a single domain having smaller grain boundary. With further increase in the growth temperature the grain size increases drastically and splits into multiple domains giving rise to larger grain boundaries which takes higher external field (H_C) for the spins to overcome this barrier. Along with this a magneto crystalline anisotropy with increasing the substrate temperature can influence the variation in the H_C.

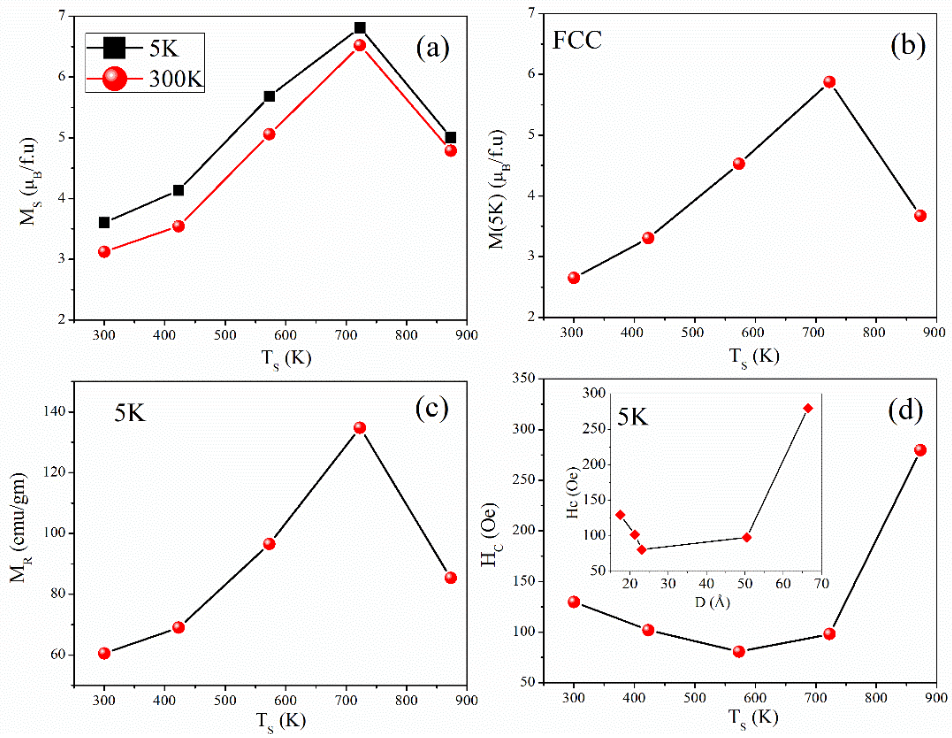

Figure-5.11: Variation of the magnetization parameters of the films as (a) saturation magnetization (M_S) at 5 K and 300 K, (b) value of magnetization at 5 K (M(5 K), (c) remnant magnetization (M_R) and (d) coercive field (H_C). (Inset to the fig. (d) shows the dependence of coercive field (H_C) with the crystallize size (D).

Figure-5.11(a) shows that the value of M_S for all the samples varies almost similarly at 5K and 300K, though the values are little higher at 5K due to the lesser thermal demagnetization at low temperature. Deviation from the proper structural ordering ($L2_1$), stoichiometry and lesser crystallinity can give lesser value of total magnetic moment for the films deposited at RT and 423K in comparison to the bulk [69]. The observed value of M_S shows a linear increase with substrate temperature to the value of 6.52 μ_B/f.u and 6.81 μ_B/f.u at 300K and 5K respectively for the film deposited at 723K. These values appear to be much higher than the experimentally obtained values reported by other worker [126] and further decrease at the maximum growth temperature of 873K.

The increase in magnetic moment comes due to the improvement in the structural ordering with increasing substrate temperature. The possible cause for the higher value of saturation magnetization (~1.72μ_B higher than the SP rule) for the film deposited at 723K could be a higher concentration of Fe in the film as obtained from EDXS study [60]. In addition to this for the case of Co_2FeAl alloy, as similar to the Co_2FeGa alloy the exchange interactions between the Co – Co and Fe–Fe pairs are much weaker than the Co–Fe exchange interaction and the magnetic ordering is mainly contributed by the Co-Fe exchange interaction. Liu et.al [151] have shown that the variation in the pair exchange coupling parameters strongly depends upon the ratio of inter-site distance (*r*) to their lattice parameter (*a*), the value of (*r/a*) ratio of 0.42 for the Co-Fe exchange interaction is significantly lower than that for the Co–Co and Fe–Fe exchange interactions [150]. From our observed EXAFS results the variation in the (*r/a*) ratio for the Co–Co and Fe–Fe pairs varies within 0.66 to 0.70 while for the Co - Fe pair the value remains invariant to 0.42 with a stronger Co(*d*) / Fe(*d*) hybridization which leads to an increase in the magnetic moment for the samples. Further decrease in the value of saturation magnetization for the film deposited at 873K can be due to admixture of antiferromagnetic ordering with the long range ferromagnetic ordering, which can also be clarified from a shallow increase of the virgin curve at 5K (inset to figure-5.9).

5.2.6.2 Thermal Demagnetization (M-T) curves:

The thermal demagnetization curves (M(T)) were taken by varying the temperature from 5-350K in an external magnetic field of 500 Oe. The M (T) data shown in figure-5.12 were collected in Zero Field Cooled (ZFC) and Field Cooled Cooling (FCC) modes and it has been observed that both M (T) data almost retraces each other throughout the temperature range with a very small bifurcation at the low temperature (not shown here). However, for the film deposited at 873K, the ZFC and FCC curves do not retrace each other due to a strong magnetic irreversibility and shows a bifurcation throughout the temperature range (figure-5.12). This variation of in-field magnetization with temperature can be utilized to study the nature of spin wave excitations contributing to thermal demagnetization.

According to the localized electron model [151], the thermal demagnetization of the spontaneous magnetization in the absence of external field M (0,T) only depends on the Spin-wave (SW) excitation at low temperature region (~1/3rd of T_C) and the ratio M (0,T) / M (0,0) varies as (~$T^{3/2}$) with temperature. According to the theory based on itinerant electron model [152] the ratio decreases due to the Stoner single particle (SP) excitation following the T^2 law with increase in the temperature over a wide range of intermediate temperature region and the other higher order terms appears near to T_C [153]. The thermal demagnetization of the infield magnetization follows the similar dependence with temperature and can be plotted in terms of $T^{3/2}$ and T^2.

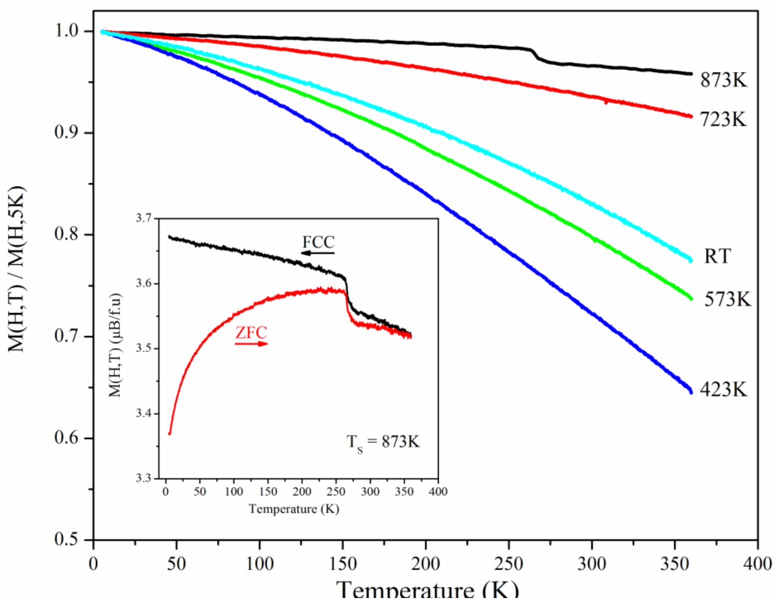

Figure-5.12: M(T) vs T curves of the thin film samples grown at various substrate temperatures. M(T) is normalized to the value of M (5 K). (Inset to the figure shows warming and cooling curves of the thin film deposited at 873 K).

The temperature dependence of the relative deviation of in-field magnetization from the spontaneous magnetization at 0 K (for our case 5K has been considered near to 0K) can be written in terms of:

$$\Delta M\ (T) = \frac{[M(H,0) - M(H,T)]}{M(H,0)} \tag{5.1}$$

which should be analyzed in terms of SW and SP excitation relation [154]:

$$\Delta M(T) = \Delta M_{SW}\ (T) + \Delta M_{SP}\ (T) \tag{5.2}$$

where, Spin wave $\Delta M_{SW}\ (T)$ contribute to the relative deviation $\Delta M(T)$ as

$$\Delta M_{SW}\ (T) = \frac{g\mu_B}{M(H,0)}\left[\xi\left(\frac{3}{2}, \mathrm{t_H}\right) \times \left[\frac{\mathrm{k_B T}}{4\pi \mathrm{D(T)}}\right]^{\frac{3}{2}}\right] \tag{5.3}$$

The constants g, μ_B and k_B are the Lande g factor, Bohr magneton and the Boltzmann constant respectively. The higher order terms of T that appear in the intermediate temperature region and contributes to D(T), have been neglected and only the spin wave stiffness constant at low temperature region can be considered as a constant quantity D(0). In Eq. 5.3 the Bose-Einstein integral function$\xi(\frac{3}{2}, \mathrm{t_H})$ is defined as:

$$\xi\left(\frac{3}{2}, \mathrm{t_H}\right) = \sum_{n=1}^{\infty} n^{-\frac{3}{2}} e^{-nt_H}\ , \text{ where } \mathrm{t_H} = \frac{g\mu_B}{k_B T} H_{eff} \tag{5.4}$$

The effective field that arises in the equation H_{eff} can be treated as external magnetic field. From the theory based on itinerant electron model the quantity $\Delta M_{SP}\ (T)$ can be written as,

$\Delta M_{SP}\ (T) = BT^2$, where B is considered as a constant quantity. (5.5)

On the basis of the Eqns. 5.3 and 5.5, the relative deviation in Eq. 5.2 can be simplified as:

$$\frac{M\ (H,T)}{M(H,0)} = 1 - A(H)T^{\frac{3}{2}} - BT^2 \tag{5.6}$$

where A(H) = $\frac{g\mu_B}{M(H,0)}\left[\frac{\mathrm{k_B}}{4\pi \mathrm{D(0)}}\right]^{\frac{3}{2}}$ be the slope of the curve

$$\frac{M(H,T)]}{M(H,0)} \text{ vs } [\xi\left(\frac{3}{2},\mathrm{t_H}\right) \times \mathrm{T}^{\frac{3}{2}}]. \tag{5.7}$$

It is quite evident for the figure-5.13 that the curves fitted well with the relation given in Eqn. 5.3 and shows a straight line with slope 'A'. Hence adding the T^2 term as mentioned in the Eqn. 5.6 does not show any significant variation to the curves except for the film deposited at 423K. It has been found that for this film the M vs. T curve deviated from the localized electron model and follows the itinerant nature near to the room temperature (~300K) and above as shown in the inset to the figure-5.13. The variation in the spin-wave stiffness constant D_0 calculated using Eqn. (5.7) for different thin film samples has been shown in the figure-5.14. The result shows a maximum value of D_0 for the film deposited at highest substrate temperature though for the other samples the values are almost same.

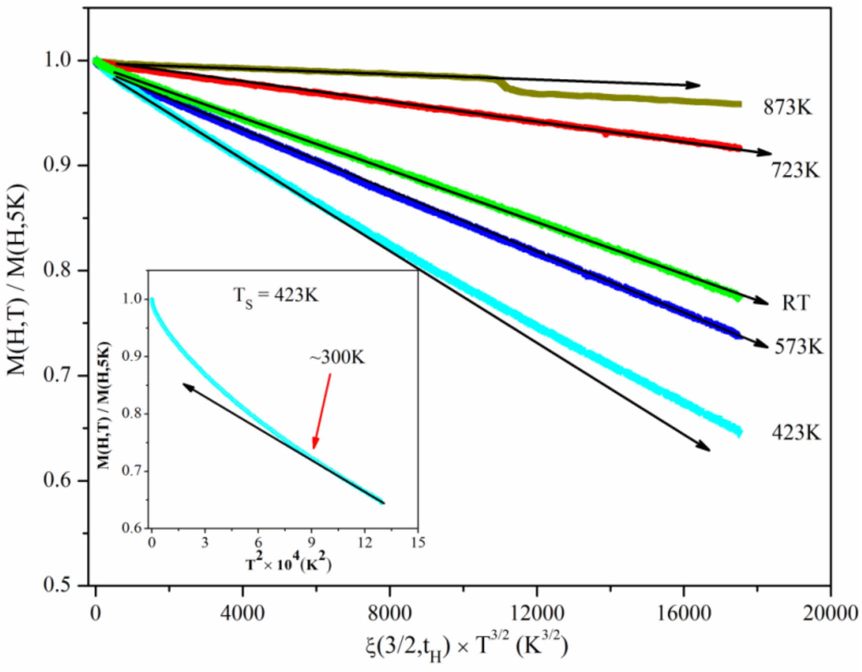

Figure-5.13: Comparison of experimental thermal demagnetization curves of the thin films with the behavior predicted by localized electron model. (Inset to the figure shows the deviation from the localized electron model for the film deposited at 423 K).

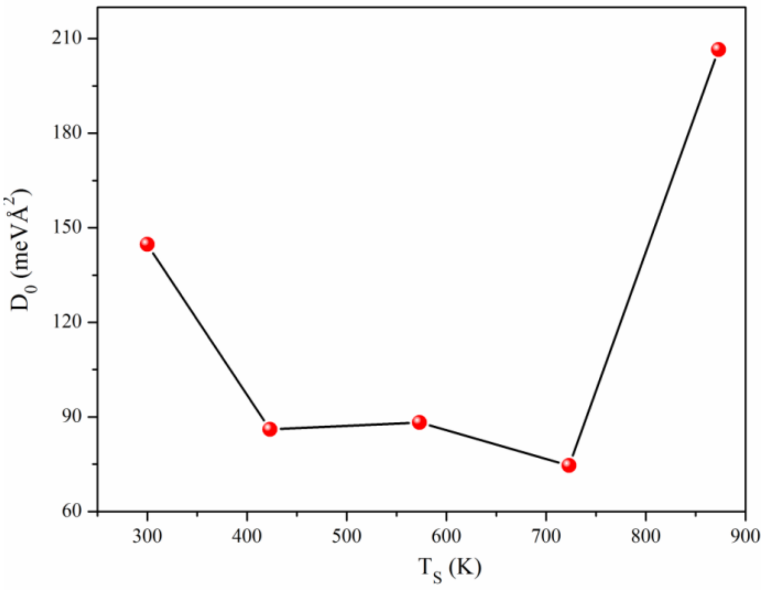

Figure-5.14: Variation in the spin wave stiffness constant (D) by considering the localized electron model.

5.3 Conclusions:

In this chapter the effect of growth temperature on the structural and magnetic properties of the CFA thin films deposited using PLD technique have been presented. GIXRD measurements on the thin film samples acsceertained the presence of Heusler phasein the films, though due to the lesser intensity of the peaks the proper ordering of the samples could not be fully understood. The stoichiometries of the samples were improved by increasing the substrate tempearture as observed from the EDXS study. Local structural study using the EXAFS technique shows that all the samples were metallic in nature and improvement of EXAFS oscillatons in the films with increase in substrate temperature suggests better crystallinity in the films. From the EXAFS data analysis, it was observed that Co-Fe bondlength is smaller than Co – Al bond suggesting stronger*d-d* hybridization. Magnetisation measurements at both 5K and 300K show similar kind of variation, where the saturation magnetization of the samples increases gradually upto substrate temperature of 723K and after which it decreases possibly due to admixture of antiferromagnetic ordering in the sample with the long range ferromagnetic ordering. The variation in the coercivity in the films as afunction of substrate temperature nicely correlates with the variation in the lateral crystallite size. M vs T curves are found to follow $T^{3/2}$ law following Bloch’s theorem and it leads to the conclusion that thermal demangetisation of the samples are driven by excitation of the spin waves throughout the series.

Chapter-6

PULSED LASER DEPOSITED Co_2FeSi HEUSLER ALLOY THIN FILMS: EFFECT OF DIFFERENT THERMAL GROWTH PROCESSES

6.1 Introduction:

Among all the Co based Heusler alloys Co_2FeSi (CFS) is an important candidate of the series having high spin polarization, large magnetic moment (~6 μB) [31], high thermal stability and high Curie temperature ~1100 K for bulk sample [155] and for the thin film samples deposited at higher substrate temperature of 650 K [156]. In this present work, thin film CFS samples were prepared using PLD technique by two different thermal growth mechanisms viz., (i) by depositing the samples at elevated substrate temperatures and (ii) by annealing the samples in vacuum after depositing at room temperature. The samples have been characterized by X-ray diffraction, Grazing Incidence X-ray diffraction, synchrotron radiation based X-ray absorption spectroscopy (XAS) comprising of both X-ray near edge absorption (XANES) and Extended X-ray absorption fine structure (EXAFS) measurements and finally by detail magnetic measurements. The main focus of the work is to study the effect of the different growth mechanisms on the structural and the magnetic properties of the deposited thin films.

6.2 Experimental:

Co_2FeSi (CFS) thin films of ~1000Å thickness were deposited on Si (111) substratesfrom a 3-inch diameter and 3mm thick stoichiometric target using PLD technique for 20 minutes of deposition. The details of the PLD system used in this study, alongwith descriptions of the deposition chamber and the laser used have been explained in details in Chapter-2 [157, 158, 159]. One set of samples were prepared at substrate temperatures of 423K, 573K, 723K and 873K, while another set of samples were deposited at the room temperature and annealed in vacuum at the above mentioned temperatures for 20 minutes. In the subsequent discussion, the two series of samples prepared at elevated substrate temperature and post deposition annealing have been referred to as 'S' and 'A' series respectively.

6.3 Results and Discussions:

6.3.1 Grazing Incidence X-ray Diffraction (GIXRD):

Figures-6.1(a) and (b) represent the experimentally obtained GIXRD pattern of the CFS thin films prepared with substrate heating and post deposition annealing process respectively together with the XRD pattern (inset to figure-6.1(b)) of the bulk target material.

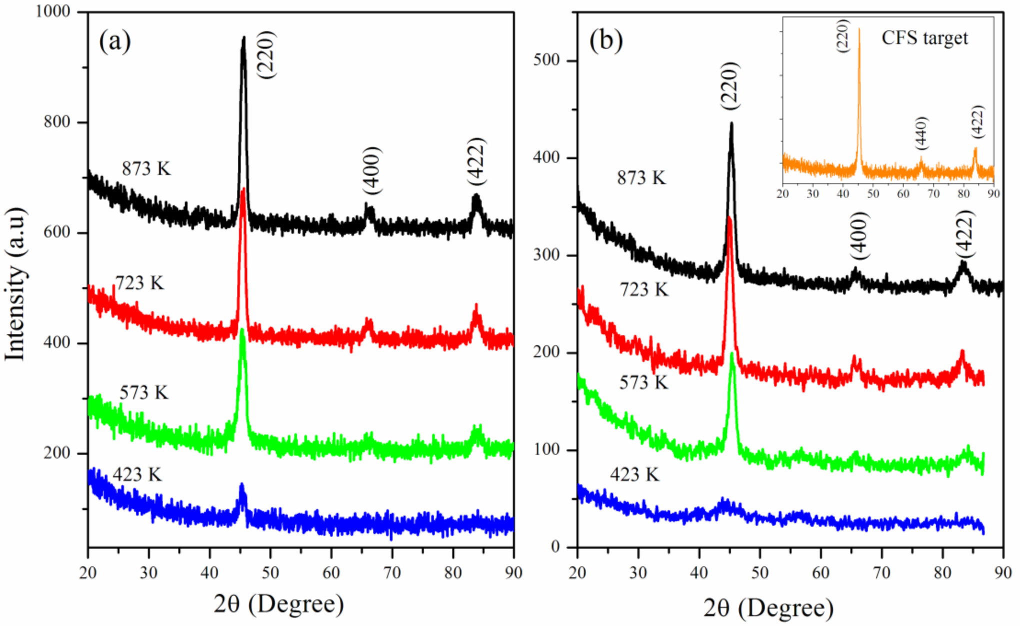

Figure-6.1: GIXRD patterns of the CFS thin films deposited using PLD technique for (a) 'S' series samples and (b) 'A' series of samples. Inset: XRD data of the CFS bulk target.

Both the XRD of the bulk target and the GIXRD patterns of prepared thin films match with each other and represent the polycrystalline nature of the films. Similar diffraction patterns suggest that the structural phase of the target material is well transferred in the plume produced by the pulsed laser from target to the film. In the diffraction patterns three main peaks appear for (220), (400) and (422) reflections, which follow the law of reflection $h+k+l = 4n$ (n be the positive integer). The laws of other reflections and their significance have been well explained elsewhere [160]. It has been reported that for a fully ordered $L2_1$ phase the (111) and (200) super lattice reflections should appear along with the fundamental (220) peak [138]. These peaks do not appear in the XRD pattern of our samples either due to their low intensity or due to possible presence of atomic disorder in the samples even in the bulk target. However, as has been explained in the previous chapters, with the laboratory based XRD measurements, due to the similar atomic scattering factors of the Co and Fe atoms, precise evaluation of different kinds of atomic disorder in the samples is difficult and we have used XAS measurements to clarify this.

Mohankumar et.al. have also observed that for Co_2FeSi thin films deposited using dc magnetron sputtering on GaAs (100), MgO (001) and Si (111) substrates, fully ordered $L2_1$ phase was only obtained at an elevated substrate temperature of 970 K [161]. Schneider et.al. have similarly observed that for Co_2FeSi films deposited on Al_2O_3 (11-20) and MgO (100) substrates by r.f magnetron sputtering, formation of the properly ordered $L2_1$ phase took place at substrate temperature above 970 K [60]. Takamura et.al. have observed mixed $L2_1$ and B2 phases in 100 nm thick Co_2FeSi films deposited on MgO substrate at a substrate temperature of 573 K by facing target sputtering (FTS) technique [162]. Zhu et. al. have also obtained mixed B2 and $L2_1$ phase in Co_2FeSi film deposited on single crystalline MgO substrate with a 7 nm thin Ta capping layer in between by dc magnetron sputtering and have observed that as substrate temperature is increased above 750 K, relative fraction of $L2_1$ phase is increased [163]. $L2_1$ ordering in CFS films have been observed by researchers at much lower substrate temperature only for films grown by Molecular Beam Epitaxy (MBE) technique [164, 165].

In both the series of samples discussed here, the intensity of the fundamental peak increases and the FWHM gradually reduces with increase in the substrate and annealing temperature, suggesting improved crystallinity in the samples. It was also observed that XRD peaks of the samples prepared at elevated substrate temperature have higher intensities than that of the samples prepared with post deposition annealing. The variation in the lateral crystallite size (D) for both the series are shown in figure-6.2 calculated using the well-known Debye-Scherrer formula D = $\frac{0.9\times\lambda}{\beta Cos\theta}$.

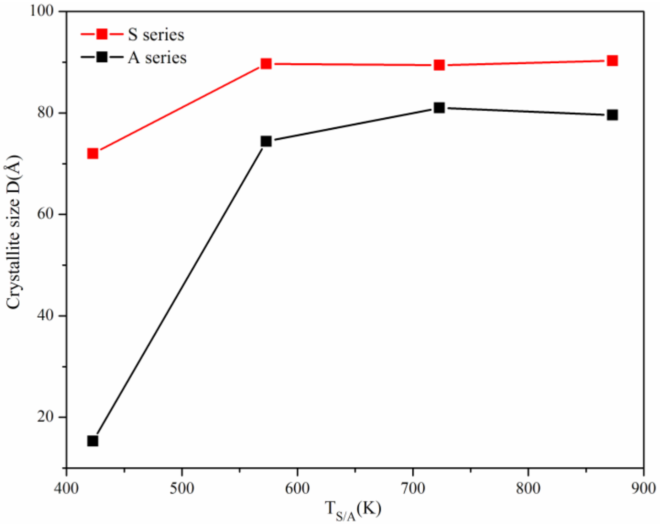

Figure-6.2. Variation in the lateral crystallite size (D) with deposition and annealing temperatures for 'S' and 'A' series samples.

The result shows that the samples deposited at elevated substrate temperatures have higher crystallite sizes than the samples prepared with post deposition annealing and the highest value of D reaches upto 90Å, which is little higher than that obtained by other workers for the CFA thin films using the same procedure [159]. This increase in the crystallite size takes place due to enhanced adatom diffusivity at higher temperatures where the adatoms get higher mobility to get agglomerated with each other leading to larger crystallites. The variation in the value of D can affect the magnetization of the samples which has been explained later.

6.3.2 Grazing Incidence X-ray Reflectivity (GIXR):

The comparison in the reflectivity plots between the ‘S’ and ‘A’ series samples are shown in figure-6.3. The oscillations in the reflectivity plots correspond to the thickness of the film. In contrast to the ‘A’ series no distinct Kissig fringes were observed in spectra of ‘S’ series samples, may be due to higher roughness of the films. The experimental reflectivity data were fitted with theoretical plots using IMD software [101] as described in Chapter-2. In such exercises a thin film is often modeled as a bi-layer structure with a bottom layer just on the substrate considered to be the main bulk layer of the film and a top layer of lower density and thickness which takes care of the surface roughness. However, as can be seen from the EDXS results presented in next section we have observed that Si content is significantly high in some of the samples which is possibly due to diffusion of Si from the substrate to the film. Hence to take care of this phenomenon we have assumed a thin low density layer just above the substrate (CFS 3) apart from the two layers (bulk layer CFS 2 and surface roughness layer CFS 1). Presence of similar low density layer due to diffusion of Si just above the substrate has been observed by several other authors also [166]. The best fit theoretical simulation along with the experimental GIXR data is shown in the inset of figure-6.3, the sample structure for a representative sample from “A” series annealed at 423K is also shown in the figure-6.3.

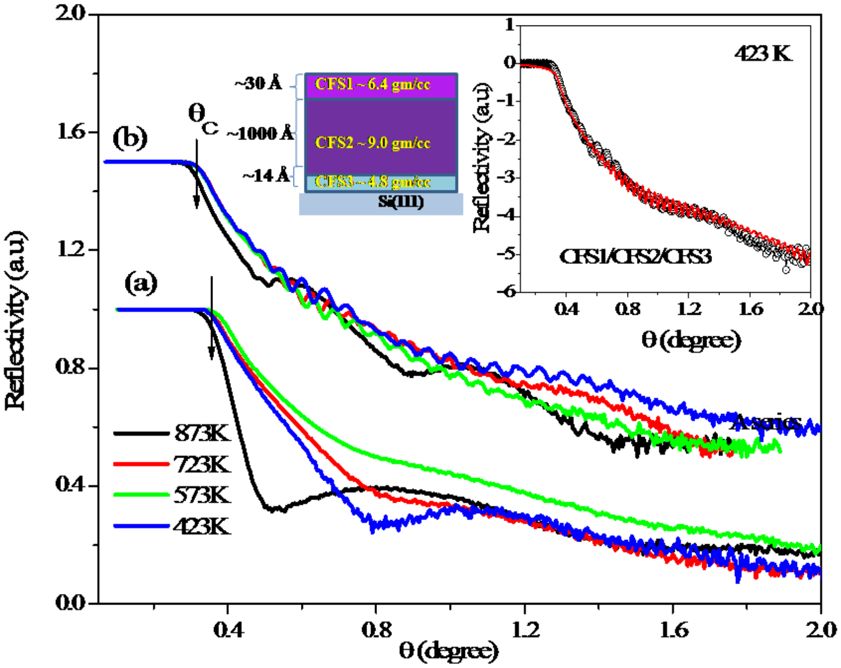

Figure-6.3. Grazing Incidence X-ray Reflectivity (GIXR) data of the CFS films of (a) 'S' and (b) 'A' series of samples. Inset: Best fit theoretical plot and the best fit sample structure for a representative 'A' series sample prepared at RT and annealed at 473 K.

It should be noted that prior to the preparation of the present samples, few CFS films with lower thicknesses had been deposited for known deposition times and their thicknesses were estimated by GIXR measurements, a rate or thickness vs. time calibration plot was thus obtained and the overall thicknesses of the present samples were estimated from the above rate calibration plot. The thickness of the upper surface obtained from the fitting remains within 26-35Å for both the series. In contrast to the 'A' series no distinct Kissig fringes were observed for the case of 'S' series samples, hence correct estimation about the thickness for these samples is little difficult. It is quite interesting that the value of the critical angle (θ_c) for the 'S' series are higher than the critical angle of 'A' series by 0.04°. This manifests the formation of denser films with substrate heating than by the post deposition annealing process. It shows that imparting kinetic energy to adatoms during deposition in the form of enhanced substrate temperature causes better re-organization and agglomeration of adatoms leading to higher density than by post deposition annealing. The density of the bottom layer and upper layer of the ‘S’ series remains between 9.00-9.55 g cm^{-3} and 7.5-8.5 g cm^{3} respectively, while for the ‘A’ series the density of the layers remain ~6.5 g $cm^{-3}$and 5.0-6.5 g cm^{-3} respectively. It was observed that the top surface roughness and the roughness at the interface increase with increasing substrate temperature. For the ‘S’ series sample, the increase in the top surface roughness from 4.62 Å to 8.76 Å and interface roughness from 3.02 Å to 9.0 Å indicate increase in the disorder of the samples with increase in substrate temperature. It should be noted here that the slope of the reflectivity plot gives a rough estimation of the roughness of the films and sharp fall in case of the samples grown at a substrate temperature of 873 K manifests high roughness in the sample due to large crystallite sizes as can be observed from figure-6.2. The increase in surface roughness with the increase in substrate temperature was also observed by Mohankumar et.al. for DC magnetron sputtered CFS films [161].

6.3.3 Field Emission Scanning Electron Microscopy (FESEM):

The FESEM electron back scattering images of ‘S’ and ‘A’ series at the lowest and highest temperatures are shown in figure-6.4. The images show the formation of the droplet type of morphology with varying size from 1 to 4 µm. The magnified image on the larger droplet for the films grown at substrate temperatures of 723K and 873K show the formation of grain structure with size less than 1µm and are separated by grain boundaries. On the other hand, no such formation of grain boundary was distinctively observed for the ‘A’ series samples even at the highest annealing temperature.

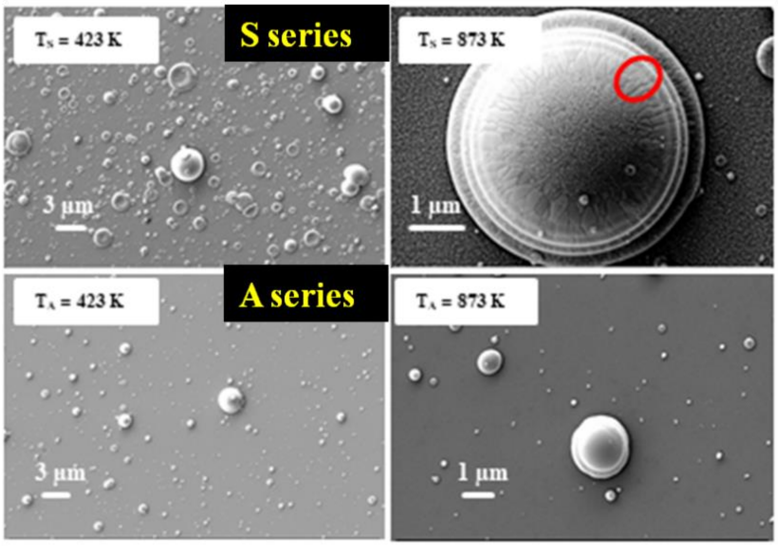

Figure-6.4: FESEM back scattering electron image of the CFS films prepared at 423 K and 873 K for ‘S’ series and ‘A’ series samples.

6.3.4 Energy Dispersive X-ray Spectroscopy (EDXS):

The elemental compositions of the ‘S’ and ‘A’ series samples are shown in figure- 6.5(a) and (b). The compositions of the films were obtained by EDXS measurements on 5 spots on the surface of the films and the average results have been reported. From the result it was observed that relative elemental composition in the films vary differently for the two series of samples. However, the Co/Fe ratio remains the same for both series and reaches near stoichiometry after 723K. The higher value of Si atomic weight % compared to Fe in the samples is possibly due to diffusion of Si atoms from the substrate to the films as obtained from GIXR measurements also discussed above.

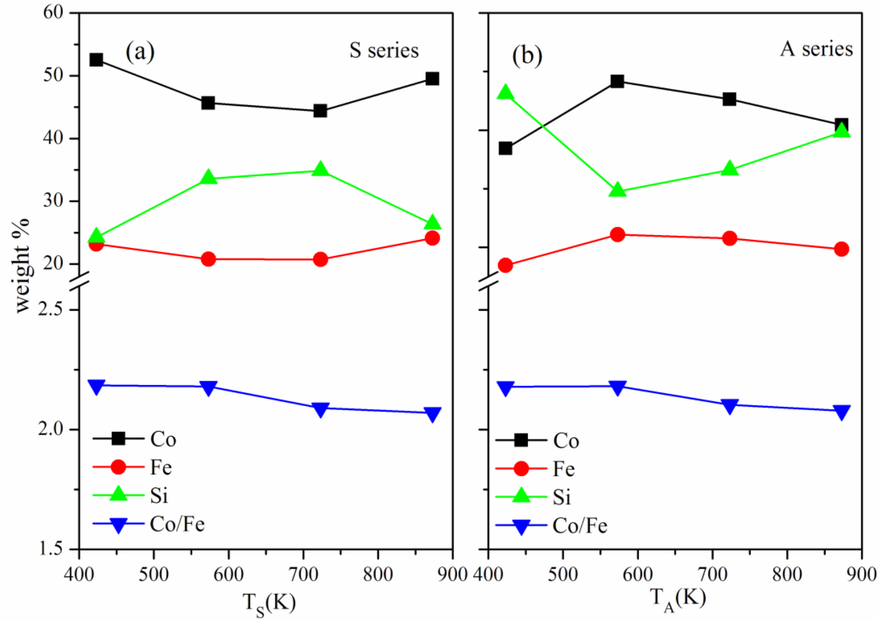

Figure-6.5: Variation in the elemental composition of the CFS films with growth temperatures for (a) 'S' series and (b) 'A' series samples.

6.3.5 X-ray Absorption Spectroscopy (XAS):

The normalized absorption spectra at Co and Fe K-edges of the 'S' and 'A' series samples along with that of Co and Fe foils are shown in the figure-6.6 (a) and (b) respectively. As shown in the figure the position of the Co and Fe absorption edges (1s → 4p transition) of the samples exactly match with their corresponding reference foils, ascertaining that the above metallic species are present in pure elemental phase in the samples.

The k^2 weighted $\chi(k)$ spectra at the Co and Fe edges for the 'S' series sample are shown in figures-6.7(a) and 6.8(a) and for 'A' series samples in figures-6.9(a) and 6.10(a) respectively. As it has been mentioned from XRD, we could not ascertain the exact crystallographic phase of the samples by laboratory XRD measurement, however, we have assumed $L2_1$ phase in the samples as an initial guess model for EXAFS data fitting. It should be noted that this is an initial guess model to generate the scattering paths used in the EXAFS fitting process, and the rest of the results obtained in this section does not depend on the assumption of the initial guess model. Similar kind of model has also been used by Balke et. al. for EXAFS analysis of CFS samples [138]. The details about the $L2_1$ structural model have been discussed in the previous chapters. As we have considered the $L2_1$ phase as the starting model so the Co K-edge data will not be able to distinguish between the different signatures, in contrast the Fe K-edge data will be able to distinguish owing to different chemical environments around the Fe atoms in $L2_1$ and B2 phases.

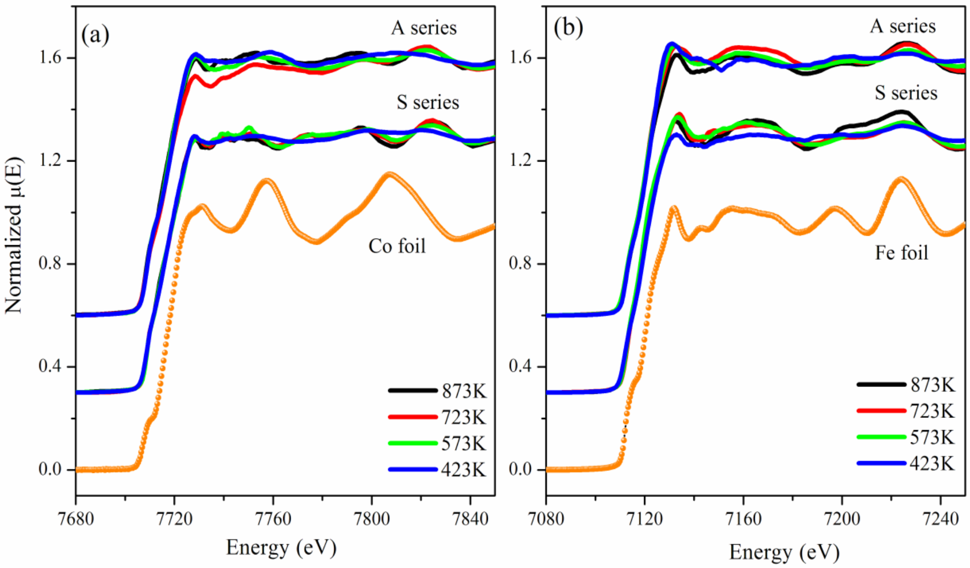

Figure-6.6: Comparison between the normalized XANES spectra (m(E) vs E spectra) of the CFS thin films at (a) Co K-edge and (b) Fe K-edge.

The Fourier transformed k^2 weighted $\chi(k)$ vs. k data or the $\chi(R)$ vs. R plots fitted with the theoretically generated model at Co and Fe edges of S and A series are shown in the figures-6.7(b),6.8(b) and figures-6.9(b), 6.10(b) respectively along with the experimental data. As has been discussed in Chapter-2, in the $\chi(R)$ vs. R plots the positions of the peaks indicate the atomic bond distances (R) and the intensity indicates the co-ordination number (C.N) of the respective atomic shell, while the peak broadness suggests the static disorder (σ^2 i.e., Debye-Waller factor) or the mean square deviation in the atomic bond distances.

During the fitting process the above mentioned parameters were varied independently by keeping the passive amplitude reduction factor (S_0^2) in between 0.8-0.9.

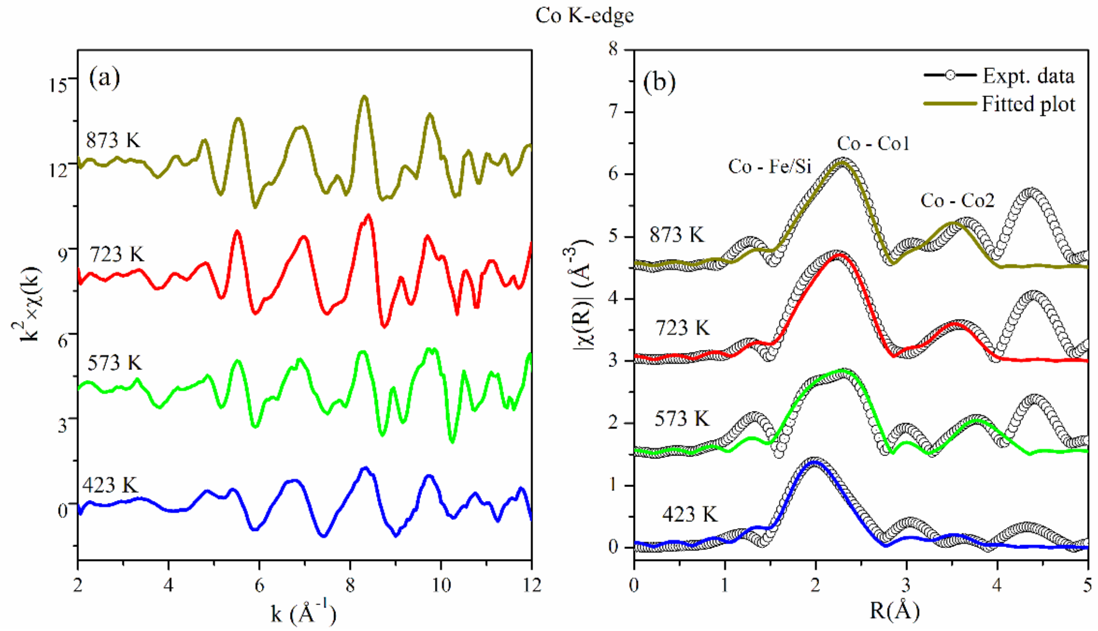

Figure-6.7: (a) k^2 weighted $\chi(k)$ vs k spectra and (b) experimentally obtained FT-EXAFS ($\chi(R)$ vs R) plots of S series of the CFS films fitted with theoretically generated plots at Co K-edge.

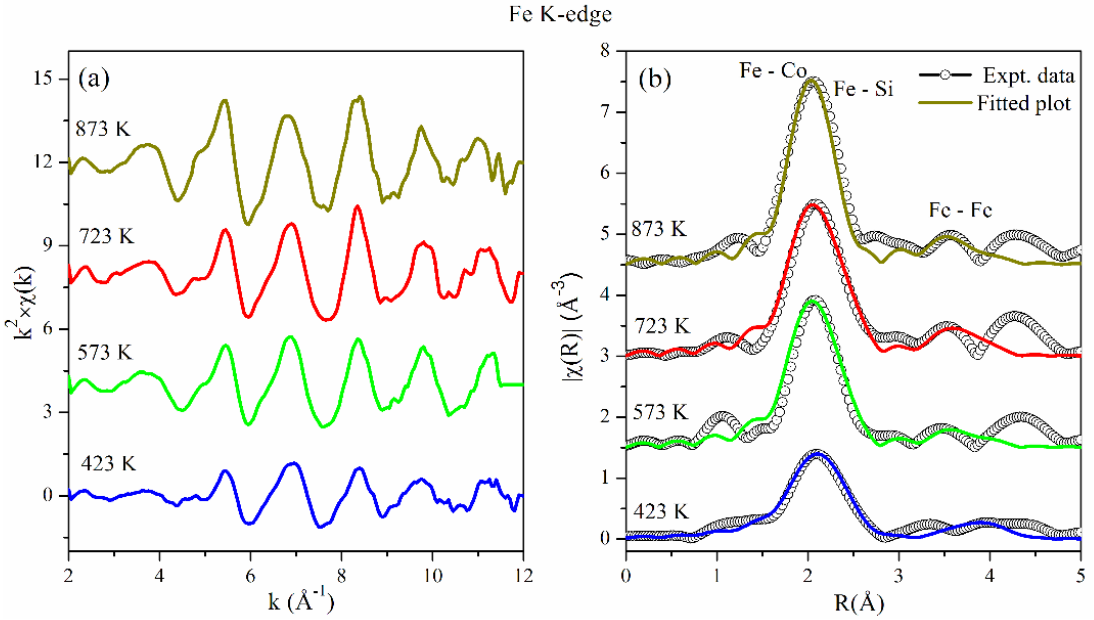

Figure-6.8: (a) k^2 weighted $\chi(k)$ vs k spectra and (b) experimentally obtained FT-EXAFS ($\chi(R)$ vs R) plots of S series of the CFS films fitted with theoretically generated plots at Fe K-edge.

As we have observed from the $\chi(k)$ vs. k plot that though there is no significant difference between the data except for the 423K sample, the gradual increase in intensity in the $\chi(R)$ vs. R plots suggest an enhancement in the crystallinity of the samples with increase in the growth temperature.

The Fourier transformed $k^2\chi(k)$ vs. k or $\chi(R)$ vs. R data are fitted in the R range of 1.4 - 4.1 Å. As it has been mentioned earlier that we are interested in studying the presence of atomic disorder due to the random occupancies or the atomic swapping between Co/Fe/Si atoms, we have analyzed the experimental data by considering two different approachesas we have done in case of Co_2FeGa samples described in Chapter-4. In the 1st approach the atomic bond length and structural disorder parameters of the different shells have been varied by keeping the C.N constant to their crystallographic values in a proper $L2_1$ phase. On the other hand, in the 2nd approach certain elements are placed at the designated positions of the other elements in a specific way to take into account antisite disorder and itseffect on the local structures of other atoms. In the 2nd case the values of the parameters obtained from 1st approach was considered as the initial guess parameters for the calculations. A detail understanding of the 1st peak in the $\chi(R)$ vs. R plot provides a lot of information about the above-mentioned disorder. In the phase uncorrected $\chi(R)$ vs. R plot at the Co K-edge the 1st peak that appears within the R range of 1.5-2.7Å is a convolution of two different scattering paths consisting of Co-Fe/Si (C.N = 4+4) and Co-Co (C.N = 6) coordination shells at 2.44 Å and 2.82Å respectively. As from the structure it is well understood that the Co atom is situated at the body center of a cube of 1/8th of the unit shell, the Fe and Si atoms are situated at the corners with equal distance from Co atoms, which makes a complete triad of [Fe-Co-Si] atoms. However, the 1st Co-Co path appears at a little higher distance making the peak slightly broader. Hence the contributions of the Co-Fe/Si and Co-Co1 paths are clearly distinguishable from the 1st peak of the ‘S’ series, where the Co-Co peak starts increasing and dominates over the Co-Fe peak from T_S = 573 K onwards, however for the 'A' series the Co-Fe/Si path dominates over the Co-Co1 path, which appears as a shoulder to higher side of *R*. This may arise due to the interplay between the co-ordination numbers of the shells due to the interchange between the Co and Fe atoms in their designated atomic sites or anitisite disorder discussed later. The intensities of the peaks in the range of 3.5-4.0 Å due to Co-Co2 scattering path (C.N = 12) in the 3rd co-ordination shell (at a nominal value of 3.98Å) is higher for 'S' series in comparison to the 'A' series. So from this observation it can be concluded that having similar crystal structures and local atomic environment the 'S' series samples have better crystalllinity than the 'A' series samples.

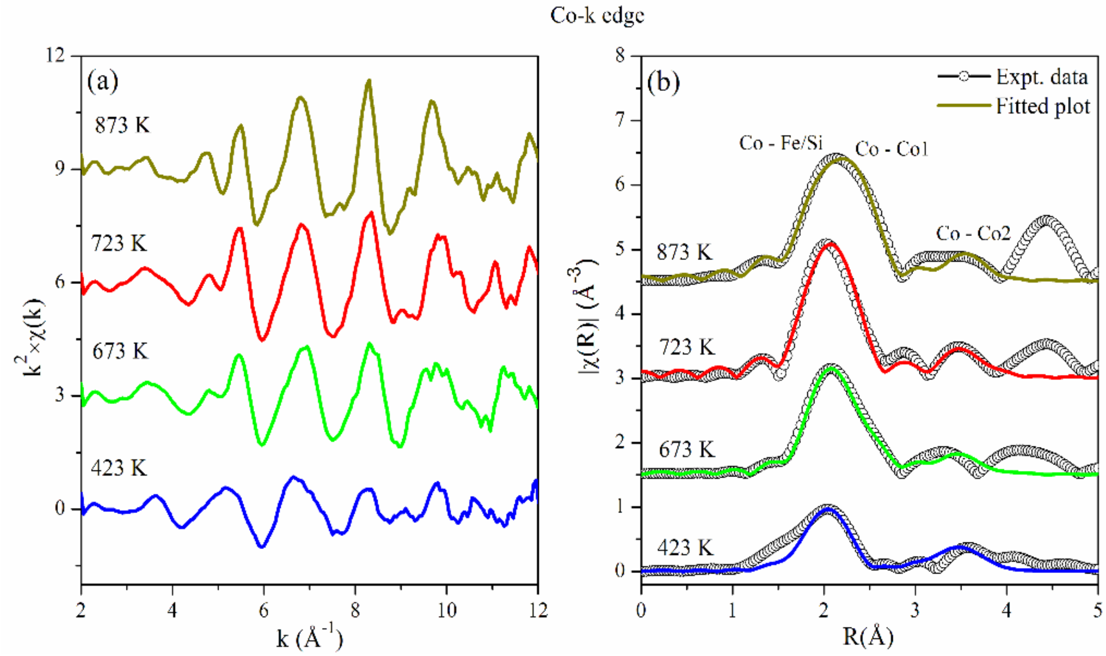

Figure-6.9: (a) k^2 weighted χ(k) vs k spectra and (b) experimentally obtained FT-EXAFS (χ(R) vs R) plots of A series of the CFS films fitted with theoretically generated plots at Co K-edge.

In case of the Fe K-edge data, the 1st peak that appears within the *R* range of 1.5-2.5 Å is a convolution of Fe-Co (C.N=8) and Fe-Si (C.N=6) paths situated at distances of 2.44 Å and 2.82 Å respectively, however the phases at the Co and Fe edges look similar as both the edges contain similar back-scattering atoms. The results obtained from the EXAFS data analysis using the 1st approach are summarized in Table-6.1 at the Co and Fe edges for 'S' series and in Table-6.2 for the 'A' series respectively.

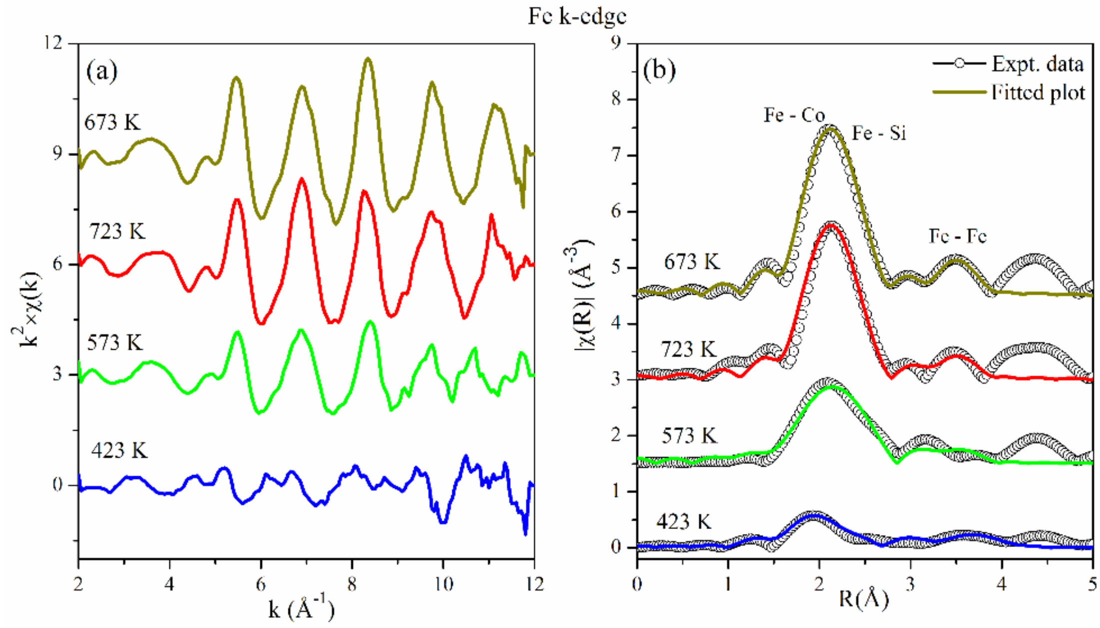

Figure-6.10:. (a) k^2 weighted $\chi(k)$ vs k spectra and (b) experimentally obtained FT-EXAFS ($\chi(R)$ vs R) plots of A series of the CFS films fitted with theoretically generated plots at Fe K-edge.

Table-6.1: Values of structural parameters i.e., bond lengths (R), Debye Waller factor (σ^2) at Co and Fe K-edge of S series.

	Scattering paths × C.N	Parameters	423K	573K	723K	873K
Co K-edge	Co – Fe × 4	R(Å) σ^2(Å^2)	2.41 ±0.01 0.005 ±0.001	2.42±0.01 0.006±0.001	2.41 ±0.01 0.006 ±0.001	2.41± 0.01 0.006±0.001
	Co – Si × 4	R(Å) σ^2(Å^2)	2.37 ±0.03 0.027±0.008	2.40±0.04 0.027±0.010	2.36 ±0.03 0.028±0.011	2.37± 0.02 0.026±0.004
	Co – Co1× 6	R(Å) σ^2(Å^2)	2.72 ±0.03 0.023 ±0.004	2.72 ±0.02 0.009 ±0.002	2.74 ±0.01 0.009 ±0.001	2.75±0.01 0.009±0.001
	Co – Co2× 12	R(Å) σ^2(Å^2)	3.94 ±0.05 0.027±0.003	4.07±0.02 0.016 ±0.003	3.93± 0.01 0.015 ±0.002	3.91±0.01 0.013±0.002
Fe K-edge	Fe – Co × 8	R(Å) σ^2(Å^2)	2.44±0.01 0.013 ±0.002	2.42 ± 0.01 0.008 ± 0.001	2.41 ±0.01 0.007 ±0.001	2.41 ±0.01 0.007 ±0.001
	Fe – Si × 6	R(Å) σ^2(Å^2)	2.96 ±0.03 0.024 ±0.012	2.93± 0.03 0.014 ± 0.004	2.95±0.02 0.010 ±0.003	2.93 ±0.04 0.027±0.003
	Fe – Fe × 12	R(Å) σ^2(Å^2)	4.14±0.05 0.022±0.010	4.06±0.04 0.023± 0.010	4.02±0.04 0.018 ±0.007	4.0 ±0.03 0.17±0.005

It was observed that though the Fe and Si atoms are situated at the same distance from Co, they have a relative displacement from each other for both the series. For the 'S' series samples the Co-Si (2.37 Å) bond is less than the Co-Fe (2.41 Å) bond whereas for the 'A' series samples Co-Si (~2.55Å) bond length is higher than Co-Fe bond length, suggesting a stronger *3d-3p* (Co-Si) hybridization for 'S' series and stronger 3*d-3d* (Co-Fe) hybridization for 'A' series. These kinds of hybridizations have been observed earlier also for the CoFe based Heusler alloys [158, 149]. Though the Co-Fe and Co-Si pairs have relative displacements, the Co-Fe bond remains almost same at 2.41 Å with much lesser value of σ^2 than the Co-Si bond. This suggests that the Co-Fe bond is much sluggish around Co atom, the Co-Co bond distance however changes slightly in the 2nd and 3rd co-ordination shells.

Table-6.2: Values of structural parameters i.e bond lengths (R), Debye Waller factor (σ^2) at Co and Fe K-edge of A series.

	Scattering paths × C.N	Parameters	423K	573K	723K	873K
Co K-edge	Co – Fe × 4	R(Å)	2.41 ±0.01	2.41 ±0.01	2.40 ±0.01	2.41 ±0.01
		σ^2(Å^2)	0.010 ±0.001	0.006 ±0.001	0.004 ±0.001	0.005 ±0.001
	Co – Si × 4	R(Å)	2.53 ±0.04	2.60 ±0.03	2.57 ±0.05	2.32±0.03
		σ^2(Å^2)	0.028 ±0.009	0.027 ±0.009	0.027 ±0.009	0.028 ±0.009
	Co – Co1× 6	R(Å)	2.65 ±0.03	2.74 ±0.01	2.73±0.01	2.75 ±0.01
		σ^2(Å^2)	0.028 ±0.001	0.013 ±0.001	0.019 ±0.002	0.009 ±0.001
	Co – Co2× 12	R(Å)	3.95 ±0.03	2.93 ±0.03	3.91 ±0.02	3.91 ±0.02
		σ^2(Å^2)	0.021 ±0.004	0.022 ±0.004	0.018 ±0.002	0.018 ±0.002
Fe K-edge	Fe – Co × 8	R(Å)	2.45±0.04	2.43 ±0.01	2.42±0.01	2.42 ±0.01
		σ^2(Å^2)	0.015 ±0.001	0.013 ±0.001	0.007±0.001	0.006 ±0.001
	Fe – Si × 6	R(Å)	2.89 ±0.05	2.91 ±0.01	2.90±0.01	2.88 ±0.03
		σ^2(Å^2)	0.006 ±0.006	0.006 ±0.002	0.006±0.002	0.004± 0.002
	Fe – Fe× 12	R(Å)	4.10±0.05	3.88±0.04	3.89±0.03	3.92 ±0.04
		σ^2(Å^2)	0.021±0.006	0.022±0.007	0.019±0.005	0.014 ±0.002

The results at Fe K-edge corroborate with the Co edge results, where the bond length of Co-Fe pair remains almost same for both the series except for the sample grown at 423K temperature. This suggests that the cubic environment around the Co and Fe atoms are well maintained. As observed from the X-ray diffraction also much higher value of σ^2 for the Co-Si path than Fe-Si path suggests higher probability of Co/Si antisite disorder in the S series samples.

On the basis of the idea obtained from the above approach, we have analyzed the data further to define the nature of possible antisite disorder present in the system. We have reported the presence of different kinds of atomic disorder in the CFG thin films on the basis EXAFS studies [159] which has been described in Chapter-4. It should be noted that atomic disorder between the Co-Si or Fe-Si pairs do not affect much the magnetic properties as the band structure does not alter, until there is a disorder between the Co and Fe atoms. So in this context without giving a random occupancy of various atoms, we have used a specific model to define the disorder between the Co and Fe pairs based on the model explained by Ravel et.al. for Co_2MnSi sample [142]. In this model, a disorder atomic path was included in the ATOMS program with the same bond length and co-ordination number of the corresponding proper sited atomic path. The final parameter which defines the Co-Fe atomic disorder is noted as '**γ**', which defines the probability of occurrence of the Co atoms at the position of the Fe site or vice versa. So if the value of '**γ**' comes to 0, it means both the atoms are properly sited and the system has a pure $L2_1$ phase and if the value comes to 1, it means it is completely disordered and present the D03 phase. For doing this at the Co K-edge an extra Co – Co path was added at the position of the Fe atoms in the 1st co-ordination shell having coordination of $\gamma \times$C.N(Fe) and the Co-Fe path is having coordination of $(1-\boldsymbol{\gamma})\times$C.N(Fe). So this suggests that after co-occupation of $\boldsymbol{\gamma}\times$C.N (Co) amount of Co atoms at the Fe site, $(1-\boldsymbol{\gamma})\times$C.N (Fe) number of Fe atoms remains at the properly sited Fe position or vice versa. Since Co atoms have two identical sites (¼, ¼, ¼) and (¾, ¾, ¾) in the Co_2FeSi structure, so the probability of antisite disorder with one Co site is the ½ times of total disorder γ, i.e., γ/2. Hence the next nearest neighbor Co-Co shell has (1-γ/2)×C.N (Co) or (2-γ)×C.N (Co)/2 coordination.

Similar co-ordination fraction has been used for the Fe edge fitting also, where instead of replacing the Fe atom; the Co atoms were replaced in the 1st co-ordination shell by adding an extra Fe – Fe path populated by **γ** fraction. Finally, for fitting the '**γ**' factor was varied independently and the *R* and σ^2 of the similar atoms were varied simultaneously by keeping other paths invariant. Figures- 6.11(a) and (b) show the theoretical fitting of the $\chi(R)$ vs. *R* plots at Co K edge for the 'S' series and 'A' series respectively where theoretical modelling has been carried out by considering antisite disorders. The values of the EXAFS parameters at the Co edge used for the fitting are summarized in the Tables-6.3 and 6.4 for the 'S' and 'A' series respectively. In the scattering paths the primed atoms indicate the added paths at the positions of other atomic sites. The variation in the values of **γ** which implies the antisite disorder is shown in the figure-6.12.

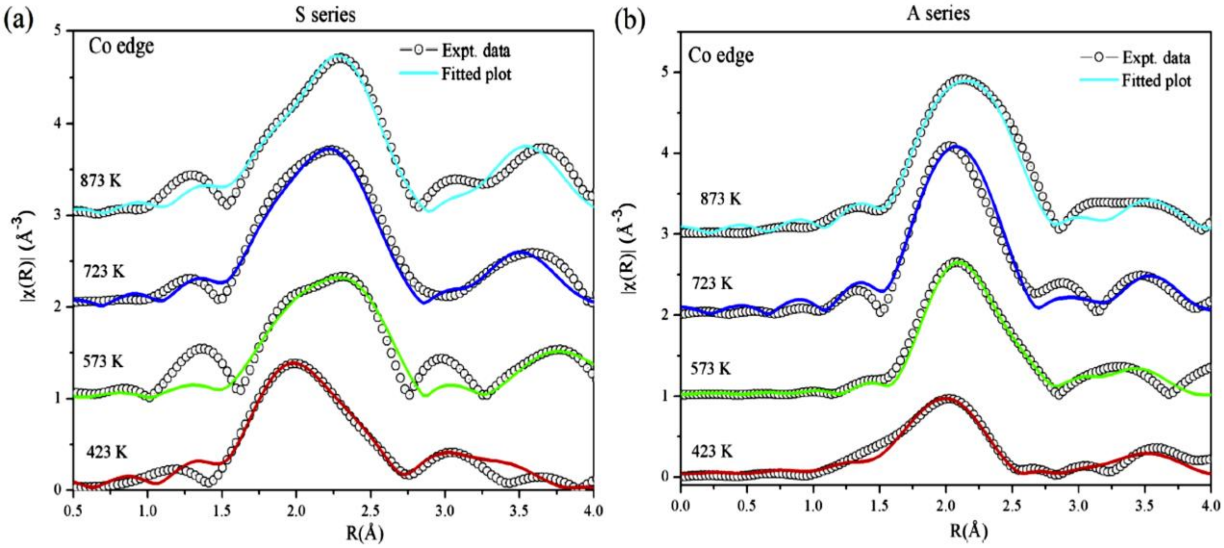

Figure-6.11: Comparison of FT-EXAFS (χ(R) vs R) data along with best fit theoretical plots where theoretical modeling has been carried out assuming antisite disorders for (a) "S" series and (b) "A" series samples.

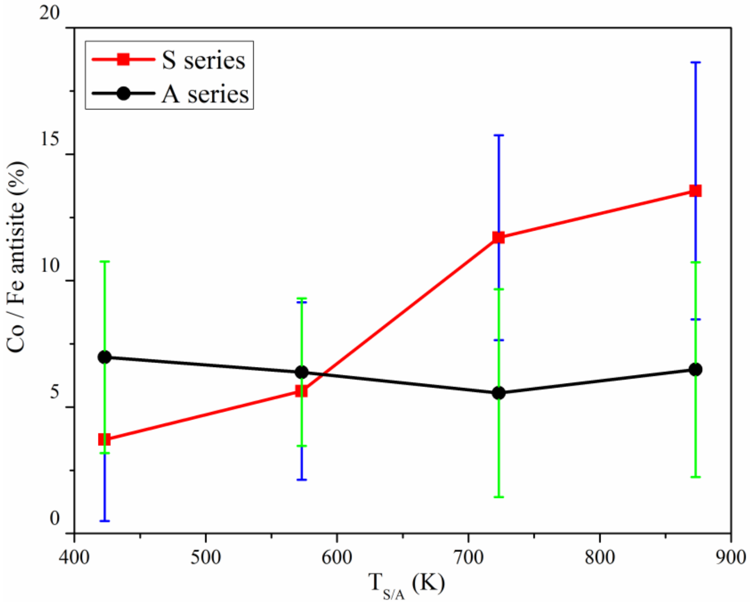

Figure-6.12: Variation in the Co-Fe antisite disorder with the growth temperatures for the S and A series of the CFS thin films.

The above figure shows that the antisite disorder between the Co and Fe atoms for the ‘A’ series remains around 6%, though for the ‘S’ series it increases with increase in the substrate temperature and reaches maximum ~14% for the sample deposited at 873 K temperature. From Tables-6.2 and 6.3 it can be seen that the bond lengths of the disordered path (Co – Co’) are higher than the ordered scattering paths (Co – Fe), while the Co – Co bond length remains invariant to the value obtained in the 1st approach. It is worth noting that the bond lengths of the disorder Co – Co’ path for ‘S’ series samples are higher than for the ‘A’ series samples, though the value of σ^2 remains almost same for both the paths. Similar variation in the bond lengths were confirmed form the Fe K edge fitting also. Thus the results obtained here explain the presence of Co-Fe antisite disorder in the system and correlates with the magnetic properties as described later. It should be noted that apparently it might be observed that EXAFS is not sufficiently sensitive for distinguishing back scattering between Co and Fe atoms, however, in Table-6.5 we have listed R_{factor} values of the theoretical fitting of Co K-edge FT-EXAFS data for the two representative samples.

Table-6.3: Comparison of R_{factor} values for Co K-edge and Fe K-edge fitting of two representative samples obtained by assuming and not assuming Co-Fe anitisite disorder grown ('S' series) and annealed ('A' series) at 873 K.

			R_{factor}	R_{factor}
Sample	Edge	Phase	Without antisite	With antisite
A series (873 K)	Co	$L2_1$	0.0036	0.0022
	Fe	$L2_1$	0.0022	0.0010
S series (873 K)	Co	$L2_1$	0.0071	0.0033
	Fe	$L2_1$	0.0040	0.0032

R_{factor} values have been shown for both cases, viz., fitting without assuming antisite disorder and with assuming antisite disorder. In both the cases it is seen that the R_{factor} values are less when we have considered the antisite disorder manifesting that EXAFS fitting is sensitive to the incorporation of antisite disorder in the theoretical model.

6.3.6 Magnetic Characterizations:

In the Co_2FeSi Heusler alloy Co (*3d*) and Fe (*3d*) atoms contribute to the total magnetic moment of the system, while Si (*p*) is a non-magnetic element. Galanakis et.al. [33] have studied magnetic moments (M_t) of several full Heusler alloys and have shown that it follows an empirical relation $M_t = Z_t - 24$, where Z_t is known as the total number of valance electrons per unit cell. Since it can be seen that maximum no. of occupied spin up states in the unit cell of a full Heusler alloy system can be 12 and maximum no. of occupied spin down states can be 5, so maximum magnetic moment in a full Heusler alloy system like CFS is theoretically possible to7μ_B/f.u. However, due to hybridization of *d* states with *sp* states, the realistic magnetic moment expected in a full Heusler alloy system equals to 6μ_B/f.u. Calculations using LDA+U method also have showed that for CFS alloys, the total magnetic moment near to 6μ_B/f.u is possible to achieve [11]. The static magnetization of the two series of CFS samples prepared by PLD technique was characterized at

300K with varying the applied magnetic field maximum upto 9T. The measured data were diamagnetically corrected by measuring the susceptibility of a similar size of Si substrate. The variation in the virgin M-H curves and hysteresis curves are shown in figures 13(a) and (b) respectively for the 'S' series samples and in figs. 14 (a) and (b) for the 'A' series samples. The variation of the magnetization parameters as saturation magnetization (M_S) and coercive field (H_C) with substrate temperature are also shown in figs.15(a) and (b). The result shows that all the samples are soft ferromagnetic in nature with a well-defined M_R and H_C.

6.3.6.1 M-H curves:

The saturation magnetization was calculated by extrapolating the linear portion in the higher field region to H=0 axis. Figure-6.15 (a) shows that the sample deposited at substrate temperature of 423K has a value of saturation magnetization equals to 6.30µB/f.u, which is close to the expected value as explained earlier.

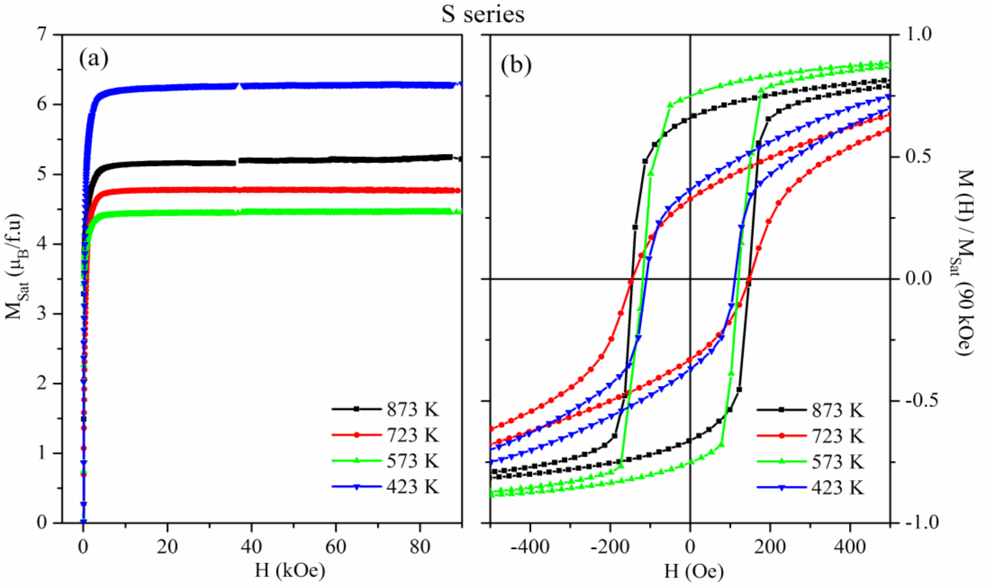

Figure-6.13: Variation in the (a) virgin curves and (b) hysteresis curves (M vs H) curves of the 'S' series samples measured at 300 K temperature.

The saturation magnetization value obtained by us for the Co_2FeSi films deposited by PLD has been found to be higher than that obtained by Mohankumar et. al. (4.9-5.5 µB/f.u), for CFS films deposited by d.c magnetron sputtering or that obtained by Schneider et.al. (4.75 µB/f.u,) for r.f magnetron sputter deposited Co_2FeSi films. Takamura et.al. have also obtained significantly low saturation magnetization value of 4.4 µB/f.u for facing target sputter deposited CFS films deposited on MgO substrate [162]. Bulk-like saturation magnetization value of 6.04 µB/f.u has been observed by Zander et.al. for CFS films deposited on Si(111) substrate using molecular beam epitaxy [164], although Yamada et.al. [165], have reported significantly less saturation magnetization value of ~ 5 µB/f.u for their 25 nm thick CFS thin films grown by MBE.

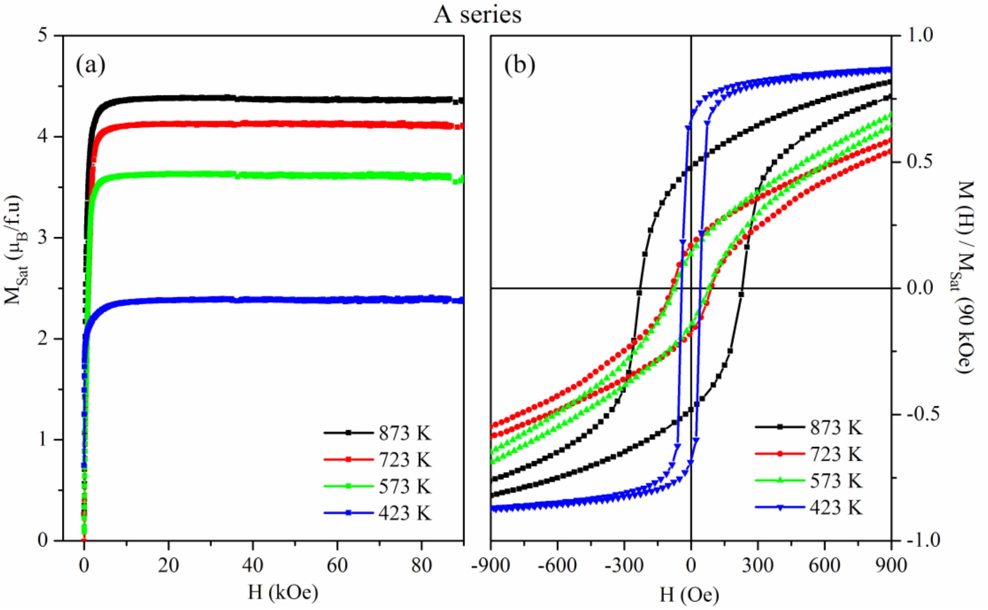

Figure-6.14: Variation in the (a) virgin curves and (b) hysteresis curves normalized to saturation magnetization (M vs H) of the 'A' series samples measured at 300 K temperature.

In case of the present samples, as the substrate temperature is increased further the saturation magnetization for the 'S' series decreases upto T_S = 600 K and then it increases again with increase in the substrate temperatures and remains below the value obtained for the sample deposited at 423K. However, for the 'A' series, the saturation magnetization increases gradually with increase in the annealing temperature, though it always remains lower than that obtained for the 'S' series samples. The higher value of saturation magnetization for the 'S' series samples deposited at elevated substrate temperatures can be explained in terms of higher crystallinity than 'A' series, though the initial decrease of M_S with increase in substrate temperature for the 'S' series samples cannot be explained from the GIXRD study. However, the observation on the antisite disorder from EXAFS study for the 'S' series as discussed above can explain this variation. Due to having Co-Fe type antisite disorder the exchange interaction between the Fe and Co atoms changes and the ferromagnetic ordering decreases with increase in this antisite disorder [26]. The dependence of saturation magnetization with the applied magnetic field for a cubic system is given by [168]:

$$M(H) = M_S[1- \frac{c}{H^2}] \tag{6.1}$$

$$\text{Or } [1-\frac{M(H)}{M_S}] = c \times \frac{1}{H^2} \tag{6.2}$$

where, M_S is the saturation magnetization and $\frac{c}{H^2}$ is contributed as the magneto-crystalline anisotropy term which reduces the magnetization and the effective anisotropy constant K_{eff} is defined as:

$$K_{eff} = \mu_0 M_S\, [\frac{105C}{8}]^{1/2} \tag{6.3}$$

Here the free magnetic space permeability $\mu_0 = 4\pi\times10^{-7}$ H/m and the unit of M_S and H is in (Amp/m), the unit of 'c' is $(\text{Amp/m})^2$ and thus the unit of K_{eff} reduces (Joule/m^3). The value of 'c', which is the slope of the straight-line $[1 - \frac{M(H)}{M_S}]$ vs $\frac{1}{H^2}$, was obtained by linearly fitting the data at the field where the magnetization saturates. The variations in the values the K_{eff} for both the series are shown in figure-6.15 (c). The order of K_{eff} obtained here matches with the value obtained by Deka et. al. for the CFS samples [167]. It shows that magneto-crystalline anisotropy is higher for the S series samples and it decreases with increase in substrate temperature. The value of H_C obtained from figure-6.15 (b) shows that for the 'S' series sample it varies very slightly and remains same at higher substrate temperatures, while for the 'A' series samples there is a significant variation in H_C with increase in the annealing temperature. From the GIXRD study (figure-6.2) we have observed that for the 'S' series samples, the crystallite size does not vary much with substrate temperature, however, the crystallite size increases significantly with annealing temperature for the 'A' series samples. H_C is strongly related to the pinning of magnetic domains at the pinning centers such as grain boundary which again depends on the crystallite size.

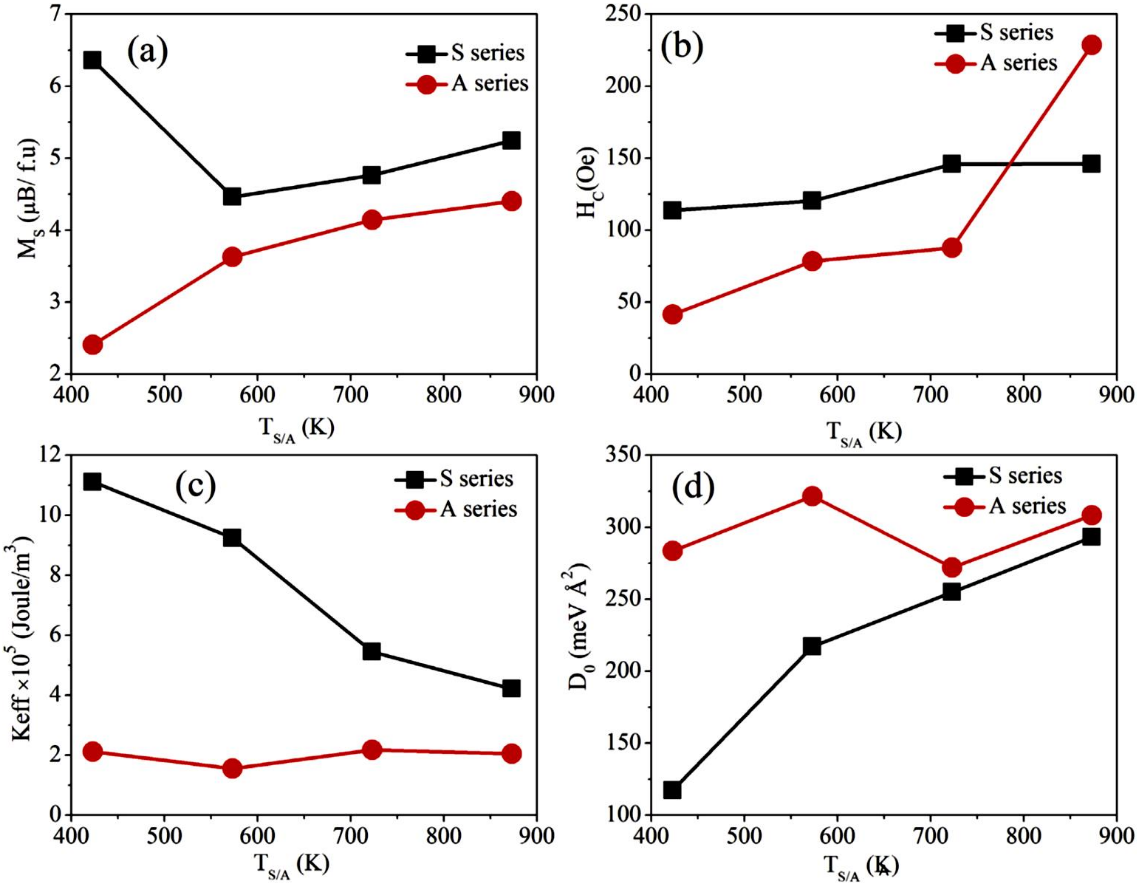

Figure-6.15: Variation in (a) saturation magnetization (M_S), (b) Coercive field (H_C), (c) effective anisotropy constant (K_{eff}) and (d) spin wave stiffness constant (D_0) with growth temperature for both 'S' series and 'A' series samples.

6.3.6.2 Thermal Demagnetization (M-T) curves:

Figures-6.16(a) and (b) show that the slopes of the M(T)/M(5K) curves for the 'S' series samples are steeper than the 'A' series samples manifesting higher value of Curie temperature (T_C)

for the samples prepared with post deposition annealing process. The slopes of the M-T curve decreases with increase in both the substrate and annealing temperatures, manifesting the increase in the T_C. A sudden increase in the value of the magnetization at low temperature was observed below 50K. Similar variation in the M-T curve was observed for CoFeAl/MgO thin film by other workers also [169]. On the basis of the localized electron model [169] the thermal demagnetization of the spontaneous magnetization M (0,T) in a field free condition (H=0) solely depends upon the spin wave (SW) excitation which is proportional to ~$T^{3/2}$ in the low temperature region (~1/3rd of T_C) and other higher order terms in the intermediate and higher temperature regions. So in this context the dependence of the higher order terms of temperature can be neglected and the ratio of M (0,T)/M(0,0) is reduced to the variation with $T^{3/2}$.

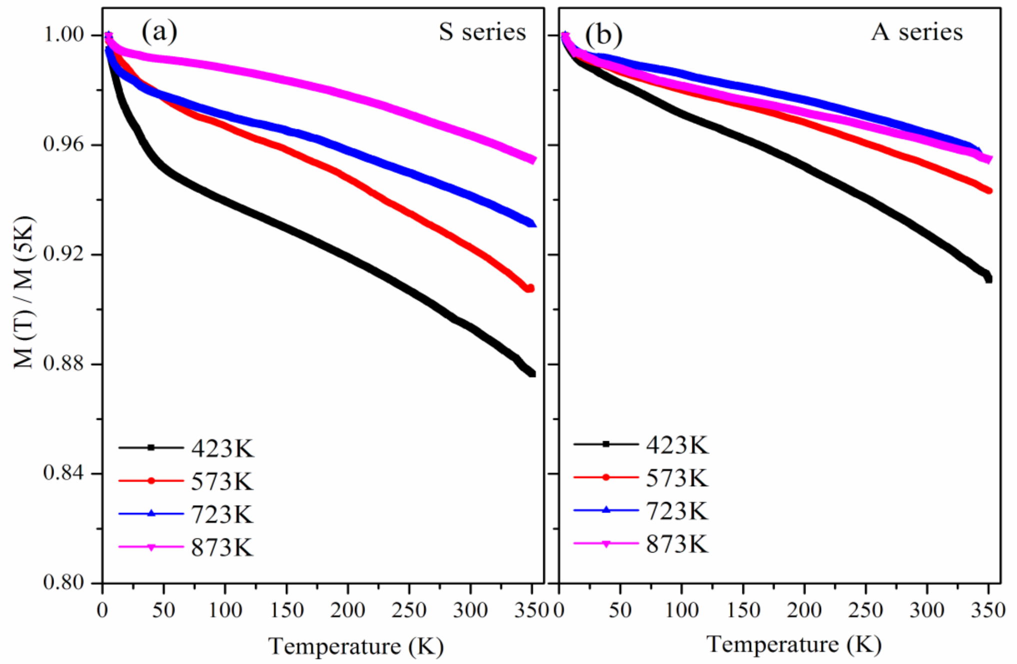

Figure-6.16: Thermal demagnetization or (M(T)/M(5 K)) vs T of the (a) S series and (b) 'A' series of CFS thin films.

Apart from the above described model, the itinerant electron model suggests that the excitation of Stoner particle (SP) contributes to the demagnetization which follows the T^2 law over a wide range of temperature region and thus the in-field thermal demagnetization can be written in terms of both $T^{3/2}$ andT^2 law. The ratio of in-field demagnetization from the spontaneous magnetization can be written as:

$$\Delta M\ (T) = \frac{[M(H,0)-M(H,T)]}{M(H,0)} \tag{6.4}$$

or $$\Delta M(T) = \Delta M_{SW}\ (T) + \Delta M_{SP}\ (T) \tag{6.5}$$

In eqn. 6.5 the $\Delta M_{SW}\ (T)$ can be written as follows [154]:

$$\Delta M_{SW}\ (T) = A(H)T^{3/2} = \frac{g\mu_B}{M(H,0)}\left[\xi(\frac{3}{2}, t_H) \times \left[\frac{k_B T}{4\pi D(0)}\right]^{\frac{3}{2}}\right] \tag{6.6}$$

where g, μ_B and k_B are the Lande g factor, Bohr magneton and the Boltzmann constant respectively, D_0 is the spin wave stiffness constant and the term $\xi\left(\frac{3}{2}, t_H\right)$is known as the Bose-Einstein integral function which was derived by a least square fitting given by Kaul et.al. [154] The above eqn. can be written as:

$$\frac{M(H,T)}{M(H,0)} = [1- A(H)\ T^{3/2} - BT^2] \tag{6.7}$$

A(H) is a field dependent quantity and B be the constant quantity. In case of the present samples it has been observed that the *M(H,T)/M(H,0)* vs. *T* data can be fitted well as per eqn. 6.4 with only the $T^{3/2}$ (SW) term and the T^2 term does not show any contribution. The plots considering equation 8 are shown in the figure-6.17 (a) and (b).

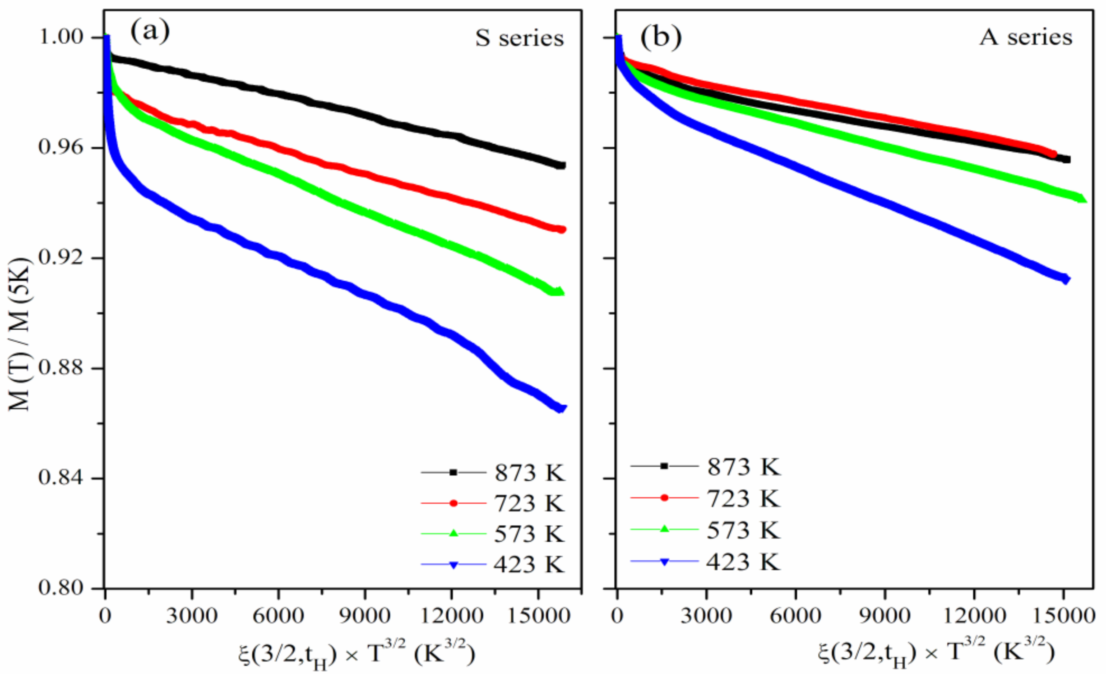

Figure-6.17: Thermal demagnetization or (M(T)/M(5K)) vs $T^{3/2}$(a) 'S' series and (b) 'A' series samples.

The value D_0 is determined from the slope of the plot and the variation in the value of D_0 is shown in the figure-6.15(d), which shows a higher value for the 'A' series samples than for the 'S' series samples manifesting the fact that spin waves for the A series are much stiffer than S series samples.

6.4 Conclusions:

In this chapter a comparative study between the two series of PLD grown Co_2FeSi thin film samples have been carried out; in one series ("S"-series) films have been prepared at elevated substrate temperaturs while in the other series ("A"-series) films have been prepared at RT followed by post deposition annealing. The objective of the study being to investigate about the effect of the different thermal growth processes on the structural and magnetic properties of the CFS films. GIXRD measurements on the thin films show that the phases of the thin films are similar and exactly match with the bulk target. However, the crystallity of the "S" series samples is found to be much better than the “A” series samples and this is also reflected on their variation in the lateral crystallite size of the films. EDXS study shows that Co to Fe ratios in the films remains close to 2:1 at higher temperatures, though higher Si contents in the films were observed due to diffusion from the Si substrate. This is also reflected in the GIXR study of the samples where less dense or Si-excess layer between the bulkfilm and Si substrate were detected. The reflectivity result also shows that though the thickness of the flms remains near to 1100 Å the density of the “S” seriessamples is higher (~9.4 gm/cc) than the “A” series samples (~6.5 gm/cc) and the former series of samples have higher surface roughness also due to larger crystallite size. A strong *p-d* and *d-d* hybridizations were observed for the S and A series samples respectively which characterizes their magnetic interactions. It has been further observed from EXAFS data analysis that Co/Fe antisite disorderexistsfor both the series, though it is higher fopr “S” series samples which increases gradullay with increase in substrate tempearture. Magnetic characterization also shows that the value of the saturation magnetization is higher for the “S” series samples due to better crystallinity though due to the presence of the anitiste disorder in this series the value of saturation magnetization decreases initially with incease in substrate temperature. From the magnetic chacterizations it was also observed that the effective aniosotory constant is higher for the ‘S” series samples.

Chapter-7

INSTALLATION OF THE FACILITY AND THE FIRST XMCD RESULTS FROM AT THE ENERGY-DISPERSIVE EXAFS BEAMLINE OF THE INDUS-2 SYNCHROTRON SOURCE

7.1 Introduction:

The basics of the XMCD technique alongwith the measurement procedures have been discussed in details in Chapter-1. Here we present details of setting up the XMCD measurement facility at the Energy-Dispersive EXAFS beamline (BL-08) at the Indus-2 synchrotron radiation source, RRCAT, Indore, India and the first signal observed from the measurement. This chapter describes the design and development of a water-cooled electromagnet having a maximum magnetic field of 2 T in a good field volume of 125 mm^3 and having a 10 mm hole throughout for passage of the synchrotron beam. This also includes the development of an (X–Z–θ) motion stage for the heavy electromagnet for aligning its axis and the beam hole along the synchrotron beam direction. Along with the above developments, here we also report the first XMCD signal measured on a thick Gd film in the above set-up which shows good agreement with the reported results. This is the first facility to carry out XMCD measurement with hard X-rays in India.

7.2 Development of the electromagnet:

To carry out the XMCD measurements a dipole magnet of maximum field 2 T in a good field volume (GFV) of 125 mm^3 has been developed. The overall size of the magnet is 500 mm × 500 mm × 400 mm and its weight is about 400 kg. Considering the field requirement, structural geometry, uniformity of the magnetic field within a certain volume and cooling process, the design of the magnet has been carried out. Pole shape optimization has been carried out to achieve a field uniformity of 100 p.p.m. in the required GFV. Along with this a motorized X–Z–θ motion stage has been used for alignment and rotation of the electromagnet axis with the beam direction to facilitate studies at different magnetization angles of the sample. The overall system has been designed in such a way that the field remains constant for the duration of the X-ray absorption scan running with a constant current. The whole magnetic system consists of several components, such as magnet coil, magnet core and cooling system.

7.2.1 Electromagnet designing parameters:

The basic requirements for the design of the electromagnet have been listed in Table-7.1. A detailed electromagnetic design for optimization of the magnet yoke and poles (taper and diameter) for the required magnetic peak field in the magnet center was carried out using the software package TOSCA (Electromagnetic Analysis Software, Vector Fields Inc., Oxford, UK).

Table-7.1: Specifications of the electromagnet

Central magnetic field	2 Tesla
Air gap	25 mm
DSV	5 mm
Magnetic field uniformity	< 100 ppm
Magnet shape	H- Dipole
Magnet outer dimensions	500 × 500 × 400 (mm^3)

Figures7.1(a) and (b) show the model for the EM analysis and the variation of the magnetic field uniformity at the air gap between the poles. A 10 mm central bore was made in the magnet poles for the X-ray beam to pass through. Generally, in this configuration the incident beam direction is parallel to the direction of the applied magnetic field. The magnetic core is made out of low-carbon steel plates, while the pole pieces were made of soft pure iron rods. EM simulations

were carried out to optimize magnet dimensions and the pole taper angle for meeting the objective of good field uniformity in the GFV. A pole taper angle of 37° was found to be the most optimum for field uniformity and matches with the theoretical estimates [170]. The minimum field increment of the electromagnet is limited by the step size of the power supply current. Thus, the magnet was designed for field uniformity over the sampled area of the X-ray beam in the geometry.

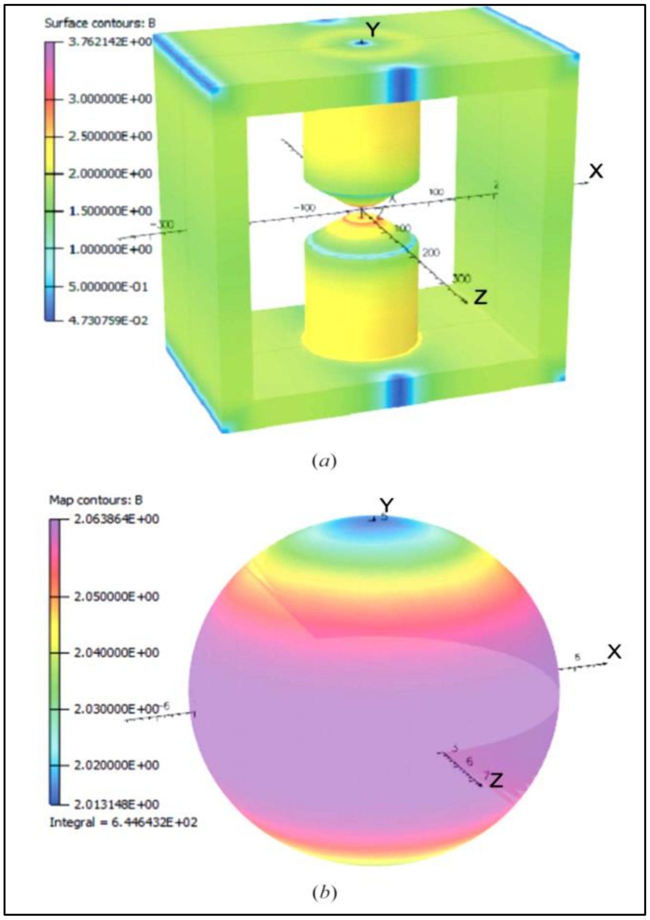

Figure-7.1: (a) Magnetic field in the core at nominal current. (b) Magnetic field uniformity in the good field volume (better than 100 p.p.m.).

7.2.2 Electromagnetic Coil design:

The input ampere turns required for the development of a 2 T magnet is 48000 Ampere Turn. Hence a standard oxygen-free electronic (OFE) grade Cu conductor with a 12 mm × 12 mm square cross section with 6 mm central hole was selected. The thickness of the wire was determined by its mechanical strength. All the electrical terminals were located at the base of the coil for the power supply. These hollow Cu conductors were arranged in a Helmholtz configuration. The joule dissipation by the Cu wire at nominal current is 5 kW, which is removed by demineralized water (flow speed of 2 m s^{-1} at a pressure of 3 bar). The maximum reachable field is limited by the ability to remove the power dissipation in the magnetic coil by water cooling. Thus, based on the above design, development of the electromagnet was carried out. The cross-sectional details of the magnet and magnetic field uniformity are shown in figure-7.2. To carry out the winding of the solenoid coils, suitable jigs were developed. The interlayer insulation was made of glass fiber tapes and the coil was epoxy impregnated to provide better mechanical strength.

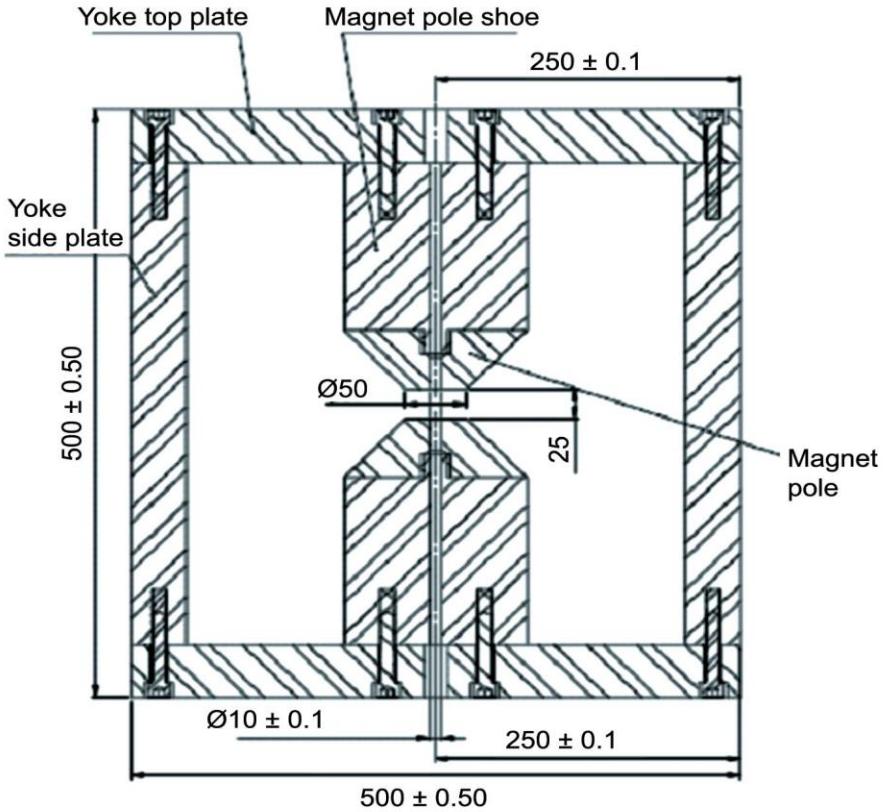

Figure-7.2: Details of the electromagnet cross section (dimensions are in mm).

7.3 Development of magnet mounting motion stage:

A motorized motion stage has been developed for easy and perfect alignment of the axis as well as the beam hole of the heavy electromagnet with that of the synchrotron beam, and also to facilitate studies on different magnetization angles of the sample. The stage can provide X, Z and θ rotation. Here the X motion is the horizontal movement perpendicular to the direction of the beam, Z is the vertical movement and θ is the angle between the beam and the magnet axis about a vertical axis. The movement along the X direction across the beam is achieved through an arrangement with ball screw and nut with linear guides, which has a stroke of ±50 mm and a resolution of 10 mm, while the motion along the Z direction is made possible by a worm gear box along with ball screw and nut with a shaft stroke of ±15 mm and resolution of 10 mm. The rotation has a stroke of ±20˚ and a resolution of 0.01˚ accomplished by a worm gear box. All the motions are remotely computer controlled and measured by independent encoders. Figure-7.3 shows a photograph of the motion stage.

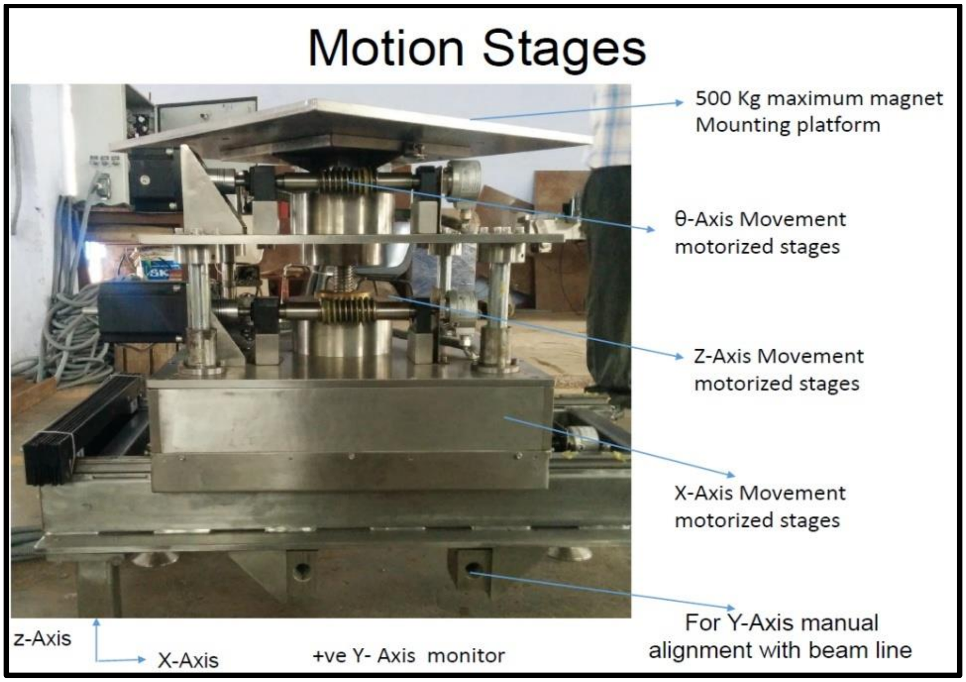

Figure-7.3: The X–Z–θ motion stage, which can carry a maximum of 500 kg.

7.4. Testing of the field of electromagnet:

The electromagnet was tested for its operating performance by increasing the current through the coil up to 300 A. The polarity of the electromagnet was changed by quickly switching at the same current, so that the intensity of the incident X-ray beam does not change within the operation. The flow rate and temperature difference between the inlet and outlet were measured, and were found to agree closely with the design estimates. The central magnetic field was measured with a Hall sensor. A good agreement between the measured and simulated magnetic field at the air gap is shown in figure-7.4.

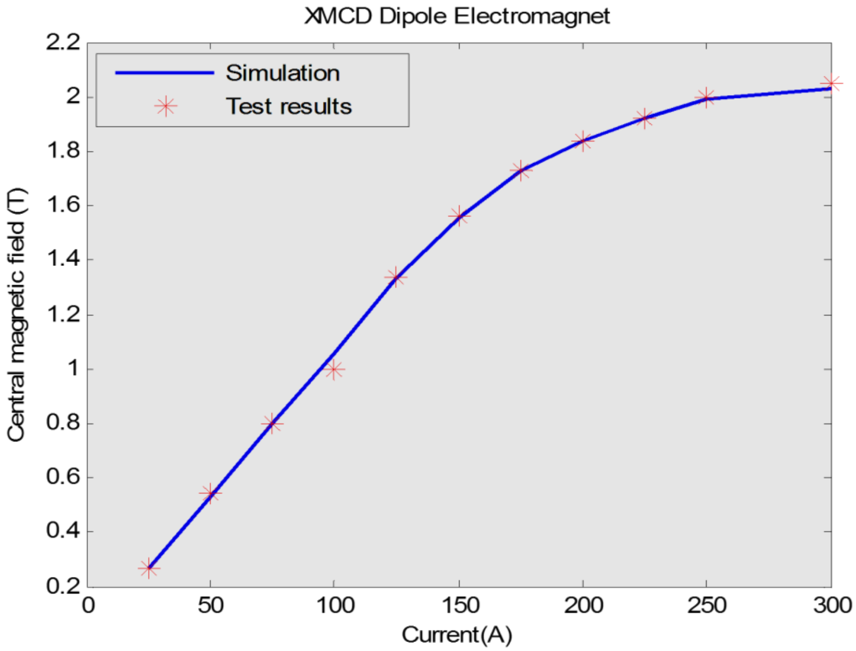

Figure-7.4: Simulated and measured magnetic field in the air gap.

7.5. Experimental description for XMCD measurement:

The details of the beamline have been explained in Chapter-2. For the present measurement, the electromagnet has been placed in the beamline in such a way that the sample position, i.e., the focal point of the bent crystal (S2), coincides with the zone of uniform magnetic field as shown in figure-7.5. In this case the electromagnet, being very heavy (approximate weight: 400 kg), has not been placed on the 2θ arm of the goniometer.

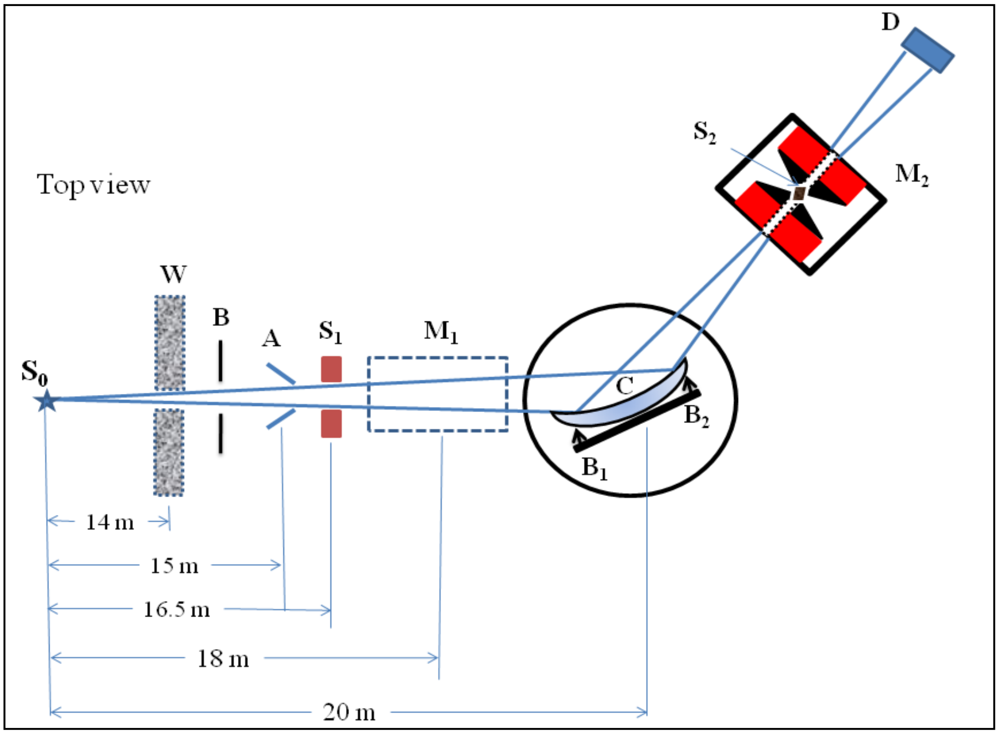

Figure-7.5: Top view of the energy dispersive EXAFS beamline (BL-08) with electromagnet.

Instead it is placed on the specially designed X–Z–θ motion stage, described above, while the detector is placed on the 2θ arm. The motions of the motion stage of the electromagnet are synchronized with the movement of the detector position. A photograph of the whole setup is shown in figure-7.6. The motorized stage of the electromagnet not only helps to align the axis of the magnetic field parallel to the beam but also facilitates studies on different magnetization angles of the sample. As has been mentioned in Chapter-1, XMCD measurement requires synchrotron beam of either right-circular or left-circular polarization. In the present beamline this has been achieved by selecting top-most portion of the beam using a precison slit system prior to the pre-mirror of the beamline. As has been discussed in Chapter-2, the sybnchrotron beam is plane polarised in the plane of the orbit of the electron ring and it is right (left) circularlypolarized as we move up (down) from the beam.

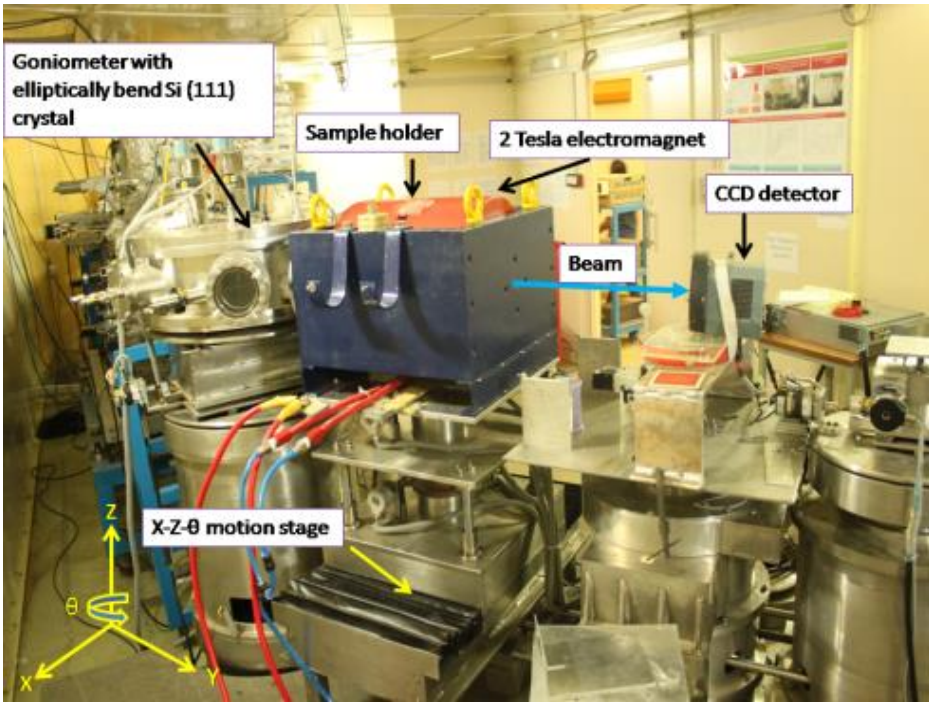

Figure-7.6: Photograph of the Energy-Dispersive EXAFS beamline with the magnet installed at the sample position.

It can also be shown that the SR beam is amlost 90% circularly polarized if we chose the top or bottom most portion of the beam (assuming 0.2 mrad vertical divergence), which is suffiecient for XMCD measurement. Thus the present configuration ensures right circular piolarisation of the beam and finally XMCD measurements on the samples have been carried out under forward and reverse magnetic fields keeping this beam fixed. The setup has been tested by measuring the XMCD signal of a thick Gd film.

7.6 Results and Discussion:

In transmission mode measurement the absorption coefficient (μ) is obtained as $\mu = \ln \frac{I_0}{I_t}$ where I_0 and I_t are the intensities of the photon beam at a particular CCD pixel without and with the sample and the XMCD signal is obtained as μ^+ - μ^- for two different polarities of the electromagnet (+ve and -ve) at a certain polarization of incident X-rays. To reduce the symmetric error the scan at a constant magnetic field was taken for multiple times and averaged. The CCD channel numbers have been calibrated to the energy scale by measuring the absorption edges of a standard Fe foil and Gd L_3 edge of standard Gd_2O_3 powders having nominal K and L_3 energy edges at 7112 eV and 7243 eV respectively. Finally, the setup has been tested by measuring the XMCD signal of a ~4 mm-thick Gd film prepared by DC magnetron sputtering of a 99.99% pure Gd metallic target on an Al foil substrate. The foil was mounted on a rigid teflon support with a hole at the center for passage of the synchrotron beam and was placed at the center of the air gap between two magnetic poles by holding the teflon support by a custom-made teflon holder. Figure-7.7 shows the normalized XANES spectra and the XMCD signal of the Gd foil taken at a magnetic field of 2 T by switching the polarity of the electromagnet.

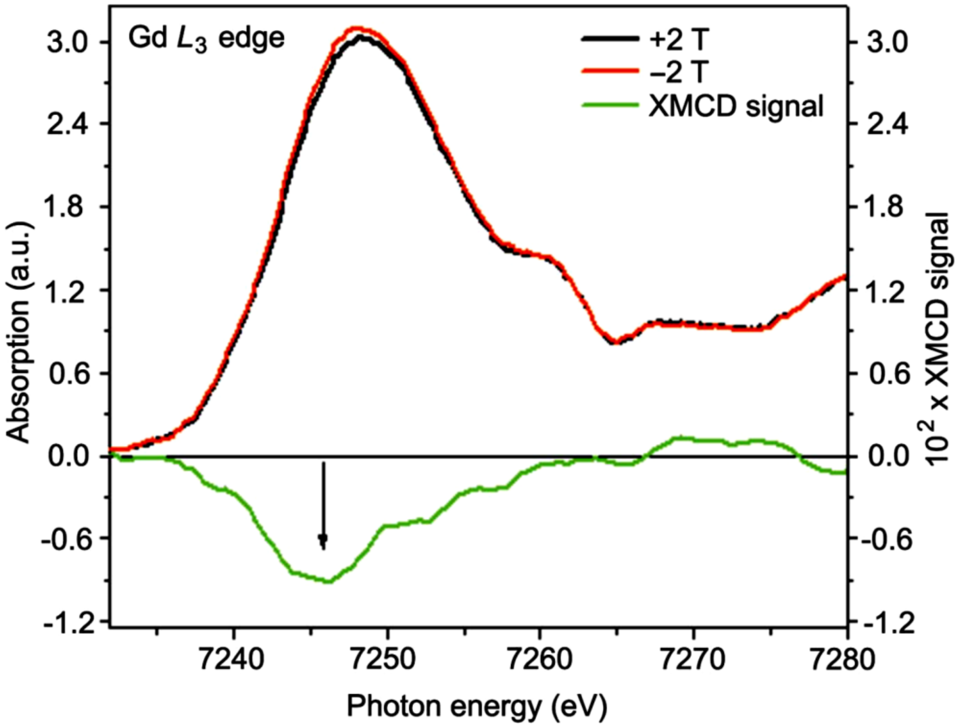

Figure-7.7: Normalized XANES spectra and the magnified XMCD signal of a thick Gd film.

The magnitude of the field was chosen so that the magnetic moments saturate. It has been observed that the XMCD signal profile of the thick Gd film agrees well with that reported by other workers [171]

7.7 Conclusions:

In this chapter the details of the installation and comissioning of the hard X-ray XMCD facility at the Energy Dispersive EXAFS beamline at Indus-2 synchrotorn source has been described. A water cooled electromagnet was designed and fabricated for this purpose which delivers a maximum magnetic field of 2T at the centre between the two magnetic poles. The electromagnet has been placed on an indigenously built X-Z-θ stage in the 2θ axis of the the Energy Dispersive EXAFS beamline (BL-08) with the pole gap coinciding with the sample position. The beam passes through the sample and the absorption spectra are detected at a position sensitive CCD detector. For the polarization selection of the synchrotron beam the top most portion of beam was selected by a pceision slit placed prior to the pre-mirror of the beramluine and the absorption data were taken by changing the polarity of the electromagnet, the difference of which gives the XMCD signal. The set-up has been tested sucessfully by measuring the Gd L_3 edge XAS and XMCD spectra of a standard Gd foil whichagrees with the previously reported results.

Chapter-8

Ab-INITIO THEORETICAL SIMULATION OF XAS AND XMCD SPECTRA OF FULL HEUSLER ALLOYS AND K- EDGE XMCD MEASUREMNT

8.1 Introduction:

This chapter is divided into two parts. In the first part we have described density functional theory (DFT) based theoretical calculations on Ni_2FeGa, Co_2FeGa (CFG), Co_2FeAl (CFA), Co_2FeSi (CFS) compoundsusing the Spin-Polarized Relativistic Korringa-Kohn-Rostoker (SPR-KKR) computer code [103]. In the DFT study the SCF calculations were done on the off-stoichiomentric compositions using two different XC functions and the values of the total magnetic moments were compared with the literatures. On this basis the DOS plots on the off-stoichiometric compounds along with the stoichiometric compounds were done and the values of spin polarizations were obtained. Finally, both the K and L-edge XAS and XMCD spectra were generated and those were correlated with their band structure. In the second part we have shown the XAS and XMCD spectra of Co_2FeSi Heusler alloy thin film measured using the installed XMCD facility at the Energy Dispersive EXAFS beamline (BL-08) at Indus-2 SRS.

8.2 Computational Method:

In this present work we have carried out DFT simulation of XMCD spectra of few full Heusler alloys of Ni_2GeGa and Co_2FeZ (Z = Ga, Al, Si) to study the effect of antisite disorder on the XMCD spectra as well as on the magnetic moments. Apart from stoichiometric composition, two off-stoichiometric compositions were chosen with Co to Fe ratio as 1.5 and 2.75. The lattice parameters of Co_2FeZ samples were taken from the previously reported values [172]. These X_2YZ type

Heusler alloy compounds crystallize in cubic $L2_1$ structures with space group *Fm-3m* (space group no. 225), which consists of four interpenetrating f.c.c sublattices. Here the X and Y atoms are the transition metal elements and Z is a sp element. In general, in the full Heusler alloys the X atom is placed at the Wyckoff position 8c (¼, ¼, ¼), the Y and Z atoms are located at 4b (½, ½, ½) and 4a (0, 0, 0) positions. For the off-stoichiometric materials the excess amount of Co (>2) and Fe (>1) were considered to be placed at the Y and X positions, respectively.

In order to calculate the partial, total spin magnetic moments, density of states (DOS) and to generate the XAS and XMCD spectra, we have used Green's function based Spin-Polarized Relativistic Korringa-Kohn-Rostoker (SPR-KKR) computer code [103]. The Brillouin Zone (BZ) integration was done by taking number of *k* points (NKTAB) equal to 1000 and 2000 for the SCF/XAS and DOS calculations respectively, using special points sampling method [103]. The angular momentum cut-off parameter (NL) was taken as $l_{max}+1 = 4$, according to the atomic types (transition metals) in the system. For the comparison of the magnetic moments we have carried out the relativistic SCF calculations using local density approximation (LDA) (Vosko-Wilk-Nusair parameterization) [173] and generalized gradient approximation (GGA) (Perdew-Burke-Ernzehof parameterization) [174] for the exchange correlation (XC) functionals. The ratio of orbital and spin magnetic moments of Co and Fe atoms have also been calculated. The off-stoichiometric alloys $Co_2(Co_{0.2}Fe_{0.8})Ga$ or $(Co_{1.8}Fe_{0.2})FeGa$ have been treated by the coherent potential approximation (CPA) as implemented in the SPR-KKR computer code [103].

8.3 Results and Discussions:

In this section we have discussed the estimation of total (μ_{tot}) and atom projected spin (μ_s) and orbital (μ_r) magnetic moments of Ni, Co and Fe atoms in the Heusler alloy systems with two different approaches of exchange correlation (XC) functions. Following this we have also discussed the variation in the density of states (DOS) and spin polarization (SP) of the system at the Fermi level for different stoichiometry of the materials. Further, simulations of both the K and $L_{3,2}$-edges XAS and XMCD results corresponding to the magnetic moment and DOS have also been presented. The magnetic moments and DOS of alloys with stoichiometric compositions (X_2YZ) have been compared with the previously reported results.

8.3.1 SCF calculations:

The values of the magnetic moment of the materials were calculated using Self Consistent Field (SCF) calculations. In Tables-8.1 -8.4, the theoretically simulated values of partial and total moments of different atoms for the Heusler compounds have been listed. While in Tables 8.1(a). 8.2(a), 8.3(a) and 8.4(a) the values of the moments for the stoichiometric alloys have been listed, in the other tables (Tables 8.1(b), (c); 8.2(b), (c); 8.3(b), (c) and 8.4(b), (c)) the values for the non-stoichiometric alloys have been given. In tables of the off-stoichiometric compositions the sites mentioning as Ni2/Co2 and Fe2 atoms are situated at ordered sites i.e., X and Y positions and Ni1/Co1 and Fe1 atoms are situated at antisites i.e., Y and X positions respectively).

The values of the magnetic moments have been calculated using both the Linear Density Approximation (LDA) and Generalized Gradient Approximation (GGA) exchange correlation (XC) functionals, considering the relativistic effect in the system. It was observed that while LDA XC functional leads to underestimation of the magnetic moments, the results obtained using GGA XC functional match well with the literature [172, 175]. For the off-stoichiometric cases, we found that as in the stoichiometric cases, the total moment of the system is slightly higher when GGA is considered in comparison with the results obtained from LDA XC functional. As partial moment of the Fe atom (which is the major moment-carrying atom in these systems) is higher than that of the Ni or Co atoms, for Ni/Co-excess samples the total moment is less than that of stoichiometric compositions. However, the Fe-excess samples exhibit higher total moment as expected. In Ni/Co-excess samples, the Ni/Co atom at the Y site has moment similar to the one for Ni/Co at the X site in stoichiometry, while the Ni/Co atom at the X site shows an increase in the moment value (Tables-8.1(b) - 8.4(b)). On the other hand, in the Fe-rich cases, Fe atom at the X site has lower (by about 1 μ_B) moment compared to the Y site. It is interesting to note that while for CFA the total moment as well as the moment of Fe atom is smaller compared to CFG, for CFS, the partial and total moments are the highest. It is to be noted that though for the stoichiometric compositions the total magnetic moment is near to the sum of the magnetic moment of atoms situated at X site (2 times), Y and Z sites, the contradiction appears for the off-stoichiometric compositions. In these compositions the total magnetic moment is not the direct sum of the magnetic moment of the constituent atomsdue to the magnetic moment of the interstitial sites between to non-overlapping spheres [172]

We observe from Tables-8.1(b), (c) to 8.4(b), (c) that in the off-stoichiometric compositions after adding excess amount of Ni/Co and Fe atoms which occupy the antisites (Fe and Ni/Co, respectively) the value of total moment does not decrease unlike the stoichiometric cases. This suggests that the Ni/Co or Fe atoms occupying the antisites interact ferromagnetically with the atoms occupying their original positions (X and Y, respectively).

Table-8.1 (a) – (c): Value of spin (μ_s), orbital (μ_l) and total magnetic moment (μ_{tot}) in μB/f.u of different elements of stoichiometric and off-stoichiometric Ni_2FeGa Heusler alloy

(a) Ni_2FeGa								
	LDA				GGA			
Atom site	μ_s	μ_l	$\mu_{l/}\ \mu_s$	μ_{tot}	μ_s	μ_l	$\mu_{l/}\ \mu_s$	μ_{tot}
Ni	0.28	0.03	0.11	0.31	0.29	0.03	0.10	0.32
Fe	2.82	0.06	0.02	2.88	2.93	0.07	0.02	3.00
Ga	-0.04	0.00	0.00	-0.04	-0.05	0.00	0.00	-0.05
Total	3.33	0.12	0.04	3.45	3.46	0.13	0.04	3.59

(b) $Ni_{2.2}Fe_{0.8}Ga$								
	LDA				GGA			
Atom site	μ_s	μ_l	$\mu_{l/}\ \mu_s$	μ_{tot}	μ_s	μ_l	$\mu_{l/}\ \mu_s$	μ_{tot}
Ni1	0.26	0.03	0.12	0.29	0.27	0.03	0.11	0.30
Ni2	0.11	0.01	0.09	0.12	0.13	0.02	0.15	0.15
Fe	2.79	0.07	0.03	2.86	2.91	0.07	0.02	2.98
Ga	-0.03	0.00	0.00	0.03	-0.05	0.00	0.00	-0.05
Total	2.73	0.11	0.04	2.84	2.85	0.11	0.04	2.96

(c) $Ni_{1.8}Fe_{1.2}Ga$								
	LDA				GGA			
Atom site	μ_s	μ_l	$\mu_{l/}\ \mu_s$	μ_{tot}	μ_s	μ_l	$\mu_{l/}\ \mu_s$	μ_{tot}
Ni	0.30	0.03	0.10	0.33	0.32	0.03	0.09	0.35
Fe1	2.79	0.07	0.03	2.86	2.90	0.07	0.02	2.97
Fe2	1.89	0.05	0.03	1.94	2.01	0.05	0.02	2.06
Ga	-0.04	0.00	0.00	-0.04	-0.06	0.00	0.00	0.06
Total	3.66	0.13	0.04	3.79	3.83	0.14	0.04	3.97

Table-8.2 (a) – (c): Value of spin (μ_s), orbital (μ_l) and total magnetic moment (μ_{tot}) in μB/f.u of different elements of stoichiometric and off-stoichiometric Co_2FeGa Heusler alloy. (Co2 and Fe2 atoms at ordered site i.e X and Y positions and Co1 and Fe1 atoms at other site i.e Y and X sites respectively).

(a) Co_2FeGa								
	LDA				GGA			
Atom site	μ_s	μ_l	μ_l/μ_s	μ_{tot}	μ_s	μ_l	μ_l/μ_s	μ_{tot}
Co	1.12	0.05	0.05	1.17	1.14	0.05	0.04	1.19
Fe	2.76	0.14	0.05	2.90	2.83	0.06	0.02	2.89
Ga	-0.08	0.00	-0.00	-0.08	-0.11	0.00	0.00	-0.11
Total	4.90	0.15	0.03	5.05	5.00	0.16	0.03 0.0	5.16

(b) $Co_{2.2}Fe_{0.8}Ga$								
	LDA				GGA			
Atom site	μ_s	μ_l	μ_l/μ_s	μ_{tot}	μ_s	μ_l	μ_l/μ_s	μ_{tot}
Co1	1.70	0.11	0.06	1.81	1.80	0.10	0.06	1.90
Co2	1.13	0.05	0.04	1.18	1.17	0.05	0.04	1.22
Fe	2.73	0.06	0.02	2.79	2.80	0.06	0.02	2.86
Ga	-0.08	0.00	0.00	-0.08	-0.10	0.00	0.00	-0.10
Total	4.71	0.16	0.03	4.87	4.83	0.06	0.01	4.89

(c) $Co_{1.8}Fe_{1.2}Ga$								
	LDA				GGA			
Atom site	μ_s	μ_l	μ_l/μ_s	μ_{tot}	μ_s	μ_l	μ_l/μ_s	μ_{tot}
Co	1.05	0.04	0.04	1.09	1.12	0.05	0.04	1.17
Fe1	2.72	0.06	0.02	2.79	2.78	0.06	0.02	2.84
Fe2	1.54	0.03	0.02	1.57	1.83	0.05	0.03	1.88
Ga	-0.08	0.00	0.00	-0.08	-0.11	0.00	0.00	-0.11
Total	4.84	0.15	0.03	4.99	5.05	0.15	0.03	5.20

Table-8.3 (a) – (c): Value of spin (μ_s), orbital (μ_l) and total magnetic moment (μ_{tot}) in μB/f.u of different elements of stoichiometric and off-stoichiometric Co_2FeAl Heusler alloy. (Co2 and Fe2 atoms at ordered site i.e X and Y positions and Co1 and Fe1 atoms at other site i.e Y and X sites respectively).

(a) Co_2FeAl								
	LDA				GGA			
Atom site	μ_s	μ_l	μ_l/μ_s	μ_{tot}	μ_s	μ_l	μ_l/μ_s	μ_{tot}
Co	1.15	0.05	0.04	1.20	1.17	0.05	0.04	1.22
Fe	2.66	0.06	0.02	2.72	2.74	0.06	0.02	2.80
Al	-0.11	0.00	0.00	-0.11	-0.15	0.00	0.00	-0.15
Total	4.85	0.16	0.03	5.01	4.93	0.16	0.03	5.09

(b) $Co_{2.2}Fe_{0.8}Al$								
	LDA				GGA			
Atom site	μ_s	μ_l	μ_l/μ_s	μ_{tot}	μ_s	μ_l	μ_l/μ_s	μ_{tot}
Co1	1.62	0.10	0.06	1.72	1.73	0.10	0.06	1.83
Co2	1.16	0.05	0.04	1.21	1.19	0.05	0.04	1.24
Fe	2.64	0.06	0.02	2.70	2.72	0.06	0.02	2.78
Al	-0.11	0.00	0.00	-0.11	-0.15	0.00	0.00	-0.15
Total	4.64	0.16	0.03	4.80	4.76	0.16	0.03	4.92

(c) $Co_{1.8}Fe_{1.2}Al$								
	LDA				GGA			
Atom site	μ_s	μ_l	μ_l/μ_s	μ_{tot}	μ_s	μ_l	μ_l/μ_s	μ_{tot}
Co	1.10	0.04	0.04	1.14	1.13	0.05	0.04	1.18
Fe1	2.62	0.06	0.02	2.68	2.70	0.06	0.02	2.76
Fe2	1.51	0.03	0.02	1.54	1.72	0.04	0.02	1.76
Al	-0.12	0.00	0.00	-0.12	-0.16	0.00	0.00	-0.16
Total	4.75	0.14	0.03	4.89	4.92	0.15	0.03	5.07

Table-8.4 (a) – (c): Value of spin (μ_s), orbital (μ_l) and total magnetic moment (μ_{tot}) in µB/f.u of different elements of stoichiometric and off-stoichiometric Co_2FeSi Heusler alloy. (Co2 and Fe2 atoms at ordered site i.e X and Y positions and Co1 and Fe1 atoms at other site i.e Y and X sites respectively).

(a) Co_2FeSi								
	LDA				GGA			
Atom site	μ_s	μ_l	μ_l/μ_s	μ_{tot}	μ_s	μ_l	μ_l/μ_s	μ_{tot}
Co	1.23	0.07	0.06	1.30	1.30	0.04	0.03	1.34
Fe	2.76	0.06	0.02	2.82	2.87	0.06	0.02	2.93
Si	-0.03	0.00	0.00	-0.03	-0.05	0.00	-0.03	-0.05
Total	5.19	0.15	0.03	5.34	5.42	0.15	0.03	5.57

(b) $Co_{2.2}Fe_{0.8}Si$								
	LDA				GGA			
Atom site	μ_s	μ_l	μ_l/μ_s	μ_{tot}	μ_s	μ_l	μ_l/μ_s	μ_{tot}
Co1	1.52	0.17	0.11	1.69	1.62	0.17	0.10	1.79
Co2	1.23	0.04	0.03	1.27	1.29	0.04	0.03	1.33
Fe	2.75	0.06	0.02	2.81	2.85	0.06	0.02	2.91
Si	-0.04	0.00	0.00	-0.04	-0.05	0.00	0.00	-0.05
Total	4.91	0.17	0.03	5.08	5.13	0.17	0.03	5.30

(c) $Co_{1.8}Fe_{1.2}Si$								
	LDA				GGA			
Atom site	μ_s	μ_l	μ_l/μ_s	μ_{tot}	μ_s	μ_l	μ_l/μ_s	μ_{tot}
Co	0.09	0.03	0.33	0.12	1.25	0.04	0.03	1.29
Fe1	2.61	0.05	0.02	2.67	2.85	0.06	0.02	2.91
Fe2	1.28	0.03	0.02	1.31	1.70	0.03	0.02	1.73
Si	-0.08	0.00	0.00	-0.09	-0.06	0.00	0.00	-0.06
Total	5.02	0.10	0.02	5.12	5.38	0.14	0.03	5.52

For the case of Co_2FeSi sample, the values of total magnetic moment obtained (Table-8.4(a) – (c)) using both LDA and GGA are found to be less than the experimentally observed and S-P rule predicted values of ~ 6 μB [175]. It is argued in the literature thaCo_2FeSi turns out to be a correlated system where on-site Coulomb interaction term is needed to explain the experimental results [176,177]. In this work, therefore, we have also used GGA+U approach for the calculation of moment in case of CFS. The on-site Coulomb correlation has been found to have a significant impact and it increases the value of moment substantially. The on-site Coulomb correlation term (U) and the exchange interaction term (J) were taken as 2.5 and 0.8 eV, respectively. The values of the magnetic moments obtained are summarized in Table-8.5(a) – (c). The value of total moment of the CFS sample has increased by 0.59 µB/f.u. and it matches well with the literature [175].

Table-8.5 (a) – (c): Value of spin (μ_s), orbital (μ_l) and total magnetic moment (μ_{tot}) in µB/f.u of different elements of stoichiometric and off-stoichiometric Co_2FeSi Heusler alloy using GGA+U XC; (Co2 and Fe2 atoms at ordered site i.e X and Y positions and Co1 and Fe1 atoms at other site i.e Y and X sites respectively).

(a) Co_2FeSi				
Atom site	μ_s	μ_l	μ_l/μ_s	μ_{tot}
Co	1.39	0.07	0.05	1.46
Fe	3.11	0.10	0.03	3.21
Si	-0.07	0.00	0.00	-0.07
Total	5.82	0.24	0.04	6.06

(b) $Co_{2.2}Fe_{0.8}Si$				
Atom site	μ_s	μ_l	μ_l/μ_s	μ_{tot}
Co1	1.75	0.87	0.50	2.62
Co2	1.33	0.06	0.05	1.39
Fe	3.08	0.11	0.04	3.19
Si	-0.08	0.00	0.00	-0.08
Total	5.39	0.39	0.07	5.78

(c) $Co_{1.8}Fe_{1.2}Si$				
Atom site	μ_s	μ_l	μ_l/μ_s	μ_{tot}
Co	1.31	0.07	0.05	1.38
Fe1	3.07	0.10	0.03	3.17
Fe2	1.83	0.05	0.03	1.88
Si	-0.09	0.00	0.00	-0.09
Total	5.69	0.23	0.04	5.92

8.3.2 Density of States (DOS) calculation:

We have carried out calculations of spin-polarized density of states (DOS) of the Co-based full Heusler alloys for both the stoichiometric and off-stoichiometric compositions. The total density of states plots obtained using GGA XC functional have been shown in the figures-8.1(a) – (d). The DOS results of our calculations have overall matching with the previously reported data for Co_2FeZ alloys [178, 179]. However, it was observed that close to the Fermi energy, the matching is not quite good, leading to a mismatch in the values of spin-polarization (SP) at the Fermi level (E_F) for these alloys. To probe the features of DOS near the E_F in detail, we have carried out the calculations using full potential (with spin-polarized scalar relativistic Hamiltonian) as implemented in SPR-KKR program [103]. The DOS plots using full potential of the stoichiometric compounds Co_2FeZ (Z=Al, Ga and Si) have been depicted in the figures-8.2 (a)-(c). It was observed that not only the half-metallic property improves for Co_2FeAl and Co_2FeGa, when compared with the data from the literature [172], consequently, the spin polarization (SP) and the gap between the valance and conduction band increases as well at E_F. However, for the Co_2FeSi, the results still do not match with the literature and the value of SP is still negative. Taking the clue from the literatures as well as from our results on magnetic moment, we use the GGA+U XC functional in this case. We find that with U and J values of 2.5 and 0.8 eV, respectively, the spin polarization at the Fermi energy (Figure-8.3) changes from a negative value to a position value. This trend matches well with the literatures also.

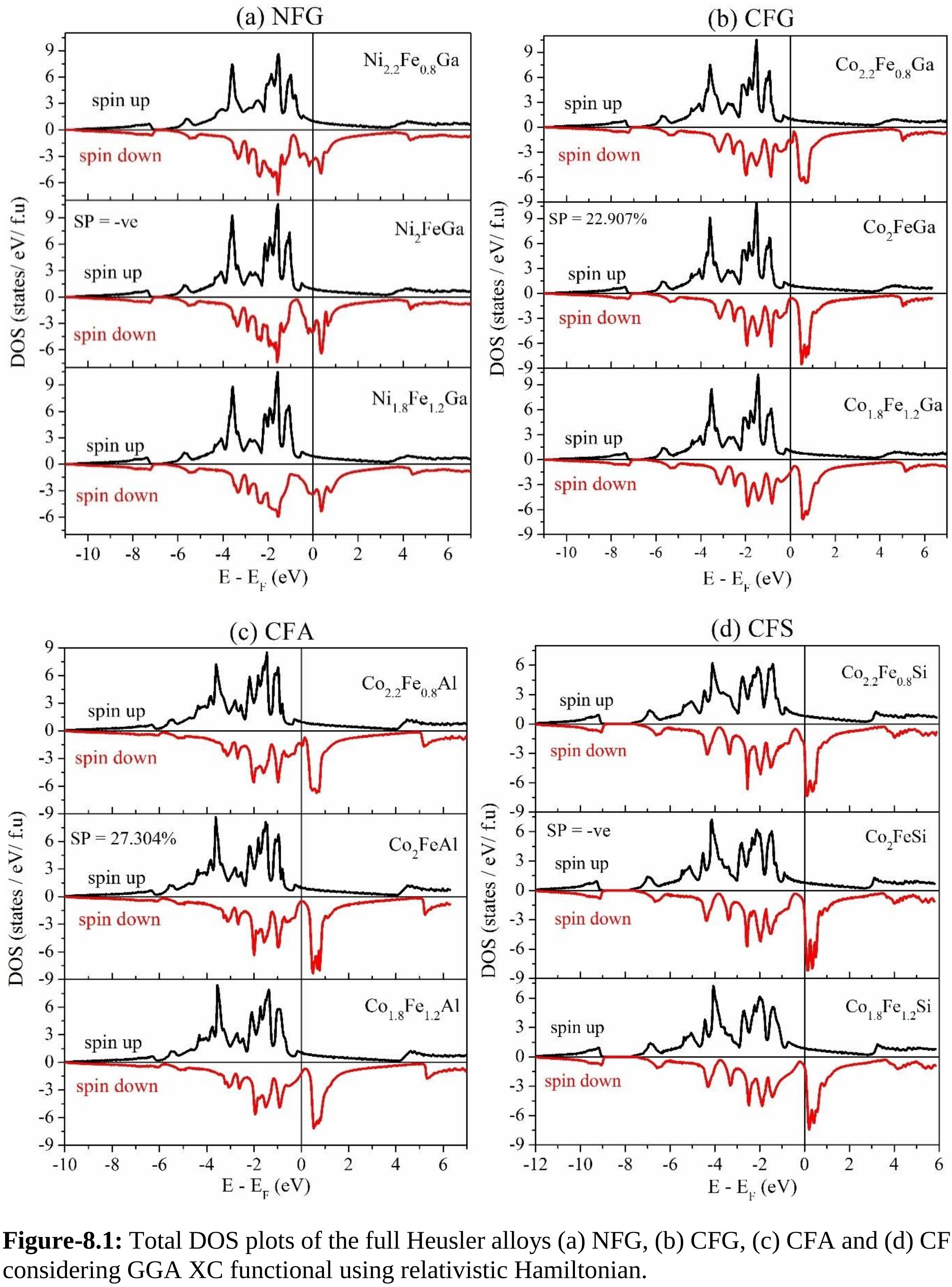

Figure-8.1: Total DOS plots of the full Heusler alloys (a) NFG, (b) CFG, (c) CFA and (d) CFS by considering GGA XC functional using relativistic Hamiltonian.

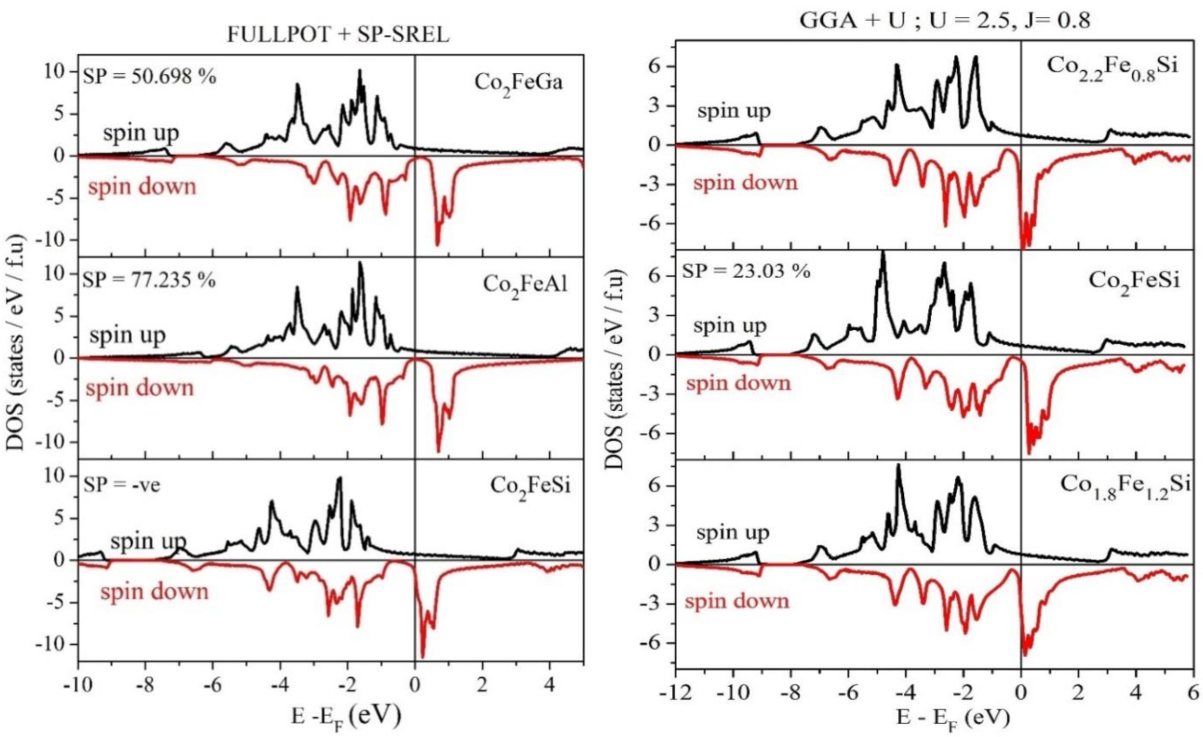

Figure-8.2: Total DOS plots of the (a) stoichiometric compositions using full potential (b) CFS compound using GGA+U approach for different compositions

8.3.3 XAS and XMCD characterization:

We now discuss our result of the calculated XAS and XMCD spectra of the Full Heusler alloys both at the K and $L_{2,3}$ edges of the transition metal elements at different atomic sites. At the K absorption edge, the excitation of the photoelectrons occurs from the 1s→4p orbital and in the $L_{3,2}$ absorption edges, the transition occurs from $2p_{3/2\ ,1/2} \rightarrow 3d$ orbital. As both the XANES and the XMCD signals depend upon the dipole transitions from the inner shell states to the final unoccupied valance states, we have tried to correlate the observed XANES and the XMCD spectra with the Partial DOS of the individual atoms. Figures-8.3 (a), (b) show the variation in the K and L-edges of the XAS and XMCD spectra of the stoichiometric compounds of the Co based Heusler alloys.

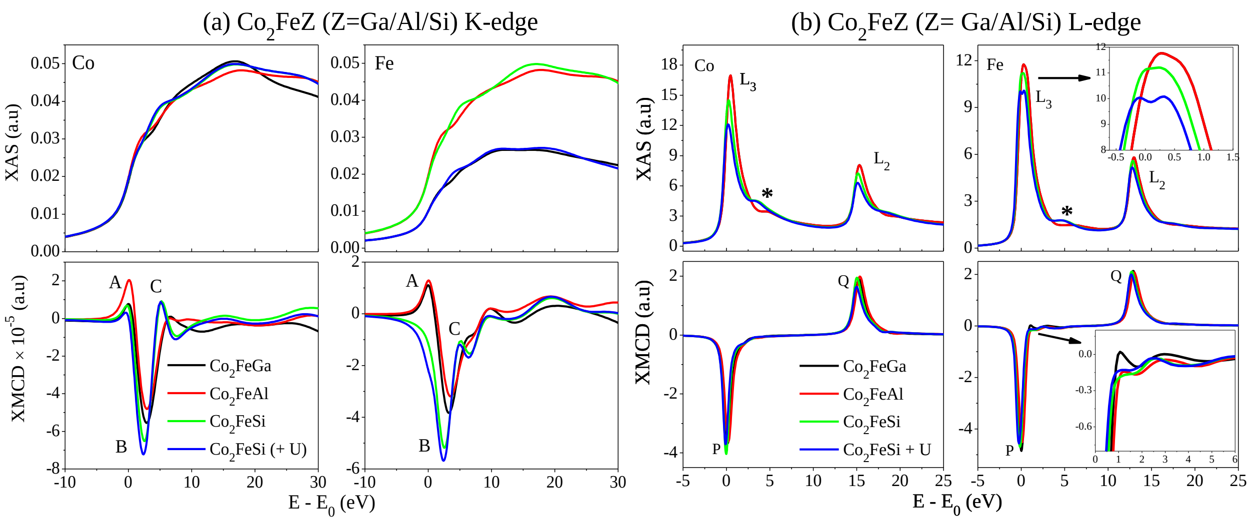

Figure-8.3: Co and Fe (a) K-edge and (b) L-edge XAS and XMCD spectra of the stoichiometric Heusler compounds.

A detailed analysis of the spectral features of the XAS and XMCD spectrareveals the effect of band structure and magnetic moment on the absorption spectra. The first inflection in the absorption spectra is known as the absorption edges of the atom which is followed by the other peaks due to the transition to the other upper levels. Both the K-edge and L-edge XAS and XMCD spectra show overall good correspondence to each other and identical variation in the peak intensities. The K-edge XMCD spectra are characterized by 3 peaks, where ‘A’, ‘C’ are the two positive peaks and ‘B’ is intense negative peak near to the absorption edge, while the L-edge XMCD spectraare characterized by one negative peak ‘P’ at L_3-edge and one positive peak ‘Q’ at the L_2-edge. All the absorption edges show the features similar to the metallic phases except for the Fe L_3 edge of the Co_2FeSi sample. The splitting of the peak becomes more prominent for Co_2FeSi sample after adding +U over GGA. A little hump at about 3.5 eV and 4.8eV above the Co and Fe L_3-edges were observed for the Co_2FeSi and Co_2FeGa/Co_2FeAl compounds. These satellite peaks correspond to the features present in the respective partial DOS of the Co and Fe atoms for the spin up conduction band above the Fermi level, as observed earlier [180].

At the Fe L_3-edge XMCD spectra the multiplet structure can be observed for all the stoichiometric and off-stoichiometric compounds. The spectral features and intensities of the multiplet structures at Fe L_3 edge remain almost same for the off-stoichiometric compositions, though multiplet feature at Co L_3 edge appears to be insignificant. This kind of multiplet structure is indicative of the localized behavior of transition metal atomsand hence it shows that Fe atoms are more localized compared to the Co atoms. This was confirmed from the PDOS plots of Co and Fe above E_F (figure-8.5 [181]. It is also argued that the splitting in the L_3 edge of the transition metal elements is related to the interatomic *2p-3d* Coulomb, exchange interactionsand spin orbit coupling [182].

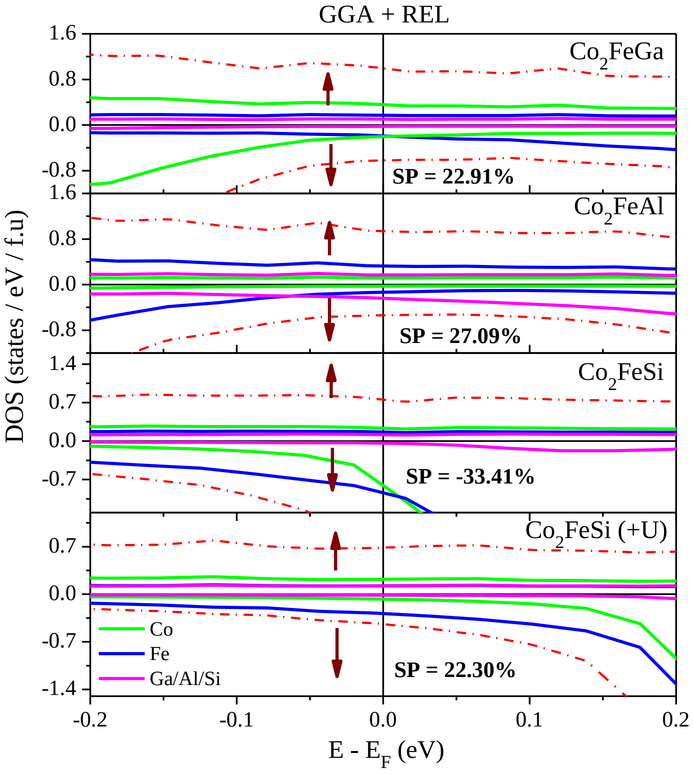

Figure-8.4: Partial DOS plots of the stoichiometric compounds near to the Fermi level (E_F).

The comparison of the K and $L_{3,2}$-edges of the XAS and XMCD spectra of the stoichiometric and off-stoichiometric Ni_2FeGa and Co_2FeZ (Z= Ga, Al, Si) compounds are shown in the figures-

8.5(a), (b) to 8.8 (a), (b). The K and L edges of XAS and XMCD spectra on the Co_2FeSi series using GGA+U approach are also shown in the figures-8.9(a), (b). In the figures the solid lines are the spectra due to properly sited paths and the dotted lines show the spectra of excess Co and Fe atoms at their antisites.

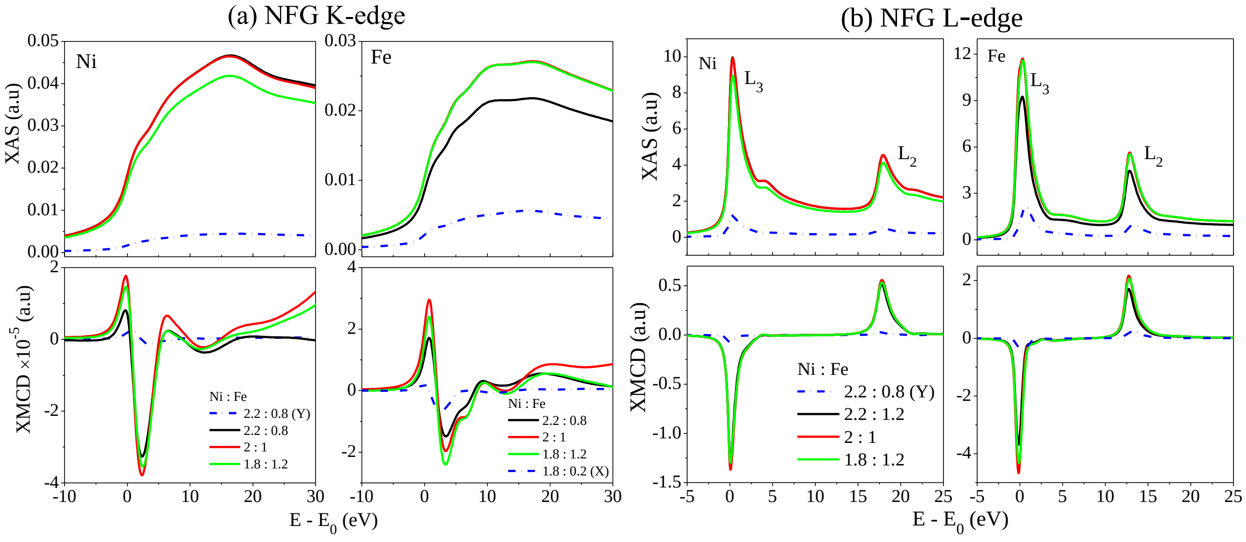
(a) NFG K-edge

(b) NFG L-edge

Figures-8.5: (a) Ni and (b) Fe K-edge and L-edge XAS and XMCD spectra of the stoichiometric and off-stoichiometric NFG compounds.

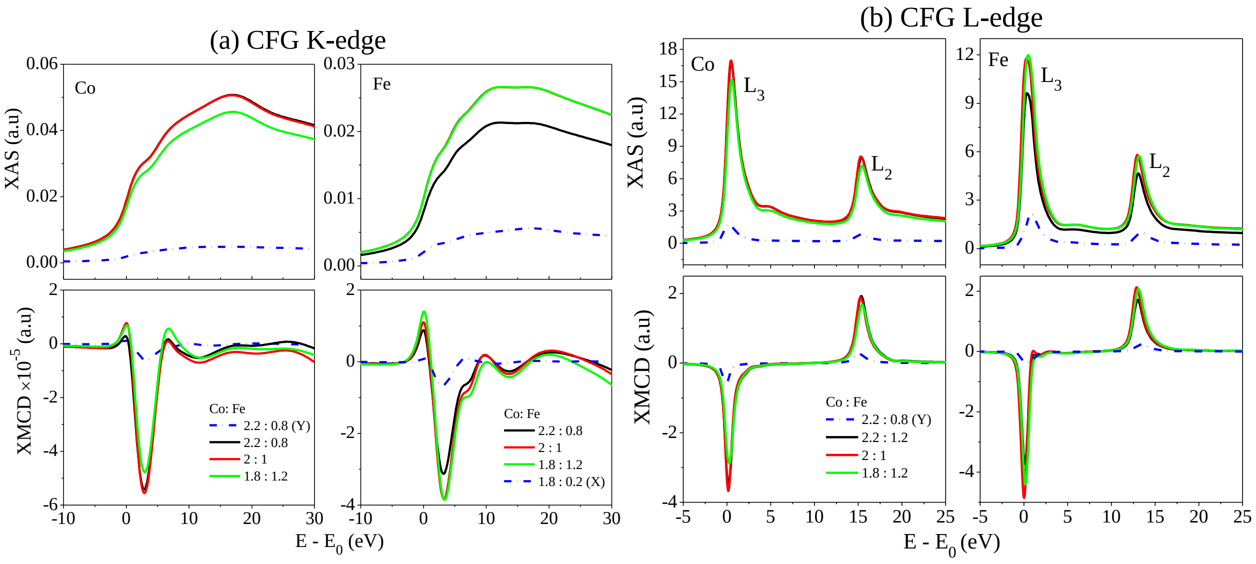
(a) CFG K-edge

(b) CFG L-edge

Figures-8.6: (a) Co and (b) Fe K-edge and L-edge XAS and XMCD spectra of the stoichiometric and off-stoichiometric CFG compounds.

The intensity of the dichroic signal varies monotonically with different stoichiometric compositions, however, the spectroscopic feature remains similar for all. It is discussed above that in the off-stoichiometric compositions, the excess amount of Co ($Co_{0.2}$) or Fe ($Fe_{0.2}$) atoms occupy the Fe (Y) and Co (X) antisites respectively by keeping the atoms for stoichiometric value (Co_2 or Fe) at their usual crystallographic sites. This excess amount of Co or Fe atoms is compensated by lesser quantity of Fe or Co atoms, respectively. Thus the XAS and XMCD spectra at both the K and L-edges for the stoichiometric or off-stoichiometric compositions of a particular system remain exactly the same for the atoms situated at the regular positions. The atoms at antisite positions exhibit much lessr XAS and XMCD signals (as shown by dotted lines in the respective figures) compared to the proper sited atoms.

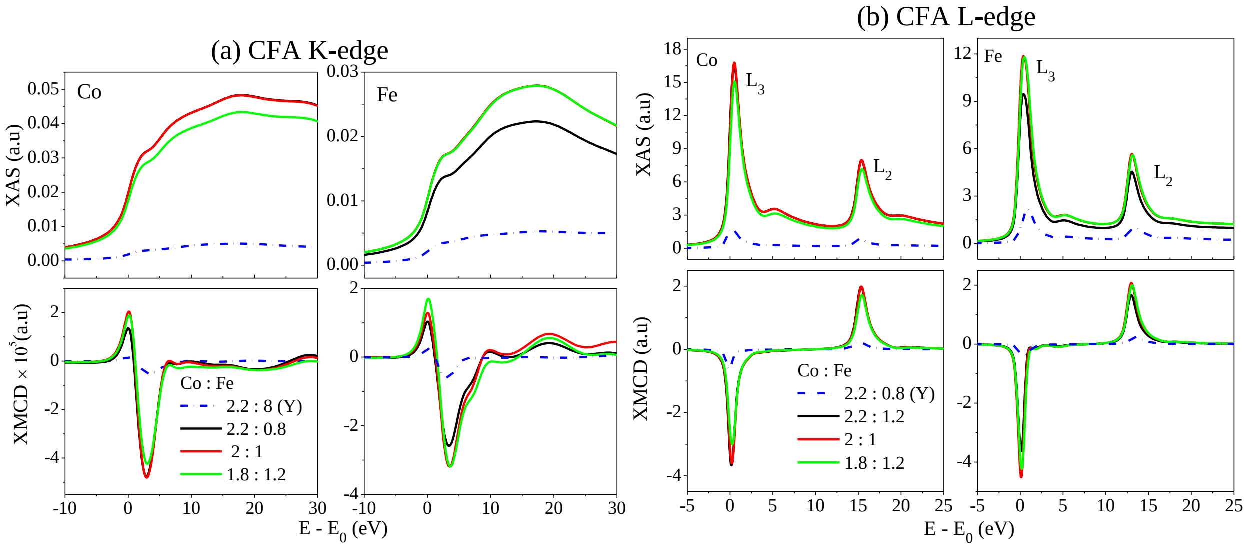

Figures-8.7: (a) Co and (b) Fe K-edge and L-edge XAS and XMCD spectra of the stoichiometric and off-stoichiometric CFA compounds.

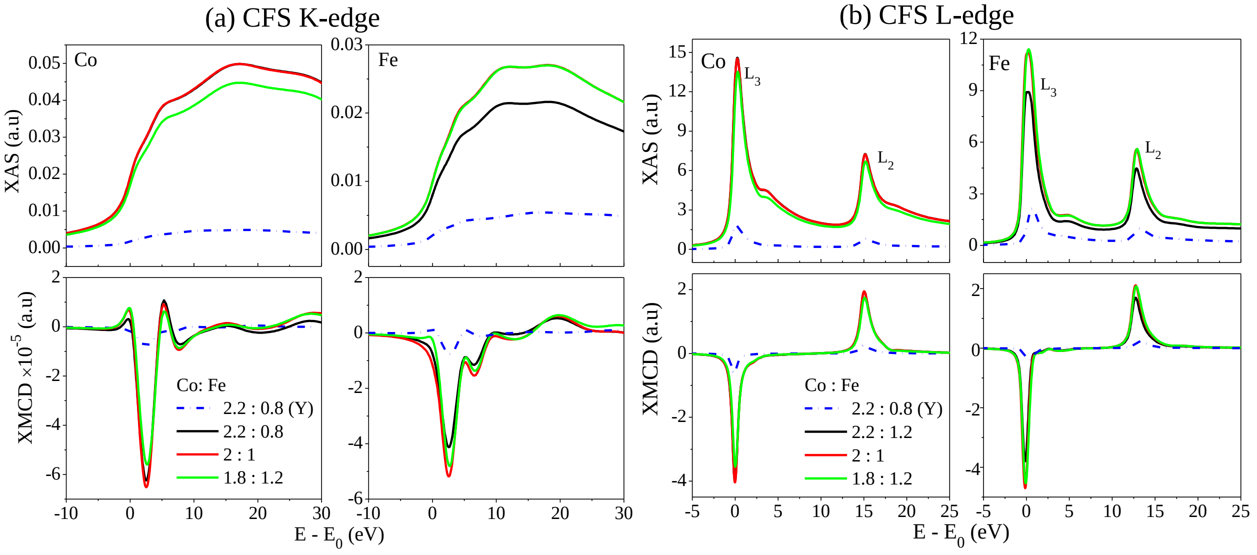

Figures-8.8: (a) Co and (b) Fe K-edge and L-edge XAS and XMCD spectra of the stoichiometric and off-stoichiometric CFS compounds.

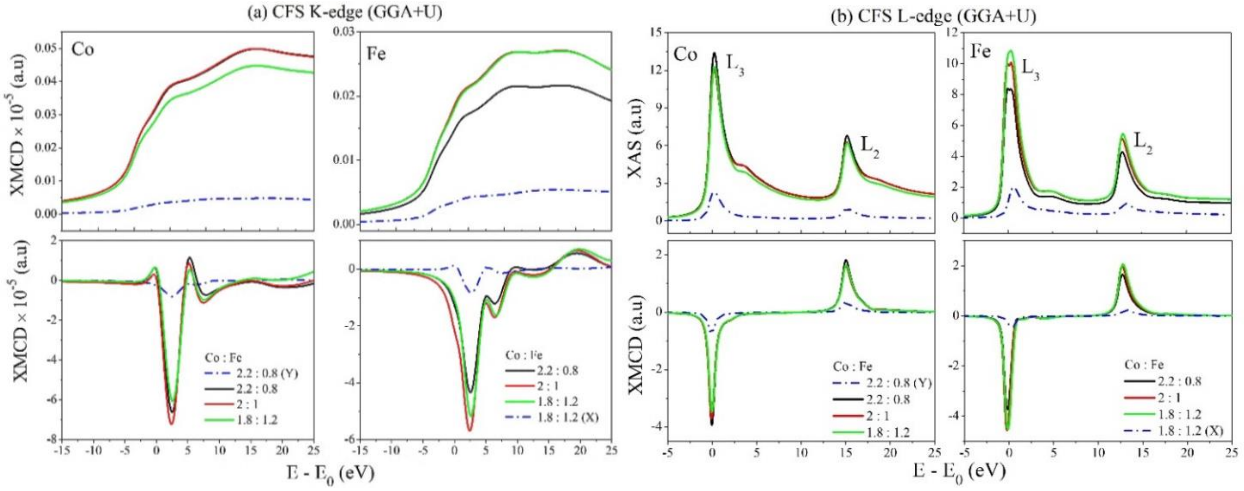

Figures-8.9: (a) Co and (b) Fe K-edge and L-edge XAS and XMCD spectra of the stoichiometric and off-stoichiometric CFS compounds using GGA+U approach.

It has been observed previously by EXAFS studies [158, 159] that in the (Co_2FeGa/Al) $L2_1$ structure, the Co atom is co-ordinated by 4 Fe (and 4 Ga/Al/Si) atoms situating in a tetrahedral co-ordination in the 1st co-ordination shell. Telling et. al. [183] have shown a consistent result with the experimental observation by considering the tetrahedral symmetry around the Co atoms. On the other hand, the Co atoms (C.N = 6) in the 2nd co-ordination shell creates an octahedral symmetry around the central Co atom. This leads to an octahedral crystal field splitting. This crystal field splitting and the stronger hybridization between the Co-Co and Co-Fe atoms lead to the multiplet structure at Co or Fe L_3 edges [183, 33]. Though the transition at the K absorption edge is not at the vicinity of E_F, the multiplet structures at the Fe edges are clearly observable around the positive point ‘C’. So the stronger Co-Fe or Co-Co hybridization can lead to this multiplet structure.

8.4 XMCD measurement on Co_2FeAl thin film:

Since the K-edge XMCD measurement on the Heusler alloy thin films discussed in Chapters 3-6 were carried out at the Energy Dispersive EXAFS beamline (BL-08) [75], in which the measurements have to be done in transmission mode, the films were deposited on X-ray transparent substratesunder similar deposition conditions. For this 7-8 µm thick B_4C films were deposited on c-Si substrates by chemical vapor deposition (CVD) technique. Subsequently c-Si substrates were etched out using a mixture of Hydrofluoric (HF) and Nitric (HNO_3) acid and free standing B_4C film was obtained which were used as substrates for depositing the Heusler alloy films. The prepared thin films were kept in a circular aluminumsample holder with an inner diameter of 6 mm forthe passage of the beam through the sample, the alunium holder was in turn held in the teflon sample holder and kept at the centre of the magntic field. The XMCD measurement set-up and the procedure of collection of the XMCD signal have been explained in details in Chapter-7. Figure-8.10 shows the measured XAS and XMCD spectra of the Co_2FeAl thin film. All features of XMCD spectra characterized by three main peaks A, B and C were observed which agrees with the theoretically simulated spectra as shown in fig. 8.8 (a). Though it was observed that the peaks are little broader than the theoretically simulated spectrum due to intrinsic limitation of the resolution of the beamline at 7 keV and due to the thermal disorder of the samples because the measurements have been carried out at room temperature.

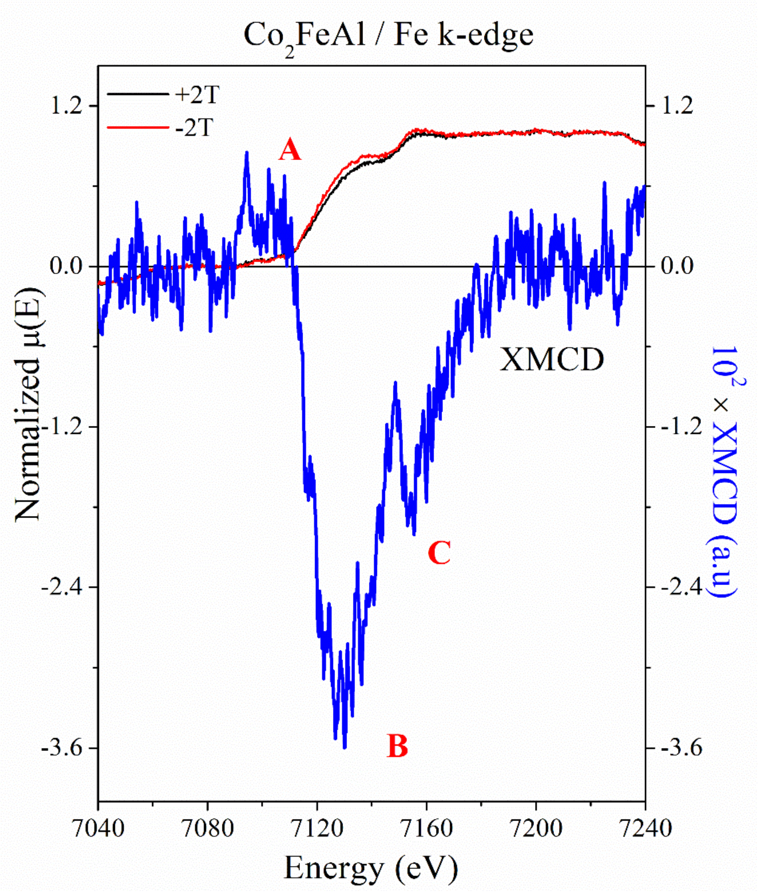

Figure-8.10: Measured K-edge XAS and XMCD spectra of the Co_2FeAl thin film

8.5 Conclusion:

In this chapter theoretical simulations of elemental magnetic moments, density of states, spin polarization and simulation of the K and L-edge XAS and XMCD spectra of Ni_2FeGa and Co_2FeZ (Z = Ga, Al, Si) Heulser alloyshave been carried out using density functional theory based SPR-KKR code. Considering the GGA approximation over LDA as exchange co-relation function, better results of total magnetic moments were obtained, though the ratio of (μ_l/μ_s) remains almost same for both the cases. It was observed that in the off-stoichiometric compounds there is presence of antisite disorder and the disordered atoms interact ferromagnetically with the properly sited atoms. However, the value of spin polarization for the off-stoichiometric compounds is found to be less than that of the stoichiometric compounds. Both K and L-edge absorption edges of the compounds have been simulated in order to have an understanding about the core and valance electrons. To explain the variation in the spectral features total DOS and partial DOS of the constituent atoms have been calculated. It shows that the band structure above E_F and the spin polarization near to E_F influences the variation in the shape of the absorption spectra. It was further observed that the splitting in the XMCD spectra at the Fe K-edge is more prominent than the Co K-edge spectra, suggesting a more localized nature of the Fe atoms than Co. One key finding of this study is that for the case of Co_2FeSi sample, which turns out to be a correlated system, the values of total magnetic moment obtained using both LDA and GGA are found to be less than the experimentally observed values and hence we have to add theon-site Coulomb correlation term (U) to GGA for the calculations of moments. The Fe K-edge XMCD spectrum of Co_2FeAl thin film deposited on X-ray transparent B_4C substrate has been measured at the Energy Dispersive EXAFS beanline (BL-08) at Indus-2 SRS which shows all the key features of the XMCD spectrum obtained by theoretical simulations.

Chapter-9

SUMMARY AND CONCLUSIONS

In this thesis work we have prepared a series of Heusler alloy samples viz., Ni_2FeGa, Co_2FeGa, Co_2FeAl and Co_2FeSi in thin film form using the pulsed laser deposition (PLD) technique on crystalline Si (111) substrate by varying the growth temperatures and have characaerised them primarily with synchrotron radiation based XAS technique which comprises of both XANES and EXAFS measurements. The Chapter-1 of this thesis establishes the importance of Heusler alloys for the spintronic application and the challenges of preparation of thin films for the application. This chapter mainly focuses on the EXAFS technique as an important tool for characterizing the local structure of the Heusler alloys which is strongly correlated with their physical properties. Being an element specific technique EXAFS is very effective in studyingelement specific local structure including the cationic anitisite disorders between the atoms which cannot be efficiently done by other structural characterization technique like X-ray diffraction. XMCD, which is basically measurements of XAS spectra under magnetic field and ploarised synchrotron radiation also serves as a useful tool for estimation of elerment speific magnetic moments of the ternary Heusler alloy systems. Along with the above two techniques, the samples have been subjected to various other chataerisation technuiques viz., GIXRD. GIXR, FESEM, EDXS, VSM to elucidate their structural, morphological and magnetic properties

The Chapter-2 of this thesis summarises all the above techniques along with short descriptions of the equipments used and data analysis procedures.

Chapter-3 elucidates the experimental results on the off-stoichiometric $Ni_{55}Fe_{19}Ga_{26}$ ferromagnetic Heusler alloy thin films have been prepared by pulsed laser deposition (PLD) technique at different substrate temperatures. GIXRD data show that the samples deposited at lower substrate temperatures are rich in γ phase while those deposited at higher substrate temperatures have predominantly austenite phase. It further shows that the film deposited at the highest substrate temperature has martensite phase also. Low temperature XRD data of the sample deposited at the highest temperature shows that the intensity of martensite peak remains same throughout the temperature range down to 5K while there is a systematic shift in peak position showing negative thermal expansion which is a characteristic of the martensite phase. EDXS results show that the films are mostly Fe-rich. XANES data corroborate the findings of XRD measurement that there is a decrease in austenite phase in the sample deposited at the highest substrate temperature. RT-EXAFS data were fitted with a two phase model of austenite and γ phase and it has also been observed that with an increase in the substrate temperature the disordered γ phase gets reduced. It has also been observed from EXAFS study that Ni-Ga bond lengths in the samples are shorter than the Ni-Fe bond length suggesting the rigidness of the Ni-Ga bond while Fe moves to Ni and Ga sites leading to antisite disorders. For the sample deposited at the highest substrate temperature (HA-4), the low temperature EXAFS data could only be fitted well once the presence of martensite phase is taken into account. Magnetization measurement shows that there is anti-ferromagnetic interaction in the sample deposited at the highest substrate temperature arising due to antisite disorder involving Fe atoms. It has also been observed that at 5K, the samples show ferromagnetic behavior with increasing saturation magnetization as the substrate temperature is increased. However, for the sample deposited at the highest temperature, due to the presence of anti-ferromagnetic interaction, martensite phase and decrease in γ phase, saturation magnetization decreases and coercive field increases.

Chapter-4 presents the structural and magnetic characterizations of PLD grown Co_2FeGa thin films on c-Si substrates deposited at 5 different substrate temperatures of RT, 473K, 673K, 873K and 1073K. XRD measurement with lab source ascertains that the target material used for the deposition of the thin films have only A2 (or DO3) type of disordered cubic phase. However, in case of thin films, PLD grown from the above target, $L2_1$ appears to be the dominating phase whose fraction decreases with increase in substrate temperature, manifesting significant increase of disorder in the samples. Synchrotron based Anomalous X-ray Scattering measurement also supports the above result. However, GIXRD measurement shows a contradictory result with the observations made from the above lab source and synchrotron based XRD studies and shows the presence of the A2-like phase similar to the balk target. GIXR data of the samples are best fitted with a bi-layer model with a surface layer of ~30-50 Å thickness of relatively lower density on a bulk-like thick layer. Such bi-layer structure of the films might give rise to the contradictory results observed for the GIXRD and XRD measurements on the samples. EDXS results show formation of slightly off-stoichiometric films with deficiency in Ga throughout the series. Synchrotron based XANES study shows that the metallic or zero oxidation states of the atoms are preserved in the films deposited at lower substrate temperatures, though there is an indication of structural changes in the films deposited at substrate temperatures of 873 and 1073 K. EXAFS measurements confirm $L2_1$ structure of the films and a possibility of stronger Co-Ga (*d*-*p*) hybridization. EXAFS measurements have also been able to establish the presence of A2 and DO3 phases which occur due to Co/Fe/Ga and Co/Fe types of antisite disorders in the samples and could not be clearly detected by XRD measurements. Fitting of FT-EXAFS data also gives quantitative estimation of the disorder parameters which are found to increase gradually with an increase in substrate temperature. EXAFS results show negligible B2-type disorder phase in the samples, which was also confirmed by synchrotron based XRD measurement. Finally, magnetization results show soft ferromagnetic nature of the films with a saturation value of magnetization less than the theoretically expected value which may be due to the presence of antisite atomic disorder in the films. Along with this it also manifests the existence spin wave nature with lesser stiffness constant in the films deposited at relatively lower substrate temperatures.

In Chapter-5 the effect of growth temperature on the structural and magnetic properties of Co_2FeAl thin films deposited using PLD technique have been presented. The bulk target used for the deposition of the thin films shows the presence of B2 phase with lesser intense characteristic peaks, though the formation of properly ordered $L2_1$ phase for these samples is hardly reported. GIXRD measurements on the PLD grown thin films show the formation of Heusler phase in the films which slightly differs from the bulk target. However, being a Heusler alloy material where both the transition material has nearby atomic number, it is difficult to resolve other structural phases from the X-ray diffraction study. GIXR study shows the formation of the CFA films with thickness ~1000Å and the density properly matches with the standard value for a CFA Heusler alloy. EDAXS result gives a better view about the effect of growth temperature on the stoichiometry, from which it is found that the films attain near-stoichiometry with increasing the substrate temperature beyond 573K. Probing the local atomic structure the synchrotron based XAS study shows that all the films remain in their metallic state and the nature of the oscillations at highest substrate temperatures suggest the formation of better crystallinity in the films which nearly matches with that of f.c.c metals. EXAFS study also strongly correlates with the GIXRD and XANES study. The improvement in both the crystallinity and crystallite size reflected in the Fourier transformed peak. The structure maintains its cubic shape having the bond lengths of the similar atomic pairs. The result also suggests stronger *d-d* hybridization between the Co and Fe *3d* elements which is a main property of a half metallic Heusler alloy. The magnetization results show soft ferromagnetic nature of the samples where the saturation magnetization increases with increase in the growth temperature and reaches towards a near integer value at higher substrate temperature.

The variation in the coercive field at low temperature shows a strong dependence on the crystallite size of the material and it almost vanishes at room temperature. The thermal demagnetization data suggests that only the spin waves contribute within the measured temperature range with a very small value of spin wave stiffness constant except for the film deposited at 873K. This sample shows the possible presence of small anti ferromagnetic phase in which ultimately decreases its saturation magnetization value.

In Chapter-6 a comparative study between the two series of PLD grown Co_2FeSi thin film samples have been carried out; in one series ("S"-series) films have been prepared at elevated substrate temperaturs while in the other series ("A"-series) films have been prepared at RT followed by post deposition annealing. The objective of the study being to investigate about the effect of the different thermal growth processes on the structural and magnetic properties of the CFS films. GIXRD measurements on the thin films show that the phases of the thin films are similar and exactly match with the bulk target. However, the crystallity of the "S" series samples are found to be much better than the "A" series samples and this is also reflected on their variation in the lateral crystallite size of the films. EDXS study shows that Co to Fe ratios in the films remains close to 2:1 at higher temperatures, though higher Si contents in the films were observed due to inter-diffusion from the Si substrate. This is also reflected in the GIXR study of the samples where less dense or Si-excess layer between the bulk film and Si substrate were detected. The reflectivity result also shows that though the thickness of the flms remains near to 1100 Å the density of the "S" series samples is higher (~9.4 gm/cc) than the "A" series samples (~6.5 gm/cc) and the former series of samples have higher surface roughness also due to larger crystallite size. A strong *p-d* and *d-d* hybridizations were observed for the S and A series samples respectively which characterizes their magnetic interactions. It has been further observed from EXAFS data analysis that Co/Fe antisite disorder exists for both the series, though it is higher fopr "S" series samples which increases gradullay with increase in substrate tempearture. Magnetic characterization also shows that the value of the saturation magnetization is higher for the “S” series samples due to better crystallinity though due to the presence of the anitiste disorder in this series of samples the value of saturation magnetization decreases initially with incease in substrate temperature. From the magnetic chacterizations it was also observed that the effective aniosotory constant is higher for the ‘S” series samples.

In Chpater-7 the details of the installation and comissioning of the hard X-ray XMCD facility at the Energy Dispersive EXAFS beamline at Indus-2 synchrotorn source has been described. A water cooled electromagnet was designed and fabricated for this purpose which delivers a maximum magnetic field of 2T at the centre between the two magnetic poles. The electromagnet has been placed on an indigenously built built X-Z-θ stage in the 2 axis of the the Energy Dispersive EXAFS beamline (BL-08) with the pole gap coinciding with the sample position. The beam passes through the sample and the absorption spectra are detected at a position sensitive CCD detector. For the polarization selection of the synchrotron beam the top most portion of beam was selected by a pceision slit placed prior to the pre-mirror of the beramluine and the absorption data were taken by changing the polarity of the electromagnet, the difference of which gives the XMCD signal. The set-up has been tested sucessfully by measuring the Gd L_3 edge XAS and XMCD spectra of a standard Gd foil whichagrees with the previously reported results.

In Chapter-8 theoretical simulations of elemental magnetic moments, density of states, spin polarization and simulation of the K and L-edge XAS and XMCD spectra of Ni_2FeGa and Co_2FeZ (Z = Ga, Al, Si) Heulser alloys have been carried out using density functional theory based SPR-KKR code. Considering the GGA approximation over LDA as exchange co-relation function, better results of total magnetic moments were obtained, though the ratio of (μ_l/μ_s) remains almost same for both the cases. It was observed that in the off-stoichiometric compounds there is presence of antisite disorder and the disordered atoms interact ferromagnetically with the properly sited atoms. However, the value of spin polarization for the off-stoichiometric compounds is found to be less than that of the stoichiometric compounds. Both K and L-edge absorption edges of the compounds have been simulated in order to have an understanding about the core and valance electrons. To explain the variation in the spectral features total DOS and partial DOS of the constituent atoms have been calculated. It shows that the band structure above E_F and the spin polarization near to E_F influences the variation in the shape of the absorption spectra. It was further observed that the splitting in the XMCD spectra at the Fe K-edge is more prominent than the Co K-edge spectra, suggesting a more localized nature of the Fe atoms than Co. One key finding of this study is that for the case of Co_2FeSi sample, which turns out to be a correlated system, the values of total magnetic moment obtained using both LDA and GGA are found to be less than the experimentally observed values and hence we have to add the on-site Coulomb correlation term (U) to GGA for the calculations of moments. The Fe K-edge XMCD spectrum of Co_2FeAl thin film deposited on X-ray transparent B_4C substrate has been measured at the Energy Dispersive EXAFS beanline (BL-08) at Indus-2 SRS which shows all the key features of the XMCD spectrum obtained by theoretical simulations.

.

References:

1. Heusler F. "Über magnetische Manganlegierungen". Verhandlungen der Deutschen Physikalischen Gesellschaft (in German). 12: (1903) 219.
2. https://shodhganga.inflibnet.ac.in/bitstream/10603/164097/6/06_chapter%201.pdf
3. Bradley Albert James, Rodgers J. W. and Bragg William Lawrence; Proc. R. Soc. Lond. A 144 (1934) 340 – 359.
4. Balke Benjamin, Sabine Wurmehl, Gerhard H. Fecher, Claudia Felser, Jürgen Kübler, Sci. Technol. Adv. Mater. 9 (2008), 014102.
5. M. Belmeguenai, H. Tuzcuoglu, M.S. Gabor, T. Petrisor Jr., C. Tiusan, F. Zighem, S.M. Cherif, P. Moch, J. Appl. Phys. 115 (2014) 043918 – 043924.
6. Akimasa Sakuma; J. Phys. D: Appl. Phys. 48 (2015) 164011.
7. Y. Takamura, R. Nakane, S. Sugahara, J. Appl. Phys. 105 (2009), 07B109 - 07B111, B.S.D. ChS. Varaprasad, A. Srinivasan, Y.K. Takahashi, M. Hayashi, A. Rajanikanth, K. Hono, Acta Mater. 60 (2012) 6257 – 6265.
8. S. Wurmehl, M.C. Martins Alves, J. Morais, V. Ksenofontov, S.R. Teixeira, G. Machado, G.H. Fecher, C. Felser, J. Phys. D: Appl. Phys. 40 (2007) 1524 – 1533.
9. K. R. Priolkar, P. A. Bhobe, D. N. Lobo, S. W. D’Souza, S. R. Barman, Aparna Chakrabarti, and S. Emura; Phys. Rev. B 87, (2013)144412 – 144417.
10. S. Picozzi and A. Continenza, A. J. Freeman; Phys. Rev. B 66 (2002) 094421.
11. S. Wurmehl, G. H. Fecher, H. C. Kandpal, V. Ksenofontov, C. Felser, H.-J. Lin, and J. Morais, Phys. Rev. B **72**, (2005) 184434.
12. Aniruddha Deb, M. Itou, and Y. Sakurai, N. Hiraoka and N. Sakai; Phys. Rev. B 63, (2001) 064409.
13. S. O. Mariager, C. Dornes, J. A. Johnson, A. Ferrer, S. Gr¨ubel, T. Huber, A. Caviezel, S. L. Johnson, T. Eichhorn, G. Jakob, H. J. Elmers, P. Beaud, C. Quitmann and G. Ingold; Phys. Rev. B 90, (2014)161103.
14. Z. H. Liu, H. N. Hu, G. D. Liu, Y. T. Cui, M. Zhang, J. L. Chen, and G. H. Wu, Gang Xiao, Phy. Rev. B **69**, (2004) 134415.
15. Tamalika Samanta,1 P. A. Bhobe, A. Das, A. Kumar, and A. K. Nigam; Phys. Rev. B 97, (2018) 184421.

16. D. P. Oxley, R. S. Tebble, C. T. Slack & K. C. Williams; Nature 194, (1962) 465
17. Sanjay Singh, S.W. D’Souza, J. Nayak, E. Suard, L. Chapon, A. Senyshyn, V. Petricek, Y. Skourski, M. Nicklas, C. Felser & S. Chadov, Nature Communications volume 7, Article number: 12671, (2016) 1 – 6.
18. Tomoki Tsuchiya, Ryota Kobayashi, Takahide Kubota, Kotaro Saito, Kanta Ono, Takashi Ohhara, Akiko Nakao and Koki Takanashi, J. Phys. D: Appl. Phys. 51 (2018) 065001.
19. S Pramanick, P Dutta, J Sannigrahi, K Mandal, S Bandyopadhyay, S Majumdar and S Chatterjee; J. Phys.: Condens. Matter **30** (2018) 405803.
20. M. Seredina, I. Gavrikov, D. Karpenkov, M. Zhelezny, A. Bazlov, Ratnamala Chatterjee, R.Y. Umetsu, V. Khovaylo; Journal of Magnetism and Magnetic Materials 485 (2019) 193–196.
21. P.V. Midhunlal, J. Arout Chelvane, D. Prabhu, Raghavan Gopalan, N. Harish Kumar; Journal of Magnetism and Magnetic Materials 489 (2019) 165298.
22. A. T. Zayak, P. Entel, K. M. Rabe, W. A. Adeagbo, and M. Acet; Phys. Rev. B **72**, (2005) 054113.
23. R.A. de Groot, F.M. Mueller, P.G. van Engen, K.H.J. Buschow. Phys. Rev. Lett. **50**, (1983) 2024.
24. S. Ishida, S. Akazawa, Y. Kubo, J. Ishida, J. Phys. F Met. Phys. **12**, (1982) 1111.
25. S. Ishida, S. Fujii, S. Kashiwagi, S. Asano, J. Phys. Soc. Jpn. **64**, (1995) 2152.
26. R.J. Soulen Jr., J.M. Byers, M.S. Osofsky, B. Nadgorny, T. Ambrose, S.F. Cheng, P.R. Broussard, C.T. Tanaka, J. Nowak, J.S. Moodera, A. Barry, J.M.D. Coey, Science 282 (1998) 85 – 88.
27. H. Kato, T. Okuda, Y. Okimoto, Y. Tomioka, K. Oikawa, T. Kamiyama, Y. Tokura, Phys. Rev. B 69 (2004) 184412 – 184419.
28. T. Shishidou, A.J. Freeman, R. Asahi, Phys. Rev. B 64 (2001) 180401 – 180404.
29. A. Stroppa, S. Picozzi, A. Continenza, A.J. Freeman, Phys. Rev. B 68, (2003) 155203.
30. Rie Y. Umetsu, Akinari Okubo and Ryosuke Kainuma; Journal of Appl. Phys. 111 (2012) 073909 – 073914.
31. I. Galanakis, Ph Mavropoulos, P.H. Dederichs, J. Phys. D Appl. Phys. 39 (2006) 765 – 77.
32. J.L. Moran-Lopez, R. Rodrlguez-Alba, F. Aguilera-Granja; Journal of Magnetism and Magnetic Materials 131 (1994) 417-426.

33. I. Galanakis and P. H. Dederichs, N. Papanikolaou; Phys. Rev. B **66**, (2002) 174429 – 174437.
34. E. Şaşıoğlu, L. M. Sandratskii and P. Bruno; Phys. Rev. B **77**, (2008) 064417 – 064431.
35. Tufan Roy, Physics Letters A 381, (2017) 1449–1456.
36. M. A. Ruderman and C. Kittel, *Physical Review*, **96,** (1954), 99-102.
37. K. Yosida, *Physical Review*, 106 (1957), 893-898.
38. A. Pramanick, X. P. Wang, K. An, A. D. Stoica, J. Yi,2 Z. Gai, C. Hoffmann, and X.-L. Wang; Phys. Rev. B 85, (2012) 144412 – 14423.
39. J. Pons, V.A. Chernenko, R. Santamarta, E. Cesari, Acta Mater 48 (2000) 3027.
40. Rozaliya I. Barabash, Oleg M. Barabash, Dmitry Popov, Guoyin Shen, Changyong Park and Wenge Yang; Acta Materialia 87 (2015) 344–349.
41. Hrusikesh Nath and Gandham Phanikumar; Metallurgical and Materials Transactions A 46A (2015) 4947 – 4955.
42. Lluı´s Man˜osa, Alfons Gonza`lez-Comas, Eduard Obrado´, and Antoni Planes, V. A. Chernenko and V. V. Kokorin, E. Cesari; Phys. Rev, B 55 (1997) 11068 – 11071.
43. Claudia Bungaro, K. M. Rabe, A. Dal Corso; Phys. Rev. B, 68 (2003), 134104 – 134112.
44. Z. H. Liu, M. Zhang, Y. T. Cui, Y. Q. Zhou, W. H. Wang, and G. H. Wu, X. X. Zhang, Gang Xiao; Appl. Phys. Lett. 82 (2003) 424 – 426.
45. Xavier Moya, Llu´ıs Ma˜nosa, Antoni Planes, Thorsten Krenke, Mehmet Acet, Eberhard F. Wassermann, Materials Science and Engineering A 438–440 (2006) 911–915.
46. A. Sokolov, Le Zhang, I. Dubenko, T. Samanta, S. Stadler, and N. Ali; Appl. Phys. Lett. 102, (2013) 072407 – 072410.
47. Sanjay Singh, S. Esakki Muthu, A. Senyshyn, P. Rajput, E. Suard, S. Arumugam, and S. R. Barman; Appl. Phys. Lett. 104, (2014) 051905.
48. J. Kubler, A. R. Williams, C. B. Sommers; Phys. Rev. B 28, (1983), 1745 – 1755.
49. Victor A. L'vov, Eduard Cesari, Anna Kosogor, Joan Torrens-Serra, Vicente Recarte and José Ignacio Pérez-Landazábal; Metals 7, (2017) 509 – 519
50. A. Hirohata, K. Takanashi, J. Phys. D Appl. Phys. 47 (2014) 193001 – 193040.
51. J. Mathon and A. Umerski; Phys. Rev. B **71**, (2005) 220402 – 220405.
52. Seng Ghee Tan, Mansoor B.A. Jalil, in Introduction to the Physics of Nanoelectronics, 2012
53. D. Zakharov, G. Lebedev, A. Irzhak, et al., Smart Matr. Struct. **21**, (2012) 052001.

54. E. Kalimullina, A. Kamantsev, V. Koledov, V. Shavrov, V. Nizhankovskii, A. Irzhak, F. Albertini, S. Fabbrici, P. Ranzieri, P. Ari-Gur.
55. Michael Nicklas, Niels-O. Born, Claudia Felser, Robert Küchler, Sergiy A. Medvedev, Kamal Mydeen, Ajaya K. Nayak, Pavel Naumov, Catalina Salazar Mejía, Ulrich Schwarz, C. Wang;
56. J.W. Dong, L.C. Chen, J.Q. Xie, T.A.R. Muller, D.M. Carr, C.J. Palmstrom, S. Mc Kernan, Q. Pan, R.D. James, J. Appl. Phys. 88 (2000) 7357.
57. J. Dubowik, Y.V. Kudryavtsev, Y.P. Lee, J. Magn. Magn. Mater 1178 (2004) 272.
58. V.O. Golub, A.Y. Vovk, L. Malkinski, C. O'Connor, Z.J. Wabg, J.K. Tang, J. Appl. Phys. 96 (2004) 3865.
59. A. Hakola, O. Heczko, A. Jaakkola, T. Kajava, K. Ullakko, Appl. Phys. A 79 (2004) 1505.
60. H. Schneider, Ch Herbort, G. Jakob, H. Adrian, S. Wurmehl, C. Felser, J. Phys. D Appl. Phys. 40 (2007) 1548 – 1551.
61. A. Yadav, S. Chaudhary, J. Appl. Phys. 115 (2014) 133916 – 133922.
62. S. Husain, S. Akansel, A. Kumar, P. Svedlindh, S. Chaudhary, Sci. Rep. 6 (2016) 28692 – 286102.
63. W.H. Wang, M. Przybylskia, W. Kuch, L.I. Chelaru, J. Wang, Y.F. Lu, J. Barthel, J. Kirschner, J. Magn. Magn. Mater. 286 (2005) 336 – 339.
64. H. Pandey, R.C. Budhani, J. Appl. Phys. 113 (2013) 203918.
65. C.E.A. Grigorescu, E. Valerio, O. Monnereau, L. Tortet, L. Argeme, G. Pavelescu, S.A. Manea, C. Ducu, A. Malinovski, H.J. Trodahl, A. Bittar, N. Strickland, R. Notonier, W.R. Branford, M. Autric, Appl. Surf. Sci. 253 (2007) 8102 – 8106.
66. W. Wang, W. Yang, Z. Liu, Y. Lin, S. Zhou, H. Qian, F. Gao, G. Li, Cryst Eng Comm 16 (2014) 4100.
67. D. Pergolesi, E. Fabbri, A. D'Epifanio, E. Di Bartolomeo, A. Tebano, S. Sanna, S. Licoccia, G. Balestrino, E. Traversa, Nat. Mater. 9 (2010) 846 – 852
68. G. Li, W. Wang, W. Yang, H. Wang, Surf. Sci. Rep.70 (2015) 380 – 423.
69. A. Yadav, S. Chaudhary, J. Appl. Phys. 117 (2015) 083911 – 083919.
70. S.K. Sarkar, A. Biswas, P.D. Babu, S.D. Kaushik, A. Srivastava, V. Siruguri, M. Krishnan, J. Alloy Comp. 586 (2014) 515.
71. G. M¨ulhaupt and R. R¨uffer, Hyperfine Interactions 123/124 (1999) 13–30.

72. D. Angal-Kalinin, A. Banerji, P. R. Hannurkar, M.G.Karmarkar, S.Kotaiah, S.P.Mhaskar, P.K.Nema, S.S.Prabhu, M.Pravin Kumar, S.S.Ramamurthi, S.K.Shukla, G.Ssingh, H.C.Soni and B.J.Vidya; Current Science, 82 (2002) 283 – 290.
73. D. Angal-Kalinin, A. Banerji, P. R. Hannurkar, M.G.Karmarkar, S.Kotaiah, S.P.Mhaskar, P.K.Nema, S.S.Prabhu, M.Pravin Kumar, S.S.Ramamurthi, S.K.Shukla, G.Ssingh, H.C.Soni and B.J.Vidya; Current Science, 82 (2002) 283 – 290.
74. D.D. Bhawalkar, G. Singh, R.V. Nandedkar; Pramana-Journal of Physics, 50 (1998) 467 – 484.
75. D. Bhattacharyya, A. K. Poswal, S.N. Jha, Sangeeta, S.C. Sabharwal, Nuclear Instruments and Methods in Physics Research A 609 (2009) 286–293.
76. A.K. Poswal, A. Agrawal, A.K. Yadav, C. Nayak, S. Basu, S.R. Kane, C.K. Garg, D. Bhattachryya, S.N. Jha, N.K. Sahoo, AIP Conf. Proc. 1591 (2014) 649
77. S. Basu, C. Nayak, A.K. Yadav, A. Agrawal, A.K. Poswal, D. Bhattacharyya, S.N. Jha, N.K. Sahoo, J. Phys. Conf. Ser. 493 (2014) 012032.
78. Fundamentals of XAFS by Matthew Newville, Revision 1.7 July 23, 2004.
79. XAFS, a technique to probe local structure, Steven D. Conradson as told to Jay Scheker, *Los Alamos Science* Number 26, (2000) 422 – 435.
80. D.C. Konigsberger, R. Prince (Eds.), X-Ray Absorption: Principles, Applications, Techniques of EXAFS, SEXAFS and XANES, Wiley, New York, 1988
81. B. Ravel and M. Newville, *Journal of Synchrotron Radiation*, **12 (**2005), 537-541.
82. M. Newville, *Journal of Synchrotron Radiation*, **8,** (2001), 322-324
83. S. I. Zabinsky, J. J. Rehr, A. Ankudinov, R. C. Albers and M. J. Eller, *Physical Review B*, **52**, (1995) 2995-3009.
84. M. Newville, P. Līviņš, Y. Yacoby, J. J. Rehr and E. A. Stern, *Physical Review B*, **47**, (1993) 14126-14131.
85. chapter-14 shelly Kelly
86. J. J. Rehr and R. C. Albers, *Phys. Rev. B*, 41, (1990) 8139–8149.
87. J. E. Penner-Hahn, X-ray Absorption Spectroscopy.
88. Erskine & SternPhys. Rev. B 12, (1975) 5016.
89. G. Schutz, W. Wagner, W. Wilhelm, and P. Kienle; Phys. Rev. Lett. 58, (1987) 737

90. S. Imada, S. Suga, W. Kuch and J. Kirschner, Surface Review and Letters, 9, (2002) 877 – 881.
91. Tobias Funk, Aniruddha Deb, Simon J. George, Hongxin Wang, Stephen P. Cramer; Coordination Chemistry Reviews 249 (2005) 3–30.
92. B. T. Thole, Paolo Carra, F. Sette, and G. van der Laan; Phys. Rev. Lett. 68, (1992) 1943 – 1946.
93. P. Carra, B. T. Thole, M. Altarelli, and X. D. Wang, Phys. Rev. Lett. 70, (1993) 694.
94. C. T. Chen, Y.U. Idzerda, H.-J. Lin, N. V. Smith, G. Meigs, E. Chaban, G. H. Ho, E. Pellegrin, and F. Sette; Phys. Rev. Lett. 75, (1995) 152 – 155.
95. Cinthia Piamonteze, Piter Miedema and Frank M. F. de Groot; Phys. Rev. B 80, (2009) 184410.
96. M. Besse, V. Cros, A. Barth´el´emy, H. Jaffr`es, J. Vogel, F. Petroff, A. Mirone, A. Tagliaferri, P. Bencok3, P. Decorse, P. Berthet, Z. Szotek, W. M. Temmerman, S. S. Dhesi, N. B. Brookes, A. Rogalev and A. Fert; *Europhys. Lett.*, 60, (2002) 608.
97. F Wilhelm, J P Sanchez and A Rogalev; J. Phys. D: Appl. Phys. 51 (2018) 333001.
98. M. Marangolo, F. Gustavsson, M. Eddrief, Ph. Sainctavit, V. H. Etgens, V. Cros, F. Petroff, J. M. George, P. Bencok and N. B. Brookes; Phys. Rev. Lett. 88 (2002), 217202
99. F. Wilhelm, P. Poulopoulos, G. Ceballos, H. Wende, K. Baberschke, P. Srivastava, D. Benea, H. Ebert, M. Angelakeris, N. K. Flevaris, D. Niarchos, A. Rogalev, and N. B. Brookes; Phys. Rev. Lett. 85, (2000) 413.
100. P. Gambardella, A. Dallmeyer, K. Maiti, M. C. Malagoli, W. Eberhardt, K. Kern & C. Carbone; Nature 416, (2002) 301.
101. D.L. Windt, IMD Version 4.1.1, 2000. http://cletus.phys.co-lumbia.edu/windt/ idl.
102. G. Parrat, Phys. Rev. 95 (1954) 359.
103. http://olymp.cup.uni-muenchen.de/ak/ebert/SPRKKR.
104. H. Nath, G. Phanikumar, Mater. Sci. Forum 790 (2014) 199.
105. K. Oikawa, T. Ota, Y. Sutou, T. Ohmori, R. Kainuma, K. Ishida, Mater. Trans. 43 (2002) 2360.
106. M. Suzuki, M. Ohtsuka, M. Matsumoto, Y. Murakami, D. Shindo, K. Itagaki, Mater. Trans. 43 (2002) 861.
107. J. Pons, V.A. Chernenko, R. Santamarta, E. Cesari, Acta Mater 48 (2000) 3027.

108. Z. Li, H. Yang, K. Xu, Y. Zhang, D. Zheng, C. Jing, Mater. Chem. Phys. 180 (2016) 156.
109. H. Nath, G. Phanikumar, Metall. Mater. Trans. A 46A (2015) 4947.
110. S. Gardelis, J. Androulakis, O. Monnereau, P.D. Buckle, J. Giapintzakis, J. Phys. Conf. Ser. 10 (2005) 167.
111. V.G. Sathe, A. Dubey, S. Banik, S.R. Barman, L. Olivi, J. Phys. Condens. Matter 25 (2013) 046001.
112. P.A. Bhobe, K.R. Priolkar, P.R. Sarode, Phys. Rev. B 74 (2006) 224425.
113. W. Zhu, E.K. Liu, L. Feng, X.D. Tang, J.L. Chen, G.H. Wu, H.Y. Liu, F.B. Meng, H.Z. Luo, Appl. Phys. Lett. 95 (2009) 222512.
114. A. Vovk, L. Malkinski, V. Golub, C. O'Connor, Z. Wang, J. Tang, J. Appl. Phys. 97 (2005) 10C503.
115. P.A. Bhobe, K.R. Priolkar, P.R. Sarode, J. Phys. D. Appl. Phys. 41 (2008) 045004.
116. P.A. Bhobe, K.R. Priolkar, P.R. Sarode, J. Phys. C. Cond. Matter 20 (2008) 015219.
117. T. Krenke, M. Acet, E.F. Wassermann, Phys. Rev. B 72 (2005) 014412.
118. P. Lazpita, J.M. Barandiaran, J. Gutierrez, J. Feuchtwanger, V.A. Chernenko, M.L. Richard, New J. Phys. 13 (2011) 033039.
119. W. Zhang, Y. Sun, H. Wang, Y. Li, X. Zhang, Y. Sui, H. Luo, F. Meng, Z. Qian, G. Wu, J. Alloys Comp. 589 (2014) 230.
120. R. Maithieu, P. Nordblad, D.N.H. Nam, N.X. Phuc, N.C. Khiem, Phys. Rev. B 63 (2001) 174405.
121. Y. Li, C. Jiang, T. Liang, Y. Ma, H. Xu, Srip. Mater 48 (2003) 1255.
122. H.D. Nguyen, Adv. Nat. Sci. Nanosci. Nanotechnol. 4 (2013) 025011.
123. N.V.R. Rao, R. Gopalan, V. Chandrasekaran, K.G. Suresh, J. Phys. D. Appl. Phys. 42 (2009) 065002.
124. J. Rodrguez Carvajal, Phys. B Condens. Matter 192 (1993) 55 – 69.
125. M. Yin, S. Chen, P. Nash, J. Alloys Compd. 577 (2013) 49 – 56.
126. A. Yadav, S. Chaudhary, J. Appl. Phys. 118 (2015) 193902 – 193910.
127. P.J. Webster, J.Phys.Chem. Solids 32 (1971) 1221 – 1231.
128. Y. Kajikawa, J. Cryst. Growth 289 (2006) 387 – 394.
129. P.J. Chen, G. Feng, R.D. Shull, IEEE Trans. Magn. 49 (2013) 4379 – 4382.
130. A.J. Bradley, J.W. Rodgers, Proc. R. Soc. Lond. Ser. A 144 (1934) 340.

131. http://www.rrcat.gov.in/technology/accel/srul/beamlines/adxrd.html.
132. G. Jakob, F. Caspera, V. Beaumonta, S. Falk, N. Auth, H.-J. Elmers, C. Felser, H. Adrian, J. Magn. Magn. Mater. 290 (2005) 1104 – 1107.
133. J.S. Horwitvitz, K.S. Grabowski, D.B. Chrisey, R.E. Leuchtnera, Appl. Phys. Lett. 59 (1991) 1565.
134. E. van de Ret, J.C.S. Kook, J. Dieleman, J. Appl. Phys. 73 (1993) 8290 – 8296.
135. S. Yamada, K. Tanikawa, S. Oki, M. Kawano, M. Miyao, K. Hamaya, Appl. Phys. Lett. 105 (2014) 071601 – 071604.
136. C.H. Wang, Y.Z. Guo, F. Casper, B. Balke, G.H. Fecher, C. Felser, Y. Hwu, Appl. Phys. Lett. 97 (2010) 103106 – 103109.
137. Y. Takamura, R. Nakane, S. Sugahara, J. Appl. Phys. 107 (2010), 09B111 - 09B113.
138. B. Balke, S. Wurmehl, G.H. Fecher, C. Fesler, Appl. Phys. Lett. 90 (2007) 172501 – 172503.
139. S.I. Zabinsky, J.J. Rehr, A. Ankudinov, R.C. Albers, M.J. Eller, Phys. Rev. B 52 (1995) 2995 – 3009.
140. C. Wang, F. Casper, Y. Guo, T. Gasi, V. Ksenofontov, B. Balke, G.H. Fecher, C. Felser, Y.K. Hwu, J.J. Lee, J. Appl. Phys. 112 (2012) 124314 – 124321.
141. V. Niculescu, K. Raj, T.J. Burch, J.I. Budnick, Phys. Rev. B 13 (1976) 3167 – 3174.
142. B. Ravel, M.P. Raphael, V.G. Harris, Phy.Rev. B 65 (2002), 184431 – 184431.
143. Anupam, P.C. Joshi, P.K. Rout, Z. Hossain, R.C. Budhani, J. Phys. D Appl. Phys. 43 (2010) 255002 – 255007.
144. R.Y. Umetsu, A. Okubo, R. Kainuma, J.Appl. Phys. 111 (2012) 073909 – 073915.
145. D. Serrate, J.M. De Teresa, R. Cordoba, S.M. Yusuf, Solid State Commun. 142 (2007) 363 – 367.
146. D. Ristoiu, J.P. Nozieres, L. Ranno, J. Magn. Magn. Mater. 219 (2000) 97 – 103.
147. Keshab R. Sapkota, Parshu Gyawali, Andrew Forbes, Ian L. Pegg, John Philip, J. Appl. Phys. 111 (2012), 123906.
148. M. Newville, B. Ravel, D. Haskel, J.J. Rehr, E.A. Stern, Y. Yacoby, Physica B 208 (1995) 154 – 156.
149. Z.H. Liu, Y.J. Zhang, E.K. Liu, G.D. Liu, X.Q. Ma, G.H. Wu, J. Phys. D Appl. Phys. 48 (2015), 325001 – 325008.

150. Xingfeng Zhun, Yafei Dai, Chenglin Luo, J. Magn. Magn. Mater. 398 (2016) 7 – 12.
151. F. Keffer, in: H.P.J. Wijn (Ed.), Encyclopedia of Physics, vol. XVIII, Springer, Berlin, 1996, p. 1. Part 2.
152. J. Mathon, E.P. Wohlfarth, Proc. R. Soc. Lond. Ser. A 302 (1968) 409.
153. S.N. Kaul, P.D. Babu, J. Phys. Condens. Matter 10 (1998) 1563 – 1597.
154. S.N. Kaul, P.D. Babu, Phys. Rev. B 50 (1994) 9308 – 9322.
155. J. Thoene, S. Chadov, G. Fecher1, Claudia Felserand, J€urgen Kubler, J. Phys. D Appl. Phys. 42 (2009) 084013 – 084018.
156. A. Hirohata, J. Sagar, L. Lari, L.R. Fleet, V.K. Lazarov, Appl. Phys. A 111 (2013) 423 – 430.
157. N. Patra, A. Biswas, C.L. Prajapat, A. Ghosh, P.U. Sastry, S. Tripathi, P.D. Babu, Arup Biswas, S.N. Jha, D. Bhattacharyya, J. Alloy. Comp. 723 (2017) 1098 – 1112.
158. N. Patra, C.L. Prajapat, R. De, K.D. Rao, P.D. Babu, A.K. Sinha, Siju John, H.C. Barshilia, S.N. Jha, D. Bhattacharyya, J. Alloy. Comp. 748 (2018) 653 – 670.
159. N. Patra, C.L. Prajapat, P.D. Babu, S. Rai, S. Kumar, S.N. Jha, D. Bhattacharyya, J. Alloy. Comp. 779 (2019) 648 – 659.
160. M.S. Gabor, M. Belmeguenai, T. Petrisor Jr., C. Ulhaq-Bouillet, S. Colis, C. Tiusan, Phy. Rev. B 92 (2015) 054433.
161. R. Mohankumar, M. Manivel Raja, J. Kumar, J. Cryst. Growth 468 (2017) 220 – 224.
162. Y. Takamura, T. Suzuki, Y. Fujino, S. Najagawa, J. Appl. Phys. 115 (2014) 17C732.
163. Weihua Zhu, Di Wu, Bingcheng Zhao, Zhendong Zhu, Xiaodi Yang, Zongzhi Zhang, Q.Y. Jin, Phys. Rev. Appl. 8 (2017) 034012.
164. M. Zander, J. Herfort, K. Kumakura, H.-P. Sc€ohnherr, A. Trampert, J. Phys. D Appl. Phys. 43 (2010) 305004.
165. Shinya Yamada, Kohei Tanikawa, Soichiro Oki, Makoto Kawano, Masanobu Miyao, Kohei Hamaya, International Conference on Solid State Devices and Materials, Fukuoka, 2013, pp. 1074 – 1075.
166. J.K. Bal, S. Hazra, Phys. Rev. B 75 (2007) 205411 – 205416.
167. B. Deka, A. Srinivasan, Physica B 476 (2015) 118 – 121.
168. X.Y. Xiong, T.R. Finlayson, B.C. Muddle, J. Phys. D Appl. Phys. 34 (2001) 2845.
169. Di Wu, Z. Zhang, Li Le, Z. Zhang, H.B. Zhao, J. Wang, B. Ma, Q.Y. Jin, Sci. Rep. 5 (2015) 12352.
170. Arenholz, E. & Prestemon, S. O. (2005). Rev. Sci. Instrum. 76, 083908. Baudelet, F., Nataf, L. & Torchio, R. High. Press. Res. 36, (2016), 429–444.
171. Koizumi, A., Takagaki, M., Suzuki, M., Kawamura, N. & Sakai, N. Phy. Rev. B, 61, (2000), R14909.
172. H.C. Kandpal, G. H. Fecher and C. Felser, J. Phys. D. Appl. Phys. 40 (2007) 1507 – 1523.
173. S.H. Vosko, L. Wilk and M. Nusair. Canadian Journal of Physics 58, 1200 (1980).
174. J.P. Perdew, K. Burke and M. Ernzerhof, Physical Review Letters 77, 3865 (1996).

175. Hung-Lung Huang, Jen-Chuan Tung, and Guang-Yu Guo Phys. Rev. B 91(2015) 134409 – 134415.
176. Benjamin Balke, Sabine Wurmehl, Gerhard H Fecher, Claudia Felserand Jürgen Kübler, Sci. Technol. Adv. Mater. **9** (2008) 014102.
177. Hem Chandra Kandpal, Gerhard H. Fecher, and Claudia Felser, Gerd Schönhense. Phys. Rev. B **73**, (2006) 094422.
178. D. A. Kukusta, V. N. Antonov, and A. N. Yaresko, Low Temperature Physics **37** (2011) 684 – 689.
179. Lalrinkima Siakeng, Gennady M Mikhailov, and D. P. Rai, Journal of Materials Chemistry C (2018) 6 10341 – 10349.
180. Tufan Roy, Arup Banerjee, Rajeev Dutt, J. Nayak, M. Maniraj, S.R. Barman, Aparna Chakrabarti, Journal of Magnetism and Magnetic Materials 466 (2018) 143–149.
181. M Kallmayer, H J Elmers, B Balke, SWurmehl, F Emmerling, G H Fecherand C Felser. J. Phys. D: App. Phys. 39 (2006) 786 – 792.
182. Takahide Kubota, Kenji Kodama, Tetsuya Nakamura, YuyaSakuraba, Mikihiko Oogane, Koki Takanashi, and Yasuo Ando, Appl. Phys. Lett. **95**, (2009) 222503 – 222505.
183. N. D. Telling, P. S. Keatley, G. van der Laan, R. J. Hicken, E. Arenholz, Y. Sakuraba, M. Oogane, Y. Ando, K. Takanashi, A. Sakuma, and T. Miyazaki, Phys. Rev. B **78** (2008)184438 – 184444.